

Beamforming Strategies for Medical Ultrasound Imaging

Mozaffarzadeh, M.

DOI

[10.4233/uuid:31cb9dc9-0bc0-4b87-8ed2-53e9190f2f4f](https://doi.org/10.4233/uuid:31cb9dc9-0bc0-4b87-8ed2-53e9190f2f4f)

Publication date

2022

Document Version

Final published version

Citation (APA)

Mozaffarzadeh, M. (2022). *Beamforming Strategies for Medical Ultrasound Imaging*. [Dissertation (TU Delft), Delft University of Technology]. <https://doi.org/10.4233/uuid:31cb9dc9-0bc0-4b87-8ed2-53e9190f2f4f>

Important note

To cite this publication, please use the final published version (if applicable).
Please check the document version above.

Copyright

Other than for strictly personal use, it is not permitted to download, forward or distribute the text or part of it, without the consent of the author(s) and/or copyright holder(s), unless the work is under an open content license such as Creative Commons.

Takedown policy

Please contact us and provide details if you believe this document breaches copyrights.
We will remove access to the work immediately and investigate your claim.

BEAMFORMING STRATEGIES FOR MEDICAL ULTRASOUND IMAGING

BEAMFORMING STRATEGIES FOR MEDICAL ULTRASOUND IMAGING

Dissertation

for the purpose of obtaining the degree of doctor
at Delft University of Technology
by the authority of the Rector Magnificus, Prof.dr.ir. T.H.J.J. van der Hagen
chair of the Board for Doctorates
to be defended publicly on
Monday 12 December 2022 at 17.30 o'clock

by

Moein MOZAFFARZADEH

Master of Science in Biomedical-Bioelectric Engineering
Tarbiat Modares University, Iran
Born in Sary, Iran

This dissertation has been approved by the promotor.

Composition of the doctoral committee:

Rector magnificus,	voorzitter
Prof.dr.ir. N. de Jong	Technische Universiteit Delft, promotor
Dr.ir. M.D. Verweij	Technische Universiteit Delft, promotor
Dr.ir. G.G.J. Renaud	Technische Universiteit Delft, copromotor

Independent members:

Prof.dr.ir. C.P.A. Wapenaar	Technische Universiteit Delft
Prof.dr. S. Manohar	University of Twente
Prof.dr.ir. C.L. de Korte	Radboud University Medical Center
Dr. G.M. Pinton	University of North Carolina at Chapel Hill



The work in this dissertation was conducted at the laboratory of Medical Imaging, department Imaging Physics, Faculty of Applied Sciences, Delft University of Technology.

Printed by: : proefschrift specialist | www.proefschriftspecialist.nl

Copyright © 2022 by Moein Mozaffarzadeh

ISBN 978-94-6384-371-3

An electronic version of this dissertation is available at
<http://repository.tudelft.nl/>.

This thesis is dedicated to my parents
for their love, endless support and encouragement.

CONTENTS

Summary	xi
Samenvatting	xiii
1 Introduction	1
1.1 Overview of Ultrasound Imaging	1
1.2 Characterization of the pressure field of a disk transducer	3
1.3 Ultrasound beamforming	4
1.4 Transcranial Ultrasound Imaging	4
1.5 Conventional beamforming in transcranial ultrasound imaging	5
1.6 Thesis outline	6
2 Lamb Waves and Adaptive Beamforming for Aberration Correction in Medical Ultrasound Imaging	9
2.1 Introduction	11
2.2 Materials and Methods	12
2.2.1 Sound speed and thickness estimation of a slab	12
2.2.2 Adaptive beamforming.	14
2.2.3 Numerical study	14
2.2.4 Experimental study	14
2.3 Results	16
2.3.1 Longitudinal sound speed estimation	16
2.3.2 In Vitro imaging	16
2.4 Discussion	18
2.5 Conclusion	20
2.6 Erratum	20
3 Refraction-Corrected Transcranial Ultrasound Imaging through the Human Temporal Window using a Single Probe	23
3.1 Introduction	25
3.2 Materials and Methods	26
3.2.1 Compressional wave speed estimation in the aberrator	27
3.2.2 Adaptive beamforming.	28
3.2.3 Numerical study	28
3.2.4 Experimental study	29
3.2.5 Evaluation metrics	29
3.3 Results	30
3.3.1 Numerical results	30
3.3.2 Experimental results	31

3.4	Discussion	34
3.4.1	comparison with previous relevant works	34
3.4.2	Limitations and assumptions of the proposed approach	38
3.4.3	Imaging scheme and implementation	38
3.4.4	Improving cerebral blood flow characterization with TUI and frame rate	39
3.5	Conclusion	39
3.6	Supplementary document	40
4	Accelerated 2D Real-Time Refraction-Corrected Transcranial Ultrasound Imaging	43
4.1	Introduction	45
4.2	Accelerated Ray-Tracing Based Reconstruction	46
4.2.1	Principle of the proposed method	46
4.2.2	GPU implementation	47
4.2.3	Compressional wave speed estimation in the aberrator	49
4.3	Materials and Methods	50
4.3.1	Numerical and Experimental studies.	50
4.3.2	Evaluation metrics	51
4.4	Results	52
4.4.1	Numerical results	52
4.4.2	Experimental results	53
4.4.3	Processing time with the GPU implementation of the ARC technique	55
4.5	Discussion	56
4.5.1	Imaging scheme	56
4.5.2	Analytic signal calculation	58
4.5.3	Limitations of the proposed approach	58
4.5.4	Future work	59
4.6	Conclusion	59
4.7	Supplementary document	59
5	Comparison of Phase-Screen and Geometry-Based Phase Aberration Correction Techniques for Real-Time Transcranial Ultrasound Imaging	61
5.1	Introduction	63
5.2	Materials and Methods	64
5.2.1	Accelerated refraction-corrected geometry-based phase aberration correction	64
5.2.2	Near field phase screen approach	65
5.2.3	Numerical study	66
5.2.4	Experimental study	67
5.2.5	Evaluation metrics	68
5.3	Results	69
5.3.1	Numerical simulations.	69
5.3.2	Experiments	71

5.4	Discussion	72
5.4.1	Advantages and limitations of the near field phase screen technique for ultrafast transcranial ultrasound	72
5.4.2	Advantages and limitations of the Geometry-based phase aberration correction technique for ultrafast transcranial ultrasound	74
5.4.3	Limitations in the implementation of the near field phase screen technique in this work, possible improvements	75
5.4.4	Limitations in the implementation of the geometry-based aberration correction technique in this work, possible improvements.	76
5.5	Conclusion	77
6	Receive/Transmit Aperture Selection for 3D Ultrasound Imaging with a 2D Matrix Transducer	79
6.1	Introduction	81
6.2	Materials and Methods	82
6.2.1	Imaging schemes	82
6.2.2	Numerical studies on beam profile.	84
6.2.3	Experimental study	85
6.3	Results	85
6.3.1	Numerical results: point scatterer	85
6.3.2	Numerical results: cysts phantom	91
6.3.3	Experimental results	91
6.4	Discussion	92
6.5	Conclusion	95
6.6	Supplementary document	95
7	Multi-angle data acquisition to compensate transducer finite size in photoacoustic tomography	99
7.1	Introduction	100
7.2	Materials and methods	101
7.2.1	Effects of finite-size transducer on radial/tangential resolution in PAT.	101
7.2.2	Blind angles and reconstruction range calculation in PAT	102
7.2.3	Proposed method: multi-angle detection geometry	104
7.2.4	Numerical and experimental study	106
7.3	Results	108
7.3.1	Numerical results	108
7.3.2	Experimental results	109
7.3.3	Effects of number of spatial samples	111
7.3.4	Comparison with previous works	111
7.4	Discussion	112
7.4.1	Overview.	112
7.4.2	Limitations of the proposed data acquisition approach	114
7.5	Conclusion	114

8	Design of a Dual-Ring Interstitial Photoacoustic/Ultrasound Imaging Needle	115
8.1	Introduction	116
8.2	Materials and Methods	117
8.2.1	Concept	117
8.2.2	Acoustic stack	117
8.2.3	Numerical study	118
8.2.4	Experimental study	119
8.3	Results	121
8.3.1	Numerical acoustic characterization	121
8.3.2	Raster scanning and imaging	122
8.3.3	Experimental acoustic characterization	122
8.3.4	Experimental photoacoustic imaging	125
8.4	Discussion and conclusion	127
9	Conclusion and recommendations	129
9.1	Conclusion	129
9.2	Recommendations for further research	130
9.2.1	Transcranial ultrasound imaging.	130
9.2.2	multi-angle data acquisition for PACT systems.	131
9.2.3	Imaging Needles	131
	Bibliography	133
	Acknowledgement	157
	Curriculum Vitae	159
	List of Publications	161

SUMMARY

The brain has attracted a growing number of recent ultrasound-related technologies over the past decades. Transcranial ultrasound imaging (TUI) is a diagnostic modality with numerous applications such as stroke diagnosis, detection of vasospasm after subarachnoid hemorrhage (most often caused by head trauma) and microemboli, and endonasal trans-sphenoidal surgery. It is radiation free, relatively inexpensive and available in hospitals and emergency medical services nowadays. Despite its advantages, TUI is still hindered by the low image quality caused by the strong phase aberration and multiple scattering caused by the skull, and mode conversion. Four chapters of this thesis are mainly dedicated to tackle the phase aberration and multiple scattering effects.

First, we investigated a dual-probe setup to minimize multiple scattering artifacts. We imaged a surgical needle (mimicking the electrode(s) in deep brain stimulation procedure) inserted in an Agar phantom (mimicking the brain) from two opposite directions while a polyvinylchloride (PVC) slab was placed in front of the probes as the aberrator. The final image was the minimum intensity projection of the inherently co-registered images of the opposed probes. An adaptive beamforming technique was used to compensate the higher sound speed of the aberrator during image formation. The proposed dual probe configuration shows 7 dB improvement in removing reverberation artifacts of the needle. The limitation of this study was that while the higher sound speed in the aberrator was considered during image formation, wave refraction was ignored.

In our next study, we developed a technique to correct the refraction caused by the temporal bone in single-sided two-dimensional transcranial ultrasound imaging using a commercial (P4-1) probe. The novelty of our approach lies in the fact that it corrects for the true position and the true geometry of the bone layer without the need for CT/MR scans. The results with the bone-mimicking plate and the skull indicated that the proposed method reconstructs image of point-like targets with a nearly 10-fold reduction of the localization error (i.e. reduced shape distortion) and improved contrast (10 dB) and improved spatial lateral resolution (40 %).

The real-time image reconstruction (i.e. at least 20 images per second) is essential in practice as it allows the operator to freely move the probe to find the proper imaging window and imaging plane and look for biomarkers related to a possible brain disorder in either B-mode or flow images. Therefore, in our next work, we introduced an accelerated image reconstruction technique (implemented on a GPU) that corrects for phase aberration and wave refraction caused by the human temporal bone during real time imaging. The two-point ray tracing concept was used to find the shortest (following Fermat's principle) travel-time connecting an image pixel to an array element or a virtual point source (for diverging or plane wave imaging). The introduced approach was not iterative and the near and far surfaces of the bone layer were described in a discrete manner using the image grid points. For an imaging depth of 70 mm, the proposed GPU-implementation allows reconstructing 19 frames per second with full synthetic aperture (96 transmission

events) and 32 frames per second with multi-angle plane wave imaging schemes (with 11 steering angles) for a pixel size of $200\ \mu\text{m}$.

We compared our refraction-corrected TUI method with the near-field phase screen modeling (PS) which was successful in correcting phase aberration during abdominal scanning and applied to diagnostic transcranial ultrasound with focused transmit beams. We used an ultrafast imaging sequence (5 plane waves tilted from -15 to $+15$ degrees in the cutaneous tissue layer) for data acquisition with a single transducer. With simulation data, the aberration profile (AP) of two aberrator models (flat and realistic temporal bone) was estimated in five isoplanatic patches while the wave-speed of the brain tissue surrounding the point targets was either modeled homogeneous (ideal) or slightly heterogeneous to generate speckle to mimic a more realistic brain tissue. For comparing the performance of the two phase-aberration correction methods, the images with the two aberrator models and 30 point-targets in a homogeneous brain tissue were reconstructed. The numerical results indicated that while all scatterers are detectable in the image reconstructed by the our method method, many scatterers are not detected with the PS method when the dataset used for AP estimation is generated with a realistic bone model and a heterogeneous brain tissue. Our comparison study suggests that our refraction corrected TUI method outperforms the PS method when an ultrafast multi-angle plane wave sequence is used for transcranial imaging with a single transducer.

Next, we evaluated the effects of receive/transmit parameters on the image quality provided by a linear array in which elements were mutually interconnected, which mimics the elevation direction of our prototype 2D matrix transducer. The parameter selection procedure was based on the effective covered aperture size, level of grating lobes, and resolution/sidelobes. The proposed imaging sequence provided a volume rate of 1000 per second, which is needed for applications such as carotid pulse wave imaging. An angular weighting method based on the directivity pattern of the transducer elements was also used to suppress the grating lobes caused by interconnecting the elements and increment of the effective pitch.

We introduced an acquisition technique to mimic a point-like transducer and evaluated the proposed technique in a photoacoustic computed tomography system through numerical and experimental studies. The transducer used for data acquisition rotates around its center (with specific angles) as well as around the scanning center. The angles were calculated based on the central frequency and diameter of the transducer and the radius of the region-of-interest. Our results showed that a location-independent tangential resolution is obtained by the proposed method.

In the last chapter of this thesis, the design and evaluation of an imaging needle (which can be used for endoscopic third ventriculostomy and brain abscess draining) was reported. A two-ring annular array was deigned such that they have the same sensitivity (surface area). A delay-and-sum beamforming was used to increase the on-axis sensitivity of the array. The results showed that that one ring works as good as two rings considering the space available for the ring transducer(s).

SAMENVATTING

De hersenen hebben de afgelopen decennia een groeiend aantal recente ultrageluid gerelateerde technologieën aangetrokken. Transcraniële echografie (TUI) is een diagnostische modaliteit met talrijke toepassingen zoals de diagnose van een beroerte, detectie van vasospasme na subarachnoïdale bloeding (meestal veroorzaakt door hoofdtrauma) en micro-embolie, en endonasale trans-sphenoïdale chirurgie. Het is stralingsvrij, relatief goedkoop en tegenwoordig verkrijgbaar in ziekenhuizen en bij spoedeisende hulpdiensten. Ondanks de voordelen wordt TUI nog steeds gehinderd door de lage beeldkwaliteit veroorzaakt door de sterke fase-aberratie en meervoudige verstrooiing veroorzaakt door de schedel en mode omschakeling. Vier hoofdstukken van dit proefschrift zijn voornamelijk gewijd aan het aanpakken van de fase-afwijking en meervoudige verstrooiingseffecten.

Ten eerste hebben we een opstelling met twee transducers onderzocht om meerdere verstrooiingsartefacten te minimaliseren. We beeldden een chirurgische naald af (die de elektrode(s) nabootste in een diepe hersenstimulatieprocedure) ingebracht in een agar-fantom (die de hersenen nabootste) vanuit twee tegengestelde richtingen, terwijl een polyvinylchloride (PVC) plaat voor de transducers werd geplaatst als de aberrator. Dit resulteerde in de minimale intensiteitsprojectie van de inherent co-geregistreerde beelden van de tegenoverliggende transducers. Een adaptieve bundelvormingstechniek werd gebruikt om de hogere geluidssnelheid van de aberrator tijdens beeldvorming te compenseren. De voorgestelde dubbele transducerconfiguratie laat een verbetering van 7 dB zien bij het verwijderen van reverberatie artefacten van de naald. De beperking van deze studie was dat de golfbreking werd genegeerd, terwijl de hogere geluidssnelheid in de aberrator werd meegenomen tijdens de beeldvorming.

In onze volgende studie ontwikkelden we een techniek om de breking te corrigeren die wordt veroorzaakt door het slaapbeen in enkelzijdige tweedimensionale transcraniële echografie met behulp van een commerciële (P4-1) transducer. Onze vernieuwende aanpak corrigeert voor de ware positie en de ware geometrie van de botlaag zonder gebruik te maken van CT/MR-scans. De resultaten met de bot nabootsende plaat en de schedel lieten zien dat de voorgestelde methode puntachtige doelen reconstrueert met een bijna 10-voudige vermindering van de lokalisatiefout (d.w.z. verminderde vormvervalsing), verbeterd contrast (10 dB) en verbeterde ruimtelijke laterale resolutie (40 %).

De real-time beeldreconstructie (d.w.z. ten minste 20 beelden per seconde) is essentieel in de praktijk, omdat het de laborant in staat stelt de transducer vrij te bewegen om de juiste positie en beeldvlak te vinden en te zoeken naar biomarkers die verband houden met een mogelijke hersenaandoening in zowel B-mode als bloedstromings afbeeldingen. Daarom hebben we in ons volgende werk een versnelde beeldreconstructietechniek geïntroduceerd (geïmplementeerd op een GPU) die corrigeert voor fase-aberratie en golfbreking veroorzaakt door het menselijke slaapbeen tijdens realtime beeldvorming. Het tweepunts ray tracing-concept werd gebruikt om de kortste (volgens het principe van Fer-

mat) reistijd te vinden die een beeldpixel verbindt met een array-element of een virtuele puntbron (voor divergerende of vlakke golfbeeldvorming). De geïntroduceerde benadering was niet iteratief en de nabije en verre oppervlakken van de botlaag werden apart van elkaar beschreven met behulp van de beeldraasterpunten. Voor een beelddiepte van 70 mm maakt de voorgestelde GPU-implementatie het mogelijk om 19 frames per seconde te reconstrueren met volledig synthetisch diafragma (96 transmissiegebeurtenissen) en 32 frames per seconde gebruik makend van plane wave imaging-schema's met 11 stuurhoeken voor een pixel grootte van 200 μm .

We vergeleken onze refractie-gecorrigeerde TUI-methode met de near-field phase screen-modellering (PS) die succesvol was in het corrigeren van fase-afwijkingen tijdens abdominale scanning en toegepast op diagnostische transcraniële echografie met gefocuseerde ultrageluid bundels. We gebruikten een ultrasnelle beeldvormingssequentie (5 plane waves gekanteld van -15 tot +15 graden in de huidweefsellaag) voor data-acquisitie met een enkele transducer. Met simulatiegegevens werd het aberratieprofiel (AP) van twee aberrator modellen (plat en realistisch slaapbeen) geschat in vijf isoplanatic patches, terwijl de golfsnelheid van het hersenweefsel rond de puntdoelen homogeen (ideaal) of enigszins heterogeen werd gemodelleerd om speckels te genereren om realistischer hersenweefsel na te bootsen. Om de prestaties van de twee fase-afwijkingscorrectie methodes te vergelijken, werden de beelden met de twee aberrator modellen en 30 puntdoelen in een homogeen hersenweefsel gereconstrueerd. De numerieke resultaten gaven aan dat hoewel alle verstrooiers detecteerbaar zijn in de afbeelding die is gereconstrueerd met onze methode, veel verstrooiers niet worden gedetecteerd met de PS-methode wanneer de dataset die wordt gebruikt voor AP-schatting wordt gegenereerd met een realistisch botmodel en een heterogeen hersenweefsel. Onze vergelijkende studie suggereert dat onze voor breking gecorrigeerde TUI-methode beter presteert dan de PS-methode wanneer een ultrasnelle multi-angle plane wave-sequentie wordt gebruikt voor transcraniële beeldvorming met een enkele transducer.

Vervolgens evalueerden we de effecten van ontvangst-/zendparameters op de beeldkwaliteit die wordt geleverd door een lineaire array waarin elementen onderling met elkaar zijn verbonden, wat de elevatierichting van ons prototype 2D-matrixtransducer nabootst. De parametersselectieprocedure was gebaseerd op de effectieve grootte van de afgedekte opening, het niveau van de grating lobes en de resolutie/zij lobes. De voorgestelde beeldvormingssequentie leverde 1000 volumes per seconde op, wat nodig is voor toepassingen zoals halsslagader pulsgolf beeldvorming. Een hoek afhankelijke reconstructie methode gebaseerd op het richtingspatroon van de transducerelementen werd ook gebruikt om de grating lobes te onderdrukken die worden veroorzaakt door de vergrote effectieve pitch ten gevolgen van de onderliggende connectie van elementen.

We introduceerden een acquisitietechniek om een puntachtige transducer na te bootsen en evalueerden de voorgestelde techniek in een foto akoestisch computertomografiesysteem door middel van numerieke en experimentele studies. De transducer die wordt gebruikt voor data-acquisitie roteert zowel rond het midden (met specifieke hoeken) als rond het scancentrum. De hoeken werden berekend op basis van de centrale frequentie en diameter van de transducer en de straal van het interessegebied. Onze resultaten toonden aan dat een locatie-onafhankelijke tangentiële resolutie wordt verkregen door de voorgestelde methode.

In het laatste hoofdstuk van dit proefschrift wordt het ontwerp en de evaluatie van een beeldvormende naald (die kan worden gebruikt voor endoscopische derde ventriculostomy en drainage van hersenabcessen) beschreven. Een ringvormige array met twee ringen is zo ontworpen dat ze dezelfde gevoeligheid (oppervlakte) hebben. Delay-and-sum beamforming wordt gebruikt om de gevoeligheid op de as van de array te vergroten. De resultaten toonden aan dat één ring net zo goed werkt als het gebruik van twee ringen, rekening houdend met de beschikbare ruimte voor de ringtransducer(s).

1

INTRODUCTION

1.1. OVERVIEW OF ULTRASOUND IMAGING

Sound is an acoustic wave that we can hear because its frequency is in the human auditory band (20 Hz-20 kHz). When the frequency of the acoustic wave is higher than 20 kHz, it is called Ultrasound, which has turned out to be useful for many applications over the past decades. Important advances have been made toward using ultrasound waves to see the internal structure of human body over the past 50 years. Between July 2016 to 2017, over 9.2 million ultrasound scans were conducted in National Health Service (NHS) patients in England. This is twice the number of computed tomography (CT) scans and three times the number of magnetic resonance imaging (MRI) scans conducted during the same period [1]. Compared to CT and MRI, ultrasound imaging is free from radiation (non-ionizing), portable (can be used at bed-site and emergency medicine services) and relatively inexpensive.

Ultrasound waves travel through the body by transferring the mechanical energy from a local change in the stress or pressure field in the medium (generated by an ultrasound transducer). The transmitted wave interacts with the organ and generates reflection/backscattered waves (ultrasound echo) due to differences between the acoustical properties of the tissue and the organ (see Figure 1.1). These echoes are then detected by the ultrasound transducer and used to form an ultrasound image. The image is finally displayed on a screen.

There are three ways to show the ultrasound echoes:

1. A-mode: This stands for amplitude mode. It is generated as a result of transmit and receive along a scanline. Assuming a constant sound speed for the medium, the round trip travel times of echoes converts to distance between the transducer and the reflecting objects and therefore the scanline shows the amplitude as a function of the axial distance (i.e. depth).
2. B-mode: This stands for brightness mode. It is generated by swiping the scanline over different parts of the medium. As each scanline represents the echo amplitude

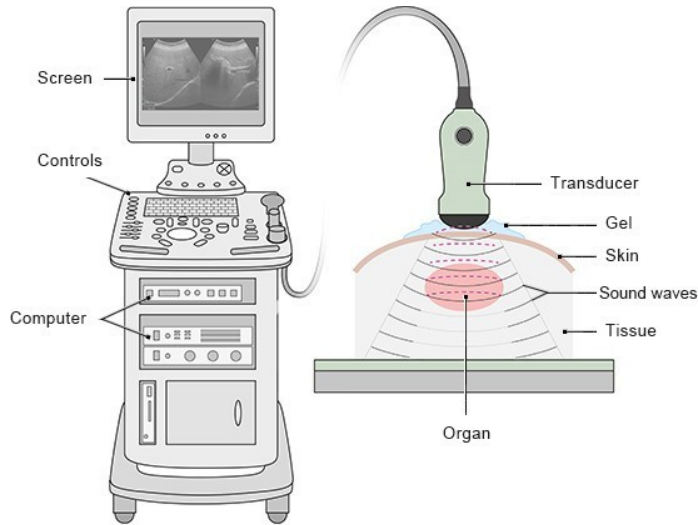


Figure 1.1: A schematic on how ultrasound imaging is carried out [2].

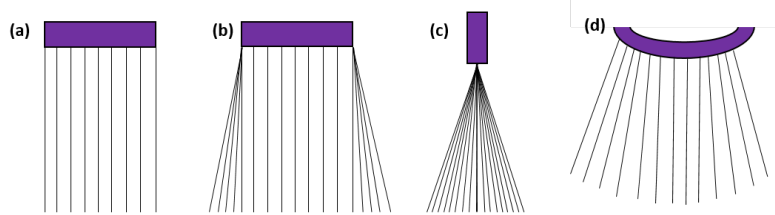


Figure 1.2: Most commonly used B-mode image formats in ultrasound imaging. (a) Linear, (b) Trapezoidal, (c) Sector and (d) Convex.

as a function of depth, it is possible to form B-mode 2D images in which the amplitude converts to the pixel brightness, after envelope detection, and the swiping direction converts to the lateral spatial axis.

3. M-mode: This stands for motion mode and is used to represent the motion of an organ over time along one single scanline. It is obtained by repeating rapidly an A-mode acquisition.

The most commonly used B-mode image formats are presented in Figure 1.2. Panel (a) shows the linear format where the B-mode lines are perpendicular to the surface of the probe and result in rectangular images. The trapezoidal format (Figure 1.2(b)) enables imaging superficial organs as good as the linear format (Figure 1.2(a)) with a wider field of view to also properly image organs in deeper regions. The sector and convex formats provide a wide field of view for organs at higher depths; for example, it is a great choice for imaging of heart because transmit focused beams can pass through the space between

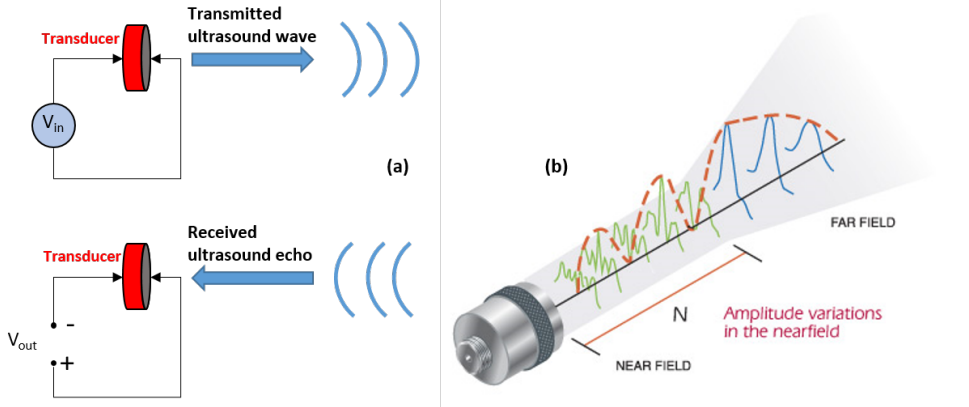


Figure 1.3: (a) An ultrasound transducer acting as transmitter and receiver. (b) A single element plane disk ultrasound transducer [4];

the ribs. Convex images are also very common for abdominal scans. Real time (i.e. more than 20 images per second) in all the four formats is available with ultrasound imaging machines available in medial centers nowadays.

1.2. CHARACTERIZATION OF THE PRESSURE FIELD OF A DISK TRANSDUCER

A transducer is made of a piezoelectric material which converts electrical energy to acoustic wave and the other way around (see Figure 1.3(a)). Usually, it is designed such that it mainly vibrates along the thickness direction (i.e., a piston-like behavior) so that all the surface moves backwards and forwards in phase and with the same amplitude [3]. The natural resonance frequency of a transducer is determined by its thickness. As frequency decreases, the imaging depth increases because ultrasound attenuation in biological tissues increases with frequency. With a higher frequency, the spatial resolution increases.

In medical ultrasound imaging, it is always desired to have better spatial resolution to produce distinct echoes from interfaces. While the lateral resolution mainly depends on the central frequency of the transducer and the size of the transducer aperture, the axial resolution is determined by the bandwidth of the transducer (the frequency range at which the transducer has a relatively high energy conversion efficiency). Although transmission of short ultrasound pulses is desired, but the transmitted waveform is mainly determined by the impulse response of the transducer and the electrical excitation signal (typically a few cycles at the center frequency of the transducer bandwidth).

One simple example of a single element ultrasound transducer is a plane disk transducer (see Figure 1.3(b)). The near field distance N represents the natural focus of the transducer. The pressure in the near field has many peaks and dips, which makes this region not suitable for imaging. At the end of the near field, all the partial waves start to sum coherently and form a strong maximum. In the far field, the pressure progressively decreases. The near field of a plane disk transducer (if wavelength $\ll D$) ends at the focal

distance and it given by:

$$F = D^2 f / 4c, \quad (1.1)$$

where c is the sound speed in the medium (assumed 1540 m/s), f is the ultrasound frequency, D is the diameter of the disk transducer.

In order to calculate the pressure field at an arbitrary point $P(R, \theta)$ in the medium (R and θ are the radial distance and degree with respect to the center of the transducer, respectively), the contribution of the all the point-like elements on the surface of the transducer should be integrated. This results (in the far-field approximation) in [5]

$$P(R, \theta) = [\pi a^2 P_0] \left[\frac{e^{j(\omega t - kR)}}{R} \right] \left[\frac{2J_1(k a \sin \theta)}{(k a \sin \theta)} \right], \quad (1.2)$$

where J_1 is the Bessel functions of order 1, a is the radius of the disk, P_0 is the pressure at the surface of the transducer, ω is the angular frequency, t is the time, and k is the wavenumber. Assuming that the mainlobe can be approximated with a cone, the cone head angle ϕ can be approximated by

$$\phi = \sin^{-1} \left(\frac{0.61c}{af} \right) \quad (1.3)$$

1.3. ULTRASOUND BEAMFORMING

Beamforming is a synonym of image reconstruction. It consists in back-propagating the recorded echoes to the reflecting objects that created them. The most common algorithm for image reconstruction is called delay-and-sum. As can be seen in Figure 1.4, the echoes coming from a target (the black circle) are detected by the red elements with a time delay (see the blue dashed line). After applying opposite time delays (calculated based on the location of the target and the elements of the array), the signals become coherent (the green echoes in Figure 1.4). Finally, the summation of the echo signals results in a large echo signal from the desired focal zone (the location of the target). The time delay t calculated for element i is calculated by:

$$t_i = d_i / c, \quad (1.4)$$

where d_i is the distance between the focal zone and i^{th} element. Note that the same procedure can be applied in transmit to obtain transmit focusing at a given point in the scanned medium.

1.4. TRANSCRANIAL ULTRASOUND IMAGING

Real-time ultrasound imaging of the brain started in the late sixties with the development of the first electronic two-dimensional scanner developed by Somer [6]. Decades after, transcranial ultrasound imaging (TUI) remains very challenging and offers poor image quality compared to ultrasound imaging of many other body regions. TUI is often performed through the temporal window (the thinnest part of the skull that gives the best ultrasound access to the brain) where the squamous part of the temporal bone often consists of a single layer of cortical bone [7]–[10]; see Figure 1.5. Poor image quality of TUI results from strong wave aberration [11] and multiple scattering caused by the skull [12],

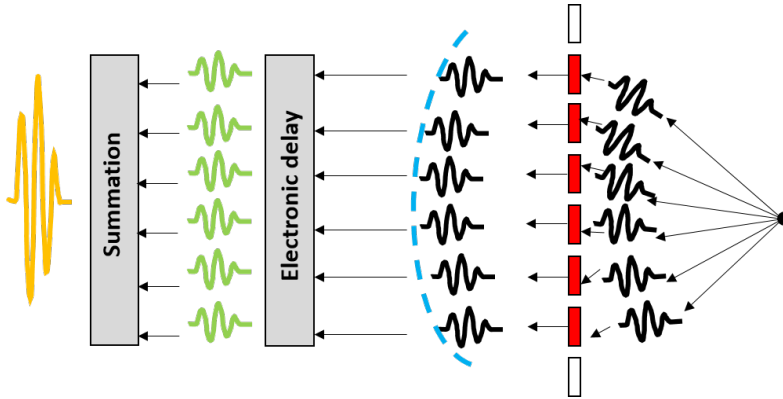


Figure 1.4: The delay-and-sum beamforming technique to create a receiving focus.

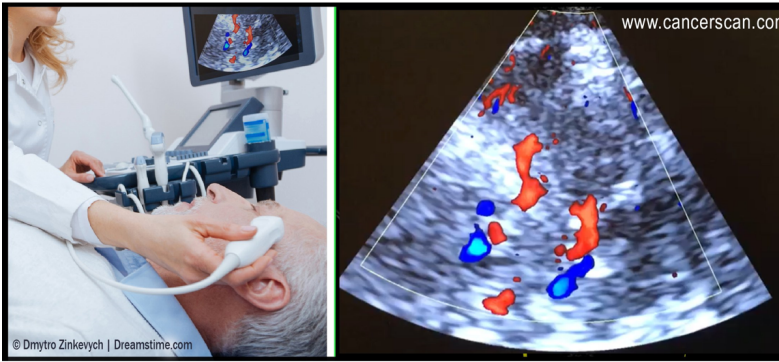


Figure 1.5: Transcranial ultrasound imaging through the temporal window [26].

[13]. Despite its poor image quality, TUI was shown to be useful for the diagnosis of stroke [14]–[20], prevention of stroke in children (between an age of 2 and 16) with sickle cell disease [21]–[23], and vasospasm detection after subarachnoid hemorrhage [24], [25].

1.5. CONVENTIONAL BEAMFORMING IN TRANSCRANIAL ULTRASOUND IMAGING

Current commercial TUI devices use traditional focused transmit beams that are not ideal for transcranial imaging. Moreover, they ignore the skull and use simple triangulation to calculate the travel time between each pixel of the image and array elements (Equation 1.4). To better clarify where the problem comes from, see Figure 1.6(a) where the medium is discretized. A single-element synthetic aperture imaging scheme is used for transmission. Elements s and r are the transmitter and receiver, respectively, and the goal is to determine the intensity of the red pixel. The round trip distance is the distance from element s to the red pixel plus that from the red pixel to the element r . Assuming that the

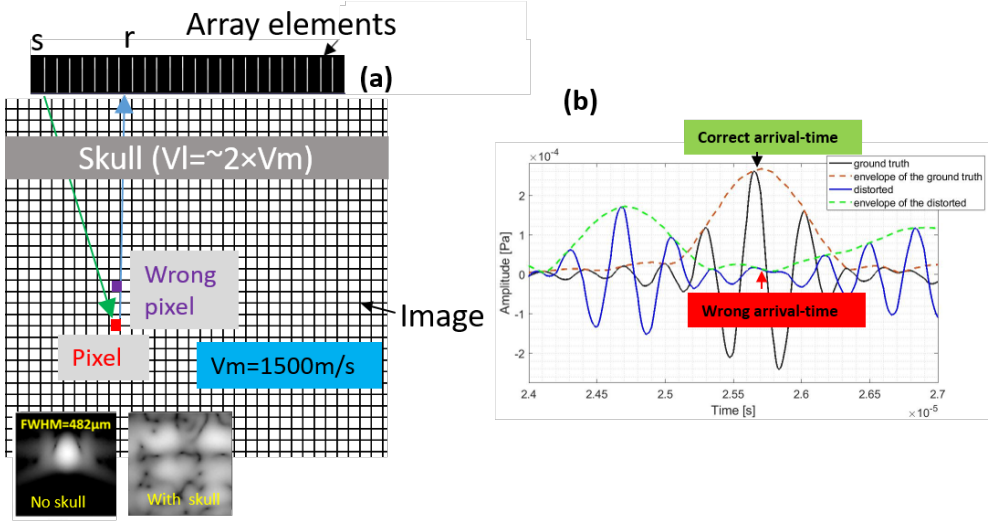


Figure 1.6: (a) Conventional travel time calculation using triangulation. (b) The zoomed version of the detected echo signal by element s in (a).

sound speed of the medium is known and constant (1500 m/s)- this is a fair assumption when imaging most of tissues in human body-, the parameter t in Equation 1.4 can be calculated. Note that this t is the correct travel time when there is no skull in the medium. Assuming that there is a scatterer at the location of the red pixel, the calculated t should correspond to the maximum of the detected echo (see the black arrow and signal in Figure 1.6(b)). The sample received at time t is summed up for all combinations of transmitter and receiver and the result indicates the brightness of the red pixel. If we do it for the red pixel and some of the pixels around it, the image titled "no skull" will be obtained, which has a decent quality.

When there is a skull layer in the medium, the echo wavefront gets distorted and arrives at an earlier time (compared to a homogeneous medium) at the location of the element s due to the higher sound speed in the skull (see the blue signal in Figure 1.6(b)). Therefore, using the procedure explained above results in a wrong travel time (see the red arrow in Figure 1.6(b) where it points out to a low amplitude sample), a significantly degraded image quality (see the image titled "with skull" in Figure 1.6(a)), and detecting the scatterer at lower depths (the pink pixel in Figure 1.6(a)). This problem could be addressed if we could correctly account for the bone layer during the calculation of the travel times.

1.6. THESIS OUTLINE

In this thesis the following outline is used.

- Chapter 2 introduces a dual-probe setup developed to track the electrodes/needles used in surgeries such as deep brain stimulation. A PVC slab was used as the ablator that mimics the temporal bone.

- Chapter 3 introduces a technique which enables refraction-corrected transcranial ultrasound imaging through the temporal window. The true position and geometry of the bone layer was estimated and then used for refraction correction during beamforming.
- Chapter 4 proposes a resource-efficient ray tracing technique. This technique along with the adaptive beamforming (taking into account the correct travel times) are implemented on a GPU, which enabled real time refraction-corrected transcranial ultrasound imaging with a 1D probe.
- Chapter 5 is a comparison study between the most common phase aberration compensation technique (called phase screen modeling) and the approach proposed in Chapters 3 and 4. This chapter is our final study on transcranial ultrasound imaging in this thesis.
- Chapter 6 reports a shifting aperture scheme and investigate the effects of receive/transmit aperture size and aperture shifting step in the elevation direction of a 2D matrix transducer. The row-level circuit is used to interconnect elements of a receive aperture in the elevation (row) direction.
- Chapter 7 presents a data acquisition approach for photoacoustic computed tomography systems. Using the proposed approach, the wide directivity pattern of a point-like transducer becomes feasible.
- Chapter 8 presents our numerical evaluation of the design and imaging with an annular two-ring array, which can be used as a guidance tool for endoscopic third ventriculostomy (to reduce the intracranial pressure) and brain abscess draining
- Chapter 9 describes the main conclusions derived from this thesis, followed by recommendations for future research.

2

LAMB WAVES AND ADAPTIVE BEAMFORMING FOR ABERRATION CORRECTION IN MEDICAL ULTRASOUND IMAGING¹

Phase aberration in transcranial ultrasound imaging (TUI) caused by the human skull leads to an inaccurate image reconstruction. In this paper, we present a novel method for estimating speed of sound and an adaptive beamforming technique for phase aberration correction in a flat polyvinylchloride (PVC) slab as a model for the human skull. First, the speed of sound of the PVC slab is found by extracting the overlapping quasi-longitudinal wave velocities of symmetrical Lamb waves in the frequency-wavenumber domain. Then, the thickness of the plate is determined by the echoes from its front and back side. Next, an adaptive beamforming method is developed, utilizing the measured sound speed map of the imaging medium. Finally, to minimize reverberation artifacts caused by strong scatterers (i.e. needles), a dual probe setup is proposed. In this setup, we image the medium from two opposite directions, and the final image can be the minimum intensity projection of the inherently co-registered images of the opposed probes. Our results confirm that the Lamb wave method estimates the longitudinal speed of the slab with an error of 3.5% and is independent of its shear wave speed. Benefiting from the acquired sound speed map, our adaptive beamformer reduces (in real-time) a mislocation error of 3.1 mm, caused by an 8 mm slab, to 0.1 mm. Finally, the dual probe configuration shows 7 dB improvement in removing reverberation artifacts of the needle, at the cost of only 2.4 dB contrast loss. The

¹This chapter has been published as:

Mozaffarzadeh et al., "Lamb Waves and Adaptive Beamforming for Aberration Correction in Medical Ultrasound Imaging," IEEE TUFFC. 68(1), 2020.

The text and notation used in this chapter may differ on minor details from the actual publication. This is done to achieve consistency between chapters.

proposed image formation method can be used e.g. to monitor deep brain stimulation procedures and localization of the electrode(s) deep inside the brain from two temporal bones on the sides of the human skull.

Keywords; *Transcranial ultrasound imaging, Lamb waves, adaptive beamforming, sound speed map, deep brain stimulation.*

2.1. INTRODUCTION

Transcranial ultrasound imaging (TUI) is a practical tool in neurology and a good candidate to monitor the brain [27], [28]. This imaging modality is cheap, user-friendly, accurate and commercially available nowadays in most of hospitals and clinics [28], [29]. However, the image quality is limited by the strong aberrating effect of the skull bone [12], [30], [31]. The sound speed and density are much larger, compared to soft brain tissues, which leads to high reverberations within the skull, large aberrations and a high absorption of the acoustic energy [32]–[35].

Ultrasound beamforming techniques usually assume a constant speed of sound [36]–[40], which leads to suboptimal focusing and image quality and accuracy. Over the past decades, researchers have been investigating to compensate the effects of the phase aberration from different perspectives (i.e. developing new algorithms and imaging setups) [41]–[43]. A wavevector-frequency domain model of the ultrasound wave propagation from a hemisphere-shaped transducer has been developed, using CT scans of the head, to non-invasively obtain an accurate focusing through the human skull for ultrasound therapy [44]. Thickness and density information obtained from CT images can also be directly used to correct the phase aberration induced by the skull [34], [45], [46]. In a study by Yin Xiangtao and Kullervo Hynynen [47], low frequency ultrasound is used to reduce the effects of the skull. A low frequency, e.g. 250 KHz, results in less attenuation and aberration, which makes the bone more transparent. The drawback of this method is its poor resolution. Another method is the time-reversal aberration correction introduced in [32], [48]–[50]. These methods usually require an invasive experimental setup for computation of the time reversed signals. A non-invasive time reversal-based technique using a dual-transducer setup has also been reported [12]. This non-invasive extension shows promising results in improving the focal spot, thus the image quality. However, it requires complex multistep modeling and processing and has not yet been used for real time imaging.

The method described by Renzel et al. [51] and implemented in Krautkramers Auto-V technology uses a combination of four transducers mounted on a multifaceted wedge. Two of these probes are oriented obliquely to the sample to launch and receive a longitudinal creeping wave along its surface. These probes provide a measurement of the sound speed. The other pair of probes sends and receives the waves through the sample, providing data for measuring its thickness. The draw back with this system is that the 4-probe technique is very complex, time consuming and very difficult to be applied for TUI. An ultrasound brain helmet has also been designed for simultaneous 3D ultrasound imaging (USI) [52]–[54]. This helmet is designed in a way that each matrix array helps the other one in phase aberration correction by being a correction source [55]. The cross-correlation of RF signals is also used to this end. The helmet has been used for 3D transcranial Doppler imaging as well [56].

A dual-array ultrasound imaging system has been designed to calculate the approximate aberration of the skull using two arrays placed on the opposing sides of the skull, one on each of the parietal (or temporal) bones. In this system, at each transmission and reception, the information regarding the wavefront achieved on attenuation and phase is used to compensate the phase aberration [12].

In this paper, we report on a method using dispersion curves of the Lamb waves for

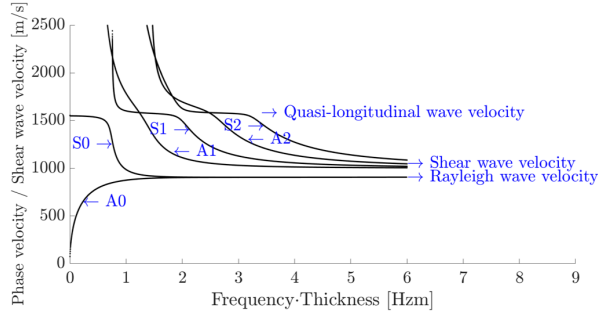


Figure 2.1: Lamb wave dispersion curves for a free plate with a longitudinal wave speed of 1581 m/s, a shear wave speed of 1000 dm/s, and a thickness of 0.2 m [58].

determining the sound speed in a flat polyvinylchloride (PVC) slab as a model for the human skull. The method benefits from many modes of vibration generated in the frequency range of 1 to 4 MHz in the plate. Then, the pulse-echo signals are used to measure the thickness of the plate. Finally, an average sound speed map is constructed, and an adaptive delay-and-sum (DAS) beamformer forms a phase compensated image. The proposed image reconstruction scenario is evaluated with simulations and in-vitro experiments. To minimize the reverberation artifact, a dual-probe setup is developed in which the medium is imaged from two opposite directions.

2.2. MATERIALS AND METHODS

2.2.1. SOUND SPEED AND THICKNESS ESTIMATION OF A SLAB

Lamb waves, which are generated once a solid plate is insonified with a wave, are commonly used in non-destructive-testing [57]. The shape of the Lamb waves depends on the frequency, the insonification angle, the thickness of the insonified media and its acoustic properties. Figure 2.1 shows the Lamb wave dispersion curves for a free plate. Each mode only exists above a certain frequency (called nascent frequency). If we increase the frequency (having other parameters constant), a higher number of modes will be generated as there is no upper frequency limit for any of the modes. At high frequencies, the first symmetric and asymmetric modes (S0 and A0) approach the Rayleigh wave velocity. In contrast, all higher modes approach the shear wave velocity of the plate. At low frequencies, the S0 dispersion curve approaches the quasi-longitudinal wave velocity. The same applies for all the higher S-modes at a certain frequency, where they form a plateau. Generally, only one or very few Lamb wave modes are generated by tuning the excitation frequency (see Figure 2.1); this happens in the low-frequency range due to the inherent cut-off frequencies of individual modes. This makes it possible to fit the numerical data obtained by Rayleigh-Lamb equations on the generated modes in order to obtain the longitudinal wave speed of the insonified material [58]. The Rayleigh-Lamb equations are:

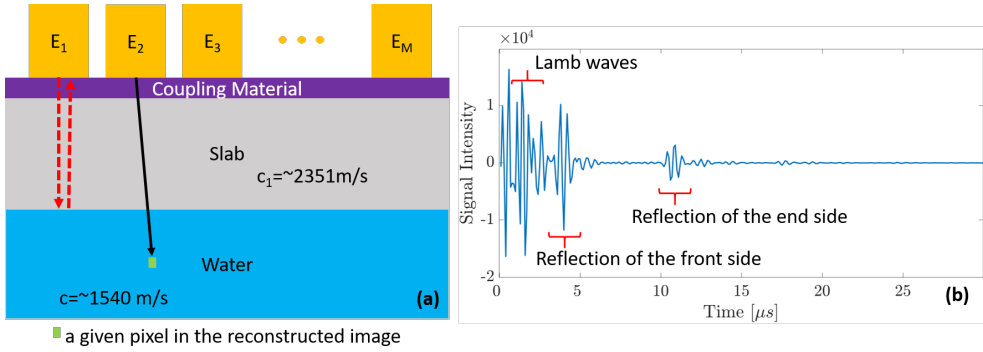


Figure 2.2: (a) Schematic of the pulse-echo technique (red arrows). The black arrow shows the path connecting an element to a pixel of the reconstructed image. (b) A-line showing the first and second reflection from two sides of the slab.

$$\begin{aligned}
 \frac{\tan(\beta h/2)}{\tan(\alpha h/2)} &= -\frac{4\alpha\beta k^2}{k^2 - \beta^2} \pm 1 \\
 \alpha^2 &= \frac{\omega^2}{v_l^2} - k^2 \\
 \beta^2 &= \frac{\omega^2}{v_s^2} - k^2,
 \end{aligned} \tag{2.1}$$

where h is the thickness of the slab, ω is the angular frequency, k is the wavenumber, v_l is the compression wave speed or longitudinal speed, and v_s is the shear wave speed [58]. The group speed v_g is defined as the slope of the dispersion curve in the frequency–wavenumber domain [59]:

$$v_g = \frac{d\omega}{dk} \tag{2.2}$$

With a medical ultrasound frequency range (1–4 MHz), many modes are generated by insonifying a slab having thickness and speed of sound similar to those in human skull. Consequently, fitting becomes very difficult. However, the superposition of the different symmetric modes in the frequency–wavenumber (f – k) domain results in a high intensity region where its slope corresponds to the quasi-longitudinal wave speed in the slab. By transferring the temporal–spatial domain data to the f – k domain, then fitting a linear line to the high intensity area (distinguishable with a threshold), and finally multiplying the slope of the line by 2π , the speed of sound in the aberration medium can be measured. Thereafter, we can use the reflection from two sides of the slab [Figure 2.2(b), obtained with the pulse-echo method shown in Figure 2.2(a), to measure the thickness of the slab [60].

2.2.2. ADAPTIVE BEAMFORMING

Knowing the thickness of the slab allows us to compensate the phase in the beamforming step. The DAS beamforming technique is described as follows:

$$y_{DAS}(r) = \sum_{i=1}^M x_i(r - \Delta_{i,r}), \quad (2.3)$$

where $y_{DAS}(r)$ is the beamformed data, r is the time index, M is the number of elements of array, and $x_i(k)$ and $\Delta_{i,r}$ are the received signals and the corresponding time delay for detector i and time index r , respectively [40]. $\Delta_{i,r}$ is calculated based on the distance between the location of the i^{th} element of the array and the focused point (indicated by the time index k):

$$\Delta_{i,k} = 2d_{i,r}/c, \quad (2.4)$$

where $d_{i,k}$ is the one-way distance (between i^{th} element and the focused point) and c is the sound speed (assumed constant) of the imaging medium. For each pixel (focused point) in the image, we calculate the average sound speed from the transducer elements to the pixel; the black arrow in Figure 2.2(a) shows the path which connects an element to a pixel. An average sound speed map for each element can be obtained using the following equation:

$$v_{avg}(j, r) = (lc_1c) / \left(cz_{jr} + (l - z_{jr})c_1 \right), \quad (2.5)$$

where j is the index of the element of the array, l is the number of the imaging grid point existing in the vector which connects the j^{th} element to a pixel [black vector in Figure 2.2(a)], and z_{jr} is the number of imaging grid points having a sound speed of c_1 , influenced by the element number (j) and focused point r . To clarify, c is the sound speed of the medium (i.e., brain) and c_1 is the sound speed of the slab. Finally, we can form a corrected B-mode image using the following equations:

$$\Delta_{j,r,corrected} = d_{j,r}/v_{avg}(j, r). \quad (2.6)$$

$$y_{DAS_{corrected}}(r) = \sum_{j=1}^M x_j(r - \Delta_{j,r,corrected}). \quad (2.7)$$

2.2.3. NUMERICAL STUDY

To evaluate the proposed method of longitudinal wave speed estimation, simulations are conducted in the GUIGUW toolbox [61]. The excitation frequency is 1–4 MHz. The shear speed and longitudinal speed are varied from 800 to 1500 m/s and 1500 to 2500 m/s for a slab with a thickness of 8 mm.

2.2.4. EXPERIMENTAL STUDY

The experimental setup is shown in Figure 2.3. It consists of two aligned P4-1 probes (Philips, 2.5 MHz, 96 elements) connected to the Verasonics Vantage 256 system, a needle (1.27 mm diameter) in an agar phantom, and two slabs (PVC, 8 mm thick, $v_l = 2351$ m/s) each of which is positioned in front of each probe. The setup with two opposing transducers is designed to image the target from two opposite sides resulting in two images

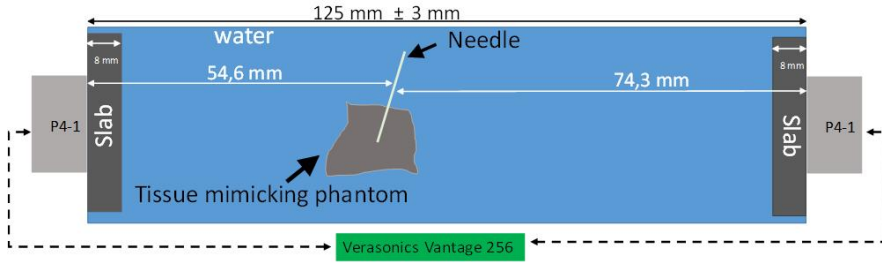


Figure 2.3: Two-probe experimental setup; the slabs have a sound speed of 2351 m/s and a thickness of 8 mm.

which are intrinsically co-registered. To generate Lamb waves in the slab, element 1 of the array is excited, and all the elements act as a receiver of the Lamb waves. This 2-D data set is converted to the frequency-wavenumber domain by a 2-D fast Fourier transform (FFT). To evaluate the performance of the Lamb wave method, we have used materials with different longitudinal velocities: PVC ($v_l = 2351$ m/s [62]), polycarbonates (PC; $v_l = 2220$ m/s [63]), polyetheretherketone (PEEK; $v_l = 2586$ m/s [64]), poly(methyl methacrylate) (PMMA; $v_l = 2727$ – 2750 m/s [62]), and VeroWhite (VW; $v_l = 2495$ m/s). A threshold of -2 dB is used to extract the high intensity region in f-k domain.

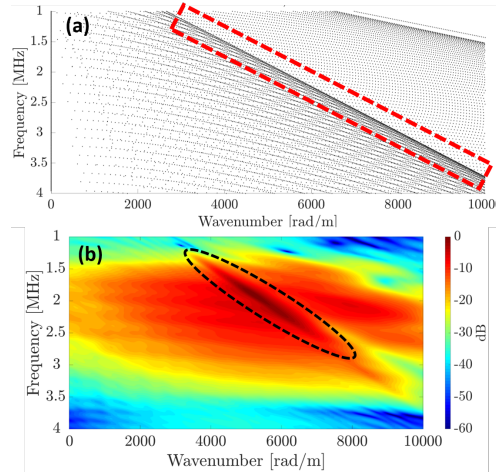


Figure 2.4: (a) Simulation results obtained by GUIGUW software using a material with the same properties as the PVC slab. (b) Experimental results showing the generation of Lamb waves in a PVC plate (a thickness of 8 mm and a longitudinal speed of about 2351 m/s) using a P4-1 probe with a central frequency of 2.5 MHz. The red-dashed rectangle and black-dashed oval indicate the high-intensity area related to the superposition of different symmetric modes.

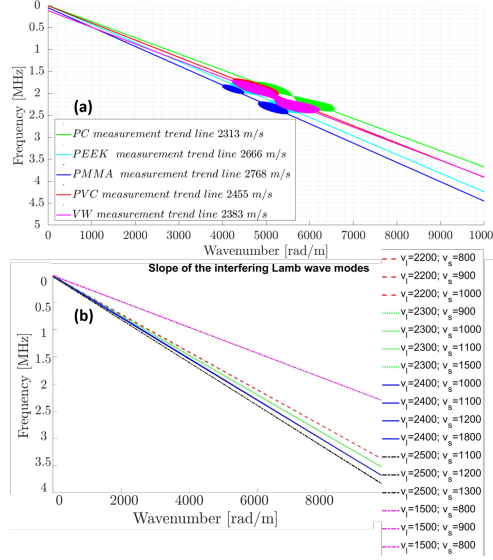


Figure 2.5: (a) Experimental results obtained with a threshold of -2 dB and different materials. (b) Numerical results showing the independency of the Lamb wave method on the shear wave speed of the insonified material.

2.3. RESULTS

2.3.1. LONGITUDINAL SOUND SPEED ESTIMATION

Figure 2.4(a) shows the simulation results for frequencies between 1 and 4 MHz and wavenumbers up to 10 000 rad/m in a PVC slab of 8 mm thickness. Fitting to a single mode is very difficult, as also proven by the experimental Lamb wave dispersion curves presented in Figure 2.4(b). However, the symmetric modes overlap and form a high intensity region [red-dashed rectangle in Figure 2.4(a) and the black-dashed oval in Figure 2.4(b)] with a specific slope which corresponds to the longitudinal wave speed. The results obtained from different materials are presented in Figure 2.5(a). Compared with v_l reported in the literature, the proposed Lamb wave method estimates v_l with an error up to 3.5%. The dependence of the Lamb wave method to the shear wave speed of the slab is shown in Figure 2.5(b). The shear wave speed does not affect the v_l estimation; the graphs for $v_l = 2200$ m/s with different shear wave velocities (800, 900, and 1000 m/s) are overlapped.

2.3.2. IN VITRO IMAGING

Fig. 6 shows the images of the needle acquired with the left-side probe, with and without the slab. The phase aberration leads to 3.1 mm error in the location of the needle [red arrow in Fig. 6(a)]. Using the adaptive beamforming, the target is well-detected at its correct location with an error of 0.1 mm [see Figure 2.6(c)]. The slab causes reverberation artifacts in front of the probe [see Figure 2.6(b) and (c)]. In addition, we see the reverberation

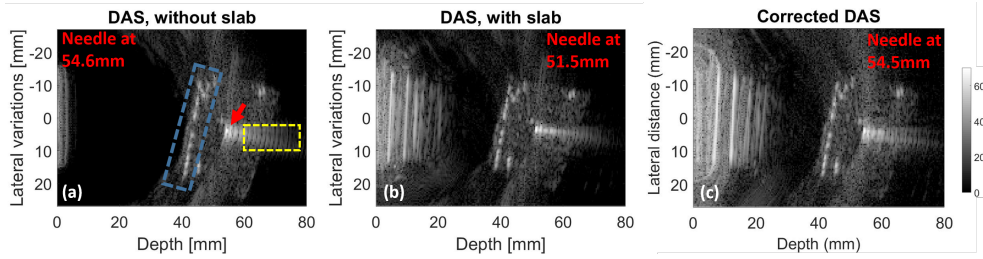


Figure 2.6: Experimental images using DAS (a) without slab, (b) with slab, and (c) with slab and the adaptive beamformer. The red arrow shows the needle. The yellow and blue rectangles show the reverberation effects of the needle and the slab itself, respectively. Images are related to the left probe shown in Figure 2.3.

effect of the needle itself [yellow rectangle in Figure 2.6(a)], due to reflections within the needle [65]. Both the reverberations can be removed using the dual-probe setup shown in Figure 2.7. The overlap of these two images can be used to generate a minimum intensity projection (MIP) image which reduces the reverberation artifacts [65], [66]. The MIP image is the minimum intensity of each pixel in the two images acquired by each of the probes. Thanks to our adaptive beamforming technique, the two images seen by the probes are correctly overlapping [compare Figure 2.7(a) and (c)]. The tissue mimicking phantom (Figure 2.7(b), the green arrow) and the needle inside (Fig. 7(b), the red arrow) in the MIP image are reconstructed with minimal reverberation artifacts [Figure 2.7(d)].

This results in an MIP image similar to that of obtained in the scenario without any slab [compare Figure 2.7(b) and (d)]. In order to quantitatively evaluate the performance of the obtained MIP image, we have defined artifact-to-tissue contrast ratio (ATCR) and

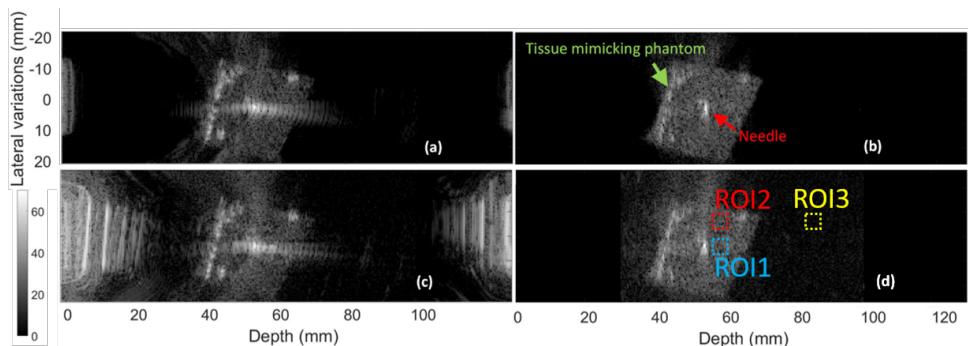


Figure 2.7: (a) Overlapped image while there is no slab. (b) MIP of (a). (c) Corrected overlapped image while there is a slab in front of each transducer. (d) MIP of (c). The Region of Interests (ROIs) shown in (d) are used to quantitatively evaluate the images.

tissue-to-noise contrast ratio (TTCR) as follows:

$$ATCR = 20 \times \log_{10}\left(\frac{I_{artifact}}{I_{tissue}}\right), \quad (2.8)$$

$$TTCR = 20 \times \log_{10}\left(\frac{I_{tissue}}{I_{noise}}\right) \quad (2.9)$$

where $I_{artifact}$, I_{tissue} , and I_{noise} are, as shown in Figure 2.7(d), the mean amplitude of the needle reverberations artifact (ROI1; blue), the mean amplitude of the tissue signal (ROI2; red), and the mean amplitude of the noise (ROI3; yellow), respectively. For the corrected overlapped and MIP images (shown in Figure 2.7(c) and (d), respectively), an ATCR of 6.98 and -0.03 dB is obtained, respectively, proving that the reverberation artifact is suppressed in the MIP image. A TTCR of 20.04 and 17.66 dB is obtained for the corrected overlapped and MIP images, respectively, indicating that the reverberation artifact is suppressed in the MIP image at the expense of a 2.38 dB loss in the image contrast.

2.4. DISCUSSION

The availability of a noninvasive real-time method for in vivo measurement of both sound speed and thickness of the human skull bone is of a great benefit to various transcranial ultrasonic imaging and treatment applications. One of such applications is deep brain stimulation (DBS) in which brain function is locally regulated via electrodes implanted deep inside the brain. Accurate implantation of these electrodes in the correct location inside the brain guarantees the successful outcome of the operation [67]. Currently, there is no intraoperative imaging modality guiding the electrode implantation in DBS in real time. In this article, we created a simple model of DBS electrode monitoring, which we demonstrated by imaging a needle inside an agar phantom at the presence of PVC slabs in front of the probe. The slabs used in front of both transducers are to mimic the human skull since they have similar thickness and sound speed.

Lamb waves are commonly used for NDT [68] to measure material properties such as thickness and speed of sound [69]. When excited with ultrasound pulses used in clinical ultrasound (1–4 MHz), the presence of multiple dispersive modes, especially in materials with speed of sound similar to human skull, complicates the implementations that are used in NDT for material characterization, namely, the speed of sound estimation. In this study, we showed that the generation of multiple dispersive modes can be used to extract the longitudinal wave speed of the slab. The overlaps of different symmetric modes in the f-k domain result in a slope which corresponds to the longitudinal wave speed of the material. Linear fitting can be used to find the slope once a threshold is applied on the f-k domain. Our experiments indicated that the estimation error of using a threshold of -2 dB is about 3.5%. The numerical results also showed that our technique is independent of the shear wave speed. The same slab but different thicknesses also led to the same slope (the results were not provided). Of note, the PVC slabs used in this study have a constant thickness and a flat surface, which is different from a real skull. The nonuniform thickness of the skull might prevent the multiple higher order modes to well overlap—for example, due to nonequal-height plateaus—and form a high intensity region. Moreover, the curved structure of the skull might lead to other types of modes, such as the torsional modes, which makes the estimation of the longitudinal sound speed even more

complicated. However, we can expect the thickness of the temporal bone (6-9 mm) to be appeared almost flat and with no large inhomogeneities in the sound speed and thickness along the width of the P4-1 probe (2.8 cm).

Knowing v_l of the slab allowed us to measure the thickness of the slab with the pulse-echo technique. In this work, the final thickness of the slab was obtained by averaging the thicknesses seen by all the elements of the array as the slab was flat. However, in practice where we face inhomogeneous and nonflat samples (i.e., skull), the thickness in front of each individual element can be estimated. This provides an overall shape of the sample. A proper identification and separation of the Lamb waves and the front side reflection are crucial. We used a slab in which the front side reflection and the Lamb waves were separable due to their time of flight. However, in clinical condition, the front side reflections might not be clearly detectable and distinguishable due to the attenuation of skull, its nonuniform shape, and the diffusive reflection caused by its surface. Sophisticated signal processing methods can be helpful to address this issue, especially as the Lamb waves and the front side reflection appear in different shapes. Effects of the lens of the probe should also be considered. Moreover, different transmit–receive procedures lead to different round trip trajectories of the front side reflection and Lamb waves. Consequently, aligning the A-lines next to each other shows different trends for Lamb waves and reflections, which can be helpful to separate them.

The estimated speed of sound and thickness of the slab were fed to our adaptive beamformer to correct the phase aberration. To minimize the reverberation artifacts (caused by the slab and the internal reflection of the needle), a dual-probe imaging setup was developed. Once the aberration effect is corrected, an MIP can be applied to the corrected images to obtain an image free of reverberation artifact. Of note, the proposed speed of sound and thickness estimation as well as the adaptive beamforming method do not require a dual probe configuration. Moreover, any sound speed map can be fed to the proposed beamformer, and we are not restricted to the simple model used in this study. The computational complexity of the proposed adaptive beamformer is in the order of the number of elements of the array. To use it in real time, it is necessary to calculate the average sound speed maps (seen by each element of the array) before an operation and then feed the beamformer with these maps during the operation. The speed of sound map and the beam forming algorithm in this study are comprehensive and generic and can be applied to any conditions without any assumption [70]. Calculation of the average sound speed maps might take a few hours due to the large number of combinations between each element of the array and each pixel of the reconstructed image. However, with some simplifications and preknowledge of the medium structure, real-time implementation of these calculations will be feasible with a graphical processing unit [71].

The reconstructed images showed that the proposed method effectively compensates the phased aberration caused by the slabs and detects the needle and the boundaries of the agar phantom at their correct locations. Specifically, for the needle, a localization error of 3.1 mm was compensated by the adaptive DAS. Moreover, taking advantages of the dual-probe configuration, the phase-corrected MIP image provided a clear visualization on the needle, about 7 dB improvement in ATRC compared with the simply overlapped images, however, at the expense of 2.38 dB image contrast. The ultrasound probe used in this study was the phased array P4-1 (Philips, 2.5 MHz, 96 elements) as it is widely avail-

able, has a proper field of view, and its frequency range provides a good compromise between resolution and attenuation. The pitch of such an array should fulfill the Nyquist criterion (smaller than half a wavelength of the Lamb waves), which is the case for P4-1 probe. The smaller the pitch, the better the discrimination of the Lamb waves. In a follow-up study, we will evaluate the effects of the heterogeneity and nonflat slabs (i.e., hemispherical models) and samples of human skull.

2.5. CONCLUSION

We have developed and validated a noninvasive technique, based on Lamb waves, to measure the longitudinal, sound speed, in a slab with a thickness and sound speed similar to those of human skull. Then, an adaptive beamformer was provided to use this information to correct the aberration effect in USI. Our numerical and experimental results showed that the Lamb wave technique detects the correct longitudinal speed (independent of shear speed) within a 3.5 mm. Moreover, the proposed beamforming method compensated a mislocation error of 3.1 mm caused by an 8-mm-thick slab. Our technique, if further validated for human skull, can be used for noninvasive and real-time imaging of the DBS electrodes during the operation, thus improving the accuracy of the electrode implantation and, therefore, the outcome of the operation.

ACKNOWLEDGEMENTS

This work was supported by a joint grant from the Netherlands Organisation for Scientific Research (NWO)/the Netherlands Organisation for Health Research and Development (ZonMw) and the Department of Biotechnology (Government of India) under the program Medical Devices for Affordable Health (MDAH) as Project Imaging Needles (Grant Number 116310008).

2.6. ERRATUM

In the above article [72], we mentioned that the superposition of the different symmetric (S) modes in the frequency-wavenumber (f-k) domain results in a high-intensity region where its slope corresponds to the longitudinal wave speed in the slab. However, we have recently understood that this high intensity region belongs to the propagation of a wave called lateral wave or head wave [73]–[76]. It is generated if the longitudinal sound speed of the aberrator (i.e., the PVC slab) is larger than that of water and if the incident wavefront is curved. When the incidence angle at the interface between water and PVC is near the critical angle, the refracted wave in PVC reradiates a small part of its energy into the fluid (i.e., the head wave). As discussed in [74], if the thickness of the waveguide is larger than the wavelength, the first arriving signal is the head wave. This is also the case in our study [72] where the ultrasound wavelength of a compressional wave in PVC was close to 1 mm, and a PVC slab with a thickness of 8 mm was used.

In this Erratum, numerical simulations (with SimSonic solver [73]) and experimental measurements (with the same PVC slab used in [72]) are conducted to investigate the propagation of the Lamb waves and head wave in detail, for the specific configuration studied in [72]. The pitch and element width of the P4-1 probe were used to assemble

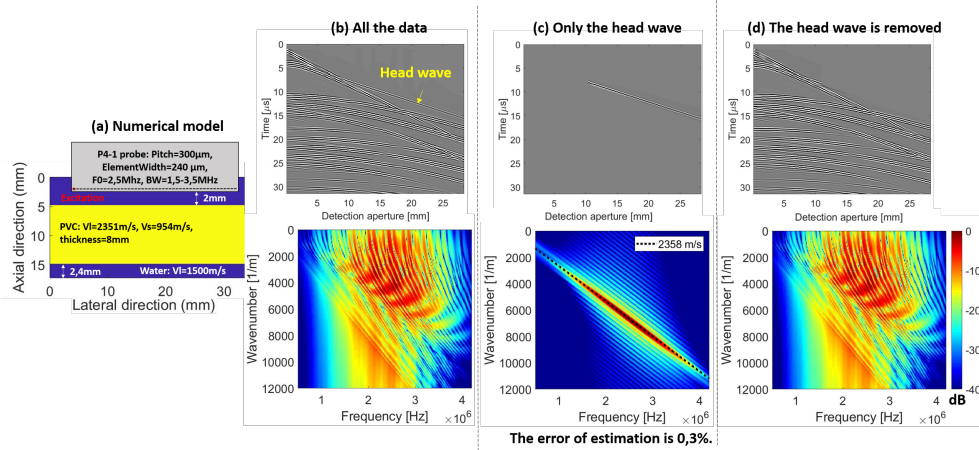


Figure 2.8: (a) Numerical model used in SimSonic. F_0 , BW , V_l , and V_s are the central frequency, bandwidth, longitudinal wave velocity, and transverse wave velocity, respectively. (b)–(d) Numerical space-time domain data and the corresponding f-k representation. (b) All the data. (c) Only the head wave. (d) Head wave is removed.

the numerical signals [see Figure 2.8(a)]. If all the data simulated for the P4-1 probe is used, there indeed is a region with a slope [see Figure 2.8(b)], but this has a low intensity, meaning that the head wave has a relatively low amplitude compared to the specular reflections. Once the head wave is isolated, the sound speed can be estimated with a 0.3% error from the f-k domain plot [see Figure 2.8(c)]. No significant difference is observed between Figure 2.8(b) and (d), in which the head wave is muted.

Our experimental results show that if only the head wave (the first arriving signal) is used [see Figure 2.9(b)], the slope of the linear fitting in the f-k domain also yields the longitudinal sound speed of the PVC with a 0.3% error. Of note, the signal processing (i.e., linear fitting in the f-k domain) used in our study [72] still works for the head wave and is correct provided that the aberrator is parallel to the probe [77]. Also, in [72] [page. 6], it is mentioned that “the curved structure of the skull might lead to other types of modes, such as the torsional modes.” Here, we acknowledge that this sentence is not correct, as torsional modes only exist in cylindrical waveguides or rectangular bars. We would like to mention that Guillaume Renaud is added as a coauthor to acknowledge his contribution to the findings reported in this Erratum.

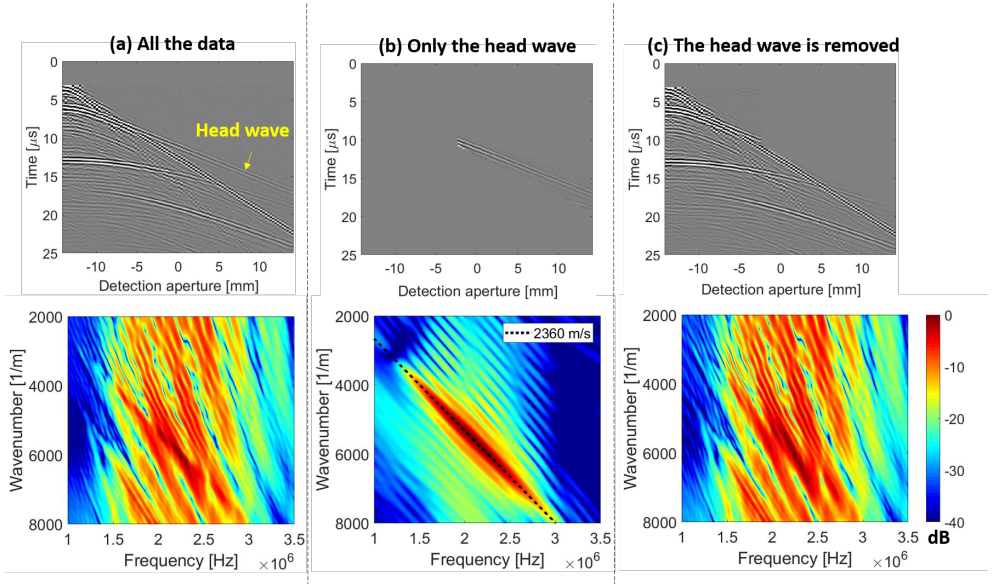


Figure 2.9: Experimental space-time domain data and the corresponding f - k representation. A P4-1 ultrasound probe and a PVC slab with a thickness of 8 mm were used in the experiment. (a) All the data. (b) Only the head wave. (c) Head wave is removed.

3

REFRACTION-CORRECTED TRANSCRANIAL ULTRASOUND IMAGING THROUGH THE HUMAN TEMPORAL WINDOW USING A SINGLE PROBE¹

Transcranial ultrasound imaging (TUI) is a diagnostic modality with numerous applications, but unfortunately, it is hindered by phase aberration caused by the skull. In this article, we propose to reconstruct a transcranial B-mode image with a refraction-corrected synthetic aperture imaging (SAI) scheme. First, the compressional sound velocity of the aberrator (i.e., the skull) is estimated using the bidirectional headwave technique. The medium is described with four layers (i.e., lens, water, skull, and water), and a fast marching method calculates the travel times between individual array elements and image pixels. Finally, a delay-and-sum algorithm is used for image reconstruction with coherent compounding. The point spread function (PSF) in a wire phantom image and reconstructed with the conventional technique (using a constant sound speed throughout the medium), and the proposed method was quantified with numerical synthetic data and experiments with a bone-mimicking plate and a human skull, compared with the PSF achieved in a ground truth image of the medium without the aberrator (i.e., the bone plate or skull). A phased-array transducer (P4-1, ATL/Philips, 2.5 MHz, 96 elements, pitch = 0.295 mm) was used for the experiments. The results with the synthetic signals, the bone-mimicking plate, and the skull

¹This chapter has been published as:

Mozaffarzadeh et al., "Refraction-Corrected Transcranial Ultrasound Imaging through the Human Temporal Window using a Single Probe," IEEE TUFFC. 69(4), 2022.

The text and notation used in this chapter may differ on minor details from the actual publication. This is done to achieve consistency between chapters.

indicated that the proposed method reconstructs the scatterers with an average lateral/axial localization error of 0.06/0.14 mm, 0.11/0.13 mm, and 1.0/0.32 mm, respectively. With the human skull, an average contrast ratio (CR) and full-width-half-maximum (FWHM) of 37.1 dB and 1.75 mm were obtained with the proposed approach, respectively. This corresponds to an improvement of CR and FWHM by 7.1 dB and 36% compared with the conventional method, respectively. These numbers were 12.7 dB and 41% with the bone-mimicking plate.

Keywords; Transcranial ultrasound imaging; Adaptive beamforming; Phase aberration correction; Head waves; Temporal bone.

3.1. INTRODUCTION

TRANSCRANIAL ultrasound imaging (TUI) is a diagnostic modality with numerous applications, such as stroke diagnosis [14]–[19], detection of vasospasm after subarachnoid hemorrhage (most often caused by head trauma) [24], [25], microemboli [78], [79], and endonasal trans-sphenoidal surgery [80]–[82]. A growing number of recent ultrasound technologies are being applied to the brain, in particular, ultrasound localization microscopy [83]–[85], functional ultrasound imaging [86], [87], and perfusion imaging with ultrasound contrast agents [88]. At present, it is safe, relatively inexpensive, and available in hospitals and emergency medicine services (EMS) [14], [89]–[91]. Despite its advantages, TUI is still hindered by the low image quality caused by the strong aberration and scattering [11], multiple reflections caused by the skull [11], [12], and mode conversion [92].

TUI is often performed through the temporal window, which enables imaging of the arteries of the circle of Willis. The temporal bone is the thinnest part of the skull that gives direct access to the brain, and unlike most parts of the skull, the squamous part of the temporal bone often consists of a single layer of cortical bone. Its thickness and mass density vary from 1.5 to 4.4 mm [7]–[10] and 1700 to 2000 kg/m³, respectively [9]. The cortical bone tissue of the temporal bone was found to have anisotropic elasticity [9]. The compressional wave velocity (V_c) was 3520 m/s in the direction normal to the surface of the skull. V_c varied between 3590 and 4000 m/s in different propagation directions within the plane of the temporal bone [9]. Moreover, a relatively lower attenuation through the temporal bone was reported (one-way attenuation at normal incidence from 13 to 22 dB/cm/MHz [93]) compared with other parts of the skull that can be as thick as 1 cm [11]. In the presence of a diploe, i.e., a layer of highly porous trabecular bone sandwiched between inner and outer tables made of dense cortical bone, the attenuation is largely determined by the thickness of the diploe. The oneway attenuation through the skull can exceed 25 dB/cm/MHz for a diploe thickness of 6 mm [11]. In contrast, a temporal bone made of a single layer of cortical bone (absence of diploe) produces a one-way attenuation at normal incidence close to 13 dB/cm/MHz [93]. While this makes the temporal bone a suitable window to image through, temporal window failure (TWF) is present in 8%–20% of people [94]. There are several parameters affecting TWF: age, sex, temporal bone thickness, pneumatization (presence of cancellous bone or air sandwiched between two layers of cortical bone instead of one single layer of cortical bone), and soft tissue thickness [8]–[10]. The larger the thickness of the temporal bone, the higher the chance of failure; the probability of TWF was 93.5% for a heterogeneous temporal bone with a thickness larger than 2.7 mm [10]. The most important cause of TWF is pneumatization with an odds ratio of 7.9 [7]. While solely reduction of the central frequency of the probe might not be helpful [54], contrast agents significantly increase the backscattered signals power and seem to reduce the chance of TWF [15], [95], [96]; depending on the concentration of the contrast agent, the average signal-to-noise enhancement could be about 12 ± 5.4 dB [96].

Since the pioneering work by Smith et al. [97], [98], different methods and techniques have been developed to compensate the phase aberration caused by the skull [41]. However, these techniques have had moderate success in diagnostic ultrasound imaging (the discussion section includes a review of earlier methods). Most approaches use the nearfield phase-screen aberration model which models the skull as an infinitesimally thin

aberrating layer at the surface of the transducer [99]–[101]. A limitation of this approach is that the effects of refraction and irregular skull thickness (or geometry) are not correctly modeled and, therefore, the correction is only valid for a certain region called the isoplanatic patch [12], [33], [99], [102]–[104]; the use of multiple isoplanatic patches enables aberration correction throughout a larger region of interest [54], [105], [106]. This strategy was used for two dimensional (2-D) [12], [104], and 3-D TUI [52], [53], [106]. More recently, approaches that model refraction through the true geometry and thickness of the skull have been proposed; however, the method requires estimates of the thickness and wave speed in the skull at multiple positions with dedicated ultrasound measurements prior to image reconstruction [107]–[109]. Another family of methods relies on a CT or MRI scan of the skull to determine its geometry and knowledge or assumption of wave speed in bone, prior to TUI [110]–[113].

As a result of the large acoustic impedance mismatch between bone and soft tissues, the near and far surfaces of the temporal bone appear as bright interfaces in the ultrasound image, and their detection and segmentation is, therefore, rather easy. This study capitalizes on this to attempt a new type of aberration correction, aiming to improve transcranial ultrasound B-mode images. The novelty of our approach lies in the fact that it corrects for the true position and the true geometry of the bone layer. This means that the tilt and the distance between the temporal bone and the probe are taken into account, and the outer and inner surfaces of the temporal bone are described as nonplanar and nonparallel surfaces. Moreover, our approach estimates the wave speed in the bone layer prior to imaging, all with a single ultrasound array transducer. As a result, delay-and-sum image reconstruction provides improved image quality because the travel times through the layered medium are accurately calculated at each image pixel. A synthetic aperture imaging (SAI) scheme is used as the transmission of spherical wave fronts facilitates the modeling of refraction (necessary for an accurate phase correction) and provides dynamic focusing in transmission [114]. As explained in [55], modeling the wave propagation through the skull and considering a bone layer with a finite irregular thickness enable the calculation of a unique set of forward and backward travel times, at each pixel, for each transmit beam and for each array element (in receive). As a consequence, we expect our approach to overcome the limitations of nearfield phase-screen methods, in particular, because the concept of isoplanatic patch does not exist in our approach.

The compressional wave speed is first estimated in the temporal bone with the bidirectional headwave method [73]–[75]. Next, sound speed maps (SSMs) are generated with adaptive beamforming [72]. Travel times are calculated with the fast marching technique (FMT) [115], [116]. The point spread function (PSF) is evaluated with numerical simulations and experiments, before and after correction, and compared with a ground truth image.

3.2. MATERIALS AND METHODS

The proposed approach is briefly presented in Figure 3.1. Image reconstruction starts with a primary SSM. After each segmentation step, the SSM is updated and new reconstruction is performed. Note that the terms far and near are in relation to the probe throughout this article.

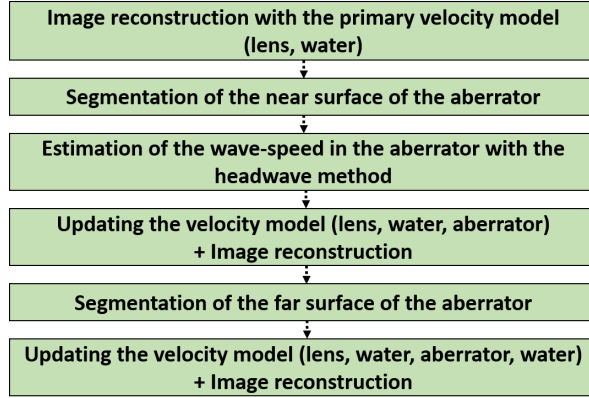


Figure 3.1: Flowchart of the proposed image reconstruction method.

3.2.1. COMPRESSIONAL WAVE SPEED ESTIMATION IN THE ABERRATOR

The bidirectional headwave method was used before to estimate the compressional wave speed of cortical bone [73]–[75]. This method works based on the propagation of the head wave (the first arriving signal) along a planar interface and is briefly explained as follows.

1. The first element of the ultrasound array transmits and other elements receive.
2. The head wave is extracted by defining a range for the compressional wave speed of the aberrator.
3. A 2-D fast Fourier transform (FFT) is applied on the extracted head wave to convert the temporal-spatial data into the frequency–wavenumber (f -k) domain [117].
4. The slope of the line fit on the high intensity region multiplied by 2π results in a compressional wave speed, V_1 .
5. V_1 is biased if the aberrator is not parallel to the probe [75]. To compensate for this, the last steps should be repeated, but the last element of the arrays should transmit and other elements receive in the step 1. This results in a second compressional wave speed, V_2 .
6. The compressional sound velocity of the aberrator is finally calculated by

$$(2V_1 V_2 \cos(\alpha)) / (V_1 + V_2), \quad (3.1)$$

where α is the angle between the surface of the probe and the aberrator [77]. The method is accurate if the thickness of the aberrator is larger than the wavelength and can also be used to estimate the compressional sound velocity in the lens of the probe. As the head wave is not dispersive, the fit line at step 4 should pass (0, 0) in the f -k domain. The wave speed estimated with the headwave technique in this study is the compressional sound speed in the temporal bone in the lateral direction (relative to the ultrasound probe).

3.2.2. ADAPTIVE BEAMFORMING

The formula of delay-and-sum (DAS) beamformer is [77], [114] as follows:

$$I(p) = \sum_{i=1}^M \sum_{j=1}^N RF(t = t_T(i, p) + T_R(j, p), i, j) \times W(p, i, j), \quad (3.2)$$

where I is the output of the beamformer at pixel p ; M and N are the number of transmission and reception events, respectively; RF is the recorded data; t_T and t_R are the transmit and receive arrival times, respectively; and $W(p, i, j)$ is a weight calculated for pixel p . In this article, this weight is based on the far-field directivity of the elements of the array [118], [119].

Traditionally, a constant wave speed is assumed throughout the medium during image reconstruction; the term "conventional" in this manuscript represents results generated with a constant wave speed. However, in transcranial scenario, this imposes inaccuracies in the calculated arrival times for each pixel of the image [77], [120], [121]. To accurately reconstruct the images, the refraction caused by the skull (directly affecting the arrival times used for beamforming) should be taken into account. To this end, the FMT was used. FMT solves the Eikonal equation and calculates the arrival times given SSMs [115], [116]. The "scikit-fmm" Python toolbox was used to employ the FMT; available in "<https://pypi.org/project/scikit-fmm/>." We used three stages of adaptive beamforming to reconstruct phase-compensated images: one to segment the near surface of the aberrator, one to segment the far surface, and one to reconstruct the region of interest (usually at depths more than 15 mm). For segmentation, a technique based on Dijkstra's algorithm was used [122], [123]. The segmentation algorithm seeks the shortest path that follows the interface with the highest intensity in the ultrasound image, by maximizing a merit, here, the sum of the pixel values along the path. Once the near/far surface of the aberrator is segmented, the sound speed of the aberrator/soft tissue is assigned to the depths higher than the near/far surface and passed to FMT.

3.2.3. NUMERICAL STUDY

The k-Wave MATLAB toolbox was used to evaluate the proposed method in a 2-D lossless medium, ignoring shear wave propagation [124]. Seven point scatterers were placed in different lateral and axial distances [see Figure 3.2(a)]. The speed of sound in lens, skull, and soft tissue was 1000, 3200, and 1600 m/s, respectively. The mass density of the soft tissue/lens and skull was 1000 and 1900 kg/m³, respectively. The grid and time step size were 20 μ m and 4 ns, respectively, to avoid numerical dispersion and maintain the stability and accuracy of the simulation. The near surface of the skull was planar and parallel to the probe, but the far surface was modeled irregular to evaluate the performance of our method under a severe condition. The minimum and maximum thickness of the skull was 2.1 and 4.1 mm, respectively. After the lens layer, 2.1 mm in depth was modeled as skin. The properties of a P4-1 phased-array transducer (ATL/Philips, 2.5 MHz, 96 elements, pitch = 0.295 mm) and the SAI sequence were used to assemble the numerical signals [114]. To have a ground truth image, the same model [Figure 3.2(a)], but without the aberrator, was simulated.

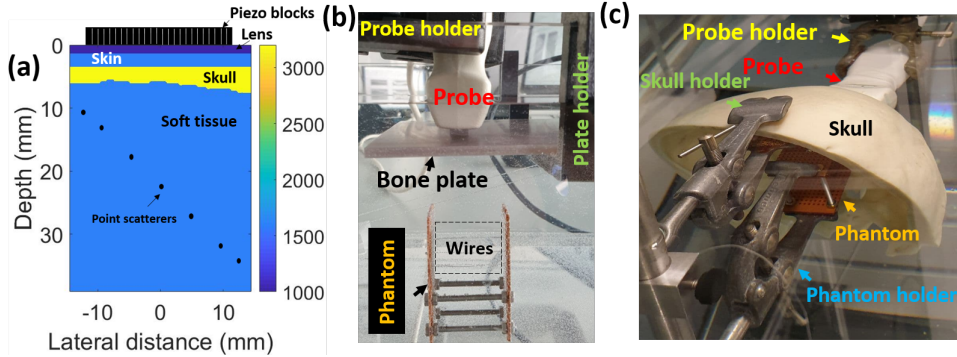


Figure 3.2: (a) Numerical model used in *k*-Wave. (b) and (c) Experimental setup used to image the wire phantom through a bone plate (Sawbones, Pacific Research Laboratory, Inc., Vashon, WA, USA) and human skull, respectively. The imaging plane is perpendicular to the wires in (b) and (c) and perpendicular to the material fibril orientation of the Sawbones plate in (b).

3.2.4. EXPERIMENTAL STUDY

We configured two experimental setups: one with a 4.23 ± 0.01 mm-thick (measured with a caliper) bone-mimicking plate (Sawbones, Pacific Research Laboratory, Inc., Vashon, WA, USA) [see Figure 3.2(b)] and one with a sagittally cut human skull [see Figure 3.2(c)]. The Sawbones plate is transverse isotropic. We used the plane perpendicular to the material fibril orientation to have isotropic compressional wave speed. The human skull (Skulls Unlimited International Inc., Oklahoma, OK, USA) was carefully prepared with the use of dermestid beetles. It was degreased and whitened using a chemical process (peroxidized) to ensure an attractive and sanitary trophy or display piece. Before experiments, the skulls were degassed at 80 mBar for 48 h.

A phantom including multiple wires (50- μ m diameter) was used. The imaging plane of the one dimensional (1-D) probe was perpendicular to the wires. Therefore, the wires are expected to mimic point scatterers considering their diameter (about one-tenth of the wavelength at the central frequency). To have a ground truth measurement, the probe was moved against the phantom with a XYZ system, the skull was carefully removed from the setup, and finally the probe was moved back to its first place; the rest of the components were fixed. All the experiments were conducted with a phasedarray transducer (P4-1, ATL/Philips, 2.5 MHz, 96 elements, pitch = 0.295 mm) connected to a Verasonics Vantage 256 system. The wire phantom was placed at a depth of 3-4 cm, which corresponds to the depth of the nearest middle cerebral artery.

3.2.5. EVALUATION METRICS

To evaluate the reconstructed images, we compared the coordinates of the scatterers, full-width-half-maximum (FWHM), contrast ratio (CR), and absolute amplitude of the main lobe of the PSF (AAM). The CR is defined as the ratio between the max brightness of scatterers to the mean brightness of background noise (indicated later in the figures) and is

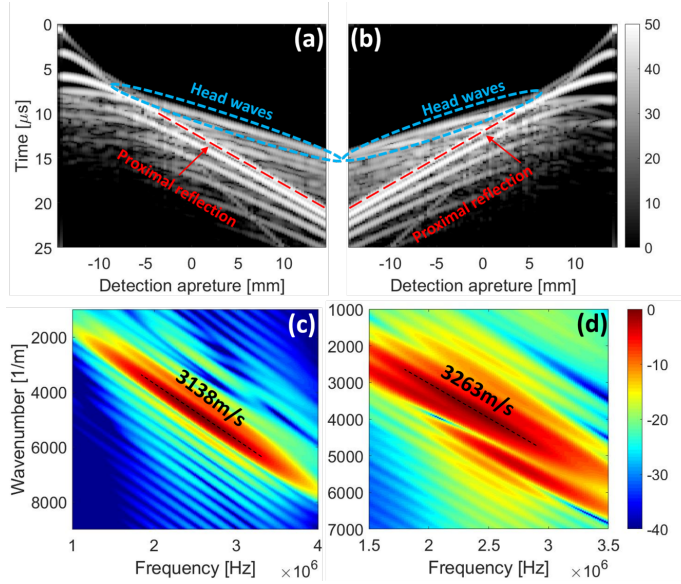


Figure 3.3: (a) and (b) Numerical space-time domain data and (c) and (d) corresponding f - k representation, respectively.

reported in decibel. The brightness is calculated from the envelope of the beamformed RF data, before normalization and log compression. It should be noted that the image reconstructed by the conventional method in the followings represents a noncorrected image in our study.

3.3. RESULTS

3.3.1. NUMERICAL RESULTS

The numerical space-time domain data and the corresponding f - k representation used to apply the bidirectional headwave method are presented in Figure 3.3. The head wave (the first arriving signal) appears as a planar wavefront because the near surface of the aberrator is planar [see Figure 3.2(a)]. The estimated wave speeds in Figure 3.3(c) and (d) with an $\alpha = 0$ (parallel near surface) result in a sound speed of 3200.5 m/s [following 3.2. This estimation has a small error of 0.5 m/s (the true sound speed is 3200 m/s).

Figure 3.4 shows the procedure taken to extract the SSM of the aberrator (see Section 3.2.2). Taking the sound speed of the lens layer into account [Figure 3.4(a)] helps with accurately reconstructing the reflections of the lens layer and near surface [see Figure 3.4(b)]. Once the SSM gets updated based on the segmented near surface [see Figure 3.4(c)], the far surface is also accurately reconstructed and segmented [see Figure 3.4(d)]. Figure 3.4(e) shows the finalized SSM closely following the actual model [the dashed line shows the far surface of the actual model presented in Figure 3.2(a)].

The scatterers are better detected with the proposed method [comparing Figure 3.5(c) and (b)] because wave physics in the layered medium is accurately described. This also

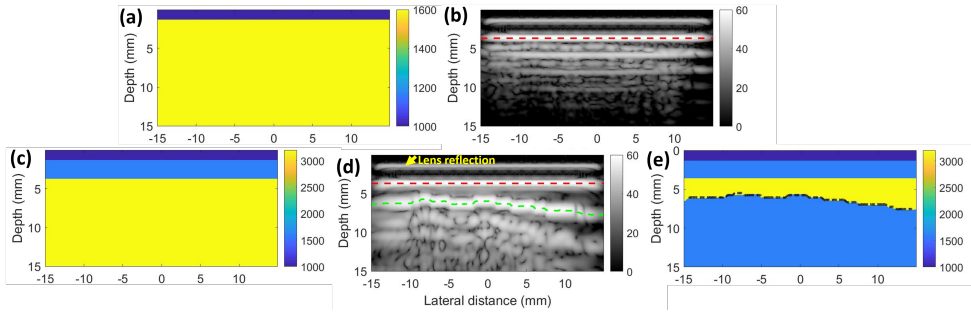


Figure 3.4: (a) and (b) SSM and corresponding reconstructed image taking the lens into account, respectively. (c) and (d) SSM and corresponding reconstructed image taking the sound speed of the aberrator into account, respectively. (e) SSM used to compensate the phase aberration and image the point scatterers; the dashed black line shows the far surface of the actual model [see Figure 3.2(a)]. The red and green dashed lines indicate the near and far surfaces of the aberrator, respectively.

results in a lower level of sidelobes and clutter; to have a fair comparison, compare Figure 3.5(e) with (d), since these images were normalized to their local maximum but not the global one. Multiple reflections within the aberrator create significant artifacts at shallow depth [see Figure 3.5(c) (red dashed rectangle)]. This causes the first two scatterers to disappear [see the red dashed square in Figure 3.5(a)]. The artifacts behind the scatterers indicated by the blue arrows are also due to multiple reflections caused by the aberrator.

As indicated in Table 8.1, the proposed method reconstructs the scatterers with an average lateral and axial localization error of about 0.06 and 0.14 mm, compared with the ground truth, respectively. For the conventional method, these quantities are 1 and 0.96 mm, respectively. The proposed method in average improves the CR by 4.4 dB, the FWHM by 22%, and the AAM by 107% (+6.3 dB), compared with the conventional method. Refer to Table 3.51 in the supplementary material for details.

Table 3.1: Quantitative evaluation of the numerical and experimental images.

	Method	Axial/Lateral localization error [mm]	FWHM [mm]	Contrast ratio [dB]
Simulation	Conventional	[1.0, 0.96]	1.00	35.5
	Proposed	[0.06, 0.14]	0.78	39.9
Sawbones plate	Conventional	[0.7, 1.9]	1.80	23.1
	Proposed	[0.11, 0.13]	1.06	35.8
Human skull	Conventional	[1.45, 1.17]	2.72	30.0
	Proposed	[1, 0.32]	1.75	37.1

3.3.2. EXPERIMENTAL RESULTS

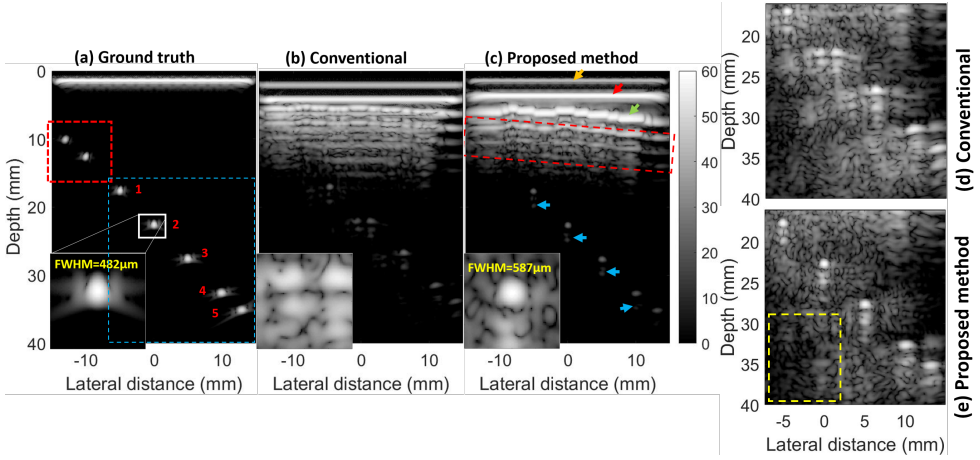


Figure 3.5: Reconstructed images (a) without and (b) and (c) with the aberrator in the numerical model. The red dashed rectangle in (c) shows the effects of multiple reflections caused by the aberrator. The red dashed square in (a) shows the two targets that are not visible in (c) due to the effects of multiple reflections caused by the aberrator. The zoomed version of the figures shows -2 to 2 mm and 20 to -24 mm in the lateral and depth directions, respectively; these images are normalized to the maximum intensity after a depth of 15 mm. This is also the case in (d) and (e) which present the area indicated by the blue dashed box shown in (a). The numbers in (a) and the yellow dashed box in (e) are used to refer scatterers for quantitative evaluation and calculate CR in Table I, respectively. The orange, red, and green arrows show the reflections of the lens, near, and far surfaces, respectively.

BONE-MIMICKING PLATE

The space-time domain data and the corresponding f-k representation of the experiment conducted with the Sawbones plate are presented in Figure 3.6. The sound speeds estimated in Figure 3.6(c) and (d) with an α of about 3.3deg result in a sound speed of 3058 m/s. A thickness of 4.2 mm was obtained with the proposed approach (0.7% error), while the conventional method underestimates the thickness for about 2 mm (comparing Figure 3.7(b) and (c)). The blue arrows [see Figure 3.7(c)] indicate the trailing clutter resulting from multiple reflections caused by the Sawbones plate [75]. The same procedure shown in Figure 3.4 is used to extract the SSM of the Sawbones plate, but results are not provided.

The proposed method reconstructs the scatterers (i.e., wires) with an average lateral and axial localization error 0.11 and 0.13 mm, compared with the ground truth, respectively (see Table 8.1). For the conventional method, these quantities are 0.7 and 1.9 mm, respectively. The proposed method in average improves the CR by 12.6 dB, the FWHM by 45%, and AAM by 167% (+8.5 dB), compared with the conventional method. Refer to Table 3.S2 in the supplementary material for details.

HUMAN SKULL

The space-time domain data and the corresponding f-k representation of the experimental data used to apply the bidirectional headwave method are presented in Figure 3.8. A

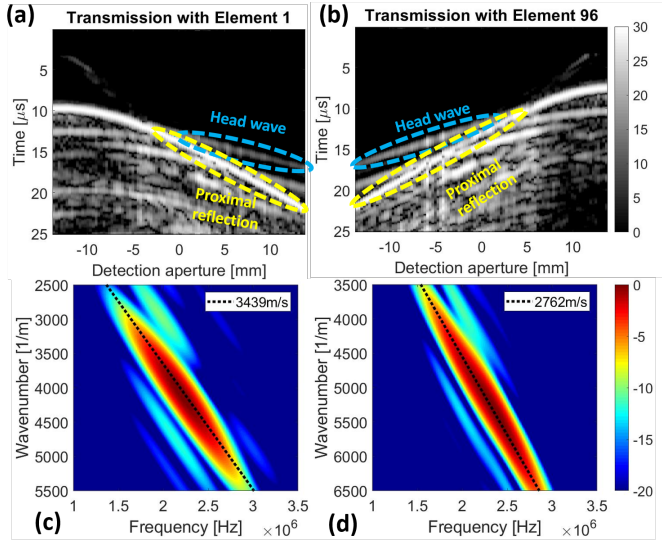


Figure 3.6: (a) and (b) Experimental space-time domain data and (c) and (d) corresponding representation after 2-D Fourier transform of the space-time domain data. The Sawbones plate was used as the aberrator.

sound speed of 3500 m/s is obtained considering V_1 [Figure 3.8(c)], V_2 [Figure 3.8(d)], and α of 3deg [see Figure 3.9(c)]. We found a compressional wave speed in temporal cortical bone in agreement with [9]. Although the elasticity of temporal cortical bone is anisotropic [9], we assume isotropic elasticity in this work.

The proposed method enhances the visibility of the wires [comparing Figure 3.9 9(c) and (b)] because the wave physics in the layered medium is accurately described. The mean thickness of cortical bone was estimated 1.3 mm; there is no information available on the true thickness of the skull within the imaging plane. The clutter shown by the yellow dashed box is caused by the multiple reflections of the backscattered wave from the far surface. The level of the clutter behind the wires in Figure 3.9(c) (see the blue arrows), caused by multiple reflections, looks higher since the images are normalized to their global maximum. Figure 3.9(d) and (e) is normalized to their local maximum and can be used for a fair visual comparison. The level of background noise is higher in Figure 3.9(d), compared with Figure 3.9(e), due to the distribution of energy to different pixels, which is mainly caused by the refraction induced by the skull. The proposed method reconstructs the scatterers with an average lateral and axial localization error of about 1 and 0.32 mm, compared with the ground truth, respectively (see Table 8.1). For the conventional method, these quantities are 1.45 and 1.17 mm, respectively. The proposed method in average improves the CR by 7.1 dB, FWHM by 36%, and AAM by 130% (+7.2 dB), compared with the conventional method. Refer to Table 3.53 in the supplementary material for details.

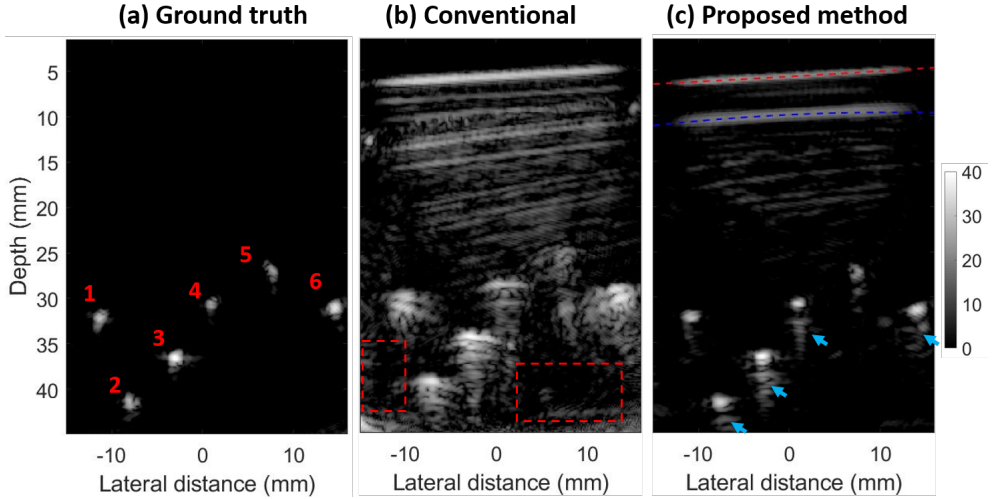


Figure 3.7: Reconstructed images (a) without and (b) and (c) with the Sawbones plate in front of the probe. The red and blue dashed lines show the reflections of near and far surfaces, respectively. The blue arrows show the effects of multiple reflections caused by the aberrator (i.e., Sawbones plate). The numbers in (a) and the red dashed boxes in (b) are used to point out the scatterers for quantitative evaluation and calculate CR in Table 8.1.

3.4. DISCUSSION

3.4.1. COMPARISON WITH PREVIOUS RELEVANT WORKS

ESTIMATING THE COMPRESSIONAL WAVE SPEED AND THICKNESS OF THE ABERRATOR

The periodicity of the frequency spectrum of the signals reflected within a bone layer was used in a model to determine the wave speed in ex vivo human skulls, assuming a known bone thickness [125]. Different strategies using a single focused transducer and a phased array were proposed in [126], [127] for independent measurement of compressional wave velocity and thickness of the cortical bone. The technique proposed by Wydra et al. [127] consists in varying the focal depth of a focused beam and searching for maximum reflected amplitude, and it was originally introduced for acoustical microscopy (see in [128]). The method is essentially a 1-D approach and requires: 1) clearly distinct reflected echoes from the near and far surfaces of the skull and 2) a locally flat skull surface and parallel to the probe. For a flat non-porous aberrator with a thickness of 7.21 mm, their approach estimated a thickness of 7.55 mm (4.9% error) with a phased-array transducer. With a thinner aberrator (4.23-mm-thick Sawbone plate used in this study) and a nearly equal ultrasound frequency (2.5 versus 2.25 MHz), and our approach estimated the plate thickness with an error of 0.7%. Tilted or non-flat surfaces reduce the accuracy of thickness and sound speed estimation with the technique proposed by Wydra et al. [127]. This method was improved by Postert et al. [129] by using a higher frequency (5 versus 2.25 MHz) and by considering the effective aperture during measurements, but was still limited to plate-shape aberrators with constant thickness and parallel to the transducer

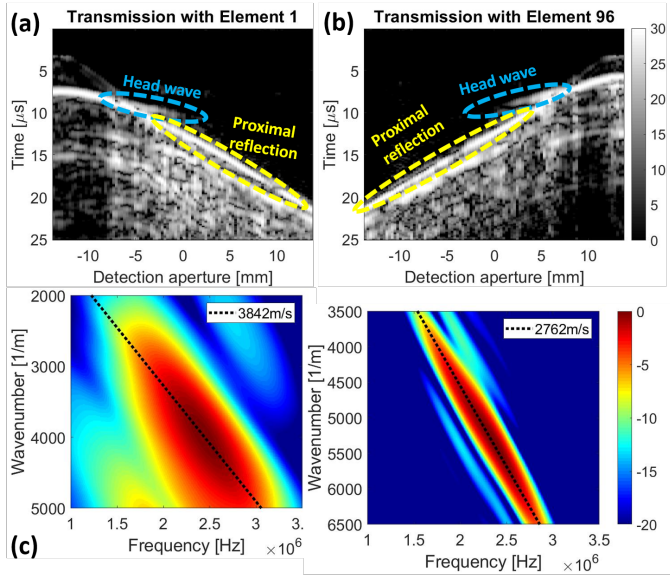


Figure 3.8: (a) and (b) Experimental space-time domain data and (c) and (d) corresponding representation after 2-D Fourier transform of the space-time domain data. The skull was used as the aberrator.

array.

An autofocus approach combined with ultrasound imaging was also proposed to estimate the wave speed and thickness of the cortex of long bones [119], [130]. The rationale of this approach is simple: a reconstructed ultrasound image shows optimal quality (intensity and sharpness) if the wave speed model used during image reconstruction is correct. Therefore, looking for the value that maximizes image intensity and sharpness provides an estimate of the wave speed.

In this work, we chose to use the bidirectional headwave technique because it provides an independent estimate of the compressional wave speed in the aberrator and the signal processing is straightforward if the near surface of the aberrator is locally sufficiently planar. In addition, the same array transducer can be used for wave speed estimation and imaging.

PHASE ABERRATION COMPENSATION

Other researchers proposed different strategies to tackle phase aberration (or refraction). Deng et al. [131] used thickness resonance frequencies in the skull for phase shift calculation, which might enable adaptive focusing during high-intensity transcranial ultrasound treatments. Clement et al. [132] and Lucht et al. [133] reported mode converted shear waves for focusing the ultrasound wave in brain. Shear wave velocity in the skull is lower than its compressional wave velocity, which results in a better impedance match with soft tissues and less refraction; at 0.74 MHz, mode converted shear wave has a smaller but exploitable amplitude compared with the compressional wave (between 35% and 55% of the

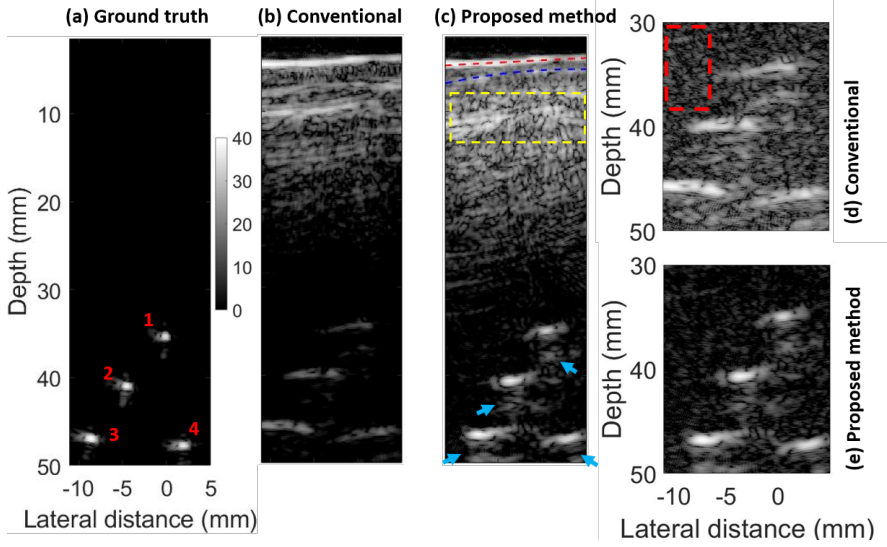


Figure 3.9: Reconstructed images (a) without and (b) and (c) with the skull in front of the probe. (d) and (e) Zoomed version of (b) and (c), respectively; these figures are normalized and log compressed to the local maximum. The red and blue dashed lines in (c) show the near and far surfaces of the skull, respectively. The yellow dashed box indicates the effects of multiple reflections. The numbers in (a) and the red dashed box in (d) were used to point out the scatterers for quantitative evaluation and calculate background noise in Table 8.1, respectively.

peak of the compressional wave). However, in a later study, White et al. [134] reported that the shear attenuation of skull can be 2–3 times higher (in dB/cm) than the compressional attenuation (a longitudinal and shear attenuation coefficient of 6.1 and 18.5 dB/cm, at a frequency of 0.84 MHz, respectively), which overshadows the relatively better impedance match of the shear wave. Yousefi et al. [135] also reported that transcranial shear wave imaging causes equal distortion and worsens lateral resolution compared with using compressional waves for imaging.

In [33], [83], [103], [104], [136], [137], the near-field phase screen aberrator model [99]–[101] was used to extract the profile of the aberrator. This model assumes an infinitely thin aberrating layer attached to the surface of the probe [103] and only works in a limited area (called isoplanatic patch) around the region of interest [99], [103], [138]. Correction of multiple isoplanatic patches was achieved in [54], [106], but with two 2-D matrix arrays placed on the opposing sides of the skull, one on each of the temporal bones; transmission from one side and reception in other side provided unique delay maps which could be used for phase compensation in the entire 3-D volume. The effectiveness of this method was evaluated in healthy volunteers; it improved the detection of large cerebral arteries (more arteries of the circle of Willis visualized and detected volume of arteries increased by 34%) [105], and the image brightness was improved by 24% [54]. Our approach increased the AAM by 130% in experiments with water in an ex vivo skull. Studies in [54]

were in vivo and thus had scattering from brain tissue. The idea of using two array transducers facing each other and sharing the same imaging plane (an imaging transducer and a calibration transducer), one on each of the temporal bones, was also proposed by Vignon et al. [12]. Their approach relies on the measurement of the impulse response between all pairs of individual elements of the two array transducers, in order to estimate a spatiotemporal inverse filter. The -6-dB width of the focal spot was improved by 32% (from 4.9 to 3.3 mm), the lateral shift of the focal spot by 63% (from 1.1 to 0.4 mm), and the contrast loss by 65% (from 15.1 to 5.3 dB), on average. The approach proposed by Vignon et al. [12] achieves improvements close to our approach (see Table I), using a more complicated setup than ours with two probes. Also, in order to migrate the spatiotemporal inverse filter (measured between the two array transducers) inside the skull, one side of the skull was assumed infinitely thin and located close to the calibration transducer array. As a result, optimal focusing with the imaging transducer was limited to a region, at rather large depth (for the imaging transducer) close to the part of the skull in contact with the calibration transducer, and at lateral positions where the skull was sufficiently flat to enable close contact with the calibration transducer. Prior knowledge on the compressional sound speed or thickness of skull [55], [113], [125], [128], [139] and correction based on CT scans [111]–[113] are also impractical on-site as these parameters vary in person [9], [11], [13], [107], [129], [140] and EMS are not always equipped with CT scanners.

Similar studies to our phase correction technique were reported. In a numerical study, Wang and Jing [109] estimated the sound speed of the aberrator by the method introduced by Wydra et al. [127] and used the FMT to calculate the arrival times. Shapoori et al. [107] also estimated the sound speed of the aberrator by the method introduced by Wydra et al. [127] and used Fermat's principle for arrival time calculation, but no transcranial image through a human skull was reported. Wang and Jing [109] and Shapoori et al. [107] used focused transmit beams, which necessitates calculating and applying transmit delays for each image line; this imposes complexity to the imaging strategy. White and Venkatesh [14] reported on phase-corrected transcranial super resolution ultrasound imaging through the temporal region of human skull with a commercial probe, but the correction was achieved with a ground truth measurement, which is not feasible in vivo.

Other approaches rely on the injection of an ultrasound contrast agent. Contrast agent microbubbles can serve as bright point sources. Each bubble enables the estimation of a phase aberration correction for optimal image reconstruction in the area close to the bubble [83]. By repeating the procedure with multiple microbubbles located at different positions in the region of interest, it is possible to design multiple isoplanatic patches.

The proposed method in this article seems to address the abovementioned limitations. It does not require any prior information on the skull (geometry, position with respect to the probe, wave speed), nor injection of an ultrasound contrast agent. Our approach is simpler to implement because it is not iterative, it only uses one ultrasound array transducer and relies on the transmission of unfocused beams and synthetic focusing in transmit and receive, which makes it simpler in terms of programming the ultrasound scanner in transmit. While our method was used before for in vivo imaging of the inner structure of the radius and tibia bone [77], here we showed that it has the potential to correct images of the brain through the human temporal bone.

3.4.2. LIMITATIONS AND ASSUMPTIONS OF THE PROPOSED APPROACH

In our approach, the wave speed in the temporal bone was considered isotropic. While a more accurate velocity model could improve the performance of our phase correction technique [77], [130], limited information is unfortunately available on the anisotropy elastic properties of the temporal bone. As reported in [9], the wave speed exhibits a maximum value for a certain direction within the plane of the bone layer and minimum value (about 13% smaller) in a direction normal to the plane of the bone layer. Like in long bones, the autofocus method could be used in combination with the bidirectional headwave technique to estimate a model of anisotropic compressional sound speed in the temporal bone [77], [130], [141], and this will be considered in future work.

In addition, the temporal bone was described as a homogeneous layer of cortical bone in this study. Therefore, the approach would likely not perform well if the temporal bone contains cancellous bone (diploe) between two cortical bone layers. Because of this limitation, we do not expect our approach to significantly reduce the rate of TWF, since it is mainly caused by temporal bone heterogeneity. The skull used in our experiment was an easy case since its estimated thickness was 1.3 mm, which is a thin temporal bone compared with the thickness range of 1.5–2.9 mm reported in the literature [8]. In follow-up experiments, more skull specimens should be studied to investigate the robustness of our method. Note that at the time of writing, the availability of human skull specimens was limited. Recently, more specimens became available (see <https://www.skullsunlimited.com/collections/all>). Our approach may be further developed by describing the temporal bone with a three-layer model.

The near surface of the temporal window was assumed planar when estimating the wave speed in bone with the headwave method [73]–[75]. This can be a fair assumption considering the small footprint of the P4-1 probe (i.e., a lateral width of 28 mm). Yet, development of techniques to compensate for the bone curvature (in the lateral direction) and even bone irregularities could be of interest for a more accurate compressional sound speed estimation [142], [143].

The elevation effect of the 1-D array was ignored. For the velocity measurement in long bone, this effect is negligible [73] due to the nearly cylindrical shape of the diaphysis of a long bone. However, the geometry of the temporal bone is more complex. In addition, the possible change of imaging plane in the elevation direction in the presence of an aberrator could explain the higher localization errors in the experimental results, compared with numerical ones (see Table 8.1). Like all aberration correction methods, the use of a matrix array would improve the performance of our approach. With a matrix array, the 3-D position and geometry of the temporal bone could be estimated with a strategy very similar to that proposed in this manuscript and travel times could be accurately calculated in a 3-D space.

To sum up, the anisotropy of the bone layer (wave speed depends on propagation direction), the skull microstructure (one-layer or three-layer bone), the 3-D geometry of the bone layer (transducer not being parallel with respect to the boundaries of the bone layer in the elevation direction), and the influence of superficial soft tissues should be taken into account for in vivo experiments.

3.4.3. IMAGING SCHEME AND IMPLEMENTATION

BEAMFORMING

Several approaches (for instance, Wang and Jing [109] and Shapoori et al. [107]) used focused transmit beams. Like [83], [110], our approach uses unfocused transmit beams and relies on a SAI sequence with single-element transmission. It allows 1) to calculate the trajectory of the wave (necessary for phase correction) and 2) to have dynamic focusing in both transmission and reception [114]. The latter provides a high image quality, which helps the segmentation of the near and far interfaces of the temporal bone and, therefore, the construction of an accurate SSM. A delay-and-sum beamformer was used to reconstruct the images. However, more advanced beamforming methods could improve the resolution, lower the level of background noise, and even reduce the effects of multiple reflections [39], [40], [144]–[149].

COMPUTATIONAL TIME

Our approach requires 8 s to estimate the arrival times, and 13 s to reconstruct a refraction-corrected image using data acquired by 96 elements (and therefore 96 single-element transmissions) with an Intel Core i7-8650U CPU, without any parallel computing. A real-time visualization is needed for in vivo applications. The processing complexity of our method is relatively low. Using a very similar strategy, a frame rate of four images per second was reported in [130] for imaging long bones. However, a relatively larger imaging depth is needed for brain imaging (the center of the circle of Willis is located at a depth of about 7 cm), which increases the computational time for reconstructing one frame. Further development of our technique with parallel computing on GPUs or CPUs might provide a fast enough reconstruction [71], [150]–[152].

3.4.4. IMPROVING CEREBRAL BLOOD FLOW CHARACTERIZATION WITH TUI AND FRAME RATE

As shown in [54], [83], [105], [106], aberration correction improves blood flow imaging with TUI in subjects without TWF. The improvement of spatial resolution and contrast also improves the detection of blood flow. Future work should investigate the added value of our approach for imaging blood flow in the cerebral arteries.

The frame rate of SAI sequence is limited to about 100 Hz (considering 96 elements for transmission, a depth of 7 cm [8], and a sound speed of 1500 m/s for the brain). This frame rate is sufficient for brain anatomical imaging, but not high enough for blood flow quantification in the brain [153]. Once the sonographer has found the best window on the temporal region of skull to image through using the synthetic aperture sequence, the correction method could be extended to a high frame rate mode, using the transmission of plane waves or diverging waves (with the concept of virtual point sources). This also ensures a good signal-to-noise ratio since all the array elements can be activated (with the appropriate transmit delays) for the transmission of a plane or diverging wave.

3.5. CONCLUSION

In this article, we introduced a technique to improve the correction of the refraction caused by the temporal bone in single-sided 2-D TUI using a commercial probe. The novelty lies in the fact that the position and true geometry of the bone layer and the wave speed in the cortical bone are estimated with a single ultrasound probe. First, the head

wave was used for compressional sound velocity estimation. Then, SSMs were fed to the FMT for arrival time calculation. Finally, images were reconstructed through adaptive beamforming. The proposed approach substantially improved the image quality in experiments consisting of imaging a wire phantom placed behind a bone-mimicking plate or a human skull.

ACKNOWLEDGEMENTS

This work was supported by a joint grant from the Netherlands Organisation for Scientific Research (NWO)/the Netherlands Organisation for Health Research and Development (ZonMw) and the Department of Biotechnology (Government of India) under the program Medical Devices for Affordable Health (MDAH) as Project Imaging Needles (Grant Number 116310008).

3.6. SUPPLEMENTARY DOCUMENT

Table 3.S1: The quantitative evaluation of the numerical results presented in Figure 3.5.

Scatterer number	Coordinates (mm) [Lateral, Depth]			FWHM (mm)			Contrast ratio (dB)		
	G.T.	Con.	P.M.	G.T.	Con.	P.M.	G.T.	Con.	P.M.
1	[-5.0, 17.6]	[-4.6, 16.7]	[-5.0, 17.6]	0.43	0.70	0.61	78.9	38.5	41.5
2	[0, 22.6]	[1.4, 22.0]	[0, 22.7]	0.48	1	0.58	79.3	35	43.7
3	[5.0, 27.5]	[6.3, 26.7]	[5.0, 27.6]	0.57	0.86	0.72	78.3	39.9	42.5
4	[9.9, 32.6]	[10.9, 31.5]	[10.0, 32.1]	0.67	1.16	0.93	76.6	35.0	38.3
5	[12.9, 35.1]	[13.9, 33.7]	[13.1, 35.1]	0.75	1.31	1.06	75.2	29.0	34.2
	Average difference compared to the G.T.			Average for all the scatterers			Average for all the scatterers		
	—	[1.0, 0.96]	[0.06, 0.14]	0.58	1.00	0.78	77.7	35.5	39.9

Table 3.S2: The quantitative evaluation of the experimental results with the bone-mimicking plate presented in Figure 3.7.

Scatterer number	Coordinates (mm) [Lateral, Depth]			FWHM (mm)			Contrast ratio (dB)		
	G.T.	Con.	P.M.	G.T.	Con.	P.M.	G.T.	Con.	P.M.
1	[-11.2, 32.2]	[-10.2, 31.0]	[-11.1, 32.1]	0.87	2.13	1.31	42.8	22.1	34.1
2	[-8.0, 41.3]	[-7.1, 39.2]	[-7.7, 41.5]	0.75	1.71	1.09	39.8	26.7	38.0
3	[-3.0, 36.5]	[-2.8, 34.3]	[-3.0, 36.5]	0.84	1.84	0.95	52.4	30.5	42.7
4	[0.9, 30.9]	[0.3, 28.5]	[1.0, 30.7]	0.77	1.90	0.91	46.8	20.3	37.8
5	[7.7, 26.9]	[7.1, 24.7]	[7.9, 27.1]	0.77	1.2	1.02	36.8	12.1	23.0
6	[14.5, 31.2]	[13.8, 30.1]	[14.5, 31.3]	0.78	2.00	1.08	48.5	27.2	39.1
	Average difference compared to the G.T.			Average for all the scatterers			Average for all the scatterers		
	—	[0.7, 1.9]	[0.11, 0.13]	0.80	1.80	1.06	44.5	23.1	35.8

Table 3.S3: The quantitative evaluation of the experimental results with the bone-mimicking plate presented in Figure 3.9.

Scatterer number	Coordinates (mm) [Lateral, Depth]			FWHM (mm)			Contrast ratio (dB)		
	G.T.	Con.	P.M.	G.T.	Con.	P.M.	G.T.	Con.	P.M.
1	[-0.2, 35.3]	[1.0, 34.4]	[0.5, 34.9]	0.62	1.63	1.30	53.1	28.1	34.0
2	[-4.5, 41.0]	[-3.0, 39.7]	[-3.7, 40.6]	0.74	2.52	1.71	55.3	31.0	38.9
3	[-8.6, 46.9]	[-6.3, 45.7]	[-7.2, 46.8]	0.85	2.67	1.93	58.0	32.7	40.2
4	[1.9, 47.7]	[2.7, 46.4]	[3.0, 47.3]	0.84	4.08	2.06	54.0	28.3	35.5
Average difference compared to the G.T.				Average for all the scatterers			Average for all the scatterers		
	—	[1.45, 1.17]	[1, 0.32]	0.76	2.72	1.75	55.1	30.0	37.1

4

ACCELERATED 2D REAL-TIME REFRACTION-CORRECTED TRANSCRANIAL ULTRASOUND IMAGING¹

In a recent study, we proposed a technique to correct aberration caused by the skull and reconstruct a transcranial B-mode image with a refraction-corrected synthetic aperture imaging scheme. Given a sound speed map, the arrival times were calculated using a fast marching technique (FMT), which solves the Eikonal equation and therefore is computationally expensive for real-time imaging. In this paper, we introduce a two-point ray tracing method, based on Fermat's principle, for fast calculation of the travel times in the presence of a layered aberrator in front of the ultrasound probe. The ray tracing method along with the reconstruction technique are implemented on a graphical processing unite (GPU). The point spread function (PSF) in a wire phantom image reconstructed with the FMT and the GPU-implementation was studied with numerical synthetic data and experiments with a bone-mimicking plate and a sagittally-cut human skull. The numerical analysis showed that the error on travel-times is less than 10% of the ultrasound temporal period at 2.5MHz. As a result, the lateral resolution was not significantly degraded compared with images reconstructed with FMT-calculated travel times. The results using the synthetic, bone-mimicking plate and skull dataset showed that the GPU-implementation causes a lateral/axial localization error of 0.10/0.20 mm, 0.15/0.13 mm and 0.26/0.32 mm compared to a reference measurement (no aberrator in front of the ultrasound probe), respectively. For

¹This chapter has been published as:
Mozaffarzadeh et al., "Accelerated 2D Real-Time Refraction-Corrected Transcranial Ultrasound Imaging", IEEE TUFFC., 2022.

The text and notation used in this chapter may differ on minor details from the actual publication. This is done to achieve consistency between chapters.

an imaging depth of 70 mm, the proposed GPU-implementation allows reconstructing 19 frames per second with full synthetic aperture (96 transmission events) and 32 frames per second with multi-angle plane wave imaging schemes (with 11 steering angles) for a pixel size of 200 μm . Finally refraction-corrected power Doppler imaging is demonstrated with a string phantom and a bone-mimicking plate placed between the probe and the moving string. The proposed approach achieves a suitable frame rate for clinical scanning while maintaining the image quality.

Keywords; *Transcranial ultrasound imaging; Adaptive beamforming; Phase aberration correction; Head waves; Temporal bone.*

4.1. INTRODUCTION

Real time ultrasound imaging of the brain started in the late sixties with the development of the first electronic two-dimensional scanner developed by Somer [6]. Decades after, transcranial ultrasound imaging (TUI) remains very challenging and offers poor image quality compared to ultrasound imaging of many body regions where no ultrasound propagation through bone occurs. Poor image quality of TUI results from strong wave aberration [11] and multiple scattering caused by the skull [12], [13]. Current commercial TUI devices ignore the skull.

TUI is nowadays available in most hospitals, clinics and emergency medicine services (EMS) worldwide [14], [89]–[91]. Compared to CT and MRI, ultrasound imaging is safe (non-ionizing), portable (can be used at bed-site and EMS) and relatively inexpensive. Despite its poor image quality, TUI was shown to be useful for the diagnosis of stroke [14]–[20], prevention of stroke in children (between an age of 2 and 16) with sickle cell disease [21]–[23], and vasospasm detection after subarachnoid hemorrhage [24], [25].

TUI is often performed through the temporal window (the thinnest part of the skull that gives the most optimal ultrasound access to the brain) where the squamous part of the temporal bone often consists of a single layer of cortical bone [Cite: brisson2021association, lee2020factors, peterson2003material, kwon2006thickness]. Phase aberration correction was first proposed by modeling the temporal bone as an infinitesimally thin aberrating layer at the surface of the transducer (so called the near-field phase-screen aberration model) [99]–[101], but the correction obtained by this approach is limited (axially and laterally) to a certain region called the isoplanatic patch [12], [33], [102]–[104]. Another approach is using either ultrasound measurements [107]–[109] or CT/MRI scans of the skull to obtain the true geometry and sound speed of the temporal bone prior to image reconstruction, and then correct phase aberration and refraction during image reconstruction [110]–[113]. Recently, we have shown the feasibility of single-sided two-dimensional transcranial ultrasound through the human temporal window using a single handheld commercial probe, where the position, true geometry and sound speed of the bone layer were estimated for an accurate correction of phase aberration and refraction [120], [154]. The same methodology was used before for in vivo imaging of the inner structure of the radius and tibia bone [77], [130]. While promising results were achieved, no fast-enough implementation is available for real-time transcranial imaging, i.e. enabling an imaging rate of at least 20 images per second, which limits its application in practice, especially for translation to 3D TUI [115], [116], [154], [155]. Real-time image reconstruction is essential in practice as it allows the operator to freely move the probe find the proper imaging window and imaging plane, and look for biomarkers related to a possible brain disorder in either B-mode or flow images. A frame rate of 4 Hz was reported in [130], but still not fast enough for real-time visualization.

Over the past two decades, the emergence of graphics processing units (GPUs) has facilitated high performance computing [156]–[158]. Medical ultrasound imaging also took advantage of this technology [151], [159], [160]. Different beamforming techniques such as Capon [160]–[163], short-lag spatial coherence [152], [164], [165], synthetic aperture sequential beamforming [166], [167], delay-multiply-and-sum [168] and double-stage delay-multiply-and-sum [40], [71], and volumetric imaging systems [169]–[171] were accelerated by GPU. GPU-based beamforming softwares were developed [169], [172], and

ultrasound vector flow imaging systems were accelerated [173]–[175]. Yiu, et al. [150] reported on a very high frame rate realization of the synthetic aperture and multi-angle plane wave imaging schemes with 2 GPUs and a recursive implementation, which can output between 1000 and 5000 frames per second depending on the number of receive channels and image depth.

Despite all the acceleration achieved by GPUs in medical ultrasound imaging field, implementations are all based on a strong assumption: an imaging medium with a constant wave-speed (1540 m/s). This does not apply to TUI. In this paper, we introduce an accelerated image reconstruction technique that corrects for phase aberration and wave refraction caused by the human temporal bone for real time imaging. The two-point ray tracing concept (introduced by Waltham [155]) was used to find the shortest (following Fermat's principle) travel-time connecting an image pixel to an array element or a virtual point source (for diverging or plane wave imaging) [176]. Unlike in [77], [130], the approach is not iterative and the near and far surfaces of the bone layer are described in a discrete manner using the image grid points. This allows a faster calculation of the travel-times and therefore tremendously reduces computational time for image reconstruction. Its implementation on a GPU further reduces computational time.

4.2. ACCELERATED RAY-TRACING BASED RECONSTRUCTION

4.2.1. PRINCIPLE OF THE PROPOSED METHOD

Image reconstruction is most often performed with a delay-and-sum algorithm, which requires the accurate calculation of the ultrasound round-trip travel times (i.e. from the source to the image pixel and from the image pixel back to the array elements). Several techniques exist to calculate these travel times in a layered medium. Eikonal solvers propagate the wavefront through the medium to calculate the travel-time from a array element or a virtual point source to an image pixel in the brain region [115], [116], [130], [154]. Another approach is iterative two-point ray tracing, where the ray path providing the minimum travel time (Fermat's principle) is searched iteratively and accurately using a method for function minimization, for instance a ray bending approach using Brent's algorithm [77], [120], [130]. However, eikonal solvers and iterative two-point ray tracing are too computationally expensive to reconstruct more than 20 images per second. In contrast, our approach is less accurate but much faster because it seeks the shortest travel-times by evaluating the travel time for a limited number of possible ray paths passing through a limited number of intermediate points (IPs). IPs are defined as the image pixels describing the near and far surfaces of the bone layer in the image. The terms "near surface" and "far surface" are defined with respect to the probe. A summary of the proposed accelerated ray-tracing based imaging approach is provided in Figure 1. We propose the following three steps to reconstruct a refraction-corrected image:

1. The pixels on the far surface of the silicone rubber front layer in the transducer are defined as intermediate points (SIPs; the red squares in Figure 4.1). The ray tracing starts to find the shortest travel-time from pixels in the skin (up to a certain maximum depth where we expect to detect the near surface of the bone, see the red dashed line in Figure 4.1(a)) to each array element through the SIPs; see the red vectors in Figure 4.1(a). The sound speed of the skin should be used to convert the

distance to travel-time. The image is reconstructed within the skin area up to the maximum expected depth of the near surface of the skull and using the estimated travel-times. Thus, the image contains the near surface of the bone layer, which is then segmented using Dijkstra's algorithm [122]. This algorithm seeks the path that crosses the image from left to right and follows the image pixels with the highest intensity in the ultrasound image, by maximizing a merit; here the sum of the pixel values along the path is used.

2. The IPs are updated (called NIPs) to the pixels on the segmented near surface (see the black squares in Figure 4.1(b)). The ray tracing finds the shortest travel-time from pixels in the bone (up to a certain maximum depth where we expect to detect the far surface of the bone (see the black dashed line in Figure 4.1(b)) to each array element through the NIPs; the black vectors in Figure 4.1(b) are examples of the paths. The compressional wave speed of the bone should be used to convert the distances to travel-times. The image is reconstructed up to the maximum expected depth of the far surface of the skull and using the estimated travel-times. The far surface of the bone layer is segmented using Dijkstra's algorithm.
3. The IPs are updated along the far surface of the bone layer (called FIPs; see the purple squares in Figure 4.1(c)). Finally, the ray tracing finds the shortest travel-time from pixels in the brain (up to the maximum imaging depth) to each array element through the FIPs (the purple squares in Figure 4.1(c)), and the rest of the image is reconstructed.

We use prior knowledge of the silicone rubber front layer thickness and wave speed in the silicone rubber front layer in step 1. We also assume that the wave speed in the layer between the probe and the aberrator and the wave speed in bone is known. A value from the literature [9] can be used or it can be estimated with the bidirectional head-wave technique and an autofocus approach as described in [72], [77]. Describing locally the skull as a single homogeneous layer is only valid for a temporal bone without a diploe. Moreover we hypothesize negligible wave-speed anisotropy in bone, in the image plane. The depths of the first and second reconstruction steps (the red and black dashed lines, respectively, see Figure 4.1) are determined by prior knowledge on the thickness of the skin and the temporal bone [7], [177]; the temporal bone thickness of the adult human skull was measured 2.5 ± 0.9 mm with CT [7]. Results obtained by the proposed reconstruction method are titled/captioned ARC (standing for Accelerated Refraction Correction technique) throughout the paper. While the near surface of the bone layer is depicted flat in Figure 4.1, our approach can be applied to any irregular interface (such as the far surface of the bone layer in Figure 4.1).

4.2.2. GPU IMPLEMENTATION

OVERVIEW

The proposed approach for estimating the arrival-times and image reconstruction are implemented in a GPU using the compute unified device architecture (CUDA) platform and the application programming interface (API) model created by Nvidia. Figure 4.2 shows a schematic of the hardware/software level setup. Matlab is used to run the Verasonics

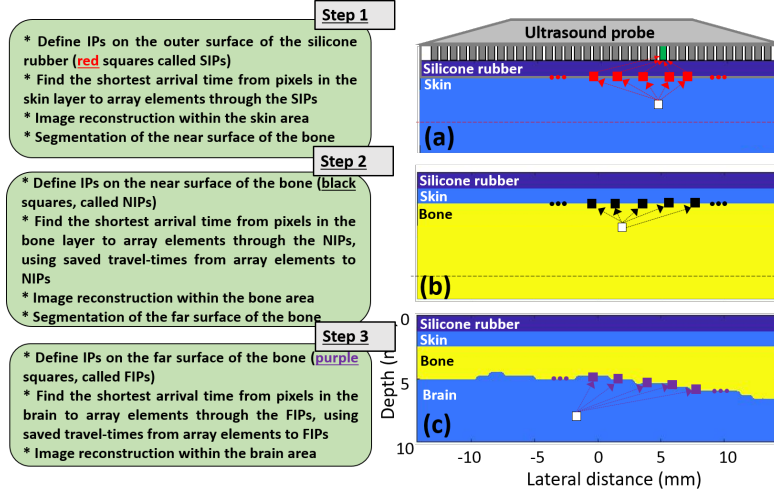


Figure 4.1: A summary of the proposed refraction-corrected image reconstruction approach. Three steps of ray tracing and adaptive beamforming are used for reconstructing the image in the brain area; the illustration is shown only for one pixel (white square) and one element (the element colored green). The rays pass through intermediate points (IPs). A limited number of IPs and travel-paths are shown for simplicity. Red, black and purple squares are IPs defined on the surface of the silicone rubber front layer in the transducer (SIPs), near (NIPs) and far (FIPs) surfaces of the bone layer, respectively. The model shown in (c) presents the numerical model used for imaging in our previous [154] and this study.

Vantage 256 system. Once the echo data of one frame is fully stored in the Vantage local memory, it is transferred to the host (PC) random-access memory (RAM) using a PCI express bus; the echo data is time gain compensated and filtered (based on the bandwidth of the probe) during data acquisition by the Vantage. The echo data along with the properties of the imaging system (e.g., the properties of the array, the size of the medium, the coordinates of the pixels and primary IPs, the minimum/maximum bone thickness and etc.) are then passed to a CUDA-written Matlab executable (MEX) function. The MEX function synchronously and asynchronously copies the properties of the imaging system and the pre-beamformed echo data to the GPU global memory, respectively, and then the image reconstruction starts.

We developed two kernels: 1) the ray tracing kernel to find the arrival-times and 2) the reconstruction kernel to form the images. These two kernels are utilized three times: 1) to find the near surface of the bone, 2) to find the far surface of the bone and 3) to generate the final image. The travel-times calculated by the ray-tracing kernel in the first two times are stored in the global memory (see the Travel-time blue block in Figure 4.2). This strategy makes it possible to reduce the combinational search from NIP3 (NIP is the number of intermediate points (IPs) used to describe each of the three interfaces) travel-times to 3NIP for each pixel in the brain (Figure 4.1).

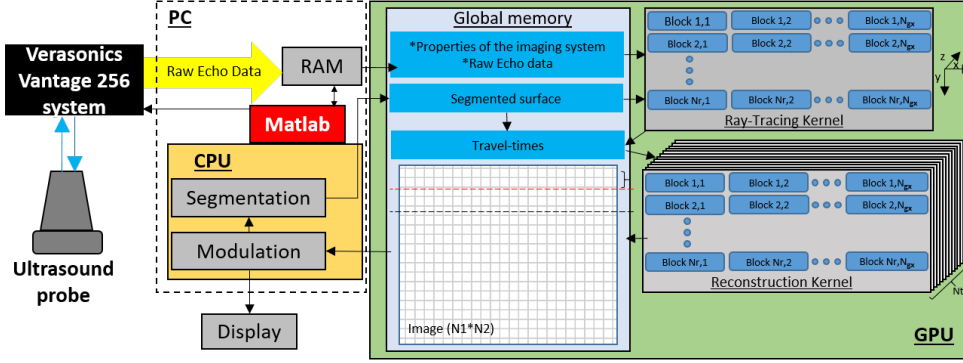


Figure 4.2: The system-level overview of the hardware/software setup for the GPU-based refraction-corrected image reconstruction approach. N_{gx} , N_r/N_t are the GPU grid size in the X direction and the number of receivers/transmitters, respectively. N_1 and N_2 are the number of image pixels in the axial and lateral directions, respectively.

ANALYTIC SIGNAL CALCULATION

The MEX function is developed based on a sampling frequency four times of the transducer central frequency to use the direct sampling concept [178]; the quadrature component (Q) of the analytic signal (I/Q) is approximately the in-phase signal delayed by one data sample.

KERNEL SIZE

For each transmit event (N_t in total), there are N_r receivers and $N_1 \times N_2$ image pixels (depth \times lateral direction). One-dimensional (1D) blocks (block.x) with a size of 1024 are used in this study. The grid size used for the ray tracing kernel is two dimensional and calculated based on the number of pixels, block size and number of receivers as "dim3 grid1(N_{gx} , N_r)".

The proposed approach is briefly presented in Figure 4.1. Image reconstruction starts with a primary SSM. After each segmentation step, the SSM is updated and new reconstruction is performed. Note that the terms far and near are in relation to the probe throughout this article.

4.2.3. COMPRESSIONAL WAVE SPEED ESTIMATION IN THE ABERRATOR

The bidirectional headwave method was used before to estimate the compressional wave speed of cortical bone [73]–[75]. This method works based on the propagation of the head wave (the first arriving signal) along a planar interface and is briefly explained as follows.

$$N_{gx} = \begin{cases} \frac{N_{op}}{block.x}, & \text{if } \frac{N_{op}}{block.x} \in N \\ \frac{N_{op}}{block.x} + 1, & \text{otherwise} \end{cases}$$

where N_{gx} and $N_{op}=N_1*N_2$ are the GPU grid size in the X direction (see Figure 4.2) and

the number of pixels, respectively. The GPU grid size in the Y direction is equal to number receivers. This indicates that each row of grids calculates the correct travel-times for each receiving element. The grid used for the reconstruction kernel is three-dimensional. The first two dimensions are the same as the ray-tracing kernel, and the third one (in the Z direction) is the number of transmitter (Nt).

4.3. MATERIALS AND METHODS

4.3.1. NUMERICAL AND EXPERIMENTAL STUDIES

In this work, the same numerical model and experimental setups reported in [154] were used for the sake of comparison (except for evaluating the effect of pixel size on the resolution, and power Doppler imaging (shown in Figure 4.3(b))). For the numerical study, the k-Wave MATLAB toolbox was used in a two dimensional (2D) lossless medium, and the shear wave propagation was ignored [124]. As shown in [179], neglecting mode-converted shear waves does not significantly change the main lobe of the point spread function. Because a shear wave propagates slower than a compressional wave, mode-converted shear waves in bone generate additional echo signals that arrive later than those related to purely compressional waves and hence contribute only to the trailing clutter in the point spread function [180]. The speed of sound in lens, skull and soft tissue was 1000 m/s, 3200 m/s and 1600 m/s, respectively. The mass density of the soft tissue/lens and skull was 1000 kg/m³ and 1900 kg/m³, respectively. A single-element transmission sequence was used to excite the medium for generating the numerical and experimental B-mode images.

A 4.2 mm-thick bone-mimicking plate (Sawbones, Pacific Research Laboratory, Inc., Vashon, WA) (see Figure 2(b) of [154]) having attenuation close to that in low-porosity cortical bone, a compressional wave speed in the image plane of 3000 m/s and mass density of 1640 kg/m³ [130] was used in the first experiment. A sagittally-cut human skull (see Figure 2(c) of [154]) was used in the second experiment. The temporal bone of the skull was used as the imaging window. The wave speed in the bone layer and water was considered 3500 m/s and 1500 m/s, respectively. We imaged multiple wires having a diameter of 50 μ m with a one-dimensional phased array probe (P4-1, ATL/Philips, 2.5 MHz, 96 elements, pitch = 0.295 mm). To reconstruct power Doppler images, a moving string was imaged with a multi-angle plane wave imaging sequence (5 plane waves in -15:15 degrees in water) with (see Figure 4.3(b)) and without (to acquire a reference dataset) the Sawbones plate in front of the probe; the near surface of the Sawbones plate was at the depth of 5.7 mm. An ensemble length of 100 frames was used to compute the power Doppler images. Singular value decomposition (SVD) filtering was used to remove the stationary signals; Matlab "svd" command was utilized and the first 10 singular values were removed. Spatio-temporal SVD filtering generally performs better than a simple temporal high pass filter for power Doppler imaging, especially when the signal-to-noise ratio is poor or with slow tissue motion [181]. The numerical and experimental images presented in the followings are reconstructed using a pixel size of 100 μ m to maintain the ray tracing accuracy. The PC connected to the vantage has an Intel® Xeon® E5-2680 v3 CPU and a GeForce RTX-2080Ti GPU. As our MEX function is developed based on the direct sampling concept [178], the numerical dataset obtained by a sampling frequency of 533.3MHz was down-sampled to a sampling frequency of 10 MHz, like in the experiments, and then passed to the MEX

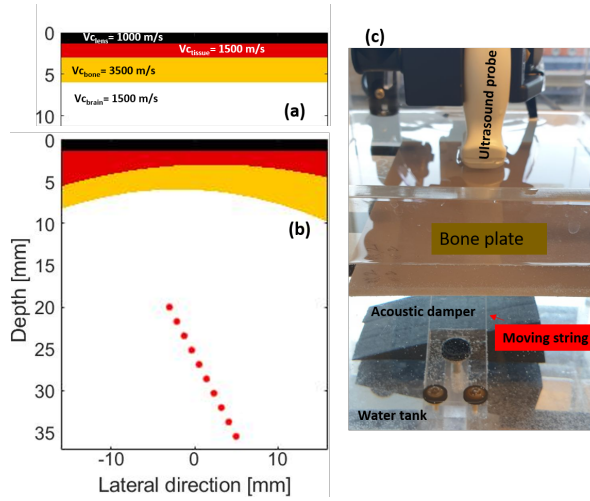


Figure 4.3: The numerical models used for evaluation of the effects of pixel size on (a) the accuracy of the proposed ray tracing technique to calculate travel times and (b) point spread function. The red circles in (b) show the location of the scatterers. The evaluation in (a) is conducted up to a depth of 60 mm, but the model is only shown up to a depth of 12 mm for better clarity. The bone layer in (a) starts at 3 mm and ends at 6 mm depth. Panel (c) depicts the experimental setup with the string phantom and the bone-mimicking plate for power Doppler imaging.

function.

4.3.2. EVALUATION METRICS

The proposed method (ARC) aims to be much faster than our previous approach relying on an eikonal solver (FMT), while maintaining image quality. Therefore the difference between image quality metrics assessed in ARC images and in FMT images is reported. Lateral resolution calculated as the full-width-half-maximum (FWHM) and localization error (calculated with respect to the reference images) were used for quantitative evaluation of the image quality. The axial resolution is determined by the frequency bandwidth of the transmit waveform and is not significantly degraded by phase aberration. Therefore the axial resolution is not studied in this work. To evaluate the effect of pixel size on the performance of the proposed ray tracing approach, the travel-times were calculated for a known velocity model (Figure 3(a)) using an Eikonal equation solver [182] and then compared to that obtained by our method. A spatial grid step size of $5 \mu\text{m}$ was used for the Eikonal solver. The model shown in Figure 4.3(b) is used to evaluate the effect of the pixel size on point spread function (PSF) and FWHM; ten point scatterers were positioned with lateral and axial coordinates of -3 mm to 5 mm and 20 mm to 36 mm, respectively. The processing time of the MEX function was measured in full single element synthetic aperture imaging (SAI) and multi-angle plane (or diverging) wave imaging (PWI; with 11 virtual sources) schemes for depths of 20 mm up to 70 mm (suitable for bone imaging

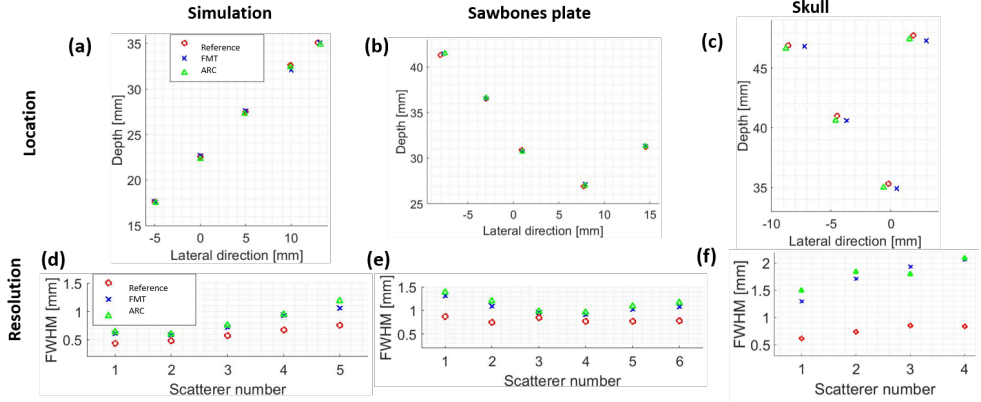


Figure 4.4: The scatterers coordinates and full width at half maximum (FWHM) obtained in the simulation study (the first column), and the experiments conducted with the Sawbones plate (the second column) and the skull (the third column). The detailed numbers corresponding to the reference and FMT can be found Table 1-3 of the supplementary document of reference [154]. The reference image was generated without an aberrator in front of the probe.

[130] and transcranial imaging [8], respectively) with a pixel size of 100 μm and 200 μm . The medium configuration shown in Figure 4.3(b) was used. For each configuration, the MEX function was run 50 times and the average processing time was reported.

4.4. RESULTS

4.4.1. NUMERICAL RESULTS

SCATTERERS LOCALIZATION AND FWHM

Figure 4.4(a, d) and Table 4.1 (the first column in the coordinates and FWHM sections) indicate that the proposed method does not significantly degrade image quality, as shown in Figure 4.S1 (see the supplementary document). The mean lateral and axial localization errors are 0 mm and 0.14 mm, compared to the FMT, respectively. The mean difference in lateral resolution (FWHM) is 0.04 mm, compared to FMT.

EFFECTS OF PIXEL SIZE

Figure 4.5(a) indicates that the pixel size does not significantly change the lateral resolution (FWHM). The PSF is not significantly altered (see Figure 4.5(b)). The maximum intensity of the PSF obtained with ARC is found very close to the true location of the scatterers indicated with the green triangle (from image without the aberrator). Figure 4.6(c) shows the absolute error calculated by subtracting the travel times obtained by the proposed ray tracing technique (Figure 4.6(a)) and the Eikonal solver (Figure 4.6(b)); a pixel size of 200 μm was used for estimation of the travel-times. The symmetry of the error map is due to symmetry of the velocity model (see Figure 4.3(a)). For pixels close to width=0, refraction is very small such that the ray is nearly vertical because all layers are parallel to the

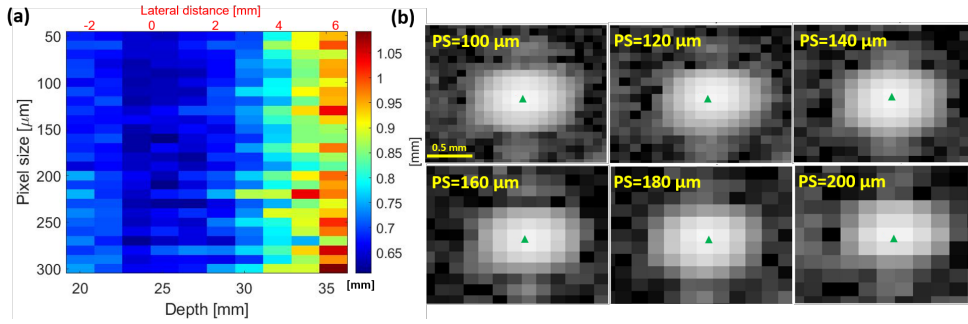


Figure 4.5: (a) The lateral FWHM (see the colorbar for the scale) at different axial (depth) and lateral locations and for different pixel sizes, obtained with the numerical model shown in Figure 4.3(b); the black and red x-axes show the depth and the lateral locations of the scatterers positioned obliquely, respectively. (b) The point spread function (PSF) obtained for different pixel size; the scatterer was positioned at the lateral and axial distance of -3 mm and 20 mm, respectively. The green mark indicates the true location of the scatterer. The PSFs are shown with a dynamic range of 40 dB. PS stands for the pixel size.

4

array. Therefore, if the lateral coordinate of the pixel is equal to the lateral coordinate of the element, the error becomes extremely small; in this case, the error is minimum close to $x=0$ for a lateral pixel coordinate of -200 μm because the lateral coordinate of the array element is -150 μm .

Figure 4.6(d) shows the distribution of the errors obtained by different pixel sizes. The errors do not linearly increase with a larger pixel size since the boundaries of the velocity model at a depth of 3 mm and 6 mm are determined by the nearest pixel on the image grid (see Figure 4.3(a)); for a pixel size of 140 μm , it causes about 30 ns shift in the errors. Yet, the errors are below 45 ns, which is slightly larger than 10 % of the ultrasound wave period (10% of 400 ns for the P4-1 probe), which results in insignificant degradation of image quality [83].

4.4.2. EXPERIMENTAL RESULTS

ESTIMATION OF THE ABERRATOR THICKNESS

Figure 4.7 compares the experimental reconstructed images using the two dataset (Sawbones plate and skull) and two reconstruction methods (ARC and FMT). A thickness of 4.2 mm and 1.46 mm was obtained for the Sawbones plate and the temporal bone of the skull, respectively (not shown here). The thickness of the Sawbones plate is in excellent agreement with that obtained with the FMT [38]. The skull thickness is about 0.16 mm larger with the ARC technique compared with the FMT [154]; this error is consider minor comparing to the pixel size of 100 μm . The image quality in Figure 4.7(a, c) is close to Figure 4.7(b, d), which is our goal. The red boxes show the effects of multiple scattering caused by the aberrator.

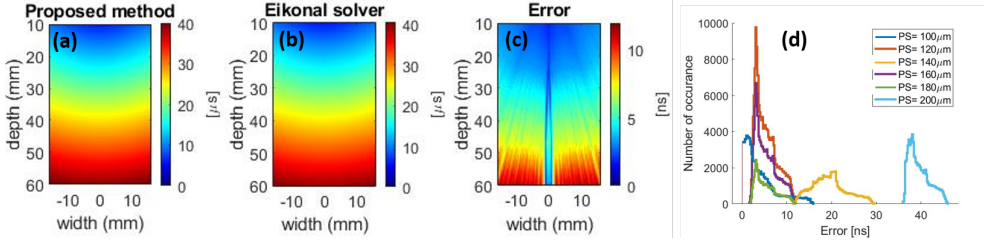


Figure 4.6: Travel-times between the center element of the transducer array and pixels in the brain estimated with (a) the proposed ray tracing ARC technique for a pixel size of 200 μm and (b) the accurate travel times calculated with an Eikonal solver, respectively, using the configuration shown in Figure 4.3(a). Panel (c) shows the absolute error map (which is obtained by subtracting panel (a) and (b)). (d) The distribution of the errors on the travel times from an element in the center of the transducer aperture to pixels in the brain, for different pixel sizes. PS stands for the pixel size.

Table 4.1: The quantitative evaluation of image quality obtained with the ARC technique compared to our previous approach relying on an eikonal solver for the numerical and experimental results presented in Figure 4.4-4.5. The localization error and lateral FWHM difference were calculated with respect to the eikonal solver approach relying on a Fast Marching Technique (FMT); see Table 1-3 of the supplementary document of reference [154].

Scatterer number	Localization error (mm)			Lateral FWHM difference (mm)		
	[Lateral, Axial]			Simulations	Sawbones plate	Skull
1	[0.1, -0.1]	[0, 0]	[-1.1, 0.1]	0.0	0.08	0.2
2	[0, -0.4]	[0.2, 0]	[-0.9, 0]	0.02	0.11	0.13
3	[-0.1, -0.3]	[0, 0.1]	[-1.6, -0.2]	0.03	0.03	-0.13
4	[-0.1, 0.3]	[0, 0]	[-1.44, 0.1]	0.02	0.04	0.03
5	[0.1, -0.2]	[0, -0.1]	—	0.13	0.07	—
6	—	[0, 0]	—	—	0.09	—
Mean \pm standard deviation				Mean \pm standard deviation		
[0 \pm 0.1, 0.14 \pm 0.27]				0.04 \pm 0.05	0.07 \pm 0.03	0.05 \pm 0.14

SCATTERERS LOCALIZATION AND FWHM: SAWBONES PLATE

Figure 4.4(b, e) and Table 4.1 (the second column in the coordinates and FWHM sections) indicate that the proposed method reconstructs the scatterers with an average lateral and axial localization error of 0.03 mm and 0 mm, compared to FMT, respectively. The mean difference in lateral resolution (FWHM) is 0.07 mm, compared to FMT..

SCATTERERS LOCALIZATION AND FWHM: HUMAN SKULL

Figure 4.4(c, f) and Table 4.1 (the third column in the coordinates and FWHM sections) indicate that the proposed method reconstructs the scatterers with an average lateral and axial localization error of -1.2 mm and 0 mm, compared to the FMT, respectively. The lateral error is 0.3 mm with respect to reference image (values are available in the supplementary document of reference [154]) though. The mean difference in lateral resolution

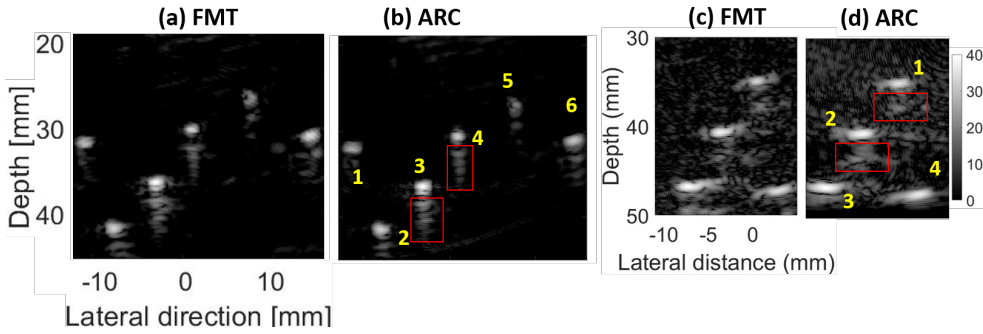


Figure 4.7: The experimental reconstructed image with the (a, b) Sawbones plate and (c, d) the real human skull in front of the probe. All the images are locally-normalized and log-compressed. The red boxes show the effects of multiple scattering caused by the aberrating layer (plate and bone). The numbers (in yellow) are referred for quantitative evaluation in Table 4.1 and Figure 4.4.

(FWHM) is 0.05 mm, compared to FMT.

POWER DOPPLER IMAGING

The reconstructed power Doppler images with or without the Sawbones plate in front of the probe are presented in Figure 4.8. The yellow arrows in Figure 4.8(a) show bubbles floating in the water tank. With the aberrator inserted, the clutter around the string is significantly weaker in the image reconstructed by the ARC technique, compared to the conventional reconstruction which ignores the aberrator. The width of string (measured as the FWHM in a direction normal to the string) was 0.37 mm with the ARC technique (Figure 4.8(c)), which is close to the width in the reference image (0.32 mm). The width of the wire obtained with conventional reconstruction appears wider (0.54 mm) as a consequence of degraded lateral resolution caused by phase aberration.

4.4.3. PROCESSING TIME WITH THE GPU IMPLEMENTATION OF THE ARC TECHNIQUE

The processing time of the proposed reconstruction approach, calculated for the configuration shown in Figure 4.3(b), is presented in Figure 4.9. The red and black curves represent the processing time and frame rate, respectively. The frame rate with a pixel size of 100 μm is lower than with a pixel size of 200 μm , because the processing time increases with the number of pixels. Using SAI scheme with 96 single-element transmissions to reconstruct the image up to depths of 20 mm and 70 mm, a frame rate of 32 Hz and 19 Hz is obtained for a pixel size of 200 μm . Using PWI scheme with 11 transmit steered plane waves to reconstruct the image up to depths of 20 mm and 70 mm, a frame rate of 40 Hz and 32 Hz is obtained for a pixel size of 200 μm . The processing time for each step in the ARC technique for PWI mode and an imaging depth of 70 mm with a pixel size of 200 μm is presented in Table 4.2.

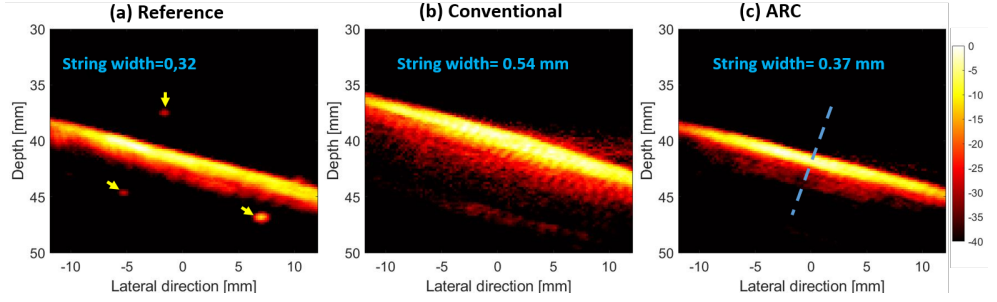


Figure 4.8: Power Doppler images using the experimental dataset generated (a) without and (b, c) with the Sawbones plate in front of the probe (Figure 4.3(c)). The yellow arrows in (a) show bubbles floating in the water tank. The blue dashed line shows the line (normal to the string) used to calculate the width of the string. The reference image was generated without an aberrator in front of the probe.

Table 4.2: The processing time of each step of the ARC technique for PWI with 11 transmit steered plane waves and an image depth of 70 .

Scatterer	Time [ms]
Primary memory allocation	8
First layer ray-tracing	6
First layer reconstruction	1
Second layer ray-tracing	5
Second layer reconstruction	1
Third layer ray-tracing	6
Third layer reconstruction	2
memory allocation and deallocation, segmentation	2
Total	31

4.5. DISCUSSION

4.5.1. IMAGING SCHEME

To calculate the round-trip travel-times that are required to reconstruct the image with a delay-and-sum algorithm, both the transmit and receive travel-times are needed. In full single element SAI scheme, the number of transmitters (N_t) and receivers (N_r) and their coordinates are the same. Therefore, the receive travel-times calculated with respect to N_r receivers (see the ray tracing kernel in Figure 2) can be used as transmit travel-times. In practice, however, single element SAI is likely not the optimal imaging strategy for TUI due to 1) a low signal-to-noise ratio (i.e., transmitting with a single element generates a low acoustic pressure in the brain) and 2) a low data acquisition frame rate, which does not allow blood flow quantification in the brain (usually used for diagnosis of brain disorders) [153]. To address these issues, PWI [183] and diverging waves imaging (DWI) [184] schemes have a great potential since 1) a good image quality can be achieved while a faster data acquisition allows capturing transient phenomena in the brain, as reported by Montaldo, et al. [185], and 2) transmitting with sub-apertures or with all the elements of the

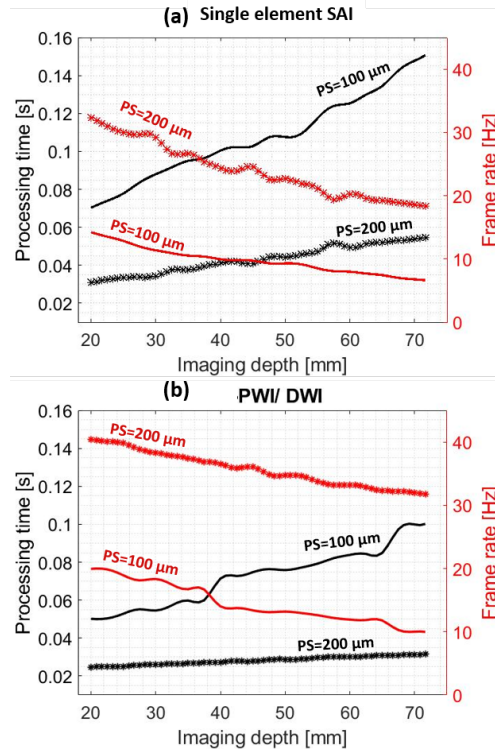


Figure 4.9: The processing time/ frame rate of the MEX function in (a) full single element synthetic aperture imaging and (b) plane wave imaging/ diverging waves imaging (with 11 steering angles) schemes for different imaging depths and pixel sizes (PS). The black and red graphs belong to the left (Processing time) and right (Frame rate) horizontal panels, respectively.

probe (with appropriate transmit delays) ensures a good signal-to-noise ratio. For TUI with a phased array transducer, DWI is more desired as it enables a larger field of view, compared to PWI. Using PWI/ DWI schemes requires estimating the transmit travel-times from virtual transmitters (usually defined behind the ultrasound probe) to pixels. This requires an additional ray tracing in steps 2, 4 and 6 of Section II.A. To do so, the ray tracing kernel in Figure 2 is configured with a Z grid size equal to the number of virtual transmitters.

As presented in Figure 9, PWI or DWI offers faster image reconstruction compared to single element SAI. That is because 1) the size of the third dimension (Z) of the reconstruction kernel (see Figure 2) equals to the number of virtual transmitter (from 3 [87] to 15 [183]), 2) less load/copy transactions from the global memory to on-chip memories, and the other way around, are needed. And, 3) the additional ray tracing (for estimating the transmit travel-times) is not computationally expensive. It should be noted that the processing time for PWI and DWI with the same number of virtual transmitters is the

same.

4.5.2. ANALYTIC SIGNAL CALCULATION

Yiu, et al. [150] and Gonzalez and Bell [152] used Hilbert transform in the time and frequency domain to calculate the analytic echo data, respectively. In this study, however, the direct sampling concept is used to avoid dedicating processing power to calculate the analytic signal, which includes copy/load memory transactions as well [178]. The same methodology was used by Choe, et al. [169] before.

4.5.3. LIMITATIONS OF THE PROPOSED APPROACH

WAVE-SPEED MODELING

While the cortical bone of the temporal region of the skull is known to exhibit anisotropic wavespeed [9], the wavespeed in the bone layer was assumed isotropic to simplify ray-tracing and therefore enable the fastest frame rate with our approach. Image distortions (depending on the anisotropy level) are expected if the anisotropy is neglected.

IMPLEMENTATION

As can be seen in Table 4.2, there are two modules that increase the processing time: 1) primary memory allocation, 2) ray-tracing kernel.

The primary memory allocation includes defining host (CPU) memories to save the results of the GPU kernels/ CPU functions and copying the properties of the imaging system to the GPU global memory (as shown in Figure 4.2). Currently, the memory allocation, and also memory freeing at the end of the MEX function, happens each time the MEX function runs. To further increase the frame rate, Matlab GPU arrays can be used to define these memories once (when the MEX function runs for the first time), and free them at the end of imaging. It should be also mentioned that the RF-data is transferred to the global memory in an asynchronous way during the first reconstruction step. Therefore, the size of the RF-data is not a bottleneck.

Our ray-tracing kernel calculates the travel-time of all the pixels in parallel. However, finding the shortest travel-time between a pixel and an array element through IPs is implemented sequentially with a for-loop in GPU. This kernel can be improved by re-defining the kernel architecture in a way that it evaluates all the travel-times (through the IPs) in parallel. Another option is to implement it on CPU with parallel programming (such as OpenMP). In the current implementation, ray-tracing is calculated for each frame because the position and geometry of the skull (in the current image plane) must be updated to achieve real-time refraction-corrected TUI as the sonographer moves the probe to search for the optimal image plane. However, once the proper imaging window and imaging plane are found by the operator and the probe is stabilized on the temporal bone, the travel-times could be only calculated once and reused as long as the probe remains still. An automated approach could be implemented to evaluate the stability of the probe in order to decide whether or not the refraction-corrected travel times must be updated. This would further increase the frame rate of our method.

4.5.4. FUTURE WORK

Our future studies include the in vivo evaluation of the proposed approach in adult human subjects, the development of a GPU-accelerated reconstruction technique that addresses the wavespeed anisotropy in the bone layer and the bottlenecks discussed above, and the translation of the approach to a matrix array transducer where the 3D geometry of the skull will be described.

4.6. CONCLUSION

In this paper, we reported a reconstruction technique for transcranial ultrasound imaging through the temporal bone, which uses a fast ray-tracing approach and a GPU implementation to speed up the calculation of the refraction-corrected arrival-times and image reconstruction. The results showed that the error on travel-times using a pixel size of $200\text{ }\mu\text{m}$ is not significant (about 10% of the ultrasound temporal period at 2.5MHz), and hence resulting in insignificant degradation of image quality and resolution, and negligible localization errors. We believe the approach enables real-time refraction-corrected transcranial ultrasound imaging with a frame rate between 20 and 30 Hz, and real-time refraction-corrected power Doppler imaging.

ACKNOWLEDGEMENTS

This work was supported by a joint grant from the Netherlands Organisation for Scientific Research (NWO)/the Netherlands Organisation for Health Research and Development (ZonMw) and the Department of Biotechnology (Government of India) under the program Medical Devices for Affordable Health (MDAH) as Project Imaging Needles (Grant Number 116310008).

4.7. SUPPLEMENTARY DOCUMENT

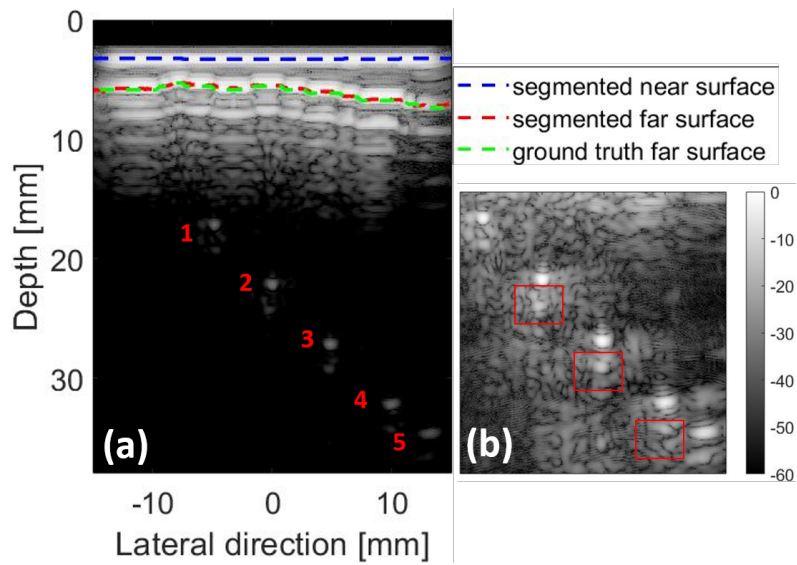


Figure 4.S1: (a) The reconstructed image using a numerical dataset which was generated using the model shown in Figure 4.1(c) (b) The zoomed and locally normalized version of (a). The red boxes show the effects of multiple scattering caused by the aberrator Both the images are reconstructed with the ARC technique.

5

COMPARISON OF PHASE-SCREEN AND GEOMETRY-BASED PHASE ABERRATION CORRECTION TECHNIQUES FOR REAL-TIME TRANSCRANIAL ULTRASOUND IMAGING¹

While transcranial ultrasound imaging is a promising diagnostic modality, it is still hindered due to the phase aberration and multiple scattering caused by the skull. In this paper, we compare the near-field phase screen modeling (PS) to a geometry-based phase aberration correction technique (GB) when an ultrafast imaging sequence (5 plane waves tilted from -15 to +15 degrees in the cutaneous tissue layer) is used for data acquisition. With simulation data, the aberration profile (AP) of two aberrator models (flat and realistic temporal bone) was estimated in five isoplanatic patches while the wave-speed of the brain tissue surrounding the point targets was either modeled homogeneous (ideal) or slightly heterogeneous to generate speckle (for mimicking a more realistic brain tissue). For the experiment, a phased array P4-1 transducer was used to image a wire phantom; a 4.2 mm-thick bone-mimicking plate was placed in front of the probe. The AP of the plate was estimated in 3 isoplanatic patches. The numerical results indicate that while all scatterers are detectable in the image reconstructed by the GB method, many scatterers are not detected with the PS method when the dataset used for AP estimation is generated with a realistic bone model

¹This chapter has been published as:

Mozaffarzadeh et al., "Comparison of Phase-Screen and Geometry-Based Phase Aberration Correction Techniques for Real-Time Transcranial Ultrasound Imaging," Applied Sciences. 12(19), 2022.

and a heterogeneous brain tissue. The experimental results show that GB method increases the signal-to-clutter ratio (SCR) by 7.5 dB and 6.5 dB compared to the PS and conventional reconstruction methods, respectively. The GB method reduces the axial/lateral localization error by 1.97/ 0.66 mm and 2.08/0.7 mm, compared to the PS method and conventional reconstruction, respectively. The lateral spatial resolution (full-width-half-maximum) is also improved by 0.1 mm and 1.06 mm, compared to the PS method and conventional reconstruction, respectively. Our comparison study suggests that GB aberration correction outperforms the PS method when an ultrafast multi-angle plane wave sequence is used for transcranial imaging with a single transducer.

Keywords; Transcranial ultrasound imaging; phase aberration correction; near-field phase screen modeling; adaptive beamforming; temporal bone.

5.1. INTRODUCTION

Transcranial ultrasound imaging (TUI) is used in hospitals for stroke diagnosis [14]–[20], prevention of stroke in children (between an age of 2 and 16) with sickle cell disease [21]–[23] and detection of vasospasm after subarachnoid hemorrhage (most often caused by head trauma) [24], [25]. Yet, the strong wave aberration [11] and multiple scattering caused by the skull [12], [13] are ignored in the current commercial TUI devices, which degrade image quality. This paper focuses on the correction of phase aberration caused by the skull.

The temporal window of the skull is usually used for TUI due to its relatively lower attenuation because it consists most often of a single layer of cortical bone with a thickness ranging from 1.5 mm to 4 mm [7]. Two categories of technique were proposed to correct phase aberration: 1) the near-field phase screen modeling [100], [101], 2) the approach relying on the estimation of the wave-speed, position and geometry of the bone layer. In near field phase-screen (PS) approaches, the temporal bone is modeled as an infinitesimally thin aberrating layer at the surface of the transducer [99]–[101]. The limitation of this method is that the correction is only limited to certain regions called the isoplanatic patches [12], [33], [102]–[104], [109], in particular because the effect of refraction is ignored. In the second category, the true position, geometry and sound speed of the temporal bone are estimated prior to image reconstruction either by ultrasound measurements [107]–[109] or CT/MRI scans of the skull, and then the phase aberration, including the effect of refraction, is corrected during image reconstruction [111]–[113]. Recently, we have shown the feasibility of a geometry-based (GB) aberration correction technique for single-sided two-dimensional transcranial ultrasound through the human temporal window using a single handheld commercial probe [154]. Our approach does not require any CT/MRI scan of the skull, the position and geometry of the bone layer is estimated in the ultrasound image. This approach was also used before for in vivo imaging of the inner structure of the radius and tibia bones [77], [130]. In [154], a fast marching technique to solve the Eikonal equation was used for ray-tracing and accurate estimation of the travel-times between image pixels and elements of the array. However, this computationally expensive implementation prevented the application of our approach for real-time imaging. To address this issue, a resource-efficient and accelerated ray-tracing approach was proposed in [186]. With an implementation on a graphics processing unit (GPU), real-time GB aberration correction TUI became feasible and was named accelerated refraction-corrected (ARC) image reconstruction.

References [108]–[110], [113] use the same geometry-based strategy but utilize a CT scan to obtain the geometry and sound speed of the skull. Real-time imaging was not also doable. In [107], a focused wave was used in transmission, which is out of the scope of this manuscript. In references [111], [112], a focused wave was used in transmission and a CT scan was used to obtain the geometry and sound speed of the skull. Our method estimates the position and geometry and the sound speed of the bone layer with ultrasound (no need for a CT or MRI scan) and using one probe [154] and enables real time imaging [186].

In this work, we aim to compare the PS approach and the ARC-GB aberration correction technique when an ultrafast imaging sequence (transmission of 5 multi-angle plane waves) is used for data acquisition and real time imaging with a single probe. This pa-

per shows that the ARC-GB method results in a higher image quality compared to the PS method. Unlike the PS method, the ARC-GB method is not affected by the speckle caused by the brain tissue heterogeneity.

5.2. MATERIALS AND METHODS

A block diagram is provided in Figure 5.1 to show the steps needed for correcting the phase aberration caused by a bone layer in front of the ultrasound probe using the ARC-GB and PS methods. Synthetic transmit focusing is necessary for the PS method as an ultrafast imaging sequence is used for data acquisition and not a set of transmit focused waves (traditional line-by-line ultrasound imaging). The images titled "conventional" throughout the paper are reconstructed with conventional delay-and-sum image reconstruction technique, i.e. assuming a medium with uniform wavespeed equal to 1600 m/s, therefore ignoring phase aberration caused by the bone layer.

5.2.1. ACCELERATED REFRACTION-CORRECTED GEOMETRY-BASED PHASE ABERRATION CORRECTION

We extensively described and evaluated the ARC-GB approach in [186]. In summary, it consists of 4 steps:

1. Estimation of the wave-speed in the bone layer with the bidirectional head-wave technique or the autofocus technique [77].
2. Intermediate points (IPs) are defined on the outer surface of the silicone rubber (called SIPs), the shortest travel-time from pixels in the superficial soft tissue layer to the array elements through the SIPs are found, the image of the superficial soft tissue layer is reconstructed using the calculated travel-times and the near-surface of the bone layer is segmented using Dijkstra's algorithm [122].
3. IPs are defined on the near-surface of the bone layer (called NIPs), the shortest travel-time from pixels in the bone layer to array elements through the NIPs are found, the image of the bone layer is reconstructed using the calculated travel-times and the far-surface of the bone layer is segmented using Dijkstra's algorithm.
4. IPs are defined on the far surface of the bone layer (called FIPs), the shortest travel-time from pixels in the brain to array elements through the FIPs are found, and the brain image is reconstructed using the calculated travel-times.

For reconstruction, a modified delay-and-sum algorithm (as explained in [77], [130], [154]) was used. The thickness and the wave speed in the silicone rubber layer can be found either by ultrasound measurements or the datasheet provided by the probe manufacturer. The image reconstruction depth used in steps 2 and 3 can be determined based on priory knowledge of the thickness of the skin and bone layers [177]. The terms "near surface" and "far surface" are defined with respect to the probe. The results captioned "Geometry-based" paper are generated with the ARC-GB reconstruction technique.

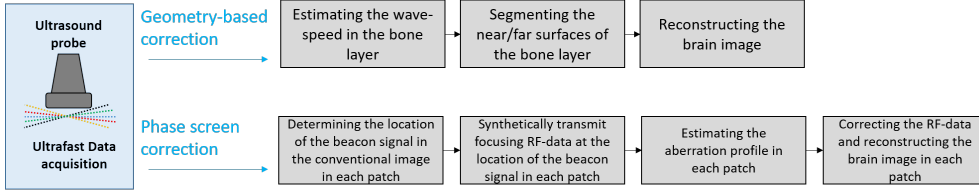


Figure 5.1: The block diagram showing the processing procedure for the geometry-based and phase screen aberration correction techniques when an ultrafast imaging sequence (multi-angle plane wave) is used for data acquisition.

5.2.2. NEAR FIELD PHASE SCREEN APPROACH

The PS correction technique requires a coherent wavefront backscattered from a small volume for estimating the aberration profile (AP) in each isoplanatic patch. Such a coherent wavefront backscattered from a small volume can be obtained if ideal echogenic point reflectors exist (such as microbubbles [83]) throughout the and/or thanks to transmit focusing in the heterogeneous medium [187]. Transmit focusing is obtained by the true transmission of a focused waves or by synthetic transmit focusing (post processing) if a set of unfocused waves (plane or diverging waves) are transmitted. In this paper, we evaluate the microbubble scenario (a more ideal situation for the PS method). Following steps are taken to determine the AP of an isoplanatic patch:

1. An image is reconstructed using a conventional delay-and-sum reconstruction technique (see Figure 5.2(a)), i.e. assuming a medium with uniform wavespeed equal to 1600 m/s. Then, we estimate the coordinates of the echogenic scatterers (used to estimate the AP of the isoplanatic patch), indicated by the green dots in Figure 5.2(a). Note that these coordinates are not the true coordinates of the targets (the red dots in Figure 5.2(a)) because phase aberration is ignored in conventional image reconstruction.
2. For synthetic transmit focusing, transmit time delays for the transmit unfocused waves to reach simultaneously the coordinates of the echogenic scatterer found in step 1 are calculated. Then, the RF-data acquired separately with each transmit unfocused wave is shifted by the calculated transmit delay.
3. By summing all the shifted RF-data, RF-data with transmit focusing is synthetically generated. As a result, the wavefront backscattered from the chosen scatterer has a higher amplitude compared to wavefronts backscattered by other scatterers and the un-focused RF-data (compare the amplitude of the backscattered wavefront from scatterer 1 and 2 in Figure 5.2(b, c) where the amplitude of the scatterer 2 in panel (c) is three times higher than from panel (b)).
4. The receive travel-times between the location of the scatterer and the array elements are calculated by triangulation (the green-dashed line in Figure 5.2(c)), assuming a medium with uniform wavespeed equal to 1600 m/s. They are used to define a time mask with which the backscattered wavefront in the RF-data after synthetic transmit focusing is extracted (Figure 5.2(d)).

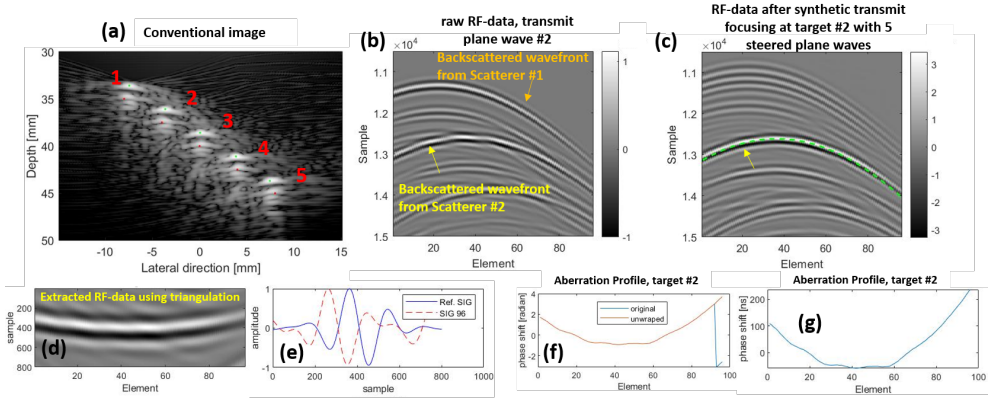


Figure 5.2: (a) The reconstructed image using the conventional delay-and-sum beam-former; the aberrator model and phantom shown in Figure 5.3(a) and Figure 5.3(c) were used to generate the numerical RF-data. (b) The numerical wavefront backscattered from scatterer 2 for a tilted (by 7.5 degree in cutaneous tissue) transmit plane wave. (c) The numerical wavefront after synthetic transmit focusing at the location of the scatterer 2 by coherent compounding of the RF-data obtained with 5 tilted plane waves (from -15 to 15 degree in cutaneous tissue). (d) The extracted wavefront using triangulation assuming a uniform medium. (e) The reference signal and the A-line received by element 96 of the array. (f) The estimated phase shifted and its unwrapped version for each element. (g) The estimated phase shift (aberration profile) in nanosecond for the isoplanatic patch around target 2. The red and green dots in (a) indicate the true location of the scatterers and the brightest pixel in the conventional image that is actually used to apply the PS method, respectively.

5. A-lines of the extracted wavefront in step 4 are summed up over all elements of the array to obtain a reference signal (see Ref. SIG in Figure 5.2(e)); also known as beam-sum reference signal [188]. Then, the phase shift between each A-line and the reference signal is calculated and unwrapped to compensate for phase jumps (Figure 5.2(f)). This results in the AP in the isoplanatic patch.

It should be noticed that a uniform-tissue medium is assumed in all the above steps. The AP of each isoplanatic patch is calculated separately based on the wavefront backscattered from the scatterer positioned in the isoplanatic patch. It is used to correct the arrival time of the raw RF-data before applying a conventional beamformer to reconstruct the image. The results captioned "Phase screen" throughout the paper are those generated with the near-field phase screen modeling technique.

5.2.3. NUMERICAL STUDY

The k-Wave MATLAB toolbox was used to evaluate the PS and GB reconstruction techniques in a two dimensional (2D) lossless medium, ignoring the generation of shear waves [124]. Our numerical study on the PS method consists of two steps: 1) estimating the AP of

each isoplanatic patch using an ideal phantom for PS technique (see the left box in Figure 5.3) and 2) applying the estimated AP on the RF-data generated using a phantom with 30 small scatterers at different lateral and axial locations (see Figure 5.3(f)) and analyzing the image.

For step 1, two aberrator models and two background wave-speed models provide four scenarios (four datasets): 1) a flat bone (Figure 5.3(a)) and a homogeneous background (Figure 5.3(e)), 2) the flat bone and a heterogeneous background generating speckle (Figure 5.3(d)), 3) a realistic bone (based on the micro CT of a human temporal bone (provided by Jing and Lindsey [189])) and homogeneous background, and 4) the realistic bone and a heterogeneous background generating speckle. The homogeneous background is an ideal situation for the PS method since individual responses of echogenic targets can be clearly identified in the RF-data. This resembles a scenario where the echoes from individual contrast agent microbubbles are used as beacon signal. The wave-speed in Figure 5.3(f) randomly varies by $\pm 0.5\%$ with a uniform distribution with respect to the homogeneous model and mimics a realistic brain tissue [190]. Five isoplanatic patches were defined (Figure 5.3(c)) by positioning the scatterers at lateral/axial coordinates of -8/35 mm, -4/37.5 mm, 0/40 mm, 4/42.5 mm, 8/45.5 mm; one in each isoplanatic patch. The numerical phantom used for estimating the AP (Figure 5.3(c)) was designed such that the hyperbolic wavefront of a scatterer in an isoplanatic patch (acting as a beacon signal) does not interfere with that of another scatterer in another isoplanatic patch; different axial and lateral locations of the scatterers ensured that. This is a very ideal situation for the PS method and most likely not the case in practice where the backscattered wavefront from contrast agent microbubbles are used for AP estimation, even if a small volume of contrast agent is injected.

For step 2 (image analysis), the two aberrator models, a homogeneous background and the phantom shown in Figure 5.3(f) - where 30 scatterers were positioned in different axial and lateral locations within each patch- were used to generate a numerical dataset. These two additional datasets were used for quantitative evaluation of both the PS and GB methods. The speed of sound (compressional wave speed) in the silicone rubber, skull and soft tissue (cutaneous tissue and brain tissue if homogeneous) was 1000 m/s, 3200 m/s and 1600 m/s, respectively. The mass density of the soft tissue/silicone rubber and skull was 1000 kg/m³ and 1900 kg/m³, respectively. The thickness of the silicone rubber, cutaneous tissue and flat bone layers was 1.3 mm, 1.7 mm and 2.5 mm, respectively. The minimum and maximum thickness of the realistic bone layer was 2.38 mm and 1.2 mm, respectively. The properties of a P4-1 phased-array transducer (ATL/Philips, 2.5 MHz, 96 elements, pitch = 0.295 mm) and 5 plane waves from -15 to +15 degrees (in cutaneous tissue) were used to generate the numerical datasets. The spatial grid and time step sizes were 10 μ m and 2 ns, respectively, to minimize numerical dispersion and maintain the stability and accuracy of the simulation.

5.2.4. EXPERIMENTAL STUDY

Our experimental setup includes a 4.2 mm-thick bone-mimicking plate (Sawbones, Pacific Research Laboratory, Inc., Vashon, WA) immersed in water (see Figure 5.3(g)). A phased-array transducer (P4-1, ATL/Philips, 2.5 MHz, 96 elements, pitch = 0.295 mm) connected to a Vantage 256 system (Verasonics Inc., Kirkland, WA, USA) was used to image a

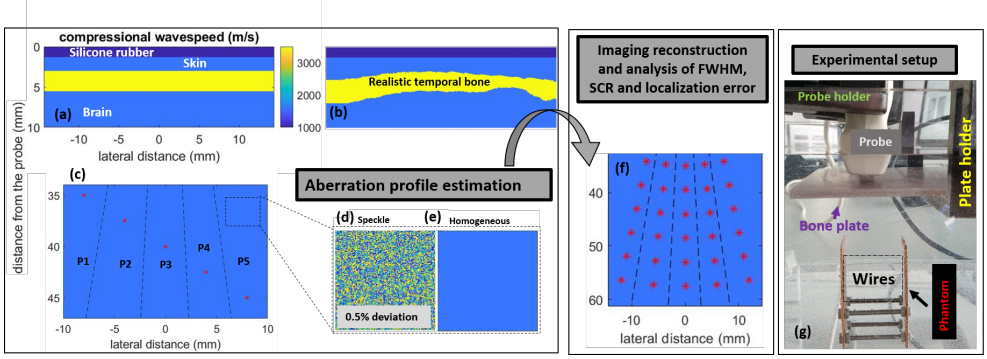


Figure 5.3: (a, b) The layered medium used in the simulation with a flat bone layer or a realistic temporal bone. (c) The numerical phantom used for estimating the aberration profile in each isoplanatic patch (P1-P5); the dashed lines separate isoplanatic patches. (d) The heterogeneous and (e) homogeneous background wave-speed model used in the simulations conducted for aberration profile estimation. (f) The numerical phantom used to generate the dataset needed for the analysis of the full-width at half-maximum (FWHM), the signal-to-clutter ratio (SCR) and localization error. (g) The experimental setup to image a wire phantom while a bone mimicking plate is positioned in front of a phased array.

phantom including 6 wires with a diameter of $50 \mu\text{m}$, with the bone-mimicking plate positioned at the depth of 5.7 mm in front of the probe and angled with 3.3 degrees; this plate has transverse isotropic elasticity, however the image plane was chosen perpendicular to the symmetry axis of the material (orientation of the glass fibers), the compressional wave-speed in this plane is isotropic. As the imaging plane of the 1D probe was perpendicular to the phantom wires, the wires are expected to act as point scatterers considering their small diameter (about one-tenth of the wavelength at the central frequency). Five transmit plane waves with steering angles from -15 to +15 degrees (in water) were used for data acquisition. Three isoplanatic patches were used for AP estimation and reconstruction. In our experimental study, the same dataset was used for the estimation of the AP with the PS method estimation and image analysis.

5.2.5. EVALUATION METRICS

Lateral spatial resolution calculated as the full-width-half-maximum (FWHM), signal-to-clutter ratio (SCR) and localization errors were used for quantitative evaluation. The SCR was the ratio of the maximum scatterer intensity and the mean clutter intensity in the image background; it is reported in decibel (dB). In experimental and numerical studies, the localization errors were calculated with respect to the ground truth image which was generated without an aberrator in front of the probe (not shown here) and the true coordinates of the scatterer. For the numerical study, the evaluation metrics reported for the PS method were calculated when the AP of each patch was estimated with the dataset generated with a homogeneous background, i.e. the most favorable scenario for the PS method. The FWHMs and SCRs reported in the text are mean values obtained for all the scatterers,

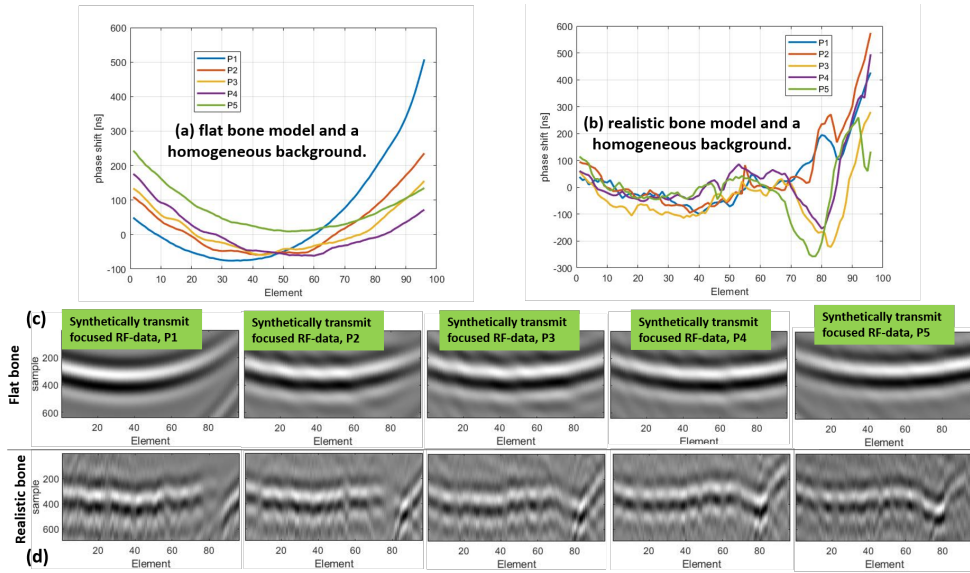


Figure 5.4: The aberration profile in five isoplanatic patches (indicated by P) when the aberrator/background model is (a) flat/homogeneous and (b) realistic/heterogeneous. The extracted synthetically transmit focused RF-data in different isoplanatic patches for the (c) flat bone and (d) realistic bone model; the background was homogeneous.

unless stated otherwise.

5.3. RESULTS

5.3.1. NUMERICAL SIMULATIONS

Our numerical study shows that the AP estimated in each patch (see the scatterers and patches in Figure 5.3(c)) varies significantly (see Figure 5.4(a and b)). For the flat bone model, the AP significantly varies even if the aberrator is laterally invariant (the plate has a constant thickness and is parallel to the probe array), because the depth and the lateral coordinate of the targets are not constant. A shallower target depth (patch 1) leads to a stronger aberration magnitude. An asymmetrical AP is obtained if the target is far from the bisector of the array. The irregular APs in Figure 5.4(b) and larger phase shift, compared to Figure 5.4(a), comes from the irregularities of the realistic bone model in its near and far surfaces and its asymmetric shape. Note that the aberration profiles in patches 1 and 2 are not accurately estimated for elements 75 to 96 (see Figure 5.4(b and d)) because the phase jump between the beamsum reference signal and the recorded wavefronts is larger than 2π and thus not properly captured with the beamsum channel correlation method [188].

Both the PS and GB techniques improve the FWHM, compared to the conventional method (compare Figure 5.5(b, d) with (a)). For the flat bone and the realistic bone models, Table 5.1 indicates that PS technique improves the FWHM by 0.18 mm and 0.14 mm, compared to the conventional reconstruction, respectively. The GB reconstruction further

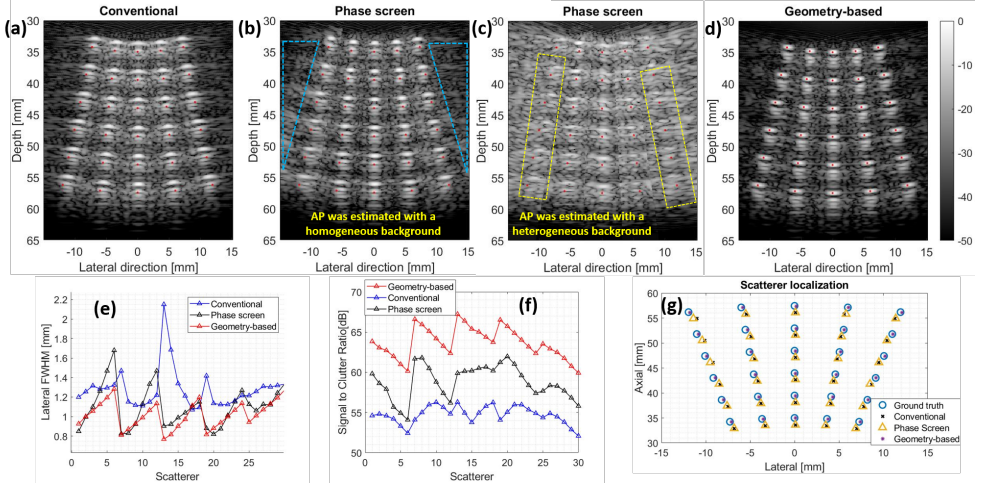


Figure 5.5: The reconstructed numerical images using (a) conventional beamforming, (b, c) phase-screen modeling and (d) geometry-based reconstruction techniques with a flat-bone model (Figure 5.3(a)). The aberration profile (AP) was estimated using the dataset generated with a (b) homogeneous and (c) heterogeneous background wave-speed model. The red dots indicate the true location of the scatterers. The blue triangles in (b) indicate the region that was used as background for quantifying the signal-to-clutter ratio calculation in Table 5.1. The yellow boxes in (c) indicate the regions at which the scatterers are completely missed. The lateral FWHM (e) and signal-to-clutter ratio (f) and localization error (g) obtained with all the methods for each scatterer.

improves the FWHM compared to the conventional PS method, by about 0.08 mm and 0.25 mm, respectively. The most significant improvement obtained by the GB method is the reduced background clutter (compare Figure 5.5(d) and Figure 5.5(b), see Figure 5.5(f) for more detail). Table 5.1 indicates that GB method improves SCR by 4.9 dB and 2.4 dB, compared to the PS technique, for the flat and realistic bone model, respectively. The PS method improves the SCR for 4 dB and 4.3 dB, compared to the conventional method, for the flat and realistic bone model, respectively.

The GB reconstruction technique detects the scatterers at their correct location (compare the location of the scatterers with the red dots in Figure 5.5(d) and see Figure 5.5(g) for more detail). As Table 5.1 indicates, the GB technique reduces the localization axial error by 1.2-1.3 mm and the localization lateral error by about 0.3 mm, compared to conventional reconstruction. In contrast, the PS method does not significantly reduce the localization axial/lateral error, compared to the conventional method.

Figure 5.5(c) shows the reconstructed image by the PS method when the AP used for phase aberration correction by the PS method is estimated with a heterogeneous background wave-speed model. Many scatterers (see the yellow boxes) are undetectable due to the low accuracy of the aberration profile estimation. As seen in Figure 5.6(f), the focused RF-data of the second scatterer (acting as the beacon signal for the patch two, see Figure 5.3(c)) is better distinguished from the background speckle noise (caused by the

Table 5.1: Quantitative evaluation of the numerical and experimental results Figure 5.4-.

	Method	[Axial, Lateral] localization error (mm)	FWHM (mm)	Signal to clutter ratio [dB]
Simulation (flat bone)	Conventional	[1.34, 0.42]	1.27±0.20	54.7±1.1
	Phase Screen	[1.31, 0.37]	1.09±0.21	58.7±2.1
	Geometry-based	[0.03, 0.14]	1.01±0.14	63.6±1.9
Simulation (realistic bone)	Conventional	[1.26, 0.90]	1.55±0.52	44.9±2.2
	Phase Screen	[1.05, 0.85]	1.41±0.28	49.2±3.0
	Geometry-based	[0.08, 0.64]	1.16±0.47	51.6±3.1
Sawbones plate	Conventional	[2.23, 0.80]	2.26±0.80	45.1±5.3
	Phase Screen	[1.05, 0.85] [2.12, 0.76]	1.30±0.17	44.1±6.0
	Geometry-based	[0.15, 0.10]	1.20±0.28	51.6±5.62

variation in the background wave-speed speed) compared to the focused RF-data of the first scatterer (see Figure 5.6(b)). This helps with better estimating the aberration profile and results in better reconstruction of the scatterers in patch 2, compared to the patch 1 (Figure 5.5(c)). Speckle noise affects each A-line and the reference beamsum signal (which is generated by summation over the A-lines recorded by all the elements of the array), and consequently the AP estimation; compare the AP in Figure 5.2(d) and Figure 65.6(g), and the fine AP in Figure 5.2(g) and Figure 5.6(h).

The irregular near and far surfaces of the realistic human temporal bone model (see Figure 5.3(b)) degrades the image reconstructed by all the methods. While, nearly all the scatterers are detected in the image reconstructed by the GB method (see Figure 5.7(d)), most scatterers are not detected by the PS method when the AP is estimated with a homogeneous background (see Figure 5.7(b)). Despite the irregular near and far surfaces of the realistic bone model, Figure 5.7(e) and Table 5.1 indicate that GB method improves the FWHM, the SCR and the localization error, compared to the conventional and PS methods.

5.3.2. EXPERIMENTS

As the background is water in our experiment, the wavefronts backscattered by the wires are well detected, the signal quality is therefore excellent to estimate the AP with the PS method. GB method results in a higher image quality (see Figure 5.8(d)) though, as the geometry and position of the bone-mimicking plate is accurately described during image reconstruction with the ARC reconstruction. Different results are obtained by switching from AP estimated with the scatterers 4 and 6 in Figure 5.8(b) to scatterers 3 and 5 in Figure 5.8(c). The image of scatterers 2 and 3 is improved in Figure 5.8(c), compared to Figure 5.8(b), since the AP for the central patch was estimated with scatterer 3, and scatterer 2 is closer to scatterer 3 than 4. This suggests that the actual size of the central isoplanatic patch is close to 10 mm, therefore more than three isoplanatic patches may be required to obtain optimal image quality with the PS method. Table 5.1 indicates that the PS method improves the FWHM by 0.96 mm compared to the conventional reconstruction. FWHM was slightly improved (0.1 mm) with GB method, compared to the PS method. The GB method increases the SCR for 6.5 dB and 8.2 dB compared to the conventional and the PS methods (see Table 5.1 and Figure 5.8(f)), respectively, and reduces the axial/lateralization error by 2.21/0.7 mm (see Table 5.1) compared to the conventional method. The SCR

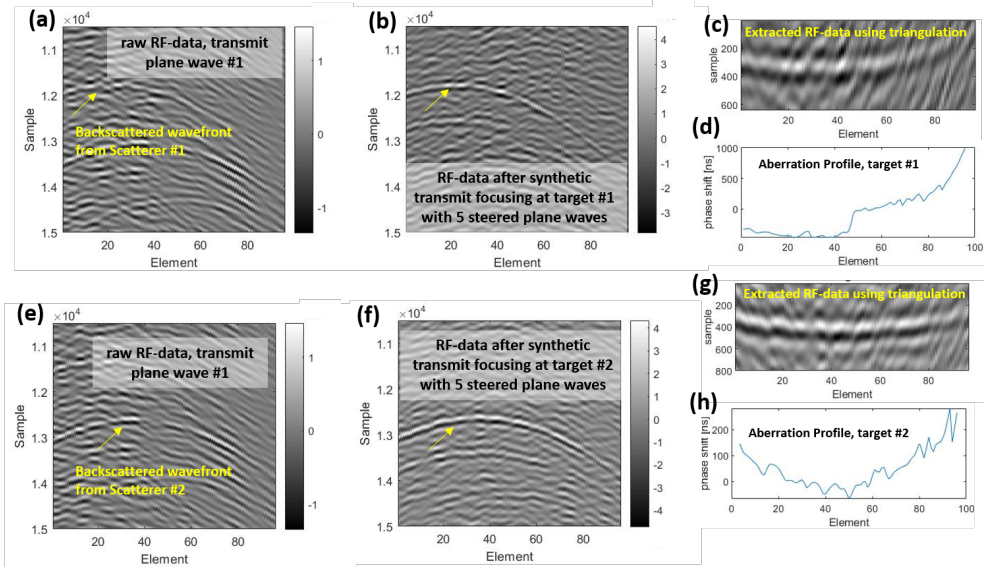


Figure 5.6: Estimation of the aberration profile with the numerical dataset generated with the flat bone model and a heterogeneous background. The wavefront backscattered from (a) scatterer 1 and (e) scatterer 2; a tilted (by 7.5 degree in cutaneous tissue) plane wave was used for excitation. The numerical wavefront backscattered by (b) scatterer 1 and (f) scatterer 2 after transmit synthetic focusing at the location of the scatterer 1 and 2, respectively, by coherent compounding of the RF-data generated by 5 tilted plane waves (from -15 to 15 degree in cutaneous tissue). (c, g) The extracted wavefront using triangulation for scatterer (c) 1 and (g) 2. The estimated phase shift (aberration profile) in nanosecond for scatterer (d) 1 and (h) 2.

obtained by the PS method is 1 dB lower than the conventional reconstruction.

5.4. DISCUSSION

5.4.1. ADVANTAGES AND LIMITATIONS OF THE NEAR FIELD PHASE SCREEN TECHNIQUE FOR ULTRAFAST TRANSCRANIAL ULTRASOUND

ADVANTAGES

In the PS method, there is no need for describing the medium and imaging the aberrator in order to estimate its position and geometry, and therefore may perform better than GB for a thin temporal bone (≤ 1 mm thick) at 2.5 MHz. As indicated by Table 5.1, the PS method improves the lateral spatial resolution and contrast (signal to clutter ratio), compared with the conventional image reconstruction technique. The lower SCR obtained by the PS method in the experimental results could be mainly due to the relatively lower clutter obtained with conventional reconstruction in the region indicated by the right red box in Figure 5.8(c).

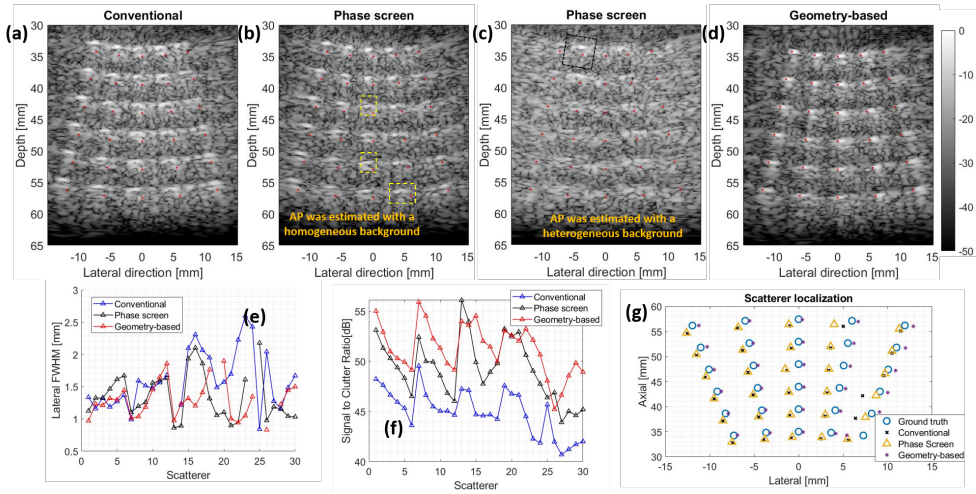


Figure 5.7: The reconstructed numerical images using (a) conventional beamforming, (b, c) phase-screen modeling and (d) geometry-based reconstruction techniques with a realistic bone model (Figure 5.3(b), based on the micro CT of a real human temporal bone). The aberration profile was estimated using a dataset generated with a (b) homogeneous and (c) heterogeneous background wave-speed model. The red dots indicate the true location of the scatterers. The lateral FWHM (e), the signal-to-clutter ratio (f) and the localization error (g) obtained with all the methods for each scatterer.

LIMITATIONS

With only 5 unfocused transmit beams (ultrafast ultrasound imaging), injection of contrast agent microbubbles is required to generate beacon signals, because synthetic transmit focusing of speckle with only 5 plane waves does not generate a strong-enough coherent wavefront.

A real-time implementation was achieved with focused transmit beams (3 frames/s abdominal scanning [188]) without injection of contrast agent. However, real-time implementation with injection of a contrast agent and using bubble echoes as beacon signals (post-processing in [83]) was never reported, and is likely very challenging because automatic detection of bubble position would be necessary. The stronger the aberration, the smaller the size of the isoplanatic patch, the more isoplanatic patches are required to improve image quality, which means that many AP must be estimated (one per isoplanatic patch); see the change in the quality of the image of scatterers 2 and 5 in Figure 5.8(b and c). This imposes a tradeoff between the image quality and computational time.

The PS method does not improve localization error, especially in depth (panel g in Figures 5.5, 5.6 and 5.8). This is because the PS method uses the information of an already miss-located scatterer (acting as the beacon signal), and therefore it does not compensate for the overall error in the calculated travel time caused by the higher wave-speed in bone. As seen in Figure 5.9, the PS leads to a travel time similar to that calculated in the conventional reconstruction. This ambiguity in the overall travel time (depth ambiguity) leads to

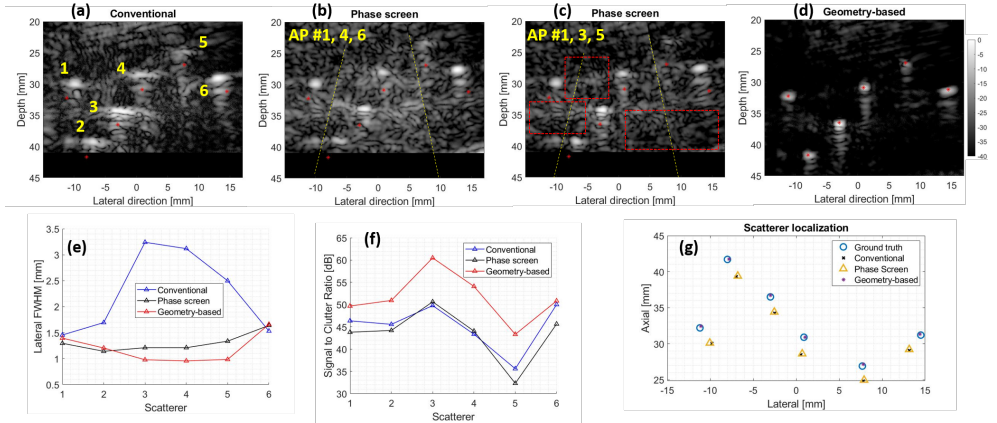


Figure 5.8: The reconstructed experimental images using the (a) conventional beamforming, (b, c) phase-screen modeling and (d) geometry-based reconstruction techniques when a Sawbones plate was used in front of the probe as an aberrator. The aberration profiles (AP) of scatterer 4/6 and 3/5 were used in (b) and (c), respectively. The red dashed-boxes were used for signal-to-clutter ratio calculation in Table 5.1. The red dots indicate the true location of the scatterers.

suboptimal image reconstruction.

As indicated by the numerical results Figure 5.6, accurate estimation of the AP with the beamsum channel correlation method when the brain tissue has a heterogeneous wave-speed model is very challenging if the amplitude of the beacon signal is not high enough. The image quality obtained by the PS method in this scenario is poor (panel c in Figures 5.5 and 5.6).

5.4.2. ADVANTAGES AND LIMITATIONS OF THE GEOMETRY-BASED PHASE ABERRATION CORRECTION TECHNIQUE FOR ULTRAFAST TRANSCRANIAL ULTRASOUND

ADVANTAGES

The GB method improves the lateral spatial resolution, signal to clutter ratio and localization error compared to the PS and conventional reconstruction techniques (see Table 5.1). It provides an optimal phase aberration correction everywhere in image as the true location and geometry of the aberrator is used to correct the phase aberration (see panel d in Figure 5.8, Figure 5.7 and Figure 5.5). In a previous publication [186], our group demonstrated that the GB method has the potential to enable real-time transcranial imaging (>10 frames/s) without injection of contrast agent and its performance is not affected by the heterogeneity (speckle) of the brain tissue; it only requires estimating the position and geometry of the bone layer, as shown in our previous publications [77], [120], [130], [154]). The GB method is not limited to a maximum bone thickness as long as the attenuation caused by a thick bone layer allows the detection of echo signals with sufficient signal-to-noise ratio.

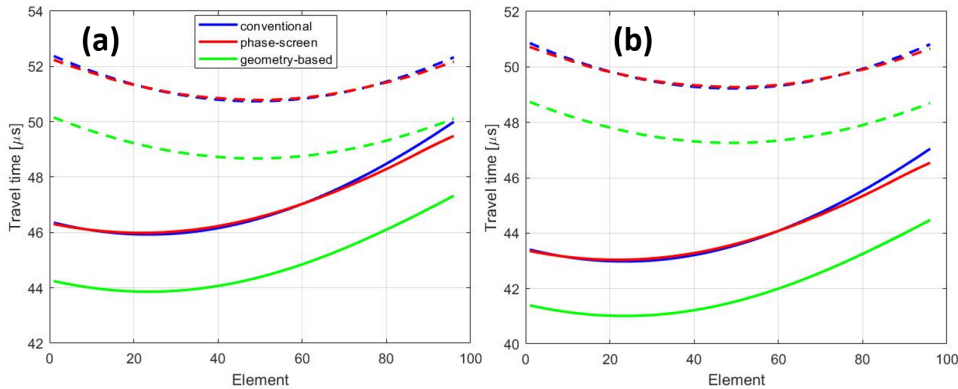


Figure 5.9: The travel time estimated for scatterer 1 (solid lines) and scatterer 3 (dashed lines) positioned in patch 1 and 3, respectively (see Figure 5.3(c)) with the three different reconstruction techniques, when a steered plane wave at (a) -15 degree and (b) 0 degree is used for transmission. The bone and background models were flat and homogeneous, respectively.

5

LIMITATIONS

The GB method needs to reconstruct an image of the aberrator in order to estimate its position and geometry. This is a challenging task for a thin temporal bone (1mm thick) at 2.5MHz, because the near and far interfaces of the bone layer cannot be clearly distinguished. The accurate estimation of travel times also requires an estimate (with the headwave or the autofocus techniques [77]) or a guess (based on literature) of the wave-speed in each layer while each layer is assumed homogeneous. The assumption of homogeneous tissue layers likely breaks down in individuals with a heterogeneous complex cutaneous tissue layer or a temporal bone containing a diploe.

5.4.3. LIMITATIONS IN THE IMPLEMENTATION OF THE NEAR FIELD PHASE SCREEN TECHNIQUE IN THIS WORK, POSSIBLE IMPROVEMENTS

The near field phase screen aberration correction technique was most often applied with focused transmit waves [188]. However, to capture the transient fast phenomena in brain (the blood velocity in the main cerebral arteries can approach 2 m/s [83]) and enable real-time feedback during clinical scans, an ultrafast imaging sequence relying on the transmission of unfocused beams is preferred. Thus, the backscattered waves should be synthetically focused in transmit (for generating the coherent wavefront backscattered from a small volume) [83] so that the wavefront from a scatterer in an isoplanatic patch becomes well-distinguished from the background speckle noise and the aberration profile estimation with the PS method is feasible. The focusing procedure includes delaying the RF-data acquired by transmitting with each unfocused beam with respect to the focal point and coherent summation.

5 steered plane waves is not optimal for efficient synthetic transmit focusing and therefore for estimating the aberration profile in each patch accurately. A better approach for

the PS approach would be to first estimate the APs in each patch with a large number (e.g., 50) of steered plane waves (or diverging waves) combined with synthetic transmit focusing or using focused transmit waves, and then using the estimated APs to correct the phase aberration in each patch when imaging with a high frame rate imaging sequence. Additionally, the PS approach can perform better if applied iteratively by improving transmit focusing at each step [188]. In this work, we used 5 transmit plane waves and a single estimation of the aberration profile to enable real time imaging and live feedback to the operator. Also, we implemented the PS method with the beamsum channel correlation method, other techniques to estimate the AP like the multilag least-squares cross-correlation method ([103]) may perform better.

The main limitation of this study is that the aberrator was invariant in the out-of-plane dimension, while the temporal bone has a complex three-dimensional shape. Our study considered two-dimensional imaging with a phased array transducer. However, as demonstrated earlier [33], [102], [103], [188], a two-dimensional matrix array transducer is required for efficient phase aberration correction with the PS method.

5

5.4.4. LIMITATIONS IN THE IMPLEMENTATION OF THE GEOMETRY-BASED ABERRATION CORRECTION TECHNIQUE IN THIS WORK, POSSIBLE IMPROVEMENTS

In this paper, we used the accelerated refraction-corrected (ARC) image reconstruction technique as the representative of the methods that use the position and geometry of the bone layer for aberration correction [186]. This approach is not iterative and the image grid points are used to describe the near and far surfaces of the bone layer and find the shortest travel time connecting a pixel to an array element (Fermat's principle). While this allows a faster calculation of the travel-times and real-time image reconstruction with a GPU, there are more accurate ray-tracing methods (such as fast marching technique) which could outperform ARC at the expense of a higher processing time [77], [120], [130], [154].

An ultrafast imaging sequence with small number of transmit unfocused beams (such as 5 steered plane waves) might not provide optimal resolution for accurately segmenting the near and far surfaces of the temporal bone layer. To improve the performance of the GB method, a single-element synthetic aperture imaging sequence could be used first to estimate the position and geometry of the bone layer. Then, this information can be used for correcting the phase aberration when imaging with the ultrafast imaging sequence (multi-angle plane waves or diverging waves). Also, a transducer operating at an ultrasound frequency higher than 2.5 MHz may help to determine the position and geometry of thin temporal bones (close to 1 mm thickness).

Like the PS method, the performance of the GB method applied to a real temporal bone with complex three-dimensional shape would improve with a two-dimensional matrix array transducer. With such a transducer, the three-dimensional position and geometry of the bone layer could be determined. This would enable accurate three-dimensional ray tracing and therefore optimal phase aberration correction.

5.5. CONCLUSION

In this paper, we compared two phase aberration correction techniques (near-field phase screen modeling (PS) and geometry-based reconstruction technique (GB)) when an ultrafast imaging sequence (5 plane waves tilted from -15 to 15 degrees in cutaneous tissue) was used for data acquisition. The numerical results showed that the PS technique is strongly affected by speckle noise caused by a heterogeneous brain tissue model and fails to reveal many scatterers in the reconstructed image, while the GB method detects nearly all the scatterers. Compared to the PS approach, the GB method improves the signal-to-clutter ratio by 7.5 dB and reduces the localization error by up to 2 mm in our experimental study. The spatial lateral resolution is only slightly improved by 0.1mm with the GB method in the experimental study, compared with the PS approach. This work indicates that the GB method outperforms the PS method in the case an ultrafast transcranial ultrasound imaging with a single phased-array transducer is used for data acquisition.

ACKNOWLEDGEMENTS

This work was supported by a joint grant from the Netherlands Organisation for Scientific Research (NWO)/the Netherlands Organisation for Health Research and Development (ZonMw) and the Department of Biotechnology (Government of India) under the program Medical Devices for Affordable Health (MDAH) as Project Imaging Needles (Grant Number 116310008).

6

RECEIVE/TRANSMIT APERTURE SELECTION FOR 3D ULTRASOUND IMAGING WITH A 2D MATRIX TRANSDUCER¹

Recently, we realized a prototype matrix transducer consisting of 48 rows of 80 elements on top of a tiled set of Application Specific Integrated Circuits (ASICs) implementing a row-level control connecting one transmit/receive channel to an arbitrary subset of elements per row. A fully sampled array data acquisition is implemented by a column-by-column (CBC) imaging scheme (80 transmit-receive shots) which achieves 250 volumes/second (V/s) at a pulse repetition frequency of 20 kHz. However, for several clinical applications such as carotid pulse wave imaging (CPWI), a volume rate of 1000 per second is needed. This allows only 20 transmit-receive shots per 3D image. In this study, we propose a shifting aperture scheme and investigate the effects of receive/transmit aperture size and aperture shifting step in the elevation direction. The row-level circuit is used to interconnect elements of a receive aperture in the elevation (row) direction. An angular weighting method is used to suppress the grating lobes caused by the enlargement of the effective elevation pitch of the array, as a result of element interconnection in the elevation direction. The effective aperture size, level of grating lobes, and resolution/sidelobes are used to select suitable reception/transmission parameters. Based on our assessment, the proposed imaging sequence is a full transmission (all 80 elements excited at the same time), a receive aperture size of 5 and an aperture shifting step of 3. Numerical results obtained at depths of 10, 15, and 20

¹This chapter has been published as:

Mozaffarzadeh et al., "Receive/Transmit Aperture Selection for 3D Ultrasound Imaging with a 2D Matrix Transducer," *Applied Sciences*. 10(15), 2020.

The text and notation used in this chapter may differ on minor details from the actual publication. This is done to achieve consistency between chapters.

mm show that, compared to the fully sampled array, the 1000 V/s is achieved at the expense of, on average, about two times wider point spread function and 4 dB higher clutter level. The resulting grating lobes were at -27 dB. The proposed imaging sequence can be used for carotid pulse wave imaging to generate an informative 3D arterial stiffness map, for cardiovascular disease assessment.

Keywords; 3D ultrasound imaging; carotid pulse wave imaging; high frame rate; 2D matrix array; grating lobes reduction.

6.1. INTRODUCTION

Arteriosclerosis is a very common cause of death worldwide, caused by deposition of lipids in the vessel wall in the form of plaques [191]. The relation between arterial stiffness and cardiovascular risk has been investigated in several studies as advanced arteriosclerosis can occlude arteries and involve changes of the vessel wall that reduce its elasticity and flexibility [192]–[194]. Estimation of the arterial stiffness would be of significant interest because it provides valuable information for diagnosis, prognosis, and therapy of a patient [195]. Among all the methods to quantify arterial stiffness, the European Society of Cardiology has recommended to use the carotid-femoral pulse wave velocity (PWV) as a favored measure of aortic stiffness [195]. However, this is a global measure of arterial stiffness, in which local plaque stiffness plays no role. Assessment of arterial stiffness by imaging the local propagation of pulse waves can identify plaque characteristics, especially in the carotid arteries [196]–[198], which are prone to plaque development associated with stroke [199].

Pulse wave imaging (PWI) is usually conducted based on two-dimensional (2D) images of the pulse wave propagation [200]–[202]. However, it is a 3D phenomenon, and elasticity of the carotid artery varies in different locations [197], [203]. Consequently, 2D images impose limitations. First, 2D elastography is sensitive to out-of-plane motion of the object, which can occur in carotid imaging [204]. Moreover, with conventional 2D ultrasound imaging, it is assumed that the propagation of the pulse wave is parallel to the imaging plane, which results in inaccuracies in PWV estimation [203]. A 3D assessment could be based on multiple cross-sectional 2D images of the 3D vessel structure, but it requires reproduction of the same imaging planes at later times, which is difficult [205]. Thus, it would be of great importance to have a comprehensive view of the arterial walls and generate a 3D elasticity map [203].

Going from 2D to 3D ultrasound imaging is challenging, and specific limitations are imposed, depending on the application [206], [207]. One approach is to mechanically sweep the conventional one-dimensional (1D) linear or phased array probes (used in 2D imaging) by a motorized system to acquire a 3D dataset [208]–[210]. With this approach, a low volume rate along with large errors due to motion artifacts is obtained. Free-hand scanning techniques, in which a position and orientation sensor is added to the conventional 1D array transducer to record the trajectory and orientation, can be used to address the motion artifacts [210]–[212]. Still, a poor out-of-plane spatial resolution and a low volume rate limit the use of the mechanical scanning approach for applications such as echocardiography, where motion needs to be accurately tracked [208].

Another approach for 3D imaging is to make a 2D matrix array [213]. With a 2D array, the transducer can remain stationary, and electronic scanning can be used to sweep the ultrasound beam over the entire volume under examination [208], which can overcome the frame rate limitation. However, the fabrication and implementation of 2D matrix transducers are challenging. A large 2D transducer is required to obtain a high elevation and azimuth resolution. On the other hand, the element pitch should preferably be kept below half a wavelength (λ) in both directions to avoid grating lobes [214]. The combination of small elements and a large aperture results in a very large number of transducer elements. It is fairly possible to make a matrix array with >1000 elements, but making electrical connections to all the elements is challenging [215].

To realize a fully populated matrix transducer that uses a reduced number of channels, different approaches have been proposed. The signals from the elements in an aperture can be locally beamformed to obtain one output receive signal [216]–[219]. With the row-column addressed array approach, the number of channels required is reduced from N^2 to $2N$, where N is the number of elements in each direction of a square matrix array, at the cost of image contrast and resolution [220]–[222]. Channel multiplexing is another approach to combine the data from several receive elements into one output line, at the cost of frame rate reduction [223].

We previously designed and manufactured a matrix transducer by fabricating an array of piezoelectric elements directly on top of an Application Specific Integrated Circuit (ASIC) [224]. A single tile of 12×40 (rows \times columns) elements was developed as a building block for a larger transducer. The ASIC provides element-level switches and control logic which allow us to connect each individual element in a row (elevation direction) to a corresponding row-level transmit/receive bus. In this study, we use a 4×2 tiles configuration to form a large transducer consisting of 48×80 (azimuth \times elevation) elements. Based on the transducer architecture, 80 transmit/receive shots are required to fully read out the element data for a single plane wave imaging. Considering a pulse repetition frequency (PRF) of 20 kHz (for a depth of 37.5 mm deep enough for carotid PWI (CPWI) [199]), a volume rate of 250 per second can be achieved. However, for CPWI, 1000 V/s are needed [8,35,36]. Therefore, we are obligated to limit the number of receive/transmit shots to 20. To do so, in this paper, we propose to interconnect elements into non-delayed apertures which can be shifted in the elevation direction. We investigate the effects of receive and transmit aperture sizes and aperture shifting step in numerical simulations and in an in vitro experimental setup. An angular weighting (AW) method (based on the directivity pattern of the receive apertures) is used in the image reconstruction procedure to reduce the effects of grating lobes (caused by the increased effective pitch in elevation direction). The goal is to find a trade-off to form good-quality B-mode images, providing suitable inputs for motion estimation methods used in wall velocity measurement [198], [203].

6.2. MATERIALS AND METHODS

6.2.1. IMAGING SCHEMES

For CPWI, the lateral direction in our 2D assessment (the elevation direction in 3D imaging) lies perpendicular to the carotid artery. For people of age over 60 years, the carotid diameter is 7.4 ± 0.7 mm and 8.2 ± 0.8 mm and over 70, it is 7.6 ± 0.8 mm and 9 ± 0.7 mm, for females and males, respectively [225]. The effective covered aperture size is calculated as $(N_r + 19N_s) \pm \text{Pitch}$, where N_r is the receive aperture size, N_s is the shift of the receiving aperture between sequential shots, and N_t is transmit aperture size. With N_s 1 and 2 and with a small N_r , the obtained effective aperture is much less than what is needed to cover the whole carotid artery. As we aim to have an effective covered aperture size big enough for all ages, we neglect N_s of 1 and 2 in our study.

A tile of 12 ± 40 elements (rows \pm columns) requires 12 channels for transmission and 12 channels for data reception (Figure 6.1(a)). The row-level circuitry allows us to put two tiles head-to-head in a row to form an array of 12×80 elements without increasing the channel count [223]. In this study, the array is fabricated using 4×2 (rows \times columns)

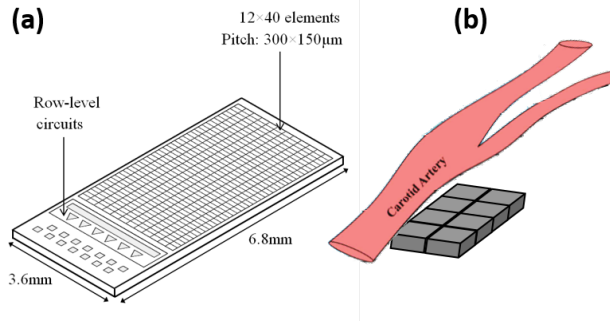


Figure 6.1: (a) Schematic of a single tile consisting of 12×40 acoustic elements on top of an Application Specific Integrated Circuit (ASIC) with element-level switches and row-level circuits. (b) The proposed transducer consisting of 4×2 tiles with respect to the carotid artery (carotid has a diameter of 6-9 mm; the array is 12×14 mm).

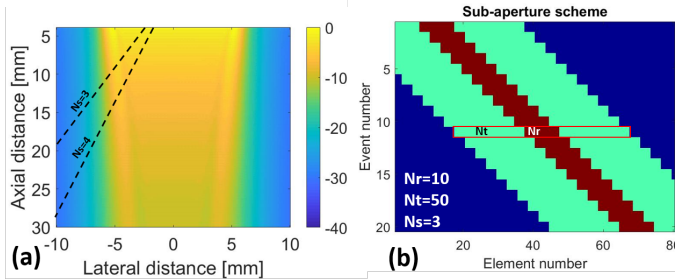


Figure 6.2: (a) The generated pressure field with a full transmission approach (all the elements are excited together); the dashed lines show the direction of grating lobes with different N_s . (b) A schematic of the aperture definition procedure; $N_s = 3$, $N_r = 10$, and $N_t = 50$. Receive and transmit apertures have the same center.

tiles providing 48×80 (azimuth \times elevation) elements (Figure 6.1(b); the carotid has a diameter of 6-9 mm [225]; the array is 14×12 mm). A single plane wave imaging with full data acquisition can be implemented using a column-by-column (CBC) data acquisition approach which requires 80 transmit/receive shots. In this approach, all the 80 elements are connected to the transmit bus, and only a single element in the elevation direction is connected to the receive bus. For CPWI, we need 1000 V/s which restricts the number of transmit-receive shots to 20 for one volume. These 20 shots can be implemented in different manners; an example is shown in Figure 6.2(b) where the transmit aperture of 50 elements is shifted over three elements for each step, co-aligned with the receive aperture of 10 elements.

Applying dynamic focusing to the received data having an effective element pitch larger than half of a wave length introduces grating lobes [214]. In our study, the 2D matrix transducer has an elevation pitch of $150 \mu\text{m}$, and the operating frequency ranges from 6 to 9 MHz, i.e., the shortest wavelength is $170 \mu\text{m}$ in tissue. Therefore, grating lobes in the

elevation direction will appear.

The current ASIC architecture can accommodate 20 arbitrary transmit/receive patterns in the provided memories, which can be used to define sparse patterns (out of the scope of this paper) [224]. In addition to these element level memories, elements can be grouped into a set of transmit/receive apertures with an arbitrary size and shifted along elevation direction with one element per clock cycle [224]. In this study, we use this feature to define regular aperture patterns (see Figure 6.2(b) for example). The elements contributing in a receive aperture are interconnected (switched in parallel without further inter-element delays) in practice, and one time series is achieved for the receive aperture.

6.2.2. NUMERICAL STUDIES ON BEAM PROFILE

As element interconnection only happens in the elevation direction, our numerical evaluation was only conducted in the elevation direction. Simulations were conducted in Field II [226], [227] to investigate the beam profile of the different transmit/receive sequences. The image reconstruction in azimuthal direction is unaffected and therefore neglected. We varied the settings provided in Table 6.1.

Table 6.1: The variables used in the numerical study.

Number of shots	20
Receive aperture (Nr)	1-20 elements
Element size	130 μm
Pitch	150 μm
Transmit aperture	1-80 elements
Shift between sequential shots of the receive aperture (Ns)	3-4 (units in Pitch)
Transmit pulse length	1.5 cycles
Central frequency	7.5 MHz, $\lambda = 0.2$ mm
Scatterer position	10, 20, and 30 mm
Speed of sound	1500 m/s
Sampling frequency	100 MHz

The impulse response consisted of a Gaussian-modulated sinusoidal waveform (central frequency of 7.5 MHz, bandwidth of 80%). Normalization and log-compression were used to form final images. The response of receive aperture size (Nr), the shift of the receiving aperture between sequential shots (Ns) and the transmit aperture size (Nt) were evaluated using point scatterers positioned at depths of 10, 15, and 20 mm, as we expect the carotid artery in this range [198]. Figure 6.2(b) illustrates the way that the Nr, Nt, and Ns parameters were defined and implemented in 20 transmit-receive shots. The receive and transmit apertures were concentric and shifted over the same distance.

The level of grating lobes, lateral width of point spread function (PSF) at -6 dB called full-width-half-maximum (FWHM) and level of sidelobes were used to evaluate the image quality as result of the different settings [214]. The finalized imaging sequence was evaluated with a numerical tissue mimicking phantom in which an anechoic cyst having a radius of 3 mm was positioned at the depth of 15 mm. The phantom contained scatterers from -15 to 15 mm in the lateral direction to visualize the off beam energy including

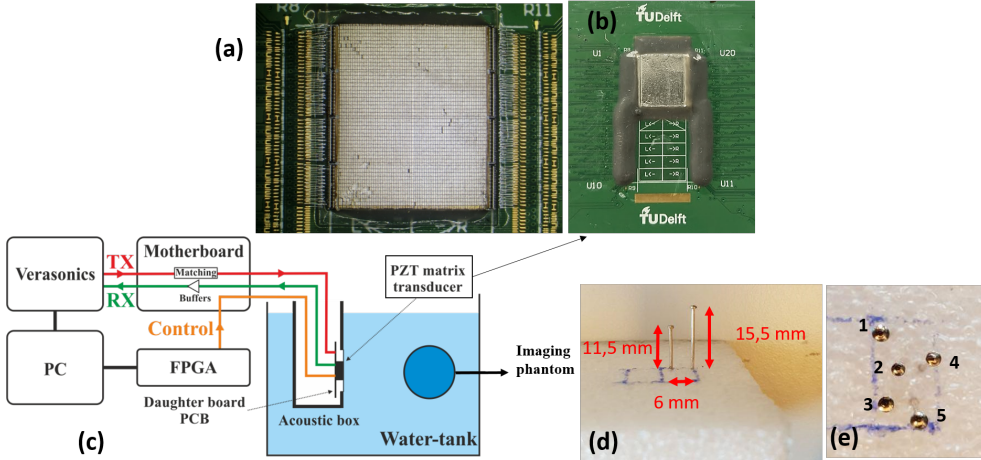


Figure 6.3: (a) The daughterboard with the transducer array before applying the ground foil. (b) The finalized 4×2 matrix array. (c) Schematic of the measurement setup. (d) The imaging phantom: a foam pad with two needles. The distance between the foam and the transducer surface is about 26 mm. (e) The imaging phantom: a foam pad with five needles, positioned in different depths (from 10 to 20 mm). The distance between the foam and the transducer surface is about 28 mm. The numbers next to the needles are used for target localization in section 6.3.

the grating lobes. Multi-scatterer and multi-cyst phantoms were also imaged. We use column-by-column imaging scheme as the ground truth (GT) in our study.

6.2.3. EXPERIMENTAL STUDY

The 2D matrix array was mounted in a box with an acoustically transparent window (25 μm thick polyimide) and the whole setup was submerged in a tank filled with water (see Figure 6.3(a)). The transducer was excited by a custom-programmed experimental ultrasound system (Vantage 256, Verasonics, Kirkland, WA, USA). A picture of the two-needle phantom used in our experiments is provided in Figure 6.3(d). The axial distance between the plastic foam, that acts as base to the needles, and the surface of our 2D transducer was about 26 mm. Matlab 2018b and MeVisLab (MeVis Medical Solutions AG, Fraunhofer MEVIS, Bremen, Germany) software was used to process the data and show 3D images, respectively.

6.3. RESULTS

6.3.1. NUMERICAL RESULTS: POINT SCATTERER

RECEIVE APERTURE

Figure 6.4(a, b) shows the PSF for varying receive aperture (N_r) between 1 and 20 elements and shifting steps (N_s) of 3 and 4. A full-aperture transmission (transmission with all the elements) is used ($N_t = 80$) and 20 shots are given. For a receive aperture equal to one

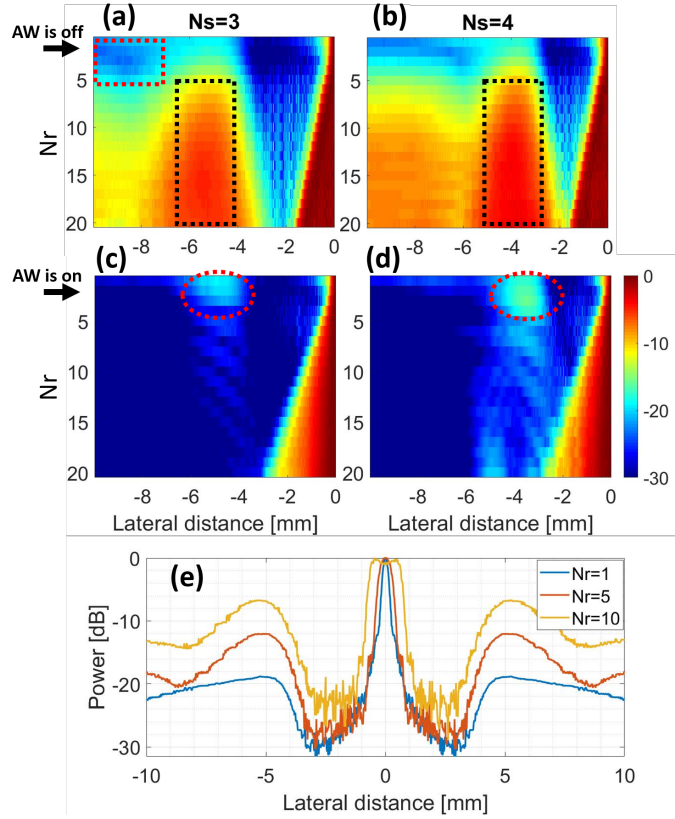


Figure 6.4: (a-d) The point spread functions (PSFs) obtained for different N_r and N_s when a full-aperture transmission is used. A point scatterer was positioned at the depth of 10 mm and the lateral distance of 0 mm. The angular weighting (AW) technique was used in the bottom row. The black and red rectangular regions were used to calculate the clutter level (Figure 6.5a)) and effects of grating lobes (Figure 6.5(b)). The red circles show the effects of grating lobes. (e) The lateral variation for $N_s = 3$ when the AW is on.

element ($N_r = 1$) and step size of three elements ($N_s = 3$), the total covered aperture is 8.7 mm resulting in a main beam width of about 2 mm at 10 mm distance. The grating lobe level is -20 dB as expected from the 1.5 cycle excitation and 20 shots and positioned at a lateral distance of -5 mm caused by the large step ($N_s = 3$, effective pitch = $450 \mu\text{m}$, $\lambda = 200 \mu\text{m}$). The mean beam width remains about the same for larger N_r up to 5 (see Figure 6.4(e)) since two opposite effects play a role. The first one is the slowly increasing covered aperture (e.g., for $N_r = 5$, the covered aperture is 9.3 mm). The opposite one is the increasing directivity of the receiving apertures (for $N_r = 5$ the directivity is about 10deg), which makes the contribution of the outer elements less. For larger receive apertures, $N_r = 10$ the main beam width is increased to about 3 mm and it further increases to 4.2 mm for $N_r = 20$. For $N_r = 20$, the covered aperture is admittedly the largest, but very directive

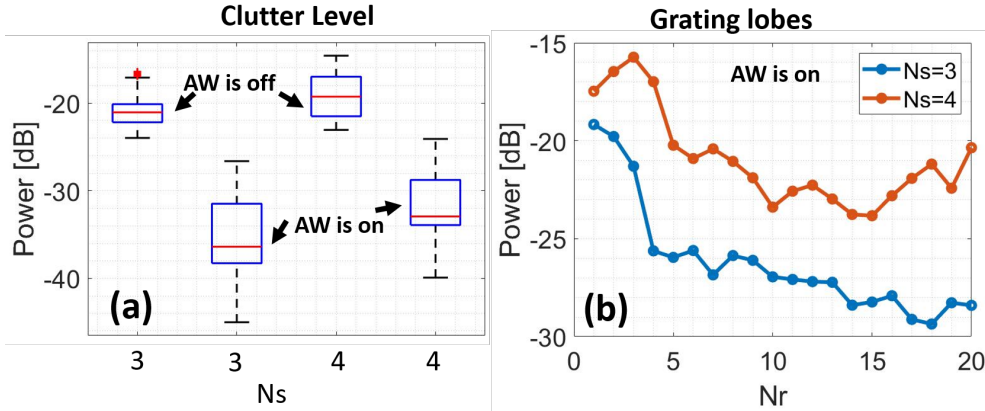


Figure 6.5: (a) Distribution of clutter level measured within the red rectangular region shown in Figure 6.4(a). The same area was used in other images. On each box, the central mark indicates the median of the clutter level inside the corresponding region. The bottom and top edges of the box indicate the 25th and 75th percentiles, respectively. The whiskers extend to the most extreme data points not considered outliers. Outliers were plotted individually using the + symbol. (b) The level of grating lobes, measured within the black rectangular regions indicated in Figure 6.4.

(2deg), and therefore only the middle part of the covered aperture is contributing in image reconstruction. For $N_s = 4$ (see Figure 6.4(b)), the grating becomes stronger, making the grating lobes appear closer to the mainlobe, at -4 mm lateral distance (see the rectangles in Figure 6.4(a, b)).

Since the effective aperture can be very large and directive, angular weighting, as described in [228], can be applied in reception. This results in reduced grating lobes (compare the first and second rows in Figure 4) and about 16 and 13 dB lower clutter level for N_s of 3 and 4, respectively (see Figure 6.5(a) where the pixel intensities within the red rectangular regions shown in Figure 6.4(a) were used for statistical analysis). The level of grating lobes (for different N_r) obtained with the AW technique is presented in Figure 6.5(b). The AW technique hardly works for N_r of 1 up to 5 due to the large angular view of the receive aperture.

Figure 6.6 shows the FWHM as function of aperture settings. It indicates that the smaller the N_r , the lower the FWHM (i.e., better lateral resolution). This is mainly because we use the dynamic focusing technique in reception, and increment in N_r results in a narrower directivity in each receive aperture, which reduces the effective number of elements (i.e., aperture size) contributing in the reconstruction of a given pixel (voxel in 3D).

An analysis of Figure 4 and Figure 6 shows that the AW technique helps with suppression of the grating lobes at the expense of resolution. With an AW, a higher contrast can be expected [198], helping the motion estimation methods used to estimate the wall velocities in CPWI [199]. Thus, we use AW technique in the reconstruction through rest of the

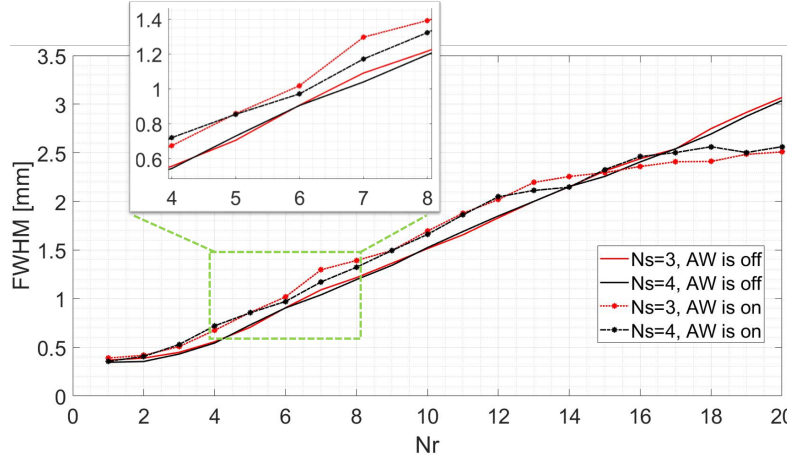


Figure 6.6: Full-width-half-maximum (FWHM) measurements for different N_r and N_s ; a full-aperture transmission was used.

paper.

As seen in Figure 6.4(c, d), grating lobes are not well-suppressed for $N_r = 1$ (see the red circles). For $N_s = 3$, these effects reduce about 6 dB from $N_r = 1$ to $N_r = 5$ and then reduce with a lower rate along with oscillation (see Figure 6.4(c) and Figure 6.5(b)). Almost the same pattern happens for $N_s = 4$ from $N_r = 1$ to $N_r = 5$. We also noticed the same trend happening at depths of 15 and 20 mm (depths of interest for CPWI [199])—results are not provided here. Based on the lower grating lobes for $N_s = 3$ than $N_s = 4$ (Figure 6.5(b)), the reduction of grating lobes from N_r of 1 to 5 for $N_s = 3$ (Figure 6.5(b)), and the same resolution in $N_r = 5$ for N_s of 3 and 4 (see zoomed version in Figure 6.6), we proceed with $N_s = 3$ and $N_r = 5$. It is true that $N_r = 5$ increases the FWHM more than a smaller N_r (see Figure 6.6), but lower grating lobes are more beneficial/needed in CPWI than a higher resolution due to motion estimation algorithms used in CPWI [199], [203]. Although even lower grating lobes can be achieved by a N_r larger than 5 (Figure 6.5(b)), the rate of FWHM increment is much larger than the rate of grating lobes decrement (see Figure 6.6) when N_r increases. It is expected to have 7 dB higher signal-to-noise ratio (SNR) with $N_r = 5$ than $N_r = 1$. Moreover, with $N_s = 3$ and $N_r = 5$, an effective covered aperture of 9.3 mm can be obtained, which is large enough to cover the carotid artery in all ages [225].

We conducted the same assessment for scatterers positioned at depths of 15 and 20 mm (results not shown). For different N_s , almost the same difference in the mean of the level of grating lobes (red lines in Figure 6.6(a)) is achieved. The same effects indicated by the red circles Figure 6.4(c, d) occur, but with lower power. Following the same procedure $N_s = 3$ and $N_r = 5$ can be selected for receive aperture in these depths as well.

TRANSMIT APERTURE

So far, we used a full-aperture transmission. In this section, we evaluate the effects of the transmit aperture size (N_t) on the PSFs obtained with the selected reception parameters ($N_r = 5$ and $N_s = 3$). Figure 6.7(a-c) shows the PSFs obtained with different N_t while a

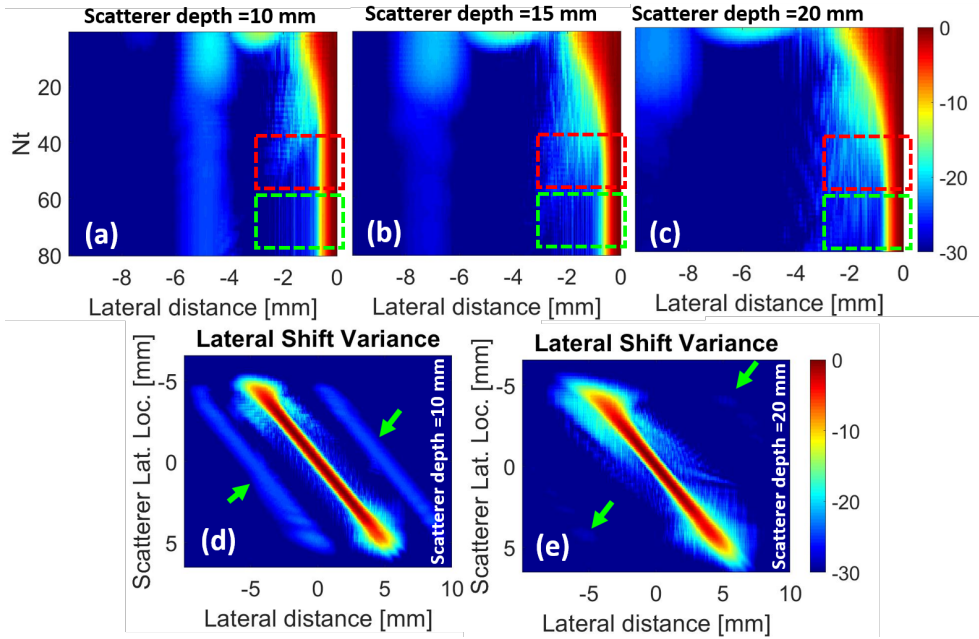


Figure 6.7: (a-c) The PSFs obtained for different Nt ; $Nr = 5$, $Ns = 3$. The green rectangular regions show a reduction of sidelobes with respect to the red rectangles. (d,e) The lateral shift variance for full-aperture transmission, $Nr = 5$ and $Ns = 3$, for a scatter at a depth of (d) 10 mm and (e) 20 mm. Green arrows: location of grating lobes.

scatterer is positioned at the depths of 10, 15, and 20 mm, respectively. A small Nt leads to strong artifacts caused by the grating lobes. This is due to the omnidirectional pressure field in transmission which causes excitation in the direction of the grating lobes with the same energy as that of main lobe. As the Nt gets larger, the transmission pressure field gets more directional toward the front side of the array and becomes like what is shown in Figure 6.2(a). In higher depths, the effects of grating lobes are lower since a lower pressure is transmitted in the direction of the grating lobes (see Figure 6.2(a)).

The effects of grating lobes are lower when Nt is larger than 20 (see Figure 6.7(a-c)). From Nt of 1 to 50 the FWHM decreases, and reaches an asymptotic minimum for Nt larger than 50. However, around a Nt of 50, the effects of sidelobes are still more powerful than larger Nt (compare the regions shown by the red and green dashed rectangles in Figure 6.7(a-c)). Since the larger the Nt , the lower the effects of sidelobes, we proceed with a full-aperture transmission ($Nt = 80$).

LATERAL SHIFT VARIANCE

In Figure 6.7(d, e), point scatterers positioned at the depths of 10 and 20 mm, respectively, are laterally shifted from -6.5 to 6.5 mm. This image is normalized to its maximum to fairly track the effects of grating lobes (see the green arrows) [229]. Figure 6.7(d, e) indicates that if a scatterer is positioned in the direction of the grating lobes, its effect is much lower

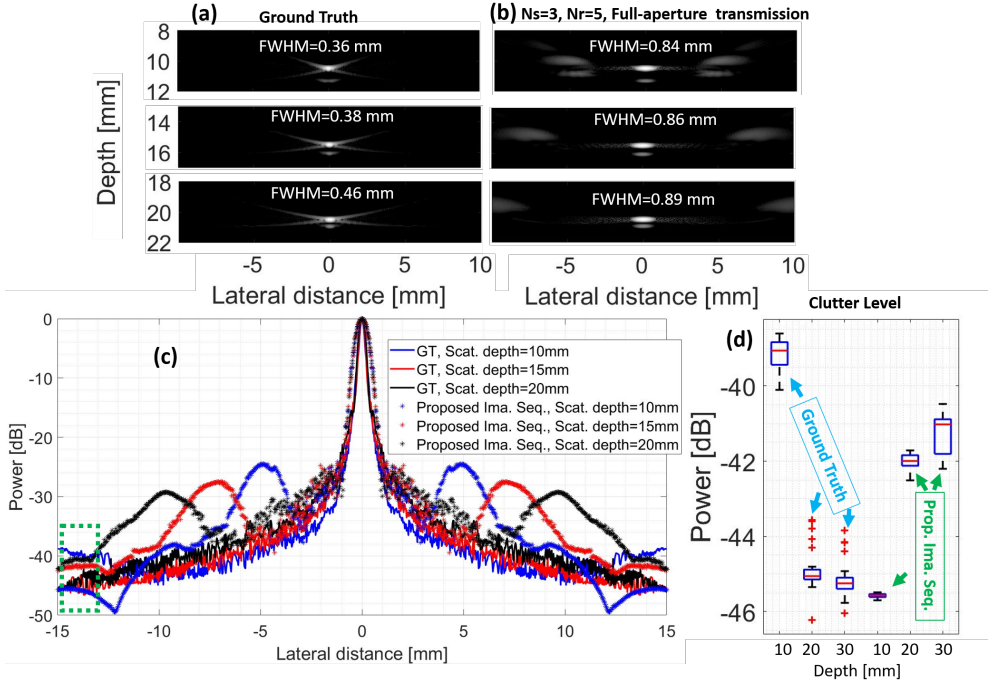


Figure 6.8: The reconstructed images using (a) the column-by-column (CBC) imaging sequence (ground truth—GT) and (b) the proposed imaging sequence (full-aperture transmission, $N_r = 5$ and $N_s = 3$), along with (c) their corresponding lateral variations. The AW is applied on the GT to have a fair comparison. (d) The clutter level using the green rectangular region in (c).

than that of a scattering target in the middle of the array. This is mainly because of the AW technique in reception and the fact that the direct transmitted pressure field excites targets in the lateral center of the array with a higher power, compared to those in the grating lobes angles (see Figure 6.2(a)). The best resolution is also obtained when the scatterer is at the lateral center.

COMPARISON WITH GROUND TRUTH

A comparison between the reconstructed images by the proposed imaging sequence (full-aperture transmission, $N_r = 5$ and $N_s = 3$) and the CBC imaging sequence (ground truth, GT) at three depths of interest is provided in Figure 6.8(c), along with their corresponding PSFs in Figure 6.8(c). The AW is applied to the GT to have a fair comparison. By the proposed imaging sequence, the FWHM is almost doubled due to the larger receiving aperture, and the mean clutter level, on average, is 4 dB higher than GT, with a level of grating lobes of about -24, -27, and -29 dB, at the depths of 10 mm, 15 mm, and 20 mm, respectively. See the Supplementary Materials (Figure 4.S1) for the results obtained using the multi-scatterer phantom.

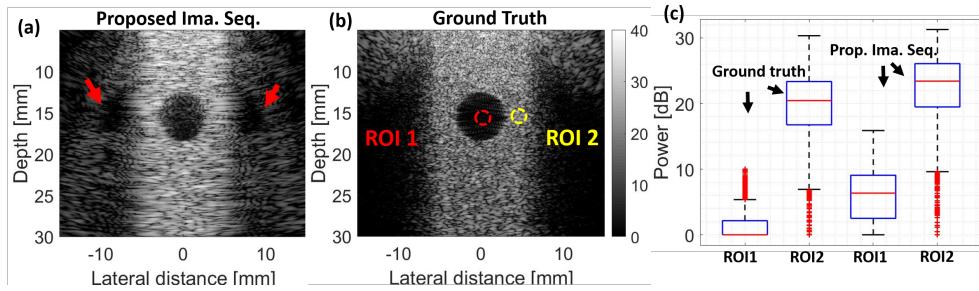


Figure 6.9: The reconstructed images using (a) the proposed imaging sequence (full-aperture transmission, $N_r = 5$ and $N_s = 3$) and (b) the CBC imaging sequence (GT). (c) Statistical analysis of the image intensities indicated by two regions of interest (ROI1 and ROI2) which are the red and yellow circles, respectively.

6.3.2. NUMERICAL RESULTS: CYSTS PHANTOM

The results obtained with the cyst phantom are shown in Figure 6.9. The images are laterally limited due to the narrow transmission beam profile (see Figure 6.2(a)). The proposed scheme (Figure 6.9(a)) is more laterally limited because of the smaller effective aperture size than the CBC GT (Figure 6.9(b)). The red arrows in Figure 6.9(a) show the effects of grating lobes. To statistically compare these images, pixel intensities within two regions of interest (ROI1 and ROI2, the red and yellow circles in Figure 6.9(b)) are used. For the proposed imaging sequence, the mean of ROI1 is 6 dB higher than GT (see Figure 6.9(c)) due to the effects of the grating lobes and sidelobes (see Figure 6.8(c)). The 3 dB higher mean in ROI2 provided by the proposed imaging sequence (Figure 6.9(c)) is also due to the larger FWHM and more constructive interferences of the point scatterers. See the Supplementary Materials (Figure 4.S2) for the results obtained using the multi-cyst phantom.

6.3.3. EXPERIMENTAL RESULTS

Figure 6.10 presents the experimental results of the 3D reconstructed images using the GT and the proposed imaging sequence (full-aperture transmission, $N_r = 5$ and $N_s = 3$). The AW is applied on the GT to have a fair comparison. The red, yellow, green, and blue arrows show the foam, the two needles, the grating lobes, and the clutter in the azimuth direction, respectively. The smaller size of foam in Figure 6.10(b, e) is due to a smaller effective aperture size in the elevation direction. A better visualization on the needles is achieved in Figure 6.10(e) compared to Figure 6.10(d) due to the AW technique.

The maximum intensity projection (MIP) over a depth of 1-23 mm of the 3D experimental images obtained with the two-needle phantom is shown in Figure 6.11(a-c). The elevation FWHM obtained with the proposed imaging sequence at the depth of about 10 mm is doubled, in accordance with the results provided in Figure 6.8(a, b). This is the reason that the targets look stretched in the elevation direction, as seen in Figure 11a and Figure 6.10(b). The azimuth FWHM for different receive parameters stays the same (about $620 \mu\text{m}$) as the proposed imaging sequence does not significantly affect the performance of the 2D transducer in the azimuth direction. The same clutter patterns for different N_s ,

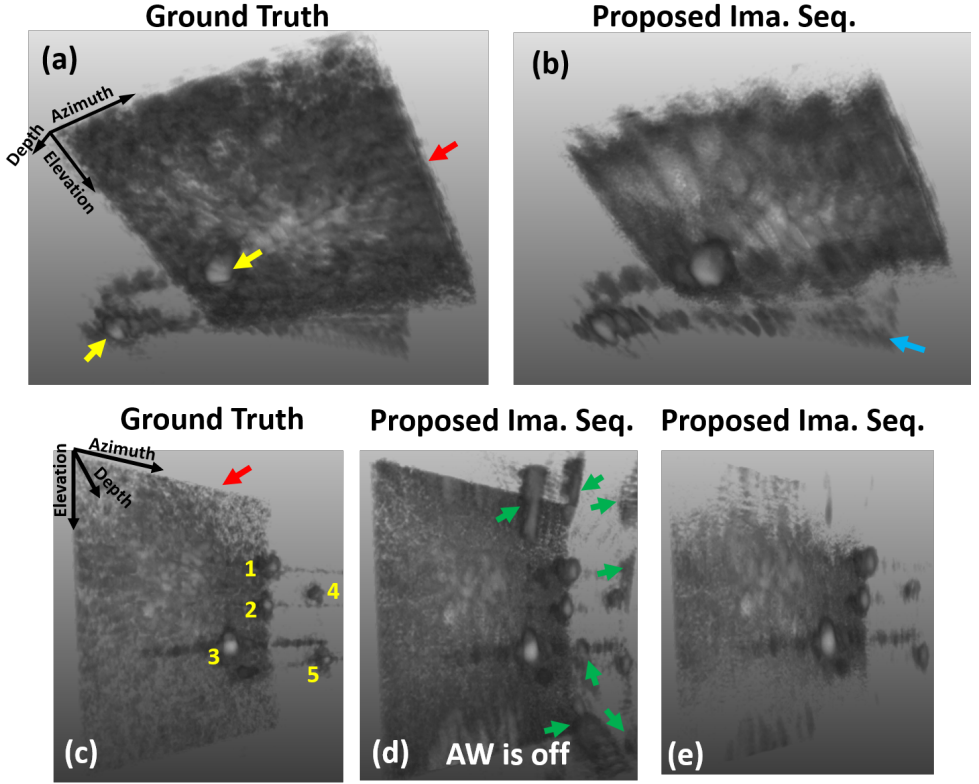


Figure 6.10: The 3D images obtained with (a,c) the CBC imaging sequence (GT) and (b,d,e) the proposed imaging sequence (full-aperture transmission, $N_r = 5$ and $N_s = 3$). The red, yellow, green, and blue arrows show the foam, the two needles, the grating lobes, and the clutter in the azimuth direction, respectively. The dynamic range was 40 dB. The numbers in (c) are related to those shown in Figure 6.3(e).

but the same N_r , also prove this matter (see Figure 6.11(d)). The clutter level in azimuth direction is higher than elevation direction due to the larger pitch ($300 \mu\text{m}$) and lower number of elements (48).

6.4. DISCUSSION

The aim of this study was to find a set of imaging parameters that provides a good image quality using an aperture-shifting matrix array, within the boundary condition of a limited number of transmissions (20), such that a volume frame rate of 1000 per second could be reached. We aimed for such high volume rate to facilitate CPWI (seeing the 4.5 m/s pulse wave pass laterally within a few volumes [198]). Depths of evaluation were 10, 15, and 20 mm as the anterior and posterior walls are expected at these depths [198]. The effects of receive aperture size (N_r), the aperture shifting distance per pitch (N_s), and transmit

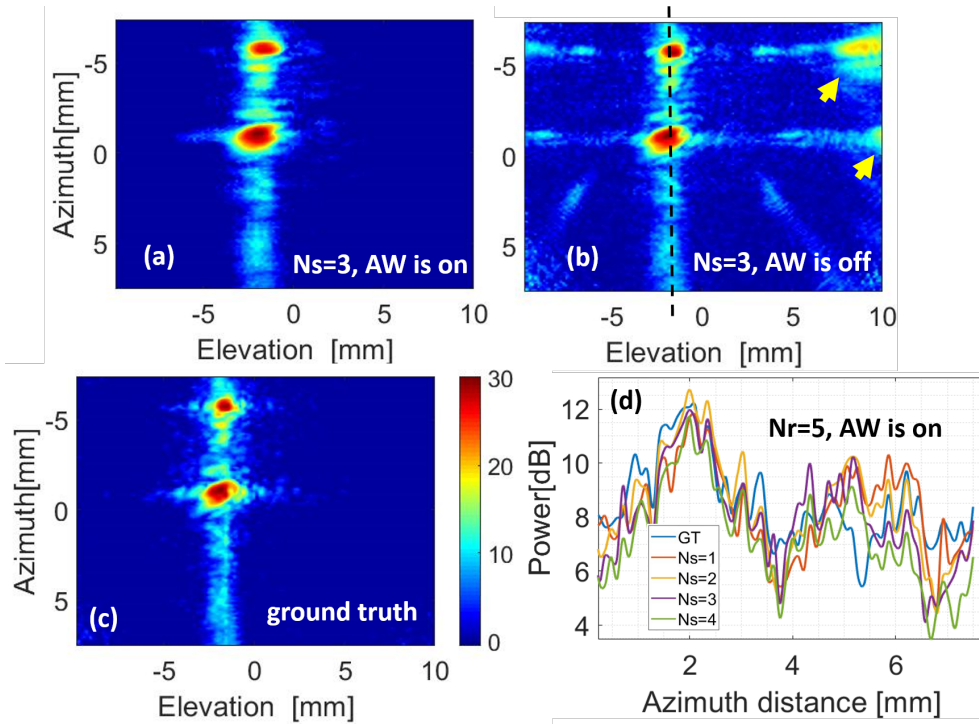


Figure 6.11: (a-c) The maximum intensity projection (MIP) of the reconstructed 3D images of Figure 6.10 using the data obtained with the two-needle phantom. (d) The clutter pattern in azimuth direction measured on the dashed black line in (b).

aperture size (N_t) were studied.

Improving the quality of B-mode images helps in CPWI as it facilitates the motion estimation algorithms to track the axial displacement of the arterial walls [198], [203]. This is essential for accurate local pulse wave velocity estimation required to generate an elasticity map. Our assessment and parameters selection priority were as follows: (1) the size of effective aperture; as it indicates whether we can have a comprehensive view on the carotid artery or not [225], (2) suppression of grating lobes; the lower the level of grating lobes, the higher the contrast, which is important for motion estimation algorithms to better estimate the axial displacement of carotid walls [198], and (3) resolution/sidelobes. Both N_s of 3 and 4 could provide sufficiently large effective aperture. Due to the lower grating lobes achieved with $N_s = 3$, compared to $N_s = 4$, $N_s = 3$ was selected. Selection of N_r imposed a trade-off between FWHM and grating lobes. The rate of decrement of grating lobes and increment of FWHM in $N_s = 3$ led to a N_r of 5. Almost the same trends happened in all the three depths of interest for CPWI [198], which led us to $N_s = 3$ and $N_r = 5$. The finalized imaging sequence, with a boundary condition of 20 transmit-receive shots, consists of a full-aperture transmission ($N_t = 80$), $N_r = 5$, $N_s = 3$ and using the angular weighting (AW) technique in the image reconstruction procedure.

Signal-to-noise ratio (SNR) is also an important criterion in the performance of motion estimation techniques. However, it is not included in our study since in previous studies, an acceptable SNR in CPWI was achievable with both 1D or 2D arrays [198], [203], and it is expected that this is the case with our 2D matrix array as well [224]. If SNR is not good enough (either for CPWI or other applications which need the same effective aperture size) to perform a reliable motion estimation, a larger N_r can be used. However, it would cause a larger FWHM as a consequence of relatively more direct receive apertures and applying the dynamic focusing in reception. Therefore, in the case of using a large N_r (i.e., 20), a more sophisticated image reconstruction method, which takes the narrow directivity of a large N_r into account, should be used in the elevation direction to form a 3D volume [166].

The final version of our 2D transducer will have 10 tiles in the azimuth (row) direction and two tiles in the elevation (column) direction, making 120×80 (row \times column) elements available to form a 3D image. Having an azimuth pitch of $300 \mu\text{m}$, the size of our 2D transducer in azimuth direction will be 36 mm, thus providing an aperture size big enough to track the carotid pulse wave velocity (estimated to be around 4.5 m/s [198]). All the evaluations and decisions in this paper were conducted using static imaging phantoms while in CPWI, there are several types of motion, i.e., carotid wall movement caused by pulse wave propagation, overall movement by breathing, and patient/transducer movement. Motion of the object might lead to unwanted decorrelation of the signals recorded by the sequentially switched apertures, leading to lower image quality. To calculate the risk of such decorrelation, we performed the following calculation. The wall velocity is, estimated from the interframe axial displacement, reported to be about 5 mm/s [198], [203]. Considering the 1 ms needed for data acquisition by the proposed imaging sequence for a 3D volume, the target moves $5 \mu\text{m}$ in the axial direction. In this scenario, the PSF obtained with a dynamic scatterer, moving $5 \mu\text{m}$ in 20 transmit-receive shots, well overlaps with a static scatterer, which is mainly because the motion is lower than 10% of the wavelength ($200 \mu\text{m}$) during the time needed to acquire the data of a 3D volume [230]. Therefore, we can assume that the coherent compounding from the 20 acquisitions is not negatively affected. In addition, the global movement is slow, will not interfere with the coherent image reconstruction, and can be removed by subtraction of displacement of the tissues and that of carotid artery [198].

With 20 kHz pulse repetition frequency, reflection artifacts come from depths higher than 37.5 mm. In this study, these reflection artifacts are ignored due to tissue attenuation ($\approx 0.4\text{--}0.6 \text{ dB/MHz/cm}$) as a scatterer at a higher depth (e.g., 50 mm) is attenuated by 28 dB compared to the reflection coming from 12.5 mm depth. A more advanced beamforming algorithm might be helpful with suppression of these artifacts as well [39], [40], [147], [231], taking the change of speckle patterns into account [232].

Finally, although the reported results are linked to the specifications of the matrix transducer reported in our previous publication (see [224]), we would like to stress that the procedure taken in this study to select receive/transmit parameters can be used for other array transducers (either 1D or 2D) to obtain a higher frame/volume rate at a given number of data acquisition channels.

As a future study, we will use the proposed imaging sequence to conduct clinical 3D carotid pulse wave imaging and generate 3D elasticity maps.

6.5. CONCLUSION

In this paper, we evaluated the effects of receive/transmit parameters on the image quality provided by a linear array in which elements are mutually interconnected, which mimics the elevation direction of our prototype 2D matrix transducer. The parameter selection procedure was based on the effective covered aperture size, level of grating lobes, and resolution/sidelobes. To achieve 1000 volumes/second, only 20 transmit-receive shots were available, considering a pulse repetition frequency of 20 kHz and imaging depth of 37.5 mm. To suppress the effects of grating lobes, an angular weighting technique was used. The proposed imaging sequence consisted of a full-aperture transmission (all 80 elements), receive aperture size of 5, and aperture shifting distance of three elements. For depths of 10-20 mm, the results show that, on average, about two times wider point spread function at -6 dB and marginally (4 dB) higher clutter level were obtained, compared to the ground truth, and grating lobes level of about -27 dB lower than the main lobe. Having a proper imaging sequence based on 1000 V/s could be beneficial to generate 3D maps of carotid artery stiffness, providing valuable information regarding the cardiovascular risk.

FUNDING

This research is a part of the 3D-ICE, PUMA and UltraXtreme projects (project numbers 14297, 13154 and P17-32, respectively), which are partly financed by the Netherlands Organisation for Scientific Research (NWO). Moreover, the authors acknowledge a joint grant from the NWO/ the Netherlands Organisation for Health Research and Development (ZonMw) and the Department of Biotechnology (Government of India) under the program Medical Devices for Affordable Health (MDAH) as Project Imaging Needles (Grant Number 116310008).

6.6. SUPPLEMENTARY DOCUMENT

Comparing the first and second rows of Figure indicates that the AW technique increases the visibility of the scatterers in the region of interest (ROI; -5 mm to 5 mm in the lateral direction). Artifacts are reduced between the targets (compare Figure 4.S1(b) and (d)) and a higher contrast is achieved (compare Figure 4.S2(c) and (d)) due to the lower sidelobes. The images generated with the proposed sequence get disturbed at the corners due to the lower number of apertures contributing in the reconstruction of those regions.

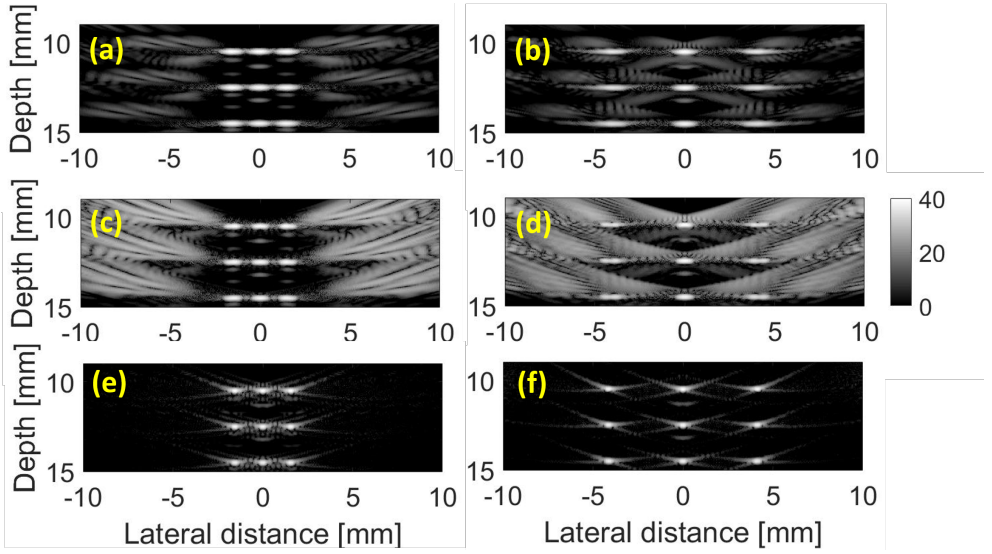


Figure 4.S1: The reconstructed images using (a-d) the proposed imaging sequence (full-aperture transmission , $N_r=5$ and $N_s=3$), when the AW is (a,b) on and (c,d) off, and (e,f) CBC imaging sequence (GT). The scatterers have a lateral distance of 1.5 mm and 4 mm in first and second column, respectively.

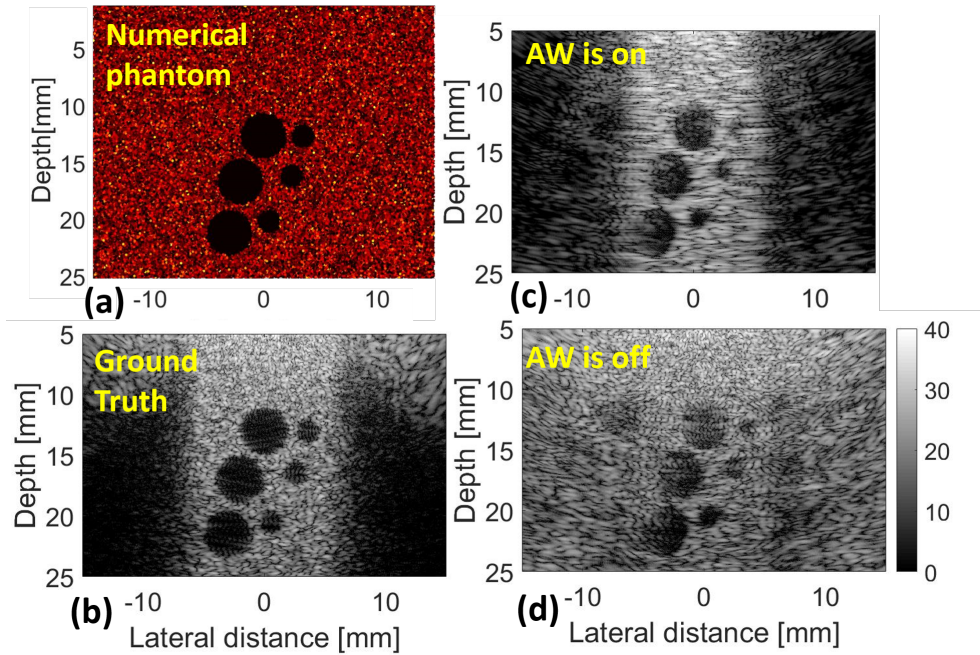


Figure 4.S2: (a) The numerical phantom containing multiple cysts. The reconstructed images using (b) the CBC imaging sequence (GT), (c,d) the proposed imaging sequence (full-aperture transmission, $N_r=5$ and $N_s=3$) when the AW is on and off, respectively.

7

MULTI-ANGLE DATA ACQUISITION TO COMPENSATE TRANSDUCER FINITE SIZE IN PHOTOACOUSTIC TOMOGRAPHY¹

In photoacoustic tomography (PAT) systems, the tangential resolution decreases due to the finite size of the transducer as the off-center distance increases. To address this problem, we propose a multi-angle detection approach in which the transducer used for data acquisition rotates around its center (with specific angles) as well as around the scanning center. The angles are calculated based on the central frequency and diameter of the transducer and the radius of the region-of-interest (ROI). Simulations with point-like absorbers (for point-spread-function evaluation) and a vasculature phantom (for quality assessment), and experiments with ten 0.5 mm-diameter pencil leads and a leaf skeleton phantom are used for evaluation of the proposed approach. The results show that a location-independent tangential resolution is achieved with 150 spatial sampling and central rotations with angles of $\pm 8^\circ$ and $\pm 16^\circ$. With further developments, the proposed detection strategy can replace the conventional detection (rotating a transducer around ROI) in PAT.

Keywords; Finite transducer size, Photoacoustic tomography, Virtual source, Tangential resolution, Artifacts reduction.

¹This chapter has been published as:

Hakakzadeh S, Mozaffarzadeh M, et. al., "Multi-angle data acquisition to compensate transducer finite size in photoacoustic tomography," Photoacoustics. 69(4), 2022.

The text and notation used in this chapter may differ on minor details from the actual publication. This is done to achieve consistency between chapters.

7.1. INTRODUCTION

Photoacoustic tomography (PAT) is a promising imaging modality with many preclinical/clinical applications [233], such as imaging from breast [234], palm and forearm [235], animal whole-body [236], [237], brain [238], [239] and rheumatoid arthritis diagnosis [240], [241]. It combines the contrast of optical and resolution of ultrasound imaging modalities [242] and is safe and relatively inexpensive compared to MRI/CT scans [234], [243]. First, a short laser excitation induces photoacoustic (PA) waves (due to photoacoustic effect). Then, Ultrasound transducers record the PA waves, and finally mathematical algorithms are used to reconstruct an image which represents the optical absorption distribution [244].

PAT systems are based on cylindrical [245]–[247], spherical [248] and planar [249] detection geometries, each of which has its own (dis)advantages [250]. For image reconstruction, it is generally assumed that point-like ultrasound detectors continuously enclose the medium. Point-like detectors record PA waves from a large acceptance angle (i.e., a wide mainlobe in the directivity pattern), which results in a location-independent axial/tangential resolution [251]. However, 1) there is no point-like ultrasound transducer (i.e., transducers have limited angular view), and 2) the spatial sampling (positioning of the transducers) is limited; of course a small transducer can mimic a point-like transducer, but the small active area causes a high noise and reduced sensitivity [252]. These two factors cause artifacts in the reconstructed image and limit the location-independent resolution of the imaging system in the cylindrical geometry; the resolution degrades as off-center distance increases [253].

There are methods reported before for improving the tangential resolution and keeping its uniformity in the ROI by compensating the effects of the finite-size transducer; mainly categorized into two groups: (a) developing advanced image reconstruction algorithms, and (b) developing new imaging set-ups.

Yuan, et al. [254] used a deconvolution with respect to the finite size of the detector in an exact frequency-domain reconstruction formula to compensate the blurring effect and resolution in a planar detection geometry. Kalva and Pramanik [255], [256] proposed the modified delay-and-sum (MDAS) algorithm for a circular detection geometry. Each photoacoustic RF signal received by the ultrasound transducer was back-projected from multiple points within the transducer surface (more than 100 points). Xiao, et al. [257] also proposed an improved version of MDAS by combining it with a sensitivity weighting factor. While promising results were achieved, MDAS and its improved version are computationally expensive (due to the multi back-projection procedure) and still suffer from a limited detection view and blurring once the detection radius is selected such that the whole ROI stays in the Fraunhofer zone of the transducer. Wang, et al. [258] proposed an approximate back-projection method by compensating the time-delay and directivity pattern of the finite-size transducer in a circular geometry. As the ROI enlarges (to a radius of 5–6 cm), this method becomes very time/cost consuming (5 minutes was taken for processing a ROI with a radius of 15 mm) due to a considerable growth in the size of the system matrix. Model-based (MB) reconstruction algorithms have also been extensively used in PAT [259]–[262]. The MB methods are less sensitive to noise and better suppress artifacts than Back-projection-based (BPB) methods [260], especially when limited-view occurs [263]. Although the computational cost of MB algorithms is high, real-time imag-

ing was realized by parallelizing on a graphics processing unit (GPU) [259]. Combining MB methods with total impulse response (TIR), spatial impulse response (SIR), and electrical impulse response (EIR) of the imaging system further improves the image quality [264], [265]. Yet, due to limited field-of-view of transducers in conventional structure, missed data could not be compensated even by MB method and needs structural modification.

Schwarz, et al. [266] placed two linear arrays perpendicular to each other (called bi-directional scanning geometry). This detection geometry imposes the limited-view issue [267] and loses most of the spatial frequencies. Li and Wang [36] used both positive and negative lab-made focused transducers with a large numerical aperture (NA) in a small ROI ($\sim 2.5\text{-}3$ cm diameter) to mimic a virtual point detector with a wide directivity pattern. Still, since the sensitivity of focused transducers is much less than the flat transducers in out-of-focus regions, more streak artifacts have appeared in the images compared to when a flat transducer is used. Li, et al. [268], Pramanik, et al. [252] and Nie, et al. [269] used an acoustic lens attached to the transducer to mimic a virtual point-like detector. However, this technique reduces the sensitivity (due to acoustic mismatch and manufacturing difficulties) and quality of the reconstructed images (due to the different speed of sound in the lens and the imaging medium).

In this study, we propose a multi-angle PAT (MA-PAT) system for compensating the finite size of the ultrasound transducer in 2D circular detection geometry. While a transducer is rotated around the region of interest (ROI) to record the PA waves needed for image reconstruction (Figure 7.1(c)) this structure is called the conventional system throughout this paper, we additionally use central rotations (rotating the transducer around its center) with certain angles at each spatial sample (Figure 7.2); The combination of all transducers with different central rotations and non-central rotated at each location mimics a virtual point detector with a large angular view (Figure 7.2(a, b)). Spatial samples in this paper refer to the location of the virtual point detectors in the proposed structure and the location of transducers in the conventional structure. This is feasible with motor-based PAT detection systems by tilting the transducer at the beginning of data acquisition for each angle. The angles are calculated based on the impulse response, the diameter of the transducer and the radius of detection surface so that each point source in the ROI is within the field of view (FOV) of either the transducer or its rotations. In this way, a uniform spatial frequency spectrum would be captured from all the absorbers in the ROI. The point spread function (PSF) is evaluated through simulations and experiments, with the conventional and proposed detection geometries. The results indicate that the proposed approach provides a location-independent resolution and more structural information.

7.2. MATERIALS AND METHODS

7.2.1. EFFECTS OF FINITE-SIZE TRANSDUCER ON RADIAL/TANGENTIAL RESOLUTION IN PAT

In a circular scanning geometry, typically a single-element transducer is rotated around the scanning center. ROI must be located in the far-field of the ultrasound transducer (Fraunhofer zone), where the pressure field changes are predictable and is convenient for imaging. The exact image reconstruction algorithm for this detection geometry is reported in [270]. Based on the finite-size transducer effect, in a circular arrangement, the

PSF of a random point-absorber positioned at radial location of r , extends along the tangential direction (see the arc around the point absorber in Fig. 7.1(a)) as:

$$W(r) = \frac{rD}{R}, \quad (7.1)$$

where, R is the radius of the detection system, and D is diameter of the transducer. Equation 7.1 indicates that the PSF extension in the tangential direction is directly proportional to the distance from the center and transducer diameter, and inversely proportional to the scanning radius. Therefore, 1) the PSF extends along the tangential direction (degrading the tangential resolution) as the off-center distance, r , increases, and furthermore 2) the tangential resolution degrades faster with a larger transducer diameter.

In general, for a limited size transducer, not all angular views of each arbitrary absorber in the ROI would be captured which results in tangential resolution degradation. Consequently, there are blind angles (discussed in section 7.2.2) for some absorbing points in the ROI. To extract the range of these blind angles, the concept of spatial frequency for each absorbing point and its relation to the transducers directivity pattern and beam-width should be first defined.

7.2.2. BLIND ANGLES AND RECONSTRUCTION RANGE CALCULATION IN PAT DIRECTIVITY PATTERN

2D schematic of the directivity pattern of a flat disc transducer with a diameter D ($D = 2a$, where a is the radius) is shown in Figure 7.1(b). where r' is the radial distance of each point relative to the center of the transducer, and θ is the divergence angle. The pressure field of a disc transducer in (r', θ, t) is given by [271]:

$$p(r', \theta, t) = \left[\pi a^2 A_0 \frac{e^{j(\omega t - kr')}}{r'} \right] \left[\frac{2J_1(ka \sin(\theta))}{ka \sin(\theta)} \right], \quad (7.2)$$

where k is the wave-number, ω is the angular-frequency, A_0 is a constant which defines the reference amplitude at the reference distance (i.e., the surface of the transducer). The Bessel function ($J_1(.)$) in (7.2) describes the directivity of the transducer. The edge of the mainlobe can be calculated as follows:

$$\sin(\theta_{MAX}) = \frac{\tau \lambda}{D}, \quad (7.3)$$

where, τ is a constant and λ is the wavelength. Based on -6 dB, -10 dB and the extreme edge of the beam pattern, τ is 0.56, 0.9 and 1.22, respectively. The smaller the transducer diameter, the larger the transducer FOV (θ_{MAX}); assuming the same wavelength in (7.3).

SPATIAL FREQUENCY COMPONENTS

Each point-absorber in the 2D ROI generates a circular wave once excited with the laser beam. This circular wave can be considered as a superposition of plane waves propagating in different ϕ directions (the range of ϕ is 0 to 2π) each with a specific spatial frequency component k_ϕ along tangential direction where ϕ is measured with respect to the radius that passes through this point. Δk_ϕ^{MAX} is received if all of these spatial frequency

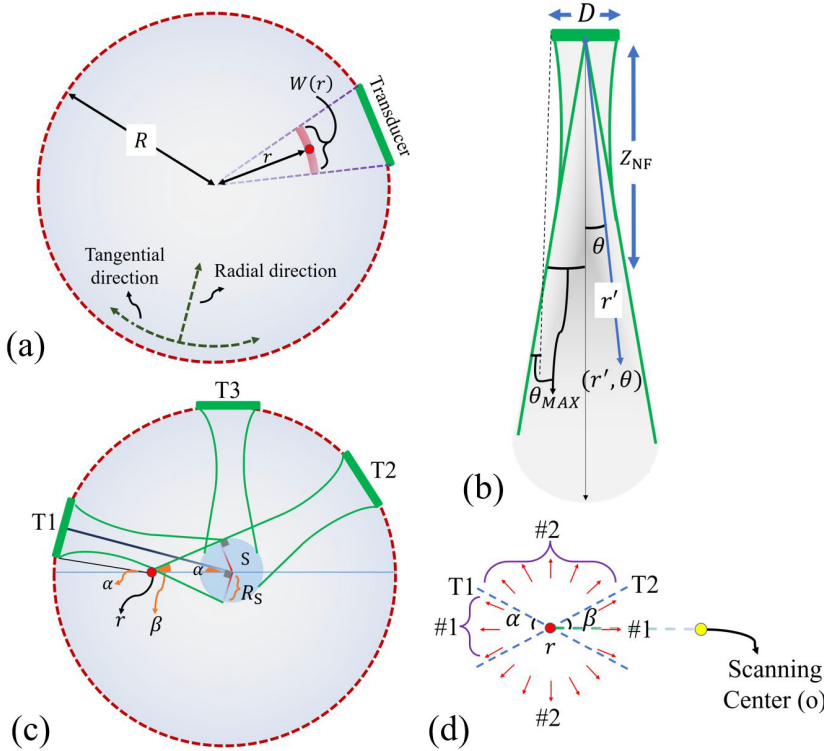


Figure 7.1: (a) The schematic of a conventional 2D PAT system. r is the distance from the center of each point-absorber in ROI, R is the scanning radius, red circle is a random point-absorber, and $W(r)$ is the PSF extension of the red circle. (b) The schematic of the directivity pattern of a flat finite-size transducer with a diameter of D . θ is the divergence angle, Z_{NF} is the Fraunhofer zone. (c) The schematic of a conventional circular scanning PAT system where S is the area (with a radius of R_S) that stays in the FOV of all the transducers. The transducers between position T1 and T2 (for example T3) do not see the absorbing point (shown in red) in their main lobe. α and β are the angles of edges of the directivity pattern of transducer T1 and T2 connecting the absorber with respect to the horizon line passing through the red absorber, respectively. (d) The #1 and #2 generated ultrasound waves of the red circle in (c) can and cannot be fully captured with the conventional detection approach, respectively.

components, or in other words, all the generated rays, are captured by the detectors arranged around the ROI. The lower the range of the spatial frequency vectors of each point-absorber captured by the detectors, the lower the tangential spatial frequency range (Δk_ϕ) becomes which results in the reduction of angular/tangential resolution [272]. The blue circle in Figure 7.1(c) stays in the FOV of all the transducers. As a result, the photoacoustic radiated k-vectors (spatial frequency components) of an absorber inside region S are fully captured by the detectors. The radius of region S is calculated as:

$$R_S \approx R \sin(\theta_{MAX}) = \tau \frac{R\lambda}{D}. \quad (7.4)$$

In Figure 7.1(c), if we move from a specific transducer in the clockwise direction, the transducers between position T1 and T2 do not see the point absorber (the red circle in Figure 7.1(c)) due to their limited mainlobe. By assuming that the edges of the directivity pattern of transducer T1 are parallel with T1 bisector (see dashed-line in Figure 7.1(b)), due to the small value of θ_{MAX} in large aperture transducer, and considering the angles specified in Figure 7.1(c) (where α and β are the angles of the line connecting the absorber and T1 and T2, respectively with respect to the horizon line passing through the point absorber), we will find that the angles between α and β in the upper and lower sides of the source are blind angles for the photoacoustic source, which is shown in Figure 7.1(d) (see #2 regions). The other angles along which the k-vectors are received are called acceptance angles for that source. The total acceptance angle for each pixel based on its distance from the scanning center (r) is given as:

$$2(\alpha + \beta) \approx 2\left(\frac{\pi}{2} - \cos^{-1}\left(\frac{R_S}{r}\right) + \sin^{-1}\left(\frac{R_S}{r}\right)\right) = 2\sin^{-1}\left(\frac{R_S}{r}\right). \quad (7.5)$$

Dividing 2π by (7.5) gives the ratio of the range of frequency components captured by transducers $\Delta k_\phi(r)$ to the range of frequency components produced by a photoacoustic source $\Delta k_\phi^{MAX}(r)$ as:

$$\Delta k_\phi(r) \approx \frac{\pi}{2\sin^{-1}\left(\frac{\tau R\lambda}{Dr}\right)} \Delta k_\phi^{MAX}. \quad (7.6)$$

Equation (7.6) indicates that as the off-center distance increases, the captured spatial frequency range by the finite-size transducers decreases.

7.2.3. PROPOSED METHOD: MULTI-ANGLE DETECTION GEOMETRY

A schematic of the proposed method is given in Figure 7.2(a). The single transducer is initially centrally-rotated before circular scanning around the ROI by a step-motor. The FOV of the transducer at each central angle ($\theta_{c,n}$) captures specific spatial frequency components that were not captured by the non-centrally-rotated ($\theta_{c,0} = 0$) case where n is the number of required central rotations which will be calculated later. For a scanning radius of R , consider the transducer is centrally rotated with $\theta_{c,n}$ degrees. The perpendicular line from the central point of the ROI to the tilted transducer beam bisector is R_c (see Figure 7.2(a)):

$$R_c = \sin(\theta_{c,n})R. \quad (7.7)$$

The overlap of the mainlobe of all the centrally-rotated transducers act like an area with an inner and outer radius of $R_c - R_S$ and $R_c + R_S$, respectively (see Figure 7.2(b)):

$$\begin{cases} R_c - R_S = \sin(\theta_{c,n})R - R_S \\ R_c + R_S = \sin(\theta_{c,n})R + R_S \end{cases}. \quad (7.8)$$

If a source is located in this area, all its spatial frequencies are fully captured by either transducers positions or its central rotations.

The radial range of the areas produced by each pair of symmetrical $\theta_{c,n}$ ($\pm\theta_{c,n}$) central rotations is $2R_S$. Equation (7.9) represents the number of required areas (A_{number}) with radius $2R_S$ to cover a ROI of radius R . An example with two areas is shown in Fig. 2(c).

$$A_{number} = \left\lfloor \frac{R - R_S}{2R_S} \right\rfloor = \left\lfloor \frac{D - \tau\lambda}{2\tau\lambda} \right\rfloor. \quad (7.9)$$

If ROI radius (R_{ROI}) is different from chamber radius (R), A_{number} is equal to $\left\lfloor \frac{R_{ROI} - R_S}{2R_S} \right\rfloor = \left\lfloor \frac{DR_{ROI} - \tau R\lambda}{2\tau R\lambda} \right\rfloor$. In order to find the values of $\theta_{c,n}$, rings with a thickness of $2R_S$ should be considered for each pair of symmetric central rotations. Ideally, the total number of required rings (i.e., the number of required $\theta_{c,n}$), is A_{number} . Therefore, based on (7.7) the variable $\theta_{c,n}$ is ideally given by (7.10):

$$\theta_{c,n} = \sin^{-1}\left(\frac{2nR_S}{R}\right) = \sin^{-1}\left(\frac{2n\tau\lambda}{D}\right), \quad (7.10)$$

where, the value of n is from 0 to A_{number} . The maximum value of $\theta_{c,n}$ ($\theta_{c,max}$) can be calculated by substituting the maximum value of $n(A_{number})$ in (7.10) and is $\sin^{-1}\left(\frac{2A_{number}\tau\lambda}{D}\right)$.

TANGENTIAL RESOLUTION ANALYSIS OF THE PROPOSED APPROACH

The combination of all transducer with different central rotations and non-centrally rotated mimic a new virtual detector with a wide main-lobe and a maximum angular width of θ_{new}^{MAX} :

$$\theta_{MAX}^{new} = \theta_{c,max} + \theta_{MAX}. \quad (7.11)$$

For θ_{new}^{MAX} , (7.3) could be rewritten as follows:

$$\sin(\theta_{MAX}^{new}) = \frac{\tau\lambda}{D_{new}}. \quad (7.12)$$

By substituting (7.3) and (7.11) in (7.12), the active diameter of the new virtual detector (D_{new}) can be extracted:

$$D_{new} = \frac{\tau\lambda}{\sin\left(\sin^{-1}\left(\frac{2\tau\lambda A_{number}}{D}\right) + \sin^{-1}\left(\frac{\tau\lambda}{D}\right)\right)}. \quad (7.13)$$

By substituting the value of D with D_{new} from (7.13), in (7.1), the PSF extension achieved by the proposed approach, $W^{new}(r)$, will be obtained as follows:

$$W^{new}(r) = \frac{r\tau\lambda}{R\sin\left(\sin^{-1}\left(\frac{2\tau\lambda A_{number}}{D}\right) + \sin^{-1}\left(\frac{\tau\lambda}{D}\right)\right)}. \quad (7.14)$$

which is apparently smaller than the PSF width of the conventional structure given in (7.7). This reduction in PSF width and thus tangential resolution improvement will be validated via experimental measurements.

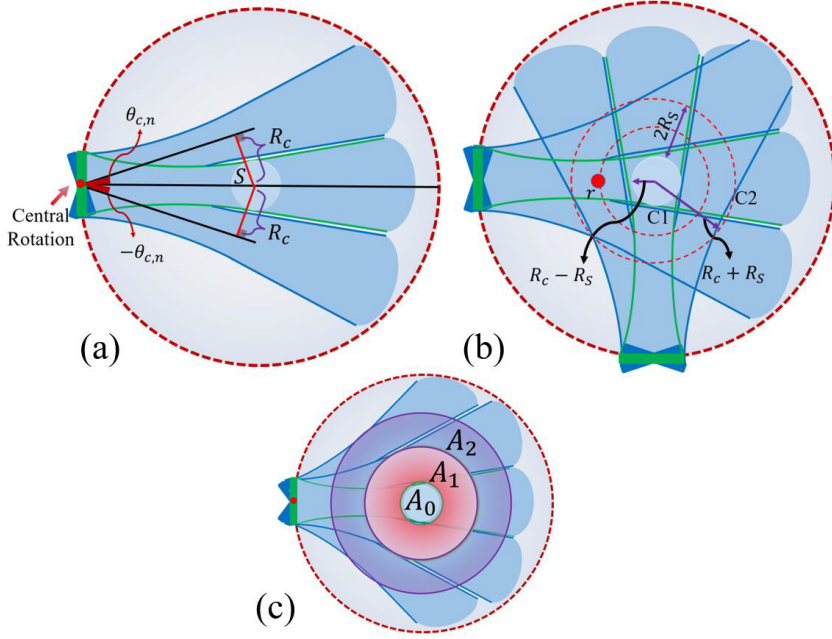


Figure 7.2: (a) A representation of the pressure field of a single element transducer with a central rotation 0° (green) and central rotation $\theta_{c,n}$ (blue). (b) The area between C1 and C2 stays in the FOV of all the tilted transducers, and the thickness of this area is $2R_S$. (c) Each area (A_n) stays in the FOV of the tilted transducers with a central rotation of $\theta_{c,n}$.

ANGULAR WEIGHING IN BACK-PROJECTION

In this work, a modified version of the Universal back-projection (UBP) algorithm is used for reconstruction [250] where the RF data is back-projected with a weighting factor. This weighting factor consists of two factors: 1) a binary directivity factor which refers to the transducer directivity pattern, and 2) a solid-angle weighting factor that is considered in the back-projection formula (see Figure 1 and 2 in [250]). In the solid-angle weighting, the value of the weighting factor in each region is inversely proportional to the distance from the transducer. To minimize the number of required central rotations for covering the entire ROI, the width of the mainlobe of the transducer at -10 dB is considered as the edge of the binary weighting factor.

7.2.4. NUMERICAL AND EXPERIMENTAL STUDY

NUMERICAL STUDY

The k-Wave toolbox [273] was used to synthesize the numerical data in 2D. Two synthetic phantoms were used: one with point absorbers to evaluate point spread function (see Figure 7.4) and one to mimic vasculature (Figure 7.5(a, b)). A flat transducer with a diameter, central frequency and bandwidth of 13 mm, of 2.25 MHz and 67% was used, respectively; properties of Olympus NDT, V306-SU transducer. The medium and grid size were 25 cm

and 0.1 mm at both directions (2500×2500 grids), respectively. The speed of sound and sampling frequency were 1500 m/s and 25 MHz, respectively. The scanning radius (the yellow circle in Fig. 5(a)) was 12 cm. The imaging ROI (the dashed circle in Figure 7.5(a)) was within a radius of 5.5 cm. The size of the point absorbers was equal to the grid size. Point detectors in our study are modeled as a one-grid detector. The PA signals recorded by many point detectors at the surface of a transducer are averaged to model a PA signal recorded by a finite-size transducer. In the conventional method, a finite-size transducer rotates around the imaging region and captures PA waves (see Figure 7.1(c)).

By substituting the transducer properties and ROI in (7.7) and (7.8), we calculated $R_S \approx 8.1$ mm and $A_{number} = 2$. By substituting R_S , A_{number} , $\tau = 0.9$ and transducer properties in (7.3, 7.9-7.12), respectively, and $N = 2\pi\rho/\lambda$, other variables for the proposed detection approach were calculated and reported in Table 7.1.

Table 7.1: THE PROPERTIES OF THE MA-PAT SYSTEM.

N	N_{new}	$\theta_{c,1}$	$\theta_{c,2}$	θ_{MAX}	θ_{MAX}^{new}	D_{new}
750	150	$\pm 8^\circ$	$\pm 16^\circ$	3.9°	22.2°	2.6

EXPERIMENTAL STUDY

Two experimental studies were conducted to evaluate the performance of the proposed method. 1) pencil leads with ~ 0.5 mm diameter to mimic point absorbers (see Figure 7.3(b) and Figure 7.2) complex leaf skeleton phantom (see Figure 7.3(c)). The photograph of the experimental set-up is shown in Figure 7.3(a). A Q-switched Nd: YAG laser delivering 532 nm at 5 ns pulse width at 10 Hz was used as the excitation source. An unfocused single ultrasound transducer (SUT) of 2.25 MHz (Olympus NDT, V306-SU) fitted with an acoustic reflector (F102, Olympus NDT) was rotated around the region of interest to acquire the PA waves. The transducer is used in the vertical mode and the acoustic reflector is used to deflect the photoacoustic waves from the sample towards the ultrasound detector. The phantom is oriented perpendicular to the laser illumination and is placed at the scanning center for imaging (see Figure 7.3). The PA signals were amplified by a low signal noise amplifier (Olympus-NDT, 5072PR) and stored in a desktop computer (IntelXeon, 3.7 GHz 64-bit processor, 16 GB RAM) equipped with a data acquisition (DAQ) card (GaGe, compuscope 4227).

COMPARISON WITH PREVIOUS STUDIES

The existing techniques to tackle the finite size transducer issue are categorized into developing advanced image reconstruction algorithms and new data acquisition set-ups. For comparison, we selected works representing each category. For data acquisition set-ups category, a comparison was conducted with Pramanik, et al. [252] which improved the tangential resolution using a negative acoustic lens, and Nie, et al. [269] which improved the tangential resolution by a convex/concave transducer. For the reconstruction category, three methods were selected: Wang, et al. [258] which compensated the time-delay and directivity pattern, Kalva and Pramanik [255] which proposed the modified delay-and-sum (MDAS) algorithm and Chowdhury, et al. [264] which combined a MB method

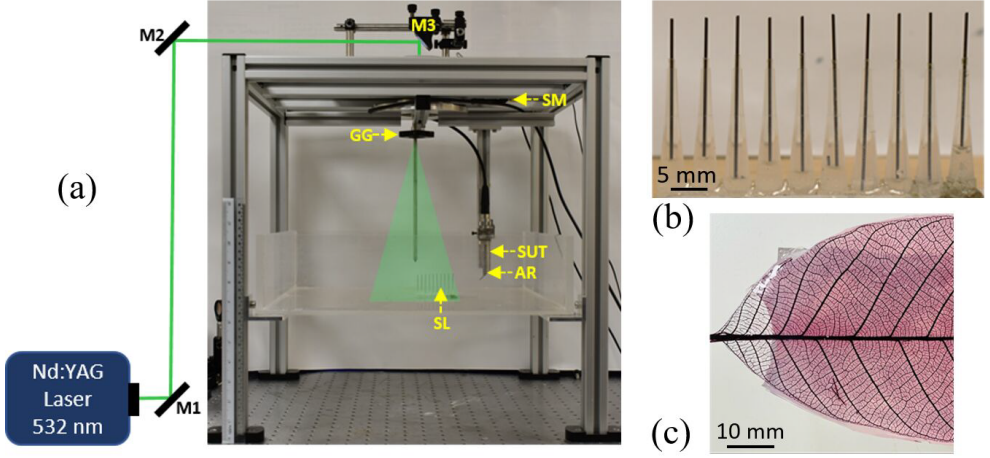


Figure 7.3: (a) Photograph of the Nd:YAG laser photoacoustic tomography system; SM, stepper motor; GG, ground glass diffuser; SUT, single-element ultrasound transducer; AR, Acoustic reflector; SL, sample; M1, M2, M3, mirror. (b) Ten pencil leads are used to mimic point absorbers. (c) Complex leaf skeleton phantom.

with TIR. Two metrics were used for quantification: 1) region-of-interest (ROI) radius to difference between the tangential resolution of the outmost to the central absorber in the ROI (Res_{slope}): The Res_{slope} metric indicates the slope of tangential resolution increment to the off-center distance increment. The smaller the Res_{slope} , the lower the dependence of the tangential resolution on the location. 2) Resolution improvement of the outmost absorber obtained by the proposed method compared to that obtained by the conventional detection (IPC; this metric is reported in percent (%)).

7.3. RESULTS

7.3.1. NUMERICAL RESULTS

Figure 7.4(a) indicates that a location-independent tangential resolution (limited to the half of the wavelength at the central frequency) is indeed achievable with a point-like transducer. The full width at half maximum (FWHM) of the image intensities on an arc passing through the maximum of each reconstructed absorber (see dashed lines in Figure 7.4(a)) are used for calculating the tangential resolution. In the conventional detection geometry, as the radial distance increases, the PSF extends (Figure 7.4(b)), and the resolution degrades (Figure 7.4(d)) along the tangential direction. At a distance of 55 mm from the scanning center, the tangential resolution reaches ~ 5.6 mm, which is about 10 times larger than that in the scanning center. This is due to the limited FOV of the transducer and causes image blurring (see arrows in Figure 7.5(c)). The proposed detection geometry addresses this issue (see Figure 7.4(c) and Figure 7.5(g)), and the resolution obtained in different radial distances follows that obtained with the point-like detector (see Figure 7.4(c, d)). In the proposed detection geometry, the tangential resolution reaches ~ 0.65 mm at a radial distance of 55 mm; improved by $\sim 88\%$ compared to the conventional de-

tection geometry.

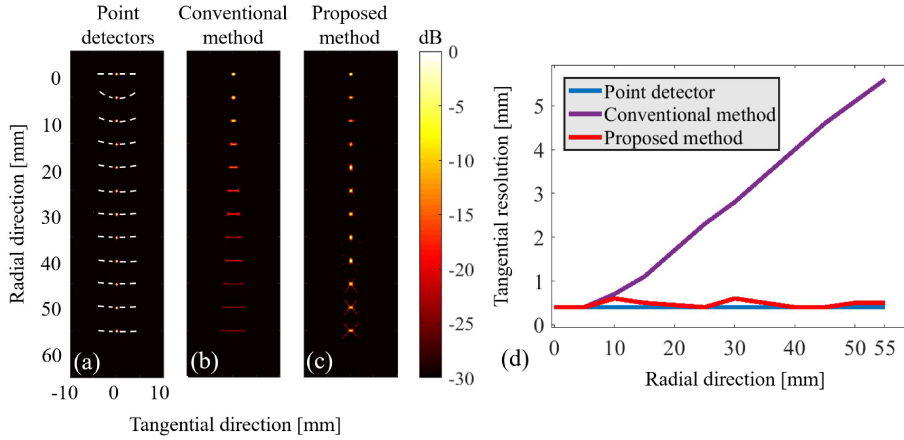


Figure 7.4: The numerical results using point absorbers. (a) The reconstructed image with point-like detectors. The reconstructed images with (b) the conventional and (c) proposed methods, respectively. (d) The tangential resolution. The image intensities on dashed-arc passing through the reconstructed absorber are used for calculating the tangential resolution.

The quality of the reconstructed images by the conventional (Figure 7.5(c)) and the proposed approach with $\theta = 0$ (Figure 7.5(d)) is close in the center of the ROI (see the white dashed circle in Figure 7.5(c, d)) while only 150 spatial samples were used in Figure 7.5(d). This is due to having a large enough spatial samples (150) to capture all the information needed to do reconstruction within a limited central region (the region inside the white dashed circle in Figure 7.5(c, d) is covered by the R_S in Figure 7.2(c)). At each central rotation, the transducers capture more solid angles of PA waves generating from specific regions in the ROI than others. Therefore, the reconstructed image corresponding to each central rotation provides visualization of different regions and certain regions are better reconstructed (compare areas shown by white arrows in Figure 7.5(d-f)). Coherent summation of the reconstructed images at each rotation angle results in a final high-quality image which is our main goal (see Figure 7.5(g)). The sensitivity of our approach in the off-center regions is higher than the conventional method (see Figure 7.5(c, g)). The peak-signal-to-noise ratio (PSNR) and structural similarity index metric (SSIM) were measured in yellow dashed area (indicated in Figure 7.5(b)). A PSNR and SSIM of 12.5/ 19.2 dB and 0.57/ 0.85 were obtained for the conventional/proposed method, respectively. Therefore, our approach increases the similarity to the phantom (SSIM) by 28% and PSNR by 6.7 dB.

7.3.2. EXPERIMENTAL RESULTS

The results of pencil lead targets (Figure 7.6(a)) show that the conventional method extends the PSF when the radial distance increases and the resolution rapidly degrades after a radial distance of 20 mm (Figure 7.6(b)). The tangential resolution of 0.5 mm pencil lead absorber reaches $\sim 3/6.4$ mm in the radial distance of 37 mm and 55 mm (see Figure

7.6(c)). However, the proposed approach prevents the PSF extension (Figure 7.6(b)) and maintains the tangential resolution as the radial distance increases (Figure 7.6(c)). The tangential resolution obtained by the proposed method in the radial distances of 37- and 55- mm is ~ 0.6 and ~ 0.8 mm, respectively; improved by 86% compared to the conventional method (Figure 7.6(c)).

For the leaf skeleton phantom experiment, the edges of the phantom are reconstructed well with the proposed method. However, due to the limited FOV of the conventional method, edges are blurred in the conventional method (see yellow arrows in Figure 7.7(a, b)). Comparing the yellow dashed rectangle in Figure 7.7(a, b) shows that the proposed method provides more structural information than the conventional method.

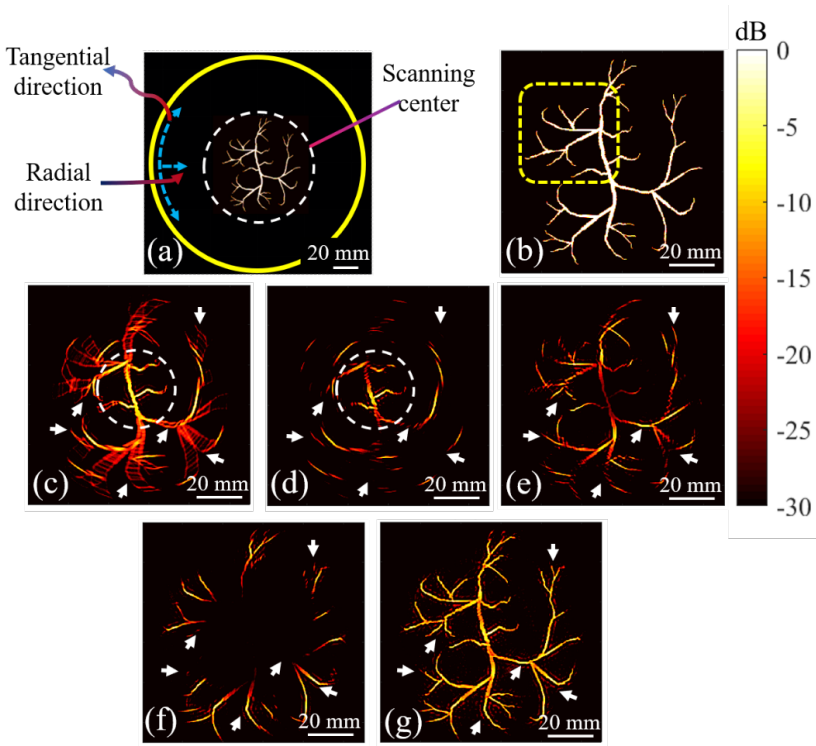


Figure 7.5: The numerical results using the vasculature phantom. In (a), the vasculature phantom, the ROI (dashed white circle) and the scanning trajectory (yellow circle) are shown. (b) The zoomed version of the ROI. (c) and (d) show the reconstructed images with the conventional method where 750 and 150 spatial samples are used, respectively. (e) and (f) show reconstructed images with 150 spatial samples and a central rotation of $+8^\circ / -8^\circ$ and $+16^\circ / -16^\circ$, respectively. (g) shows the reconstructed image with the proposed detection approach after coherent summation of the images generated with all the angles (shown by d-f). The white arrows show the structure that are not detectable with the conventional detection geometry.

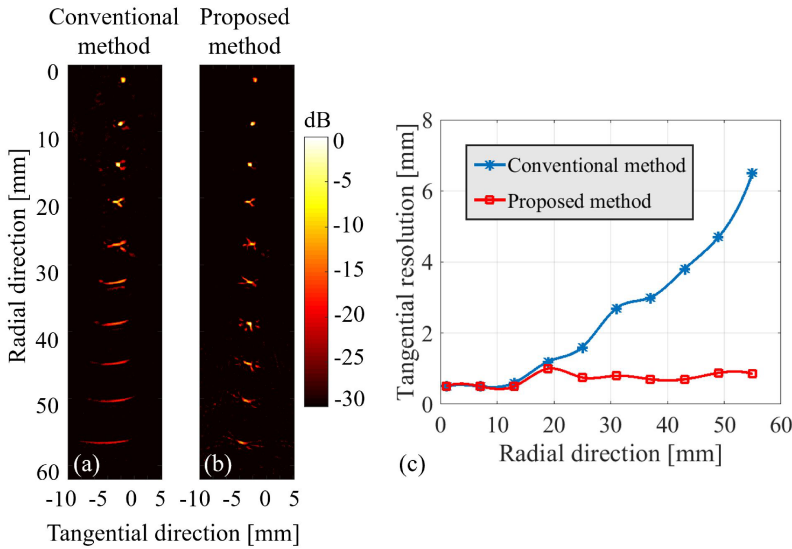


Figure 7.6: Experimental evaluation of the point spread function (PSF). (a, b) show the reconstructed images with the conventional method (750 spatial samples) and the proposed method (150 spatial samples), respectively. The tangential resolution obtained by the conventional and proposed methods are shown in (c).

7.3.3. EFFECTS OF NUMBER OF SPATIAL SAMPLES

Figure 7.8 indicates that with a number of spatial sampling (N_{SS}) less than 150, the streak artifacts increase while there is no change in the image quality with a N_{SS} higher than 150. This agrees with the experimental results (see Figure 7.9 with severe artifacts in (h) while degraded from (e) to (h)). By decreasing the number of spatial samples from 150 to 50 with step size of 25 in the proposed approach, streak artifacts increase (see white arrows and yellow dashed-rectangle in Figure 7.9(e-h)).

7.3.4. COMPARISON WITH PREVIOUS WORKS

The comparison of our method (MA-PAT) with five existing is given in Table 7.2. Res_{slope} indicates that our method has the lowest dependence of the tangential resolution on the location. Based on the IPC metric, our method improves the tangential resolution of the outmost absorber in the ROI by 88%, which is more than other techniques presented in Table 7.2.

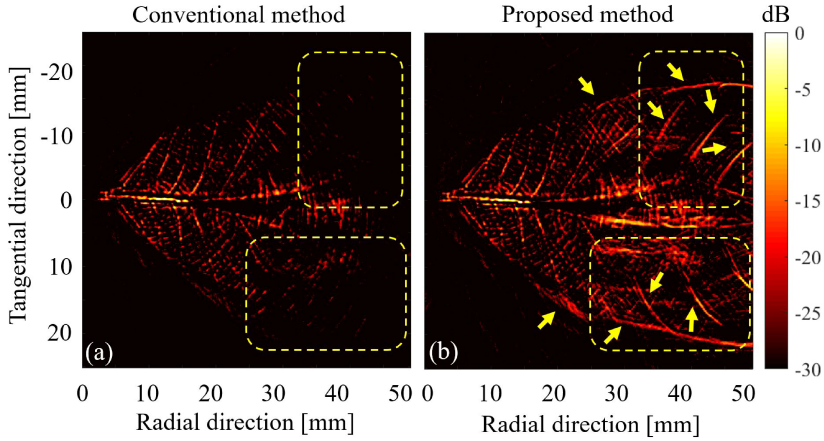


Figure 7.7: The experimental results using the complex leaf skeleton phantom. The reconstructed images with (a) the conventional method and (b) the proposed method, respectively. The yellow arrows and dashed-rectangles show the structure that are not detectable with the conventional detection geometry.

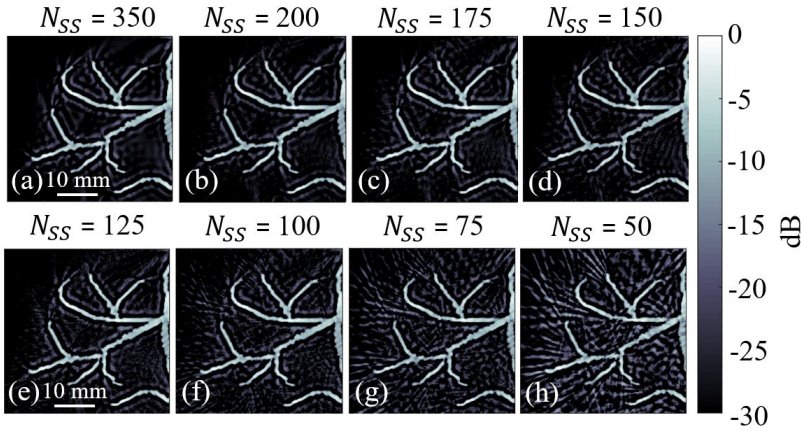


Figure 7.8: The numerical results of evaluation of the effects of the number of spatial samples (N_{SS}) used in the proposed approach. These images are corresponding to the region inside the yellow dashed rectangle in Figure 7.5(b).

7.4. DISCUSSION

7.4.1. OVERVIEW

In circular geometry PAT, usually, a large aperture single element transducer is rotated around a region of interest (ROI) of scanning radius R . As the off-center distance increases,

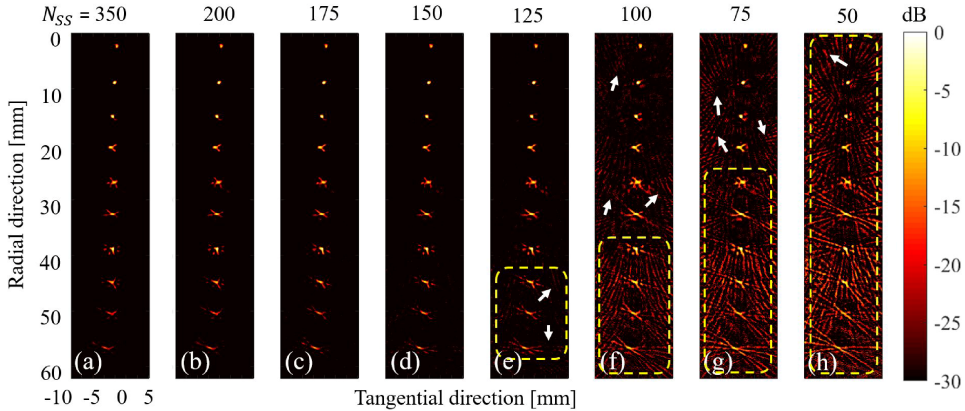


Figure 7.9: The experimental results of evaluation of the effects of the number of spatial samples (N_{SS}) used in the proposed approach.

Table 7.2: COMPARISON TO EXISTING WORKS.

Method	Res_{slope}	IPC
Pramanik, et al. [252]	38×10^{-3}	54%
Nie, et al. [269]	50×10^{-3}	54%
Kalva and Pramanik, et al. [255]	65×10^{-3}	70%
Wang, et al. [258]	4.5×10^{-3}	71%
Chowdhury, et al. [264]	9×10^{-3}	-
Our method	2.9×10^{-3}	88%

the captured spatial frequency range by the finite-size transducer decreases due to the limited main lobe of the transducer, and the PSF extends along the tangential direction. Consequently, the tangential resolution degrades in off-center regions as given by (7.1). In case of using an ideal point-like detector (with a wide main lobe), the whole range of generated spatial frequency vectors are captured given that the entire ROI fall in the field-of-view (FOV) of detector. This results in a location-independent tangential resolution. Yet, point-like transducers are hard/expensive to manufacture and suffer from a low sensitivity, which makes them impractical for photoacoustic tomography systems. In this work, we introduced a multi-angle photoacoustic tomography system in which a virtual detector with a wide detection angle (coming from combining the transducer directivity pattern at each central rotation with an angle of $(\theta_{c,n})$) is developed. With our detection approach, the entire spatial frequencies of each pixel are captured independent from its radial location and a location-independent tangential resolution is achieved. The proposed approach could be useful for human brain/breast imaging [238], [248] and whole-body small animal imaging [274] where a large ROI (10-cm diameter) should be covered.

It should be noted that a new detection strategy (which allows capturing high spa-

tial frequency components missed by the conventional data acquisition) was proposed in this work, but not a reconstruction technique. While we used the back-projection, other reconstruction techniques (e.g., model-based techniques) could also be used.

7.4.2. LIMITATIONS OF THE PROPOSED DATA ACQUISITION APPROACH

Sources with the same size and absorption coefficient might appear with different values after reconstructing with our approach. The difference is expected to be minor though. This is because the captured waves are back-projected to the regions inside the -10 dB of the directivity pattern of the transducer (either tilted or non-tilted).

Placing the transducer exactly at the central rotation angle may be problematic in practice. Yet, since these angles are approximately calculated, a small amount of alignment error (± 1 degree) slightly induces artifacts to the reconstructed images. This could explain the artifacts seen in Figure 7.9(d) after a depth of 25 mm.

Applying the central rotation is time consuming and the main drawback of our method. Currently, it is not possible to use this method for imaging live animals. There are studies that used lab-made ring array transducers with small-size elements [245], [246]. Video-rate imaging can be achieved using ring arrays, but spatial aliasing and arc artifacts may occur due to the pitch size (the spacing between the array elements); the pitch must be lower than half of the wavelength at the central frequency of the array [275]. This necessitates a very large number of elements, read-out circuits and cables, which impose manufacturing difficulties and setup complexities [276]–[279]. Further development of our data acquisition strategy in combination with ring arrays could remove the rotation step in our approach and possibly mitigate the effects of aliasing and arc artifacts caused by the large pitch size of the current ring arrays [245], [246]. GPU parallel programming can also be used to reconstruct images of each angle simultaneously, allowing real-time imaging [280].

7.5. CONCLUSION

In this work, we proposed a multi-angle detection approach for circular photoacoustic tomography systems to compensate the effects of finite transducer size. The novelty of our approach lies in the fact that the transducer rotates around its center (for limited number of angles) as well as rotating around the region of interest with a stepper motor to record the photoacoustic waves. The numerical and experimental results showed that the proposed approach allowing capturing the entire spatial frequencies of the photoacoustic waves mimics a directional point-like transducer with a large angular view and provides a location-independent tangential resolution. The proposed approach could replace the conventional detection geometry due to structural simplicity and low processing cost.

ACKNOWLEDGEMENTS

MP would like to acknowledge the support by the Tier 1 Grant funded by the Ministry of Education in Singapore (RG30/21, RT16/19).

8

DESIGN OF A DUAL-RING INTERSTITIAL PHOTOACOUSTIC/ULTRASOUND IMAGING NEEDLE¹

In this chapter, we reported on the design and evaluation of an imaging needle, which can be used for endoscopic third ventriculostomy (to reduce the intracranial pressure) and brain abscess draining. An annular array consisting of two rings is designed to narrow down the directivity of the array using beamforming. The inner and outer radius of the rings were chosen such that they have the same surface area (sensitivity). A polyvinylidene difluoride (PVdF) with a thickness of 52 μm was used as the piezo-electric material. The rings were mounted on a PCB. PZFlex simulations show that a lower cut-off frequency of about 2.15 MHz and 3.88 MHz is obtained for the big and small rings, with a higher cut-off frequency up to 25 MHz and a cross talk lower than 30 dB, respectively. The kWave Matlab simulations show that beamforming slightly improves the image quality due to the minor phase shift between the rings. A single ring with an inner and outer radius of 350 μm to 1.3 mm is good enough for guidance of the catheter placement and guidance toward the target. The experimental measurements show that at -10 dB, the high cut-off frequency is 16 MHz.

8.1. INTRODUCTION

Hydrocephalus is a condition in which the excess cerebrospinal fluid (CSF) accumulation within the brains ventricular system and leads to an increased intracranial pressure and related complications. One of the ways to alleviate this condition is a surgery called endoscopic third ventriculostomy (ETV) where the catheter creates an opening in the third ventricle allowing CSF to flow naturally to the basal cisterns. External landmarks and an orthogonal angle to the skull are usually used to determine the trajectory of distal tip of the catheter toward the lateral ventricle near the foramen of Monro [281]. However, The choice of a proper trajectory can be hindered by incomplete visualization of the tangential plane, surgical drapes obscuring external landmarks, movement of the patient and different cranial morphology in different patients. Suboptimal final placement of the catheter occurs in 2%–22% of cases and requires replacement due to low output in 3.8%–11% of total cases [282]. Thus, monitoring and navigation tools to properly determine the initial trajectory are needed.

Endoscopic devices confirm the ventricular entry, but does not provide any information for determining the initial trajectory [283]. CT and MR scans address this issue, but they are relatively expensive and non-portable with a long setup time. Ultrasound address these issues though because it is user-friendly, portable, relatively inexpensive and most importantly safe [214].

Looking into the literature over the past three decades, different ultrasound/photoacoustic interstitial/endoscopic devices have been developed. Considering the clinical application mentioned above, the device should be forward looking, and this makes the context of this chapter related to designing an ultrasound annular array [284]–[288]. In [289], a dynamically focused annular array was proposed for the first time, and it was claimed that the dynamic focus capability provides significantly improved images when compared with those obtained using single element transducers. A pipeline was proposed in [290] regarding the design of an annular array. The effects of the width of each ring in an annular array was evaluated in [291]. It was proven that the geometry of the array element should be determined by the focal range of interest, and the phase shift across the element surface should be taken into consideration when designing an annular array; a large phase shift over an element causes high sidelobes and decreases the efficiency because energy is transferred from the mainlobe to the sidelobes [292]. To localize and monitor the blood content in tissue, a double-ring photo-acoustical detector was proposed in [293] using Polyvinylidene fluoride or polyvinylidene difluoride (PVdF) as the piezo-electric material. The phase shift between the A-lines recorded by the two rings was compensated by applying delays to the A-lines and the signal to noise ratio was improved by coherent summation. Using the same design, the first in vivo photoacoustic images of single human blood vessels was reported in [294]–[296]; authors mentioned that the proposed annular array offers new perspectives for application in various clinical fields, such as micro and macrovascular imaging. The same annular array was coupled with pulsed laser diode and was used for in vivo photoacoustic imaging of blood vessels [297]. The application of annular arrays was also investigated in circular photoacoustic tomography imaging systems [298].

In this chapter, we report on the numerical design of a dual-ring annular array which can be inserted into a surgical needle, integrated with an laser-induced ultrasound

transmission for ultrasound (US) imaging and annular optical transmission for photoacoustic (PA) imaging. The proposed design aims to manufacture an interstitial ultrasound/photoacoustic imaging needle. The two rings enable suppression of off-axis signal with beamforming. To ensure a large bandwidth, the PVdF is used as the piezo-electric material. And, to ensure a good signal-to-noise ratio (SNR), ASIC (Application Specific Integrated Circuit) is amplified the recorded signals right behind the PVdF rings. The proposed needle can be used to guide surgeons toward the regions of interest and prevent multiple insertion of surgical catheters.

8.2. MATERIALS AND METHODS

8.2.1. CONCEPT

The idea behind the proposed imaging needle is illustrated in Figure 8.1. The needle can be used for both ETV and brain abscess draining. The output of the imaging needle is an A-line which indicates the differences between then acoustical properties and optical absorption of the tissue (ultrasound and photoacoustic mode, respectively) in front of the needle perpendicular to the surface of the annular two-ring array. For the seek of readability, the acoustic wave generated as a result of optical absorption of tissue (PA effect) and backscattered from tissue as a results of laser-induced ultrasound transmission is called PA wave and US wave throughout this chapter, respectively.

In the middle of the needle, an optical fiber with an absorbing tip is placed (see Figure 8.1(b)) to enable laser-induced ultrasound used for insonifying the medium with an ultrasonic wave (Figure 8.1(d)). An annular optical fiber is placed around the outer ring of the annular array to enable optical illumination needed for PA imaging (Figure 8.1(c)). The ultrasound detectors (two rings in Figure 8.1(b)) are used to record the PA and US waves. Three main factors should be considered when designing the ultrasound array: 1) The amplitude of the US and PA waves are lower than that generated with commercial ultrasound probes. Therefore, a high sensitivity to provide good enough signal-to-noise ratio is required. ASICs will be used to amplify the recorded signal right after the PvDF. 2) The PA waves are quite broad banded (depending on the absorber size) and the laser-induced ultrasound will generate frequencies in the range of 1-15 MHz; the spectrum of the PA wave depends on the absorber size. PVdF is used as the piezo-electric material to address this concern. 3) The ultrasound detector should be sensitive to on-axis direction. A two-ring annular could address this concern.

8.2.2. ACOUSTIC STACK

Figure 8.2(a) shows the acoustic stack of the annular array. Readers should rotate this schematic around the y axis (vertical direction) for 360 degree to see the model which matches with practice. The ASICs (one for each ring) are placed on the back side of the PCB (Figure 8.2(b)). PvDF films will be glued on the PCB, with a good connection to the arc gold bonds shown in Figure 8.2(c). Copper traces are used to transfer the signal recorded by the PvDF films to the ASICs. The ASICs amplify the signal and finally, co-axial cables (one for each ASIC) give the user access to the amplified signals. Either a thin layer of gold (modeled with a thickness of 1 μm) or sputtering (modeled as a gold layer with a thickness of 300 nm) can be used as the ground of the two rings. The silicone layer in the

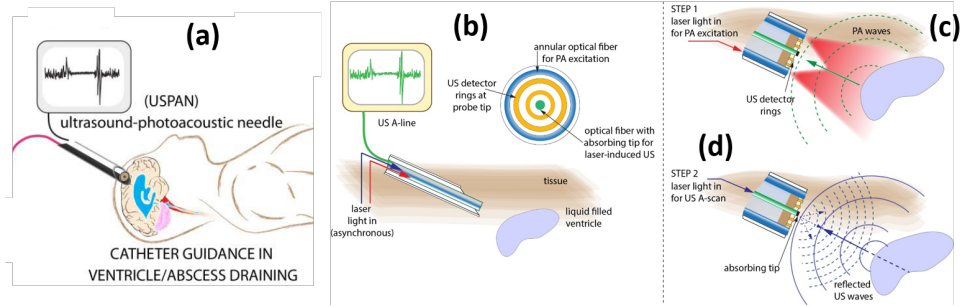


Figure 8.1: (a) The conceptual usage of the proposed needle. (b) The schematic of the two-ring array, the annular optical fiber and the optical fiber used for laser-induced ultrasound. A schematic showing the applicability of the proposed needle for (c) photoacoustic and (d) ultrasound imaging.

front side is used to make the whole design water proof. Water was used as the medium in which the generated acoustic pressure propagates. The inner and outer radius of the rings were selected such that an equal surface area (corresponding to an equal sensitivity) is obtained. The inner radius of the small ring was selected such that the optical fiber (used for the laser-induced ultrasound) could fit in the hole in the middle of the annular array; the diameter of the fiber at the time of designing this model was about $700\text{ }\mu\text{m}$. $45\text{ }\mu\text{m}$ spacing between the two rings was due to lowering the cross talk effect. In practice and from manufacturing point of view, the inner and outer radius of the PCB and the PVDF material can be the same. The electrode shading technique was used to electrically separate the two rings [299]. This technique also helps with the suppression of lateral mode vibrations (discussed in section 8.3).

8

8.2.3. NUMERICAL STUDY

To acoustically analyze the model shown in Figure 8.2(a), finite element simulations were performed in PZFlex. The properties of the materials used in the model are provided in Table 8.1. A PCB with a thickness of $50\text{ }\mu\text{m}$ and then an absorbing boundary condition was modeled for simplicity. In practice, the PCB thickness can be about $500\text{ }\mu\text{m}$ and then an attenuating layer (with an acoustic impedance equal to the PCB) should be used to prevent reflection of the acoustic wave from the back side of the PCB. To quantify the cross talk between the two rings, the small ring was excited and the generated pressure field on the surface of the big ring. To quantify the directivity pattern, each ring was excited separately, and then extrapolation toolbox in PZFlex was used to capture the acoustic pressure in far field along a certain radius. Finally, the peak-to-peak amplitude was reported for different angles.

k-Wave Matlab toolbox was used to mimic photoacoustic imaging with raster scanning the annular array in the y direction (see Figure 8.2(d)) and FWHM evaluation [124]. One point absorber was placed in the medium, and the generated pressure wave was recorded with all the grids in the plane $x=0$. Then, the acoustic pressure was used to synthetically assemble the acoustic pressure recorded by the rings, at different azimuthal locations. The

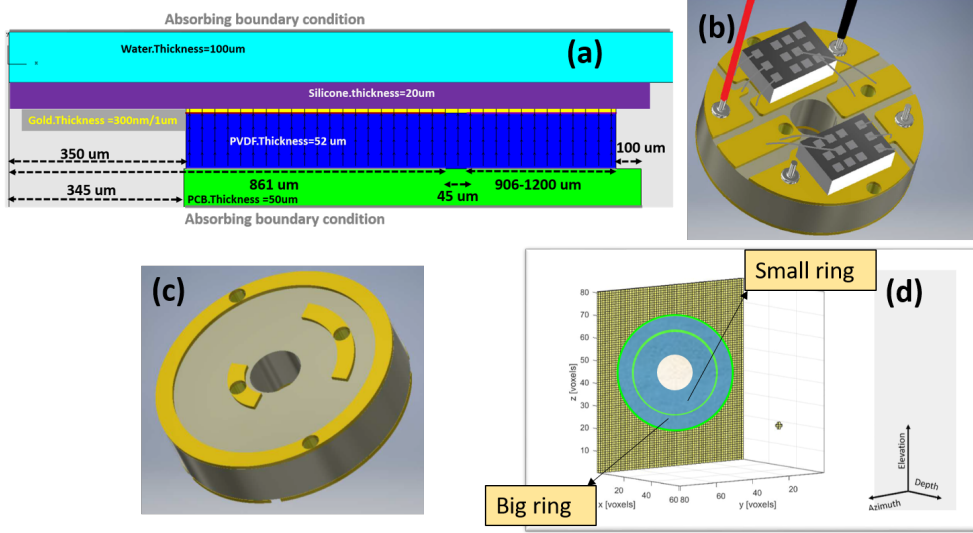


Figure 8.2: (a) The model used for simulation in PZFlex. Readers should rotate this schematic around the y axis (vertical direction) for 360 degree to see the model which matches with practice. The (b) back and (c) front side of the PCB. (d) The model used for simulation in k-Wave.

speed of sound in the medium was 1500 m/s. The grid size was 10 μm . The receive transfer function (obtained by the PZFlex simulator) was used to filter the synthetically assembled signals and then used to form the images.

Table 8.1: The properties of the materials used in PZFlex simulator.

Material	Properties
PvDF	$\rho = 1780$, $c_{11} = c_{22} = 9\text{e}9$, $c_{12} = 6\text{e}9$ Pa $c_{13} = c_{23} = 6.5\text{e}9$, $c_{33} = 8.3\text{e}9$ Pa $c_{44} = c_{55} = 2\text{e}9$, $c_{66} = 1.5\text{e}9$ Pa
PCB	$\rho = 1850$, $c_p = 3602$, $c_s = 2396$ attenuation = 3 dB/cm/MHz
Gold	$\rho = 19700$, $c_p = 3240$, $c_s = 1200$ attenuation = 1 dB/cm/MHz
RTV silicone	$\rho = 1294$, $c_p = 1022$, $c_s = 125$ attenuation = 1 dB/cm/MHz

8.2.4. EXPERIMENTAL STUDY

A photo of the imaging needle sample (INS) is presented in Figure 8.3(a). The sample consist of a single PvDF ring transducer. The experimental setup is presented in Figure 8.3(b).

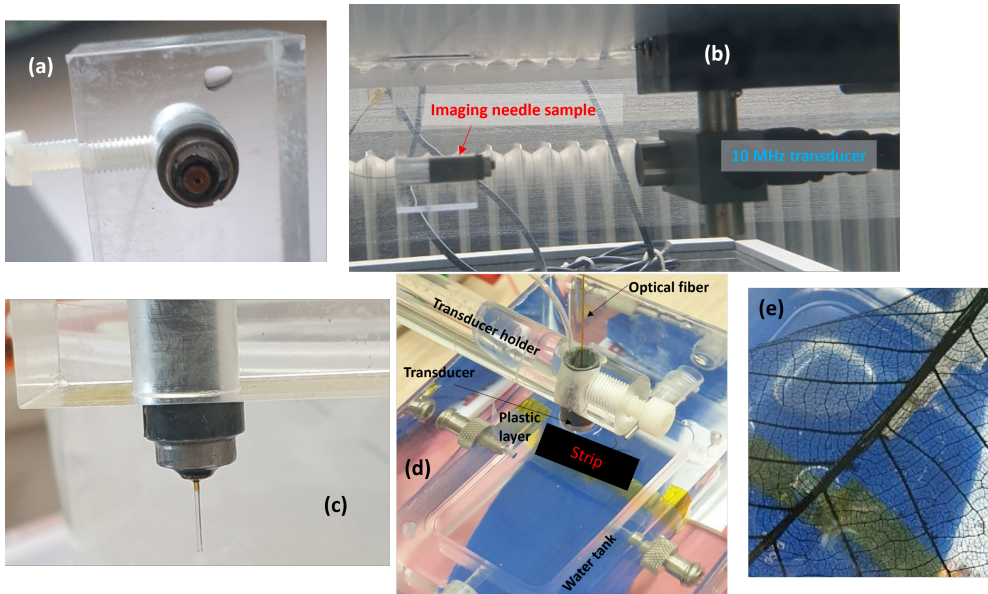


Figure 8.3: (a) A photo of the imaging needle sample consisting of one ring PVDf transducer. (b) The experimental setup for acoustic characterization. (c) The imaging needle sample with an optical fiber placed into the hole. (d) The experimental setup used for making a 2D image out of a black strip with a thickness of about 7 mm. (e) The leaf phantom.

A 10-MHz ultrasound single element transducer was used for exciting a 4-cycle sinusoidal wave at a central frequency of 10 MHz with a peak-to-peak voltage of 1 V. The acoustic pressure was recorded with a 1 mm-diameter hydrophone to measure the pressure at the position of the hydrophone.

A pulse-shape wavefront with a width of 10 ns was transmitted using the 10 MHz transducer and the 1 mm hydrophone was used to receive. This measurement was carried out to calculate the sensitivity of the transmitter (10 MHz) in different frequencies. Then, the hydrophone was replaced with the INS to measure the central frequency and bandwidth of the INS.

To measure the dynamic range of the INS, the input voltage applied to the transmitter was varied from 0.009 V to 10 V to insonify 4 cycles of sinusoidal wave at 7.5 MHz in the medium. No averaging was used in the receive.

Next, an optical fiber was placed in the hole, which enables photoacoustic imaging (Figure 8.3(c)). The wavelength of the laser was 1700 nm. The cladding of the fiber was extended about 1 cm after the core material. A black 200 μm diameter absorber was placed in front of the INS.

Finally, an experiment was made using the INS, a black strip, small water tank and an X-Y system to conduct raster scanning in 1 direction and make a 2D image by either stacking the detected A-lines next to each other or delay-and-sum beamforming. The strip was positioned on a plastic layer (see Figure 8.3(d)). The transducer holder was connected to

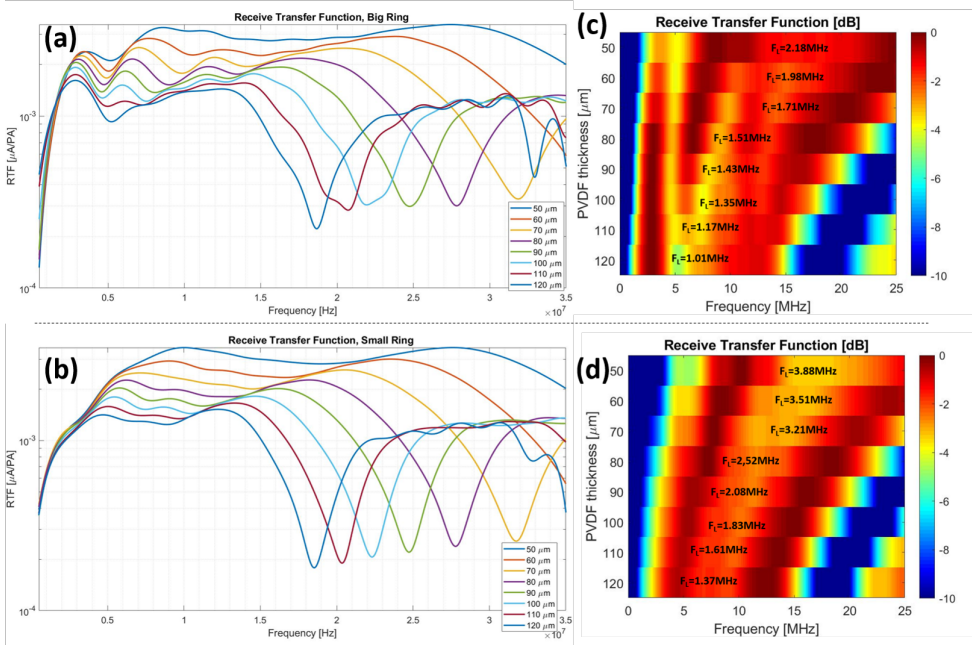


Figure 8.4: The receive transfer function (RTF) of the (a) big and (b) small rings for different PVDf thickness. (c) and (d) are the dB scaled version of (a) and (b), respectively.

the X-Y system. The scanning step and number of steps were 0.2 mm and 100, respectively.

8.3. RESULTS

8.3.1. NUMERICAL ACOUSTIC CHARACTERIZATION

The effects of the thickness of the PVDf layer on the receive transfer function (RTF) is presented in Figure 8.4(a, b) [300], [301]. For both the rings, the sensitivity to higher frequencies increases as the PVDf thickness decreases. The local peak around 3 MHz in the RTF of the big ring (see Figure 8.4) is due to the lateral mode vibration of the ring. This effects is not seen in the RTF of the small ring. This is because of the larger width of the small ring (considering the same surface area, a smaller inner/outer radius allows larger width), compared to the big ring, which allows piston-like vibration. Figure 8.4(c, d) shows the dB scaled version of the RTFs and the lower cut-off frequency.

Considering the needed bandwidth (up to 15 MHz) and Figure 8.4(c, d), one could select a thickness of 100-120 μm as this thickness range satisfies the high cut-off needed for our application and provides better coverage in lower frequencies compared to a thinner PVDf layer. In lower frequencies, however, Figure 8.4(a, b) indicate that a thinner PVDf layer provides higher sensitivity; in other words, looking just at the dB scaled RTF might be mis-leading. Looking at the website of the company which provides PVDf material to our group, a thickness of 52 μm was selected.

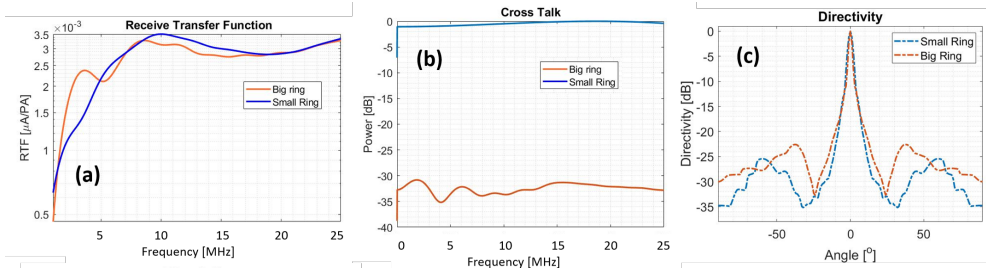


Figure 8.5: (a) The RTF, and (c) directivity pattern. (b) The cross talk between the rings when the small ring was excited, and the acoustic pressure was measured on the surface of the big ring.

We evaluated the effects of the thickness of the silicone and gold layer (results are not presented): The RTF slightly changes with changing the gold layer from 300 nm to 1 μm . The highest bandwidth is also obtained with a 20 μm -thick silicone layer. Figure 8.5(a) shows the finalized RTF of the small and big rings. The cross talk between the rings is -33 dB in average, which is good enough for clinical applications. The big ring has a narrower mainlobe at -6 dB (see Figure 8.5(c)) due to its larger inner and outer radius, compared to the small ring. This also justifies the higher sidelobes of the big ring. Figure 8.5(d) shows the acoustic pressure recorded on axis of each ring transducer.

8.3.2. RASTER SCANNING AND IMAGING

Figure 8.6 shows the received A-line when the absorber is right on the axis of the rings. As the inner/outer radius of the small ring is smaller than the big ring, the PA wavefront approaches the small ring earlier. This is why the small ring detects the absorber at lower depths, compared to the big ring. Both rings detect the absorber with a shift compared to its actual location (compare with the ground truth A-line in Figure 8.6). This is due to the phase shift caused by the inner/outer radius of the rings.

The main advantage of an annular array is enabling beamforming and increasing the on-axis sensitivity. After compensating the phase shift (i.e., applying proper delays to the A-line received by each ring), the A-lines become in phase and fairly match with the ground truth graph (see Figure 8.6).

Putting all the A-lines next to each other allows forming an image. Figure 8.7(a) and (b) are the formed images using the uncorrected and corrected (phase shift compensated) A-lines, respectively. The absorber is located at its correct location in the corrected image. The max amplitude of the point spread function is higher and the level of sidelobes are lower (see the red arrow in Figure 8.7(a) and (b) and Figure 8.8 for dB scaled images) in the corrected image. The lateral full-width-half-maximum is slightly improved when the phase shift is corrected. The axial FWHM is the same for both the images.

8.3.3. EXPERIMENTAL ACOUSTIC CHARACTERIZATION

The recorded signal using the hydrophone is shown in the Figure 8.9(a). The maximum amplitude is 2.3 mV. The datasheet of the hydrophone states that the sensitivity of the hy-

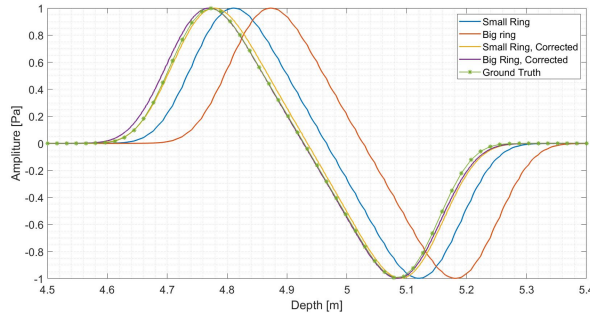


Figure 8.6: The A-lines detected by each ring before and after phase shift compensation.

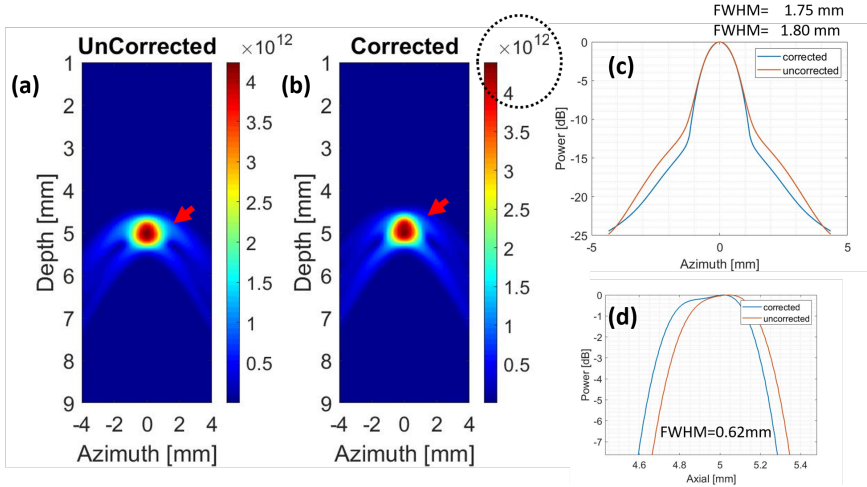


Figure 8.7: The formed images using the (a) uncorrected and (b) corrected A-lines. The (c) lateral and (d) axial full-width-half-maximum.

drophone at 10 MHz is 464 mV/MPa. This means that the acoustic pressure at the location of the hydrophone was 4.95 KPa.

Figure 8.9(b) shows the transmitted waveform by the 10 MHz transducer when a short pulse is excited. At -20 dB the upper and lower limits of the frequency response are 17.6 MHz and 2.1 MHz, respectively.

The received wavefront by the imaging needle sample (INS) when the 10 MHz transducer excites a pulse with a width of 10 ns is shown in Figure 8.9(c). After correcting for the lower sensitivity of the transmitter in lower and higher frequencies than 10 MHz, Figure 8.9(d) shows the corrected frequency response of the INS. At -10 dB, the high cut-off frequency is 16 MHz.

The dynamic range of the INS is presented in Figure 8.10. The red-dashed line represents the noise floor (3.7 mV which is corresponding to 18 Pa). Due to visualization of strange effects when the INS was inserted into a water tank and a low voltage was em-

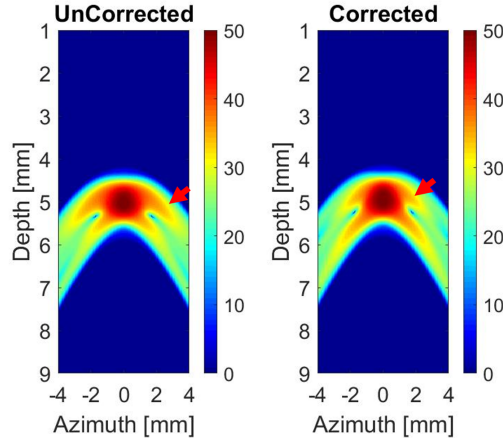


Figure 8.8: The dB scale of the uncorrected and corrected images (corresponding to Figure 8.7 (a) and (b)).

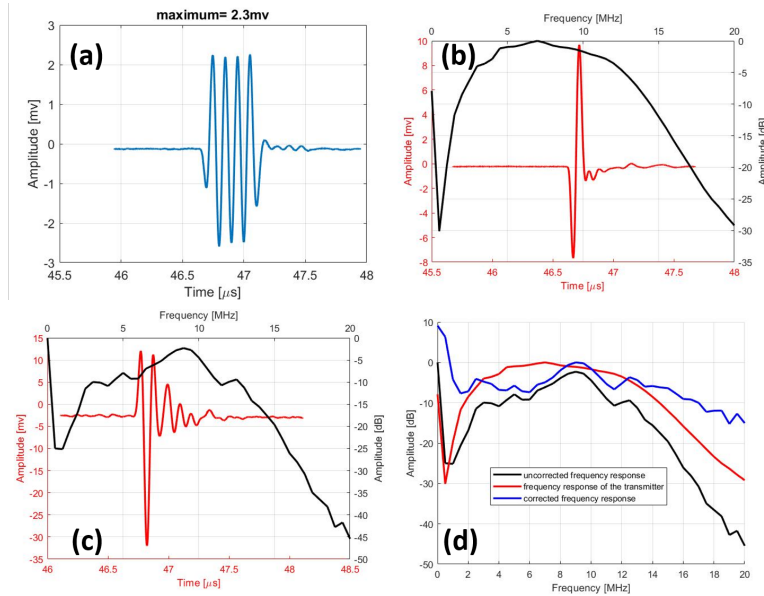


Figure 8.9: (a) The recorded signal by a 1 mm hydrophone when the transducer excites a 4-cycle sinusoidal wave with a peak-to-peak voltage of 1 V. (b) The time and frequency response of the 10 MHz transducer. (c) The uncorrected time and frequency response of the imaging needle sample (INS). (d) The corrected frequency response of the INS.

played in transmit, we were not able to measure the noise floor with our dynamic range measurement. Instead, the INS was kept in air and the recorded signal (the electronic

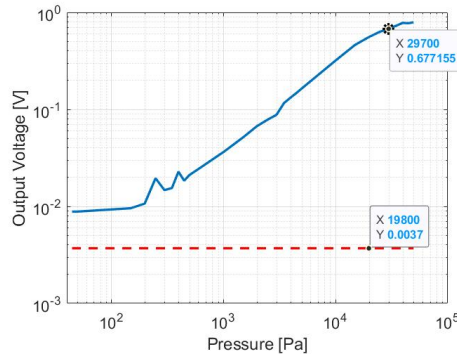


Figure 8.10: Measured output voltage (peak to peak) of the INS as a function of the transmitted pressure (peak to peak), illustrating the dynamic range of the INS; results were obtained using a 4-cycle sinusoidal pulse at 7.5 MHz.

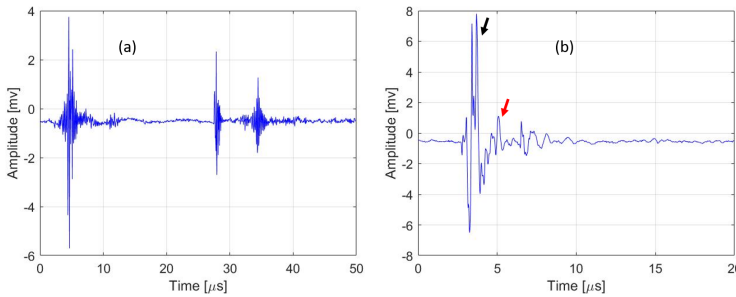


Figure 8.11: The A-line recorded (a) without and (b) with an absorber placed in front of the INS.

noise) was considered as the noise floor. The black star also indicates where the recorded signals start to clip.

8.3.4. EXPERIMENTAL PHOTOACOUSTIC IMAGING

The results of our photoacoustic measurements are presented in Figure 8.11. In Figure 8.11(a), the first peak is corresponding to the wave generated at the tip of the cladding of the optical fiber (as a results of absorption by the cladding and water) and is detected by the INS; this wavefront is referred to direct wave here. The second peak is corresponding to the reflection of the direct wave from the bottom of the small water tank that was used for the experiments. The third peak is corresponding to the multiple reflection of the direct wave between the INS surface and the bottom of the water tank.

The black arrow in Figure 8.11(b) indicates the direct wave discussed above. The red arrow indicates the wavefront generated as a result of interaction of the laser beam with the absorber placed in front of the INS. After about The thickness of the strip was

The 2D photoacoustic images generated with stacking A-lines next to each other and

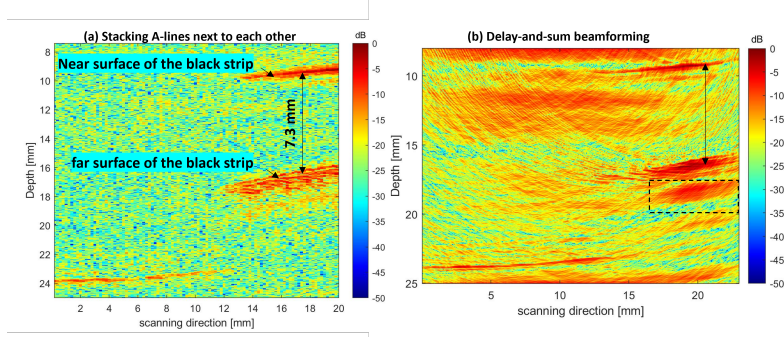


Figure 8.12: The photoacoustic image (a) generated by stacking the A-lines next to each other and (b) delay-and-sum beamforming.

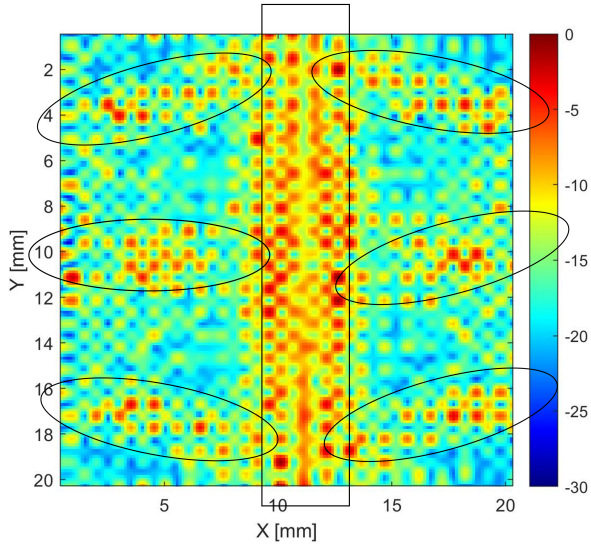


Figure 8.13: The photoacoustic image generated by stacking the A-lines next to each other.

delay-and-sum beamforming are presented in Figure 8.12. Figure 8.12(b) provides more structural information since the detected waves were properly back-projected to the pixels of the image. The PA wave representing the near and far surfaces of the strip are detected in both the images. The thickness of the strip measured by the images matches with the actual thickness. While the reflection from the plastic layer at the bottom of the strip was barely detectable in Figure 8.12(a), it is well-detected in Figure 8.12(b) (see the black-dashed box).

The maximum intensity projection of the image reconstructed using the leaf dataset is presented in Figure 8.13. The structures seen in the image is similar to the leaf phantom. The noise-like artifact in the image is due to the scanning strategy and laser triggering.

8.4. DISCUSSION AND CONCLUSION

In this chapter, we reported on the design and evaluation of an imaging needle, which can be used for endoscopic third ventriculostomy and brain abscess draining. The lateral mode vibration affects the receive transfer function of the big ring by a local peak around 3.5 MHz. As the width of the ring increases, the local peak moves to lower frequencies and fades (like the small ring). Our results indicate that beamforming using the A-lines recorded by the two rings with the mentioned inner/outer radius slightly improves the lateral FWHM and sidelobes. The improvements were minor due to the size of the rings which were determined based on the diameter of the optical fiber used for laser induced ultrasound and the inner radius of the surgical needle. If more space was available, the width of the rings could be larger and then beamforming would be much more helpful as the phase shift between the rings would be significant.

9

CONCLUSION AND RECOMMENDATIONS

9.1. CONCLUSION

Transcranial ultrasound imaging (TUI) is a promising diagnostic modality with applications such as diagnosis of stroke, prevention of stroke in children (between an age of 2 and 16) with sickle cell disease, and vasospasm detection after subarachnoid hemorrhage. It is still hindered by the low image quality caused by the strong phase aberration and multiple scattering caused by the skull, and mode conversion.

In this thesis, four chapters were dedicated to TUI. First, we developed a dual-probe setup to minimize reverberation artifacts caused by strong scatterers (i.e. needles). In this setup, we imaged the medium from two opposite directions, and the final image can be the minimum intensity projection of the inherently co-registered images of the opposed probes. The limitation of this study was that the higher sound speed in the aberrator was considered during image formation, but not the refraction. The proposed image formation method and the dual-probe setup can be used e.g. to monitor deep brain stimulation procedures and localization of the electrode(s) deep inside the brain from two temporal bones on the sides of the human skull.

In our next study, we developed a technique to correct the refraction caused by the temporal bone in single-sided two-dimensional transcranial ultrasound imaging using a commercial probe. The novelty of our approach lies in the fact that it corrects for the true position and the true geometry of the bone layer. This means that the tilt and the distance between the temporal bone and the probe are taken into account, and the outer and inner surfaces of the temporal bone are described as nonplanar and nonparallel surfaces. Moreover, our approach estimates the wave speed in the bone layer prior to imaging, all with a single ultrasound array transducer (CT/MR scans are not needed). As a result, delay-and-sum image reconstruction provides improved image quality because the travel times through the layered medium are accurately calculated at each image pixel.

To enable real time refraction-corrected TUI, we also introduced a novel two-point ray

tracing method, based on Fermat's principle, which enabled fast calculation of the travel times in the presence of a layered aberrator in front of the ultrasound probe. The ray tracing method along with the reconstruction technique were implemented on a graphical processing unite (GPU). In our GPU implementation, the travel-times calculated by the ray-tracing kernel in the first two times are stored in the global memory. This strategy made it possible to reduce the combinational search from NIP^3 (NIP is the number of intermediate points (IPs) used to describe each of the three interfaces) travel-times to $3 \times NIP$ for each pixel in the brain.

Finally, we compared the phase screen (PS) aberration correction technique to a geometry-based (GB) phase aberration correction technique when an ultrafast imaging sequence (5 plane waves tilted from -15 to +15 degrees in the cutaneous tissue layer) was used for data acquisition with a single 1D transducer. Our study suggests that GB aberration correction outperforms the PS method. The PS technique was strongly affected by speckle noise caused by a heterogeneous brain tissue model and failed to reveal many scatterers in the reconstructed image, while the GB method detected nearly all the scatterers.

Next, we evaluated the effects of receive/transmit parameters on the image quality provided by a linear array in which elements are mutually interconnected, which mimics the elevation direction of our prototype 2D matrix transducer. The parameter selection procedure was based on the effective covered aperture size, level of grating lobes, and resolution/sidelobes. The proposed imaging sequence consisted of a full-aperture transmission (all 80 elements), receive aperture size of 5, and aperture shifting distance of 3 elements. In addition, our results showed that an angular weighting technique can suppress the effects of grating lobes.

We proposed a multi-angle detection approach in which the transducer used for data acquisition rotates around its center (with specific angles) as well as around the scanning center. The angles were calculated based on the central frequency and diameter of the transducer and the radius of the region-of-interest. The numerical and experimental results showed that the proposed approach mimics a directional point-like transducer with a large angular view and provides a location-independent tangential resolution. The proposed approach could replace the conventional detection geometry due to structural simplicity and low processing complexity.

In the last chapter of this thesis, we reported on the design and evaluation of an imaging needle, which can be used for endoscopic third ventriculostomy (to reduce the intracranial pressure) and brain abscess draining. An annular array consisting of two rings was designed to narrow down the directivity of the array using beamforming. The inner and outer radius of the rings were chosen such that they have the same surface area (sensitivity). The results showed that that one ring works as good as two rings considering the space available for the ring transducer(s).

9.2. RECOMMENDATIONS FOR FURTHER RESEARCH

9.2.1. TRANSCRANIAL ULTRASOUND IMAGING

While the cortical bone of the temporal region of the skull is known to exhibit anisotropic wavespeed, the wavespeed in the bone layer was assumed isotropic to simplify ray-tracing

and therefore enable the fastest frame rate with our approach. Further development of the ray-tracing approach is needed to correct the effect of wave speed anisotropy of the cortical bone.

In addition, the temporal bone was described as a homogeneous layer of cortical bone in this thesis. In elderly people, the temporal bone can have tri-layer structure, two cortical bone layers separated with a layer of highly porous trabecular bone (diploe). Our reconstruction approach would likely not perform well if the temporal bone contains cancellous bone (diploe) between two cortical bone layers. Development of a reconstruction technique counting in the three-layer temporal bone is needed to address this limitation.

Our ray-tracing kernel calculates the travel-time of all the pixels in parallel. However, finding the shortest travel-time between a pixel and an array element through IPs is implemented sequentially with a for-loop in GPU. This kernel can be improved by re-defining the kernel architecture in a way that it evaluates all the travel-times (through the IPs) in parallel. Another option is to implement it on CPU with parallel programming (such as OpenMP).

Currently, the bidirectional head-wave technique is limited to a locally flat bone surface. Further developments are needed to tackle estimating the wave-speed on a locally curved bone surface.

The focus of this thesis was on phase aberration correction. Another factor that highly degrades the transcranial ultrasound images is multiple scattering caused by human skull. Second harmonic imaging could mitigate the effects of the multiple scattering as the pressure of the transmitted second harmonic wave in shallow depths (where the skull is placed) is negligible.

In the end, the translation of the proposed image formation approach to a matrix array transducer where the local 3D position and shape of the skull can be described would be very helpful and needed for using TUI in a wider range of applications.

9.2.2. MULTI-ANGLE DATA ACQUISITION FOR PACT SYSTEMS

Currently, the transducer is rotated around its center so that the data corresponding to each central angle could be detected. This is time consuming and not user friendly in practice. To address this issue, a probe holder can be designed so that 5 transducers could fit in. This reduces the data acquisition time by five times.

In the end, the method should be used for pre-clinical small animal photoacoustic imaging to further evaluate its limitations and advantages.

9.2.3. IMAGING NEEDLES

Using one ring instead of two could partly lower the challenges. After manufacturing the ring transducer and acoustic characterization, it should be integrated with a laser induced ultrasound and optical fibers (used for PA imaging) and then be evaluated with phantom experiments.

In the case of using an annular array, a disk and an outer ring can be used instead of two rings. The tip of the optical fiber used for laser induced ultrasound could end right behind the disk. This results in a wider outer ring, which mitigates the lateral mode vibration.

BIBLIOGRAPHY

- [1] P. R. Hoskins, K. Martin, and A. Thrush, *Diagnostic ultrasound: physics and equipment*. CRC Press, 2019.
- [2] *How do ultrasound examinations work?* [Online]. Available: <https://www.informedhealth.org/how-do-ultrasound-examinations-work.html>.
- [3] N De Jong, N Bom, J Souquet, and G Faber, "Vibration modes, matching layers and grating lobes," *Ultrasonics*, vol. 23, no. 4, pp. 176–182, 1985.
- [4] *A review of conventional beam characteristics*. [Online]. Available: <https://www.olympus-ims.com/en/ndt-tutorials/transducers/characteristics/#:~:text=Near%20field%20distance%20N%20represents,expands%20and%20its%20energy%20dissipates..>
- [5] H. Azhari, *Basics of biomedical ultrasound for engineers*. John Wiley & Sons, 2010.
- [6] J. C. Somer, "The history of real time ultrasound," in *International Congress Series*, Elsevier, vol. 1274, 2004, pp. 3–13.
- [7] R. T. Brisson, R. d. S. A. Santos, L. H. S. S. Stefano, *et al.*, "Association between tomographic characteristics of the temporal bone and transtemporal window quality on transcranial color doppler ultrasound in patients with stroke or transient ischemic attack," *Ultrasound in Medicine & Biology*, vol. 47, no. 3, pp. 511–516, 2021.
- [8] C.-H. Lee, S.-H. Jeon, S.-J. Wang, B.-S. Shin, and H. G. Kang, "Factors associated with temporal window failure in transcranial doppler sonography," *Neurological Sciences*, vol. 41, no. 11, pp. 3293–3299, 2020.
- [9] J. Peterson and P. C. Dechow, "Material properties of the human cranial vault and zygoma," *The Anatomical Record Part A: Discoveries in Molecular, Cellular, and Evolutionary Biology: An Official Publication of the American Association of Anatomists*, vol. 274, no. 1, pp. 785–797, 2003.
- [10] J.-H. Kwon, J. S. Kim, D.-W. Kang, K.-S. Bae, and S. U. Kwon, "The thickness and texture of temporal bone in brain ct predict acoustic window failure of transcranial doppler," *Journal of Neuroimaging*, vol. 16, no. 4, pp. 347–352, 2006.
- [11] F. J. Fry and J. E. Barger, "Acoustical properties of the human skull," *The Journal of the Acoustical Society of America*, vol. 63, no. 5, pp. 1576–1590, 1978.
- [12] F. Vignon, J. Aubry, M. Tanter, A. Margoum, and M. Fink, "Adaptive focusing for transcranial ultrasound imaging using dual arrays," *The Journal of the Acoustical Society of America*, vol. 120, no. 5, pp. 2737–2745, 2006.
- [13] G. Pinton, J.-F. Aubry, E. Bossy, M. Muller, M. Pernot, and M. Tanter, "Attenuation, scattering, and absorption of ultrasound in the skull bone," *Medical physics*, vol. 39, no. 1, pp. 299–307, 2012.

- [14] H. White and B. Venkatesh, "Applications of transcranial doppler in the icu: A review," *Intensive care medicine*, vol. 32, no. 7, pp. 981–994, 2006.
- [15] T. Hölscher, F. Schlachetzki, M. Zimmermann, *et al.*, "Transcranial ultrasound from diagnosis to early stroke treatment," *Cerebrovascular diseases*, vol. 26, no. 6, pp. 659–663, 2008.
- [16] F. Schlachetzki, M. Herzberg, T. Hölscher, *et al.*, "Transcranial ultrasound from diagnosis to early stroke treatment—part 2: Prehospital neurosonography in patients with acute stroke—the regensburg stroke mobile project," *Cerebrovascular diseases*, vol. 33, no. 3, pp. 262–271, 2012.
- [17] T. Holscher, "Prehospital use of portable ultrasound for stroke diagnosis and treatment initiation," *Air Rescue*, vol. 2, pp. 48–50, 2012.
- [18] D. Antipova, L. Eadie, S. Makin, H. Shannon, P. Wilson, and A. Macaden, "The use of transcranial ultrasound and clinical assessment to diagnose ischaemic stroke due to large vessel occlusion in remote and rural areas," *Plos one*, vol. 15, no. 10, e0239653, 2020.
- [19] M. Herzberg, S. Boy, T. Hölscher, *et al.*, "Prehospital stroke diagnostics based on neurological examination and transcranial ultrasound," *Critical ultrasound journal*, vol. 6, no. 1, pp. 1–13, 2014.
- [20] R. J. Adams, "Tcd in sickle cell disease: An important and useful test," *Pediatric radiology*, vol. 35, no. 3, pp. 229–234, 2005.
- [21] O. P. S. P. in Sickle Cell Anemia (STOP 2) Trial Investigators, "Discontinuing prophylactic transfusions used to prevent stroke in sickle cell disease," *New England Journal of Medicine*, vol. 353, no. 26, pp. 2769–2778, 2005.
- [22] R. J. Adams, V. C. McKie, L. Hsu, *et al.*, "Prevention of a first stroke by transfusions in children with sickle cell anemia and abnormal results on transcranial doppler ultrasonography," *New England Journal of Medicine*, vol. 339, no. 1, pp. 5–11, 1998.
- [23] R. J. Adams, F. T. Nichols, R. Figueroa, V. McKie, and T. Lott, "Transcranial doppler correlation with cerebral angiography in sickle cell disease," *Stroke*, vol. 23, no. 8, pp. 1073–1077, 1992.
- [24] D. W. Newell, S. M. Grady, J. M. Eskridge, and R. H. Winn, "Distribution of angiographic vasospasm after subarachnoid hemorrhage: Implications for diagnosis by transcranial doppler ultrasonography," *Neurosurgery*, vol. 27, no. 4, pp. 574–577, 1990.
- [25] Y. Y. Vora, M. Suarez-Almazor, D. E. Steinke, M. L. Martin, and J. M. Findlay, "Role of transcranial doppler monitoring in the diagnosis of cerebral vasospasm after subarachnoid hemorrhage," *Neurosurgery*, vol. 44, no. 6, pp. 1237–1248, 1999.
- [26] 2021 review: Transcranial doppler ultrasound imaging, 2022. [Online]. Available: <https://www.itnonline.com/article/2021-review-transcranial-doppler-ultrasound-imaging>.
- [27] V. L. Babikian, E. Feldmann, L. R. Wechsler, *et al.*, "Transcranial doppler ultrasonography: Year 2000 update," *Journal of Neuroimaging*, vol. 10, no. 2, pp. 101–115, 2000.

- [28] M. A. O'Reilly, R. M. Jones, and K. Hynynen, "Three-dimensional transcranial ultrasound imaging of microbubble clouds using a sparse hemispherical array," *IEEE Transactions on Biomedical Engineering*, vol. 61, no. 4, pp. 1285–1294, 2014.
- [29] R. Kern, F. Perren, S. Kreisel, K. Szabo, M. Hennerici, and S. Meairs, "Multiplanar transcranial ultrasound imaging: Standards, landmarks and correlation with magnetic resonance imaging," *Ultrasound in medicine & biology*, vol. 31, no. 3, pp. 311–315, 2005.
- [30] M. Tanter, M. Pernot, J.-F. Aubry, G. Montaldo, F. Marquet, and M. Fink, "Compensating for bone interfaces and respiratory motion in high-intensity focused ultrasound," *International Journal of Hyperthermia*, vol. 23, no. 2, pp. 141–151, 2007.
- [31] J. Sun and K. Hynynen, "Focusing of therapeutic ultrasound through a human skull: A numerical study," *The Journal of the Acoustical Society of America*, vol. 104, no. 3, pp. 1705–1715, 1998.
- [32] K. J. Haworth, J. B. Fowlkes, P. L. Carson, and O. D. Kripfgans, "Towards aberration correction of transcranial ultrasound using acoustic droplet vaporization," *Ultrasound in medicine & biology*, vol. 34, no. 3, pp. 435–445, 2008.
- [33] N. M. Ivancevich, G. F. Pinton, H. A. Nicoletto, E. Bennett, D. T. Laskowitz, and S. W. Smith, "Real-time 3-d contrast-enhanced transcranial ultrasound and aberration correction," *Ultrasound in medicine & biology*, vol. 34, no. 9, pp. 1387–1395, 2008.
- [34] G. Clement and K. Hynynen, "Correlation of ultrasound phase with physical skull properties," *Ultrasound in medicine & biology*, vol. 28, no. 5, pp. 617–624, 2002.
- [35] K. Meyer-Wiethe, F. Sallustio, and R. Kern, "Diagnosis of intracerebral hemorrhage with transcranial ultrasound," *Cerebrovascular Diseases*, vol. 27, no. Suppl. 2, pp. 40–47, 2009.
- [36] J.-F. Synnevag, A. Austeng, and S. Holm, "Benefits of minimum-variance beamforming in medical ultrasound imaging," *IEEE transactions on ultrasonics, ferroelectrics, and frequency control*, vol. 56, no. 9, pp. 1868–1879, 2009.
- [37] M. Mozaffarzadeh, A. Mahloojifar, V. Periyasamy, M. Pramanik, and M. Orooji, "Eigenspace-based minimum variance combined with delay multiply and sum beamformer: Application to linear-array photoacoustic imaging," *IEEE Journal of Selected Topics in Quantum Electronics*, vol. 25, no. 1, pp. 1–8, 2018.
- [38] I. K. Holfort, F. Gran, and J. A. Jensen, "Broadband minimum variance beamforming for ultrasound imaging," *IEEE transactions on ultrasonics, ferroelectrics, and frequency control*, vol. 56, no. 2, pp. 314–325, 2009.
- [39] M. Mozaffarzadeh, M. Sadeghi, A. Mahloojifar, and M. Orooji, "Double-stage delay multiply and sum beamforming algorithm applied to ultrasound medical imaging," *Ultrasound in medicine & biology*, vol. 44, no. 3, pp. 677–686, 2018.
- [40] M. Mozaffarzadeh, A. Mahloojifar, M. Orooji, S. Adabi, and M. Nasirivanaki, "Double-stage delay multiply and sum beamforming algorithm: Application to linear-array photoacoustic imaging," *IEEE Transactions on Biomedical Engineering*, vol. 65, no. 1, pp. 31–42, 2017.

- [41] A. Kyriakou, E. Neufeld, B. Werner, M. M. Paulides, G. Szekely, and N. Kuster, "A review of numerical and experimental compensation techniques for skull-induced phase aberrations in transcranial focused ultrasound," *International journal of hyperthermia*, vol. 30, no. 1, pp. 36–46, 2014.
- [42] S. Flax and M. O'Donnell, "Phase-aberration correction using signals from point reflectors and diffuse scatterers: Basic principles," *IEEE transactions on ultrasonics, ferroelectrics, and frequency control*, vol. 35, no. 6, pp. 758–767, 1988.
- [43] C. A. Carrascal, S. Aristizabal, J. F. Greenleaf, and M. W. Urban, "Phase aberration and attenuation effects on acoustic radiation force-based shear wave generation," *IEEE transactions on ultrasonics, ferroelectrics, and frequency control*, vol. 63, no. 2, pp. 222–232, 2016.
- [44] G. T. Clement and K. Hynynen, "A non-invasive method for focusing ultrasound through the human skull," *Physics in Medicine & Biology*, vol. 47, no. 8, p. 1219, 2002.
- [45] F. Marquet, M. Pernot, J.-F. Aubry, *et al.*, "Non-invasive transcranial ultrasound therapy based on a 3d ct scan: Protocol validation and in vitro results," *Physics in Medicine & Biology*, vol. 54, no. 9, p. 2597, 2009.
- [46] J.-F. Aubry, M. Tanter, M. Pernot, J.-L. Thomas, and M. Fink, "Experimental demonstration of noninvasive transskull adaptive focusing based on prior computed tomography scans," *The Journal of the Acoustical Society of America*, vol. 113, no. 1, pp. 84–93, 2003.
- [47] X. Yin and K. Hynynen, "A numerical study of transcranial focused ultrasound beam propagation at low frequency," *Physics in Medicine & Biology*, vol. 50, no. 8, p. 1821, 2005.
- [48] J. Gâteau, L. Marsac, M. Pernot, J.-F. Aubry, M. Tanter, and M. Fink, "Transcranial ultrasonic therapy based on time reversal of acoustically induced cavitation bubble signature," *IEEE Transactions on Biomedical Engineering*, vol. 57, no. 1, pp. 134–144, 2009.
- [49] J. Sadler, K. Shapoori, E. Malyarenko, F. Severin, and R. G. Maev, "Locating an acoustic point source scattered by a skull phantom via time reversal matched filtering," *The Journal of the Acoustical Society of America*, vol. 128, no. 4, pp. 1812–1822, 2010.
- [50] M. Fink, G. Montaldo, and M. Tanter, "Time-reversal acoustics in biomedical engineering," *Annual review of biomedical engineering*, vol. 5, no. 1, pp. 465–497, 2003.
- [51] P. Renzel, *Method for determining the sound velocity in a basic material, particularly for measuring the thickness of a wall*, US Patent 7,415,880, 2008.
- [52] B. D. Lindsey, E. D. Light, H. A. Nicoletto, E. R. Bennett, D. T. Laskowitz, and S. W. Smith, "The ultrasound brain helmet: New transducers and volume registration for in vivo simultaneous multi-transducer 3-d transcranial imaging," *IEEE transactions on ultrasonics, ferroelectrics, and frequency control*, vol. 58, no. 6, pp. 1189–1202, 2011.

- [53] S. W. Smith, N. M. Ivancevich, B. D. Lindsey, *et al.*, "The ultrasound brain helmet: Feasibility study of multiple simultaneous 3d scans of cerebral vasculature," *Ultrasound in medicine & biology*, vol. 35, no. 2, pp. 329–338, 2009.
- [54] B. D. Lindsey, H. A. Nicoletto, E. R. Bennett, D. T. Laskowitz, and S. W. Smith, "Simultaneous bilateral real-time 3-d transcranial ultrasound imaging at 1 mhz through poor acoustic windows," *Ultrasound in medicine & biology*, vol. 39, no. 4, pp. 721–734, 2013.
- [55] B. D. Lindsey and S. W. Smith, "Refraction correction in 3d transcranial ultrasound imaging," *Ultrasonic imaging*, vol. 36, no. 1, pp. 35–54, 2014.
- [56] B. D. Lindsey, N. M. Ivancevich, E. D. Light, *et al.*, "The ultrasound brain helmet for 3d transcranial doppler imaging," in *2009 IEEE International Ultrasonics Symposium*, IEEE, 2009, pp. 1395–1398.
- [57] M. Hong, Z. Su, Y. Lu, H. Sohn, and X. Qing, "Locating fatigue damage using temporal signal features of nonlinear lamb waves," *Mechanical Systems and Signal Processing*, vol. 60, pp. 182–197, 2015.
- [58] N. Ryden, C. B. Park, P. Ulriksen, and R. D. Miller, "Lamb wave analysis for non-destructive testing of concrete plate structures," in *16th EEGS Symposium on the Application of Geophysics to Engineering and Environmental Problems*, European Association of Geoscientists & Engineers, 2003, cp–190.
- [59] R. S. C. Cobbold, *Foundations of Biomedical Ultrasound*. Oxford university press, 2006.
- [60] S. H. Tretbar, P. K. Plinkert, and P. A. Federspil, "Accuracy of ultrasound measurements for skull bone thickness using coded signals," *IEEE Transactions on Biomedical Engineering*, vol. 56, no. 3, pp. 733–740, 2009.
- [61] P. Bocchini, A. Marzani, and E. Viola, "Graphical user interface for guided acoustic waves," *Journal of Computing in Civil Engineering*, vol. 25, no. 3, pp. 202–210, 2011.
- [62] H. A. Afifi, "Ultrasonic pulse echo studies of the physical properties of pmma, ps, and pvc," *Polymer-Plastics Technology and Engineering*, vol. 42, no. 2, pp. 193–205, 2003.
- [63] J. R. Asay and A. H. Guenther, "Experimental determination of ultrasonic wave velocities in plastics as functions of temperature. iv. shear velocities in common plastics," *Journal of Applied Polymer Science*, vol. 11, no. 7, pp. 1087–1100, 1967.
- [64] J. Carlson, J. Van Deventer, A. Scolan, and C. Carlander, "Frequency and temperature dependence of acoustic properties of polymers used in pulse-echo systems," in *IEEE Symposium on Ultrasonics*, 2003, IEEE, vol. 1, 2003, pp. 885–888.
- [65] J. Huang, J. K. Triedman, N. V. Vasilyev, Y. Suematsu, R. O. Cleveland, and P. E. Dupont, "Imaging artifacts of medical instruments in ultrasound-guided interventions," *Journal of Ultrasound in Medicine*, vol. 26, no. 10, pp. 1303–1322, 2007.
- [66] G Reusz, P Sarkany, J Gal, and A Csomos, "Needle-related ultrasound artifacts and their importance in anaesthetic practice," *British journal of anaesthesia*, vol. 112, no. 5, pp. 794–802, 2014.

- [67] F. Alonso, D. Vogel, J. Johansson, K. Wårdell, and S. Hemm, "Electric field comparison between microelectrode recording and deep brain stimulation systems—a simulation study," *Brain Sciences*, vol. 8, no. 2, 2018, ISSN: 2076-3425.
- [68] Z. Su and M. Hong, "Nonlinear ultrasonics for health monitoring of aerospace structures using active sparse sensor networks," in *Structural Health Monitoring (SHM) in Aerospace Structures*, Elsevier, 2016, pp. 353–392.
- [69] P. Khalili and P. Cawley, "Excitation of single-mode lamb waves at high-frequency-thickness products," *IEEE transactions on ultrasonics, ferroelectrics, and frequency control*, vol. 63, no. 2, pp. 303–312, 2015.
- [70] M. Mozaffarzadeh, C. Minonzio, M. D. Verweij, S. Hemm, and V. Daeichin, "Phase aberration correction in transcranial ultrasound imaging using averaged sound velocity map in delay-and-sum beamformer," in *2019 IEEE International Ultrasonics Symposium (IUS)*, IEEE, 2019, pp. 1894–1897.
- [71] S. R. Miri Rostami, M. Mozaffarzadeh, M. Ghaffari-Miab, A. Hariri, and J. Jokerst, "Gpu-accelerated double-stage delay-multiply-and-sum algorithm for fast photoacoustic tomography using led excitation and linear arrays," *Ultrasonic imaging*, vol. 41, no. 5, pp. 301–316, 2019.
- [72] M. Mozaffarzadeh, C. Minonzio, N. De Jong, M. D. Verweij, S. Hemm, and V. Daeichin, "Lamb waves and adaptive beamforming for aberration correction in medical ultrasound imaging," *IEEE transactions on ultrasonics, ferroelectrics, and frequency control*, vol. 68, no. 1, pp. 84–91, 2020.
- [73] E. Bossy, M. Talmant, and P. Laugier, "Three-dimensional simulations of ultrasonic axial transmission velocity measurement on cortical bone models," *The Journal of the Acoustical Society of America*, vol. 115, no. 5, pp. 2314–2324, 2004.
- [74] E. Bossy, M. Talmant, and P. Laugier, "Effect of bone cortical thickness on velocity measurements using ultrasonic axial transmission: A 2d simulation study," *The Journal of the Acoustical Society of America*, vol. 112, no. 1, pp. 297–307, 2002.
- [75] E. Bossy, M. Talmant, M. Defontaine, F. Patat, and P. Laugier, "Bidirectional axial transmission can improve accuracy and precision of ultrasonic velocity measurement in cortical bone: A validation on test materials," *IEEE transactions on ultrasonics, ferroelectrics, and frequency control*, vol. 51, no. 1, pp. 71–79, 2004.
- [76] E. Camus, M. Talmant, G. Berger, and P. Laugier, "Analysis of the axial transmission technique for the assessment of skeletal status," *The Journal of the Acoustical Society of America*, vol. 108, no. 6, pp. 3058–3065, 2000.
- [77] G. Renaud, P. Kruizinga, D. Cassereau, and P. Laugier, "In vivo ultrasound imaging of the bone cortex," *Physics in Medicine & Biology*, vol. 63, no. 12, p. 125 010, 2018.
- [78] D. C. Tong and G. W. Albers, "Transcranial doppler-detected microemboli in patients with acute stroke," *Stroke*, vol. 26, no. 9, pp. 1588–1592, 1995.
- [79] T. Padayachee, S. Parsons, R. Theobald, J. Linley, R. Gosling, and P. Deverall, "The detection of microemboli in the middle cerebral artery during cardiopulmonary bypass: A transcranial doppler ultrasound investigation using membrane and bubble oxygenators," *The Annals of thoracic surgery*, vol. 44, no. 3, pp. 298–302, 1987.

- [80] M. T. Graham, J. Huang, F. X. Creighton, and M. A. L. Bell, "Simulations and human cadaver head studies to identify optimal acoustic receiver locations for minimally invasive photoacoustic-guided neurosurgery," *Photoacoustics*, vol. 19, p. 100 183, 2020.
- [81] M. A. L. Bell, A. K. Ostrowski, K. Li, P. Kazanzides, and E. M. Boctor, "Localization of transcranial targets for photoacoustic-guided endonasal surgeries," *Photoacoustics*, vol. 3, no. 2, pp. 78–87, 2015.
- [82] M. A. L. Bell, A. K. Ostrowski, P. Kazanzides, and E. Boctor, "Feasibility of transcranial photoacoustic imaging for interventional guidance of endonasal surgeries," in *Photons Plus Ultrasound: Imaging and Sensing 2014*, SPIE, vol. 8943, 2014, pp. 36–42.
- [83] C. Demene, J. Robin, A. Dizeux, *et al.*, "Transcranial ultrafast ultrasound localization microscopy of brain vasculature in patients," *Nature biomedical engineering*, vol. 5, no. 3, pp. 219–228, 2021.
- [84] C. Errico, J. Pierre, S. Pezet, *et al.*, "Ultrafast ultrasound localization microscopy for deep super-resolution vascular imaging," *Nature*, vol. 527, no. 7579, pp. 499–502, 2015.
- [85] D. E. Soulioti, D. Espíndola, P. A. Dayton, and G. F. Pinton, "Super-resolution imaging through the human skull," *IEEE transactions on ultrasonics, ferroelectrics, and frequency control*, vol. 67, no. 1, pp. 25–36, 2019.
- [86] E. Tiran, J. Ferrier, T. Defieux, *et al.*, "Transcranial functional ultrasound imaging in freely moving awake mice and anesthetized young rats without contrast agent," *Ultrasound in medicine & biology*, vol. 43, no. 8, pp. 1679–1689, 2017.
- [87] J. Baranger, C. Demene, A. Frerot, *et al.*, "Bedside functional monitoring of the dynamic brain connectivity in human neonates," *Nature communications*, vol. 12, no. 1, pp. 1–10, 2021.
- [88] M. Wiesmann and G. Seidel, "Ultrasound perfusion imaging of the human brain," *Stroke*, vol. 31, no. 10, pp. 2421–2425, 2000.
- [89] J. D. Kirsch, M. Mathur, M. H. Johnson, G. Gowthaman, and L. M. Scoutt, "Advances in transcranial doppler us: Imaging ahead," *Radiographics*, vol. 33, no. 1, E1–E14, 2013.
- [90] V. I. Lau, A. Jaidka, K. Wiskar, *et al.*, "Better with ultrasound: Transcranial doppler," *Chest*, vol. 157, no. 1, pp. 142–150, 2020.
- [91] L. Saba and E. Raz, *Neurovascular imaging: from basics to advanced concepts*. Springer, 2016.
- [92] F. Vignon, W. T. Shi, X. Yin, T. Hoelscher, and J. E. Powers, "The stripe artifact in transcranial ultrasound imaging," *Journal of Ultrasound in Medicine*, vol. 29, no. 12, pp. 1779–1786, 2010.
- [93] A. Y. Ammi, T. D. Mast, I.-H. Huang, *et al.*, "Characterization of ultrasound propagation through ex-vivo human temporal bone," *Ultrasound in medicine & biology*, vol. 34, no. 10, pp. 1578–1589, 2008.

- [94] Z. Kardos, C. Oláh, M. Sepsí, *et al.*, "Increased frequency of temporal acoustic window failure in rheumatoid arthritis: A manifestation of altered bone metabolism?" *Clinical rheumatology*, vol. 37, no. 5, pp. 1183–1188, 2018.
- [95] G. Gahn, J. Gerber, S. Hallmeyer, *et al.*, "Contrast-enhanced transcranial color-coded duplexsonography in stroke patients with limited bone windows," *American journal of neuroradiology*, vol. 21, no. 3, pp. 509–514, 2000.
- [96] G. Seidel and S. Meairs, "Ultrasound contrast agents in ischemic stroke," *Cerebrovascular Diseases*, vol. 27, no. Suppl. 2, pp. 25–39, 2009.
- [97] S. Smith, G. Trahey, and O. Von Ramm, "Phased array ultrasound imaging through planar tissue layers," *Ultrasound in medicine & biology*, vol. 12, no. 3, pp. 229–243, 1986.
- [98] S. Smith, O. Von Ramm, J. Kisslo, and F. Thurstone, "Real time ultrasound tomography of the adult brain.," *Stroke*, vol. 9, no. 2, pp. 117–122, 1978.
- [99] J. J. Dahl, M. S. Soo, and G. E. Trahey, "Spatial and temporal aberrator stability for real-time adaptive imaging," *IEEE transactions on ultrasonics, ferroelectrics, and frequency control*, vol. 52, no. 9, pp. 1504–1517, 2005.
- [100] S. Baikov, A. Molotilov, and V. Svet, "Physical and technological aspects of ultrasonic imaging of brain structures through thick skull bones: 1. theoretical and model studies," *Acoustical Physics*, vol. 49, no. 3, pp. 276–284, 2003.
- [101] S. Baikov, L. Babin, A. Molotilov, *et al.*, "Physical and technical aspects of ultrasonic brain imaging through thick skull bones: 2. experimental studies," *Acoustical Physics*, vol. 49, no. 4, pp. 389–395, 2003.
- [102] N. M. Ivancevich, J. J. Dahl, and S. W. Smith, "Comparison of 3-d multi-lag cross-correlation and speckle brightness aberration correction algorithms on static and moving targets," *IEEE transactions on ultrasonics, ferroelectrics, and frequency control*, vol. 56, no. 10, pp. 2157–2166, 2009.
- [103] N. M. Ivancevich, J. J. Dahl, G. E. Trahey, and S. W. Smith, "Phase-aberration correction with a 3-d ultrasound scanner: Feasibility study," *IEEE transactions on ultrasonics, ferroelectrics, and frequency control*, vol. 53, no. 8, pp. 1432–1439, 2006.
- [104] F. Vignon, J. Aubry, M. Tanter, A. Margoum, M. Fink, and J. Lecoœur, "Dual-arrays brain imaging prototype: Experimental in vitro results," in *IEEE International Ultrasonics Symposium*, vol. 1, 2005, pp. 504–507.
- [105] B. D. Lindsey, H. A. Nicoletto, E. R. Bennett, D. T. Laskowitz, and S. W. Smith, "3-d transcranial ultrasound imaging with bilateral phase aberration correction of multiple isoplanatic patches: A pilot human study with microbubble contrast enhancement," *Ultrasound in medicine & biology*, vol. 40, no. 1, pp. 90–101, 2014.
- [106] B. D. Lindsey and S. W. Smith, "Pitch-catch phase aberration correction for 3d ultrasound brain helmet," in *2011 IEEE International Ultrasonics Symposium*, IEEE, 2011, pp. 2456–2459.

- [107] K. Shapoori, J. Sadler, A. Wydra, E. V. Malyarenko, A. N. Sinclair, and R. G. Maev, "An ultrasonic-adaptive beamforming method and its application for trans-skull imaging of certain types of head injuries; part i: Transmission mode," *IEEE Transactions on Biomedical Engineering*, vol. 62, no. 5, pp. 1253–1264, 2014.
- [108] X. Lin, M. Sun, Y. Liu, Z. Shen, Y. Shen, and N. Feng, "Variable speed of sound compensation in the linear-array photoacoustic tomography using a multi-stencils fast marching method," *Biomedical Signal Processing and Control*, vol. 44, pp. 67–74, 2018.
- [109] T. Wang and Y. Jing, "Transcranial ultrasound imaging with speed of sound-based phase correction: A numerical study," *Physics in Medicine & Biology*, vol. 58, no. 19, p. 6663, 2013.
- [110] C. Jiang, Y. Li, K. Xu, and D. Ta, "Full-matrix phase shift migration method for transcranial ultrasonic imaging," *IEEE Transactions on Ultrasonics, Ferroelectrics, and Frequency Control*, vol. 68, no. 1, pp. 72–83, 2020.
- [111] G. Bouchoux, K. B. Bader, J. J. Korfhagen, *et al.*, "Experimental validation of a finite-difference model for the prediction of transcranial ultrasound fields based on ct images," *Physics in Medicine & Biology*, vol. 57, no. 23, p. 8005, 2012.
- [112] Y. Jing, F. C. Meral, and G. T. Clement, "Time-reversal transcranial ultrasound beam focusing using a k-space method," *Physics in Medicine & Biology*, vol. 57, no. 4, p. 901, 2012.
- [113] C. Jiang, Y. Li, B. Li, *et al.*, "Ray theory-based transcranial phase correction for intracranial imaging: A phantom study," *IEEE Access*, vol. 7, pp. 163 013–163 021, 2019.
- [114] J. A. Jensen, S. I. Nikolov, K. L. Gammelmark, and M. H. Pedersen, "Synthetic aperture ultrasound imaging," *Ultrasonics*, vol. 44, e5–e15, 2006.
- [115] M. S. Hassouna and A. A. Farag, "Multistencils fast marching methods: A highly accurate solution to the eikonal equation on cartesian domains," *IEEE transactions on pattern analysis and machine intelligence*, vol. 29, no. 9, pp. 1563–1574, 2007.
- [116] J. A. Sethian, *Level set methods and fast marching methods: evolving interfaces in computational geometry, fluid mechanics, computer vision, and materials science*. Cambridge university press, 1999, vol. 3.
- [117] D. Alleyne and P. Cawley, "A two-dimensional fourier transform method for the measurement of propagating multimode signals," *The Journal of the Acoustical Society of America*, vol. 89, no. 3, pp. 1159–1168, 1991.
- [118] H. Hasegawa and H. Kanai, "Effect of element directivity on adaptive beamforming applied to high-frame-rate ultrasound," *IEEE transactions on ultrasonics, ferroelectrics, and frequency control*, vol. 62, no. 3, pp. 511–523, 2015.
- [119] M. Mozaffarzadeh, M. Soozande, F. Fool, *et al.*, "Receive/transmit aperture selection for 3d ultrasound imaging with a 2d matrix transducer," *Applied Sciences*, vol. 10, no. 15, p. 5300, 2020.

- [120] J Shepherd, G. Renaud, P Clouzet, and K van Wijk, "Photoacoustic imaging through a cortical bone replica with anisotropic elasticity," *Applied Physics Letters*, vol. 116, no. 24, p. 243 704, 2020.
- [121] G. Renaud, J. L. Johnson, and D. Cassereau, "Real-time kirchhoff migration for ultrasound imaging of the bone cortex," in *SEG Technical Program Expanded Abstracts 2018*, Society of Exploration Geophysicists, 2018, pp. 4797–4801.
- [122] D. Hong, "Medical image segmentation based on accelerated dijkstra algorithm," in *Advances in Intelligent Systems*, Springer, 2012, pp. 341–348.
- [123] E. W. Dijkstra *et al.*, "A note on two problems in connexion with graphs," *Numerische mathematik*, vol. 1, no. 1, pp. 269–271, 1959.
- [124] B. E. Treeby and B. T. Cox, "K-wave: Matlab toolbox for the simulation and reconstruction of photoacoustic wave fields," *Journal of biomedical optics*, vol. 15, no. 2, p. 021 314, 2010.
- [125] J. Aarnio, G. T. Clement, and K. Hynynen, "A new ultrasound method for determining the acoustic phase shifts caused by the skull bone," *Ultrasound in medicine and biology*, vol. 31, no. 6, pp. 771–780, 2005.
- [126] H. N. Minh, J. Du, and K. Raum, "Estimation of thickness and speed of sound in cortical bone using multifocus pulse-echo ultrasound," *IEEE transactions on ultrasonics, ferroelectrics, and frequency control*, vol. 67, no. 3, pp. 568–579, 2019.
- [127] A Wydra, E Malyarenko, K Shapoori, and R. G. Maev, "Development of a practical ultrasonic approach for simultaneous measurement of the thickness and the sound speed in human skull bones: A laboratory phantom study," *Physics in Medicine and Biology*, vol. 58, no. 4, p. 1083, 2013.
- [128] J. Karjalainen, O. Riekkinen, J. Toyras, H. Kroger, and J. Jurvelin, "Ultrasonic assessment of cortical bone thickness in vitro and in vivo," *IEEE transactions on ultrasonics, ferroelectrics, and frequency control*, vol. 55, no. 10, pp. 2191–2197, 2008.
- [129] T. Postert, J. Federlein, H. Przuntek, and T. Büttner, "Insufficient and absent acoustic temporal bone window: Potential and limitations of transcranial contrast-enhanced color-coded sonography and contrast-enhanced power-based sonography," *Ultrasound in medicine & biology*, vol. 23, no. 6, pp. 857–862, 1997.
- [130] G. Renaud, P. Clouzet, D. Cassereau, and M. Talmant, "Measuring anisotropy of elastic wave velocity with ultrasound imaging and an autofocus method: Application to cortical bone," *Physics in Medicine & Biology*, vol. 65, no. 23, p. 235 016, 2020.
- [131] L. Deng, A. Hughes, and K. Hynynen, "A noninvasive ultrasound resonance method for detecting skull induced phase shifts may provide a signal for adaptive focusing," *IEEE Transactions on Biomedical Engineering*, vol. 67, no. 9, pp. 2628–2637, 2020.
- [132] G. T. Clement, P. J. White, and K Hynynen, "Enhanced ultrasound transmission through the human skull using shear mode conversion," *The Journal of the Acoustical Society of America*, vol. 115, no. 3, pp. 1356–1364, 2004.

- [133] B. Lucht, A. Hubbell, and K. Hynynen, "Contrast-enhanced transcranial two-dimensional ultrasound imaging using shear-mode conversion at low frequency," *Ultrasound in Medicine & Biology*, vol. 39, no. 2, pp. 332–344, 2013.
- [134] P. J. White, G. T. Clement, and K. Hynynen, "Longitudinal and shear mode ultrasound propagation in human skull bone," *Ultrasound in medicine & biology*, vol. 32, no. 7, pp. 1085–1096, 2006.
- [135] A. Yousefi, D. E. Goertz, and K. Hynynen, "Transcranial shear-mode ultrasound: Assessment of imaging performance and excitation techniques," *IEEE transactions on medical imaging*, vol. 28, no. 5, pp. 763–774, 2009.
- [136] R. M. Jones, Y. Huang, Y. Meng, *et al.*, "Echo-focusing in transcranial focused ultrasound thalamotomy for essential tremor: A feasibility study," *Movement Disorders*, vol. 35, no. 12, pp. 2327–2333, 2020.
- [137] M. A. O'Reilly and K. Hynynen, "A super-resolution ultrasound method for brain vascular mapping," *Medical physics*, vol. 40, no. 11, p. 110 701, 2013.
- [138] F. Vignon, W. T. Shi, M. R. Burcher, and J. E. Powers, "Determination of temporal bone isoplanatic patch sizes for transcranial phase aberration correction," in *2008 IEEE Ultrasonics Symposium*, IEEE, 2008, pp. 1286–1289.
- [139] K. A. Wear, "Autocorrelation and cepstral methods for measurement of tibial cortical thickness," *IEEE transactions on ultrasonics, ferroelectrics, and frequency control*, vol. 50, no. 6, pp. 655–660, 2003.
- [140] B. Martin and J. H. McElhaney, "The acoustic properties of human skull bone," *Journal of biomedical materials research*, vol. 5, no. 4, pp. 325–333, 1971.
- [141] B. E. Treeby, T. K. Varshet, E. Z. Zhang, J. G. Laufer, and P. C. Beard, "Automatic sound speed selection in photoacoustic image reconstruction using an autofocus approach," *Journal of biomedical optics*, vol. 16, no. 9, p. 090 501, 2011.
- [142] G. Lowet and G. Van der Perre, "Ultrasound velocity measurement in long bones: Measurement method and simulation of ultrasound wave propagation," *Journal of biomechanics*, vol. 29, no. 10, pp. 1255–1262, 1996.
- [143] I. Lerche, "On the reflection of acoustic waves from a slightly curved interface," *The Journal of the Acoustical Society of America*, vol. 81, no. 3, pp. 611–618, 1987.
- [144] M. A. Lediju, G. E. Trahey, B. C. Byram, and J. J. Dahl, "Short-lag spatial coherence of backscattered echoes: Imaging characteristics," *IEEE transactions on ultrasonics, ferroelectrics, and frequency control*, vol. 58, no. 7, pp. 1377–1388, 2011.
- [145] M. Mozaffarzadeh, A. Mahloojifar, M. Orooji, K. Kratkiewicz, S. Adabi, and M. Nasirivanaki, "Linear-array photoacoustic imaging using minimum variance-based delay multiply and sum adaptive beamforming algorithm," *Journal of biomedical optics*, vol. 23, no. 2, p. 026 002, 2018.
- [146] F. Vignon, J.-F. Aubry, A. Saez, *et al.*, "The stokes relations linking time reversal and the inverse filter," *The Journal of the Acoustical Society of America*, vol. 119, no. 3, pp. 1335–1346, 2006.

- [147] G. Matrone, A. S. Savoia, G. Caliano, and G. Magenes, "The delay multiply and sum beamforming algorithm in ultrasound b-mode medical imaging," *IEEE transactions on medical imaging*, vol. 34, no. 4, pp. 940–949, 2014.
- [148] G. Matrone, A. S. Savoia, G. Caliano, and G. Magenes, "Ultrasound synthetic aperture focusing with the delay multiply and sum beamforming algorithm," in *2015 37th Annual International Conference of the IEEE Engineering in Medicine and Biology Society (EMBC)*, IEEE, 2015, pp. 137–140.
- [149] J. Kang, D. Go, I. Song, and Y. Yoo, "Ultrafast power doppler imaging using frame-multiply-and-sum-based nonlinear compounding," *IEEE Transactions on Ultrasonics, Ferroelectrics, and Frequency Control*, vol. 68, no. 3, pp. 453–464, 2020.
- [150] B. Y. Yiu, I. K. Tsang, and C. Alfred, "Gpu-based beamformer: Fast realization of plane wave compounding and synthetic aperture imaging," *IEEE transactions on ultrasonics, ferroelectrics, and frequency control*, vol. 58, no. 8, pp. 1698–1705, 2011.
- [151] D. Hyun, G. E. Trahey, and J. J. Dahl, "In vivo demonstration of a real-time simultaneous b-mode/spatial coherence gpu-based beamformer," in *2013 IEEE International Ultrasonics Symposium (IUS)*, IEEE, 2013, pp. 1280–1283.
- [152] E. A. Gonzalez and M. A. L. Bell, "Gpu implementation of photoacoustic short-lag spatial coherence imaging for improved image-guided interventions," *Journal of Biomedical Optics*, vol. 25, no. 7, p. 077 002, 2020.
- [153] C. Robba and G. Citerio, *Echography and Doppler of the Brain*. Springer, 2021.
- [154] M. Mozaffarzadeh, E. Verschuur, M. D. Verweij, V. Daeichin, N. De Jong, and G. Renaud, "Refraction-corrected transcranial ultrasound imaging through the human temporal window using a single probe," *IEEE Transactions on Ultrasonics, Ferroelectrics, and Frequency Control*, vol. 69, no. 4, pp. 1191–1203, 2022.
- [155] D. Waltham, "Two-point ray tracing using fermat's principle," *Geophysical Journal International*, vol. 93, no. 3, pp. 575–582, 1988.
- [156] S. R. M. Rostami and M. Ghaffari-Miab, "Finite difference generated transient potentials of open-layered media by parallel computing using openmp, mpi, openacc, and cuda," *IEEE Transactions on Antennas and Propagation*, vol. 67, no. 10, pp. 6541–6550, 2019.
- [157] K.-S. Oh and K. Jung, "Gpu implementation of neural networks," *Pattern Recognition*, vol. 37, no. 6, pp. 1311–1314, 2004.
- [158] J. Krüger and R. Westermann, "Linear algebra operators for gpu implementation of numerical algorithms," in *ACM SIGGRAPH 2005 Courses*, 2005, 234–es.
- [159] H. So, J. Chen, B. Yiu, and A. Yu, "Medical ultrasound imaging: To gpu or not to gpu?" *IEEE micro*, vol. 31, no. 5, pp. 54–65, 2011.
- [160] J. Chen, B. Y. Yiu, H. K.-H. So, and C. Alfred, "Real-time gpu-based adaptive beamformer for high quality ultrasound imaging," in *2011 IEEE International Ultrasonics Symposium*, IEEE, 2011, pp. 474–477.

- [161] J. Chen, B. Y. Yiu, B. K. Hamilton, A. C. Yu, and H. K.-H. So, "Design space exploration of adaptive beamforming acceleration for bedside and portable medical ultrasound imaging," *ACM SIGARCH Computer Architecture News*, vol. 39, no. 4, pp. 20–25, 2011.
- [162] J. P. Asen, J. I. Buskenes, C.-I. C. Nilsen, A. Austeng, and S. Holm, "Implementing capon beamforming on a gpu for real-time cardiac ultrasound imaging," *IEEE transactions on ultrasonics, ferroelectrics, and frequency control*, vol. 61, no. 1, pp. 76–85, 2014.
- [163] B. Y. Yiu and C. Alfred, "Gpu-based minimum variance beamformer for synthetic aperture imaging of the eye," *Ultrasound in medicine & biology*, vol. 41, no. 3, pp. 871–883, 2015.
- [164] D. Hyun, G. E. Trahey, and J. Dahl, "A gpu-based real-time spatial coherence imaging system," in *Medical Imaging 2013: Ultrasonic Imaging, Tomography, and Therapy*, SPIE, vol. 8675, 2013, pp. 351–358.
- [165] E. Gonzalez, M. R. Gubbi, and M. A. L. Bell, "Gpu implementation of coherence-based photoacoustic beamforming for autonomous visual servoing," in *2019 IEEE International Ultrasonics Symposium (IUS)*, IEEE, 2019, pp. 24–27.
- [166] T. Stepinski, "An implementation of synthetic aperture focusing technique in frequency domain," *IEEE Transactions on Ultrasonics, Ferroelectrics, and Frequency Control*, vol. 54, no. 7, pp. 1399–1408, 2007. DOI: [10.1109/TUFFC.2007.400](https://doi.org/10.1109/TUFFC.2007.400).
- [167] T. Kjeldsen, L. Lassen, M. C. Hemmsen, *et al.*, "Synthetic aperture sequential beamforming implemented on multi-core platforms," in *2014 IEEE International Ultrasonics Symposium*, IEEE, 2014, pp. 2181–2184.
- [168] S. Jeon, E.-Y. Park, W. Choi, R. Managuli, K. jong Lee, and C. Kim, "Real-time delay-multiply-and-sum beamforming with coherence factor for in vivo clinical photoacoustic imaging of humans," *Photoacoustics*, vol. 15, p. 100 136, 2019.
- [169] J. W. Choe, A. Nikoozadeh, Ö. Oralkan, and B. T. Khuri-Yakub, "Gpu-based real-time volumetric ultrasound image reconstruction for a ring array," *IEEE Transactions on Medical Imaging*, vol. 32, no. 7, pp. 1258–1264, 2013.
- [170] J. Zhou, S. Wei, R. Sampson, *et al.*, "Low complexity 3d ultrasound imaging using synthetic aperture sequential beamforming," in *2016 IEEE International Workshop on Signal Processing Systems (SiPS)*, IEEE, 2016, pp. 33–38.
- [171] M. B. Stuart, P. M. Jensen, J. T. R. Olsen, *et al.*, "Real-time volumetric synthetic aperture software beamforming of row-column probe data," *IEEE Transactions on Ultrasonics, Ferroelectrics, and Frequency Control*, vol. 68, no. 8, pp. 2608–2618, 2021.
- [172] D. Hyun, Y. L. Li, I. Steinberg, M. Jakovljevic, T. Klap, and J. J. Dahl, "An open source gpu-based beamformer for real-time ultrasound imaging and applications," in *2019 IEEE International Ultrasonics Symposium (IUS)*, IEEE, 2019, pp. 20–23.
- [173] Y. Du, Y. Shen, B. Y. Yiu, C. Alfred, and L. Zhu, "High frame rate vector flow imaging: Development as a new diagnostic mode on a clinical scanner," in *2018 IEEE International Ultrasonics Symposium (IUS)*, IEEE, 2018, pp. 1–4.

- [174] J. A. Ketterling, O. Aristizábal, B. Yiu, *et al.*, “High-speed, high-frequency ultrasound, in utero vector-flow imaging of mouse embryos,” *Scientific reports*, vol. 7, no. 1, pp. 1–9, 2017.
- [175] B. Y. Yiu, S. S. Lai, and C. Alfred, “Vector projectile imaging: Time-resolved dynamic visualization of complex flow patterns,” *Ultrasound in medicine & biology*, vol. 40, no. 9, pp. 2295–2309, 2014.
- [176] T. Moser, “Shortest path calculation of seismic rays,” *Geophysics*, vol. 56, no. 1, pp. 59–67, 1991.
- [177] W. Qiu, A. Bouakaz, E. E. Konofagou, and H. Zheng, “Ultrasound for the brain: A review of physical and engineering principles, and clinical applications,” *IEEE Transactions on Ultrasonics, Ferroelectrics, and Frequency Control*, vol. 68, no. 1, pp. 6–20, 2020.
- [178] K. Ranganathan, M. K. Santy, T. N. Blalock, J. A. Hossack, and W. F. Walker, “Direct sampled i/q beamforming for compact and very low-cost ultrasound imaging,” *IEEE transactions on ultrasonics, ferroelectrics, and frequency control*, vol. 51, no. 9, pp. 1082–1094, 2004.
- [179] M. T. Graham, R. A. Dunne, and M. A. L. Bell, “Comparison of compressional and elastic wave simulations for patient-specific planning prior to transcranial photoacoustic-guided neurosurgery,” *Journal of Biomedical Optics*, vol. 26, no. 7, p. 076 006, 2021.
- [180] G. Pinton and G. Trahey, “Sources of image degradation in fundamental and harmonic ultrasound imaging,” in *2008 IEEE International Ultrasonics Symposium Abstract book*, 2008.
- [181] C. Dmené, T. Deffieux, M. Pernot, *et al.*, “Spatiotemporal clutter filtering of ultrafast ultrasound data highly increases doppler and fultrasound sensitivity,” *IEEE transactions on medical imaging*, vol. 34, no. 11, pp. 2271–2285, 2015.
- [182] P. Podvin and I. Lecomte, “Finite difference computation of traveltimes in very contrasted velocity models: A massively parallel approach and its associated tools,” *Geophysical Journal International*, vol. 105, no. 1, pp. 271–284, 1991.
- [183] E. Mace, G. Montaldo, B.-F. Osmanski, I. Cohen, M. Fink, and M. Tanter, “Functional ultrasound imaging of the brain: Theory and basic principles,” *IEEE transactions on ultrasonics, ferroelectrics, and frequency control*, vol. 60, no. 3, pp. 492–506, 2013.
- [184] H. Hasegawa and H. Kanai, “High-frame-rate echocardiography using diverging transmit beams and parallel receive beamforming,” *Journal of medical ultrasonics*, vol. 38, no. 3, pp. 129–140, 2011.
- [185] G. Montaldo, M. Tanter, J. Bercoff, N. Benech, and M. Fink, “Coherent plane-wave compounding for very high frame rate ultrasonography and transient elastography,” *IEEE transactions on ultrasonics, ferroelectrics, and frequency control*, vol. 56, no. 3, pp. 489–506, 2009.

- [186] M. Mozaffarzadeh, E. Verschuur, M. D. Verweij, N. De Jong, and G. Renaud, "Accelerated 2d real-time refraction-corrected transcranial ultrasound imaging," *IEEE Transactions on Ultrasonics, Ferroelectrics, and Frequency Control*, 2022.
- [187] G. Montaldo, M. Tanter, and M. Fink, "Time reversal of speckle noise," *Physical Review Letters*, vol. 106, no. 5, p. 054 301, 2011.
- [188] K. Rigby, C. Chalek, B. Haider, *et al.*, "Improved in vivo abdominal image quality using real-time estimation and correction of wavefront arrival time errors," in *2000 IEEE Ultrasonics Symposium. Proceedings. An International Symposium (Cat. No. 00CH37121)*, IEEE, vol. 2, 2000, pp. 1645–1653.
- [189] B. Jing and B. D. Lindsey, "Effect of skull porous trabecular structure on transcranial ultrasound imaging in the presence of elastic wave mode conversion at varying incidence angle," *Ultrasound in Medicine & Biology*, vol. 47, no. 9, pp. 2734–2748, 2021.
- [190] S. Chandrasekaran, B. B. Tripathi, D. Espindola, and G. F. Pinton, "Modeling ultrasound propagation in the moving brain: Applications to shear shock waves and traumatic brain injury," *IEEE Transactions on Ultrasonics, Ferroelectrics, and Frequency Control*, vol. 68, no. 1, pp. 201–212, 2020.
- [191] H. D. Moon and J. F. RINEHART, "Histogenesis of coronary arteriosclerosis," *Circulation*, vol. 6, no. 4, pp. 481–488, 1952.
- [192] S. Laurent, S. Katsahian, C. Fassot, *et al.*, "Aortic stiffness is an independent predictor of fatal stroke in essential hypertension," *Stroke*, vol. 34, no. 5, pp. 1203–1206, 2003.
- [193] S. Laurent, P. Boutouyrie, R. Asmar, *et al.*, "Aortic stiffness is an independent predictor of all-cause and cardiovascular mortality in hypertensive patients," *Hypertension*, vol. 37, no. 5, pp. 1236–1241, 2001.
- [194] K. Sutton-Tyrrell, S. S. Najjar, R. M. Boudreau, *et al.*, "Elevated aortic pulse wave velocity, a marker of arterial stiffness, predicts cardiovascular events in well-functioning older adults," *Circulation*, vol. 111, no. 25, pp. 3384–3390, 2005.
- [195] G. Mancia, G. De Backer, A. Dominiczak, *et al.*, "2007 esh-esc practice guidelines for the management of arterial hypertension: Esh-esc task force on the management of arterial hypertension," *Journal of hypertension*, vol. 25, no. 9, pp. 1751–1762, 2007.
- [196] M. Couade, M. Pernot, C. Prada, *et al.*, "Quantitative assessment of arterial wall biomechanical properties using shear wave imaging," *Ultrasound in medicine & biology*, vol. 36, no. 10, pp. 1662–1676, 2010.
- [197] K. V. Ramnarine, J. W. Garrard, K. Dexter, S. Nduwayo, R. B. Panerai, and T. G. Robinson, "Shear wave elastography assessment of carotid plaque stiffness: In vitro reproducibility study," *Ultrasound in medicine & biology*, vol. 40, no. 1, pp. 200–209, 2014.
- [198] J. Luo, R. X. Li, and E. E. Konofagou, "Pulse wave imaging of the human carotid artery: An in vivo feasibility study," *IEEE transactions on ultrasonics, ferroelectrics, and frequency control*, vol. 59, no. 1, pp. 174–181, 2012.

- [199] T. G. Brott, "2011 asa/accf/aha/aann/aans/acr/asnr/cns/saip/scai/sir/snis/svm/svs guidelines on the management of patients with extracranial carotid and vertebral artery disease: Executive summary," *J Am Coll Cardiol*, vol. 57, pp. 1002–1044, 2011.
- [200] J. Luo, K. Fujikura, L. S. Tyrie, M. D. Tilson, and E. E. Konofagou, "Pulse wave imaging of normal and aneurysmal abdominal aortas in vivo," *IEEE transactions on medical imaging*, vol. 28, no. 4, pp. 477–486, 2008.
- [201] J. Vappou, J. Luo, and E. E. Konofagou, "Pulse wave imaging for noninvasive and quantitative measurement of arterial stiffness in vivo," *American journal of hypertension*, vol. 23, no. 4, pp. 393–398, 2010.
- [202] J. Vappou, J. Luo, K. Okajima, M. Di Tullio, and E. Konofagou, "Aortic pulse wave velocity measured by pulse wave imaging (pwi): A comparison with applanation tonometry," *Artery research*, vol. 5, no. 2, pp. 65–71, 2011.
- [203] I.-Z. Apostolakis, P. Nauleau, C. Papadacci, M. D. McGarry, and E. E. Konofagou, "Feasibility and validation of 4-d pulse wave imaging in phantoms and in vivo," *IEEE transactions on ultrasonics, ferroelectrics, and frequency control*, vol. 64, no. 9, pp. 1305–1317, 2017.
- [204] H. Li, B. Chayer, M.-H. R. Cardinal, *et al.*, "Investigation of out-of-plane motion artifacts in 2d noninvasive vascular ultrasound elastography," *Physics in Medicine & Biology*, vol. 63, no. 24, p. 245 003, 2018.
- [205] A. Fenster, D. B. Downey, and H. N. Cardinal, "Three-dimensional ultrasound imaging," *Physics in medicine & biology*, vol. 46, no. 5, R67, 2001.
- [206] A. Harloff, "Carotid plaque hemodynamics," *Interventional neurology*, vol. 1, no. 1, pp. 44–54, 2012.
- [207] S. Holbek, M. J. Pihl, C. Ewertsen, M. B. Nielsen, and J. A. Jensen, "In vivo 3-d vector velocity estimation with continuous data," in *2015 IEEE International Ultrasonics Symposium (IUS)*, IEEE, 2015, pp. 1–4.
- [208] P. A. Picot, D. W. Rickey, R. Mitchell, R. N. Rankin, and A. Fenster, "Three-dimensional colour doppler imaging," *Ultrasound in medicine & biology*, vol. 19, no. 2, pp. 95–104, 1993.
- [209] D. B. Downey and A. Fenster, "Vascular imaging with a three-dimensional power doppler system.," *AJR. American journal of roentgenology*, vol. 165, no. 3, pp. 665–668, 1995.
- [210] Q. Huang and Z. Zeng, "A review on real-time 3d ultrasound imaging technology," *BioMed research international*, vol. 2017, 2017.
- [211] J. N. Welch, J. A. Johnson, M. R. Bax, R. Badr, and R. Shahidi, "A real-time freehand 3d ultrasound system for image-guided surgery," in *2000 IEEE Ultrasonics Symposium. Proceedings. An International Symposium (Cat. No. 00CH37121)*, IEEE, vol. 2, 2000, pp. 1601–1604.
- [212] H. Gao, Q. Huang, X. Xu, and X. Li, "Wireless and sensorless 3d ultrasound imaging," *Neurocomputing*, vol. 195, pp. 159–171, 2016.

- [213] M. Soozande, F. Fool, M. Shabanimotlagh, *et al.*, "Virtually extended array imaging improves lateral resolution in high frame rate volumetric imaging," in *2018 IEEE International Ultrasonics Symposium (IUS)*, IEEE, 2018, pp. 1–9.
- [214] T. L. Szabo, *Diagnostic ultrasound imaging: inside out*. Academic press, 2004.
- [215] K. Erikson, A. Hairston, A. Nicoli, J. Stockwell, and T. White, "A128 x128 (16k) ultrasonic transducer hybrid array," in *Acoustical Imaging*, Springer, 1997, pp. 485–494.
- [216] P. Santos, G. U. Haugen, L. Lovstakken, E. Samset, and J. Dhooge, "Diverging wave volumetric imaging using subaperture beamforming," *IEEE Transactions on Ultrasonics, Ferroelectrics, and Frequency Control*, vol. 63, no. 12, pp. 2114–2124, 2016.
- [217] H. G. Kang, S. Bae, P. Kim, *et al.*, "Column-based micro-beamformer for improved 2d beamforming using a matrix array transducer," in *2015 IEEE Biomedical Circuits and Systems Conference (BioCAS)*, IEEE, 2015, pp. 1–4.
- [218] I. O. Wygant, N. S. Jamal, H. J. Lee, *et al.*, "An integrated circuit with transmit beam-forming flip-chip bonded to a 2-d cmut array for 3-d ultrasound imaging," *IEEE transactions on ultrasonics, ferroelectrics, and frequency control*, vol. 56, no. 10, pp. 2145–2156, 2009.
- [219] C. Chen, Z. Chen, D. Bera, *et al.*, "A front-end asic with receive sub-array beam-forming integrated with a 32 * 32 pzt matrix transducer for 3-d transesophageal echocardiography," *IEEE Journal of Solid-State Circuits*, vol. 52, no. 4, pp. 994–1006, 2017.
- [220] K. Chen, H.-S. Lee, and C. G. Sodini, "A column-row-parallel asic architecture for 3-d portable medical ultrasonic imaging," *IEEE Journal of Solid-State Circuits*, vol. 51, no. 3, pp. 738–751, 2015.
- [221] M. Flesch, M. Pernot, J. Provost, *et al.*, "4d in vivo ultrafast ultrasound imaging using a row-column addressed matrix and coherently-compounded orthogonal plane waves," *Physics in Medicine & Biology*, vol. 62, no. 11, p. 4571, 2017.
- [222] M. F. Rasmussen and J. A. Jensen, "3-d ultrasound imaging performance of a row-column addressed 2-d array transducer: A measurement study," in *2013 IEEE International Ultrasonics Symposium (IUS)*, IEEE, 2013, pp. 1460–1463.
- [223] B. Savord and R. Solomon, "Fully sampled matrix transducer for real time 3d ultrasonic imaging," in *IEEE Symposium on Ultrasonics, 2003*, IEEE, vol. 1, 2003, pp. 945–953.
- [224] E. Kang, Q. Ding, M. Shabanimotlagh, *et al.*, "A reconfigurable ultrasound transceiver asic with 24 * 40 elements for 3-d carotid artery imaging," *IEEE Journal of Solid-State Circuits*, vol. 53, no. 7, pp. 2065–2075, 2018.
- [225] F. Hansen, P. Mangell, B. Sonesson, and T. Lanne, "Diameter and compliance in the human common carotid artery-variations with age and sex," *Ultrasound in medicine & biology*, vol. 21, no. 1, pp. 1–9, 1995.
- [226] J. A. Jensen and N. B. Svendsen, "Calculation of pressure fields from arbitrarily shaped, apodized, and excited ultrasound transducers," *IEEE transactions on ultrasonics, ferroelectrics, and frequency control*, vol. 39, no. 2, pp. 262–267, 1992.

- [227] J. A. Jensen, "Field: A program for simulating ultrasound systems," in *10TH NORDICBALTIC CONFERENCE ON BIOMEDICAL IMAGING, VOL. 4, SUPPLEMENT 1, PART 1*: 351–353, Citeseer, 1996.
- [228] H. Hasegawa and H. Kanai, "Effect of element directivity on adaptive beamforming applied to high-frame-rate ultrasound," *IEEE Transactions on Ultrasonics, Ferroelectrics, and Frequency Control*, vol. 62, no. 3, pp. 511–523, 2015. DOI: [10.1109/TUFFC.2015.006973](https://doi.org/10.1109/TUFFC.2015.006973).
- [229] T. Hergum, T. Bjastad, K. Kristoffersen, and H. Torp, "Parallel beamforming using synthetic transmit beams," *IEEE Transactions on Ultrasonics, Ferroelectrics, and Frequency Control*, vol. 54, no. 2, pp. 271–280, 2007. DOI: [10.1109/TUFFC.2007.241](https://doi.org/10.1109/TUFFC.2007.241).
- [230] J. Wang and J.-y. Lu, "Motion artifacts of extended high frame rate imaging," *IEEE Transactions on Ultrasonics, Ferroelectrics, and Frequency Control*, vol. 54, no. 7, pp. 1303–1315, 2007. DOI: [10.1109/TUFFC.2007.391](https://doi.org/10.1109/TUFFC.2007.391).
- [231] J. Kortbek, J. A. Jensen, and K. L. Gammelmark, "Sequential beamforming for synthetic aperture imaging," *Ultrasonics*, vol. 53, no. 1, pp. 1–16, 2013, ISSN: 0041-624X.
- [232] G. Matrone, E. Lashkevich, A. Bertoni, A. Ramalli, A. S. Savoia, and G. Mageses, "Effects of coherence-based beamforming on breast ultrasound elastograms," in *2019 IEEE International Ultrasonics Symposium (IUS)*, 2019, pp. 312–315. DOI: [10.1109/ULTSYM.2019.8926022](https://doi.org/10.1109/ULTSYM.2019.8926022).
- [233] D. Das, A. Sharma, P. Rajendran, and M. Pramanik, "Another decade of photoacoustic imaging," *Physics in Medicine & Biology*, vol. 66, no. 5, 05TR01, 2021.
- [234] A. P. Rao, N. Bokde, and S. Sinha, "Photoacoustic imaging for management of breast cancer: A literature review and future perspectives," *Applied Sciences*, vol. 10, no. 3, p. 767, 2020.
- [235] P. Wray, L. Lin, P. Hu, and L. V. Wang, "Photoacoustic computed tomography of human extremities," *Journal of biomedical optics*, vol. 24, no. 2, p. 026 003, 2019.
- [236] Y. Zhang and L. Wang, "Video-rate ring-array ultrasound and photoacoustic tomography," *IEEE Transactions on Medical Imaging*, vol. 39, no. 12, pp. 4369–4375, 2020.
- [237] C. Cai, X. Wang, K. Si, J. Qian, J. Luo, and C. Ma, "Feature coupling photoacoustic computed tomography for joint reconstruction of initial pressure and sound speed in vivo," *Biomedical Optics Express*, vol. 10, no. 7, pp. 3447–3462, 2019.
- [238] S. Na, J. J. Russin, L. Lin, *et al.*, "Massively parallel functional photoacoustic computed tomography of the human brain," *Nature Biomedical Engineering*, pp. 1–9, 2021.
- [239] P. Rajendran, S. Sahu, R. A. Dienzo, and M. Pramanik, "In vivo detection of venous sinus distension due to intracranial hypotension in small animal using pulsed-laser-diode photoacoustic tomography," *Journal of biophotonics*, vol. 13, no. 6, e201960162, 2020.

- [240] M. Nishiyama, T. Namita, K. Kondo, M. Yamakawa, and T. Shiina, "Ring-array photoacoustic tomography for imaging human finger vasculature," *Journal of biomedical optics*, vol. 24, no. 9, p. 096 005, 2019.
- [241] S. Ermilov, R. Su, M. Zamora, T. Hernandez, V. Nadvoretsky, and A. Oraevsky, "Optoacoustic angiography of peripheral vasculature," in *Photons Plus Ultrasound: Imaging and Sensing 2012*, International Society for Optics and Photonics, vol. 8223, 2012, p. 82230D.
- [242] S. Zackrisson, S. Van De Ven, and S. Gambhir, "Light in and sound out: Emerging translational strategies for photoacoustic imaging," *Cancer research*, vol. 74, no. 4, pp. 979–1004, 2014.
- [243] M. Toi, Y. Asao, Y. Matsumoto, *et al.*, "Visualization of tumor-related blood vessels in human breast by photoacoustic imaging system with a hemispherical detector array," *Scientific reports*, vol. 7, no. 1, pp. 1–11, 2017.
- [244] M. Xu and L. V. Wang, "Photoacoustic imaging in biomedicine," *Review of scientific instruments*, vol. 77, no. 4, p. 041 101, 2006.
- [245] L. Lin, P. Hu, J. Shi, *et al.*, "Single-breath-hold photoacoustic computed tomography of the breast," *Nature communications*, vol. 9, no. 1, pp. 1–9, 2018.
- [246] L. Li, L. Zhu, C. Ma, *et al.*, "Single-impulse panoramic photoacoustic computed tomography of small-animal whole-body dynamics at high spatiotemporal resolution," *Nature biomedical engineering*, vol. 1, no. 5, pp. 1–11, 2017.
- [247] H.-P. F. Brecht, R. Su, M. P. Fronheiser, S. A. Ermilov, A. Conjusteau, and A. A. Oraevsky, "Whole-body three-dimensional optoacoustic tomography system for small animals," *Journal of biomedical optics*, vol. 14, no. 6, p. 064 007, 2009.
- [248] R. A. Kruger, R. B. Lam, D. R. Reinecke, S. P. Del Rio, and R. P. Doyle, "Photoacoustic angiography of the breast," *Medical physics*, vol. 37, no. 11, pp. 6096–6100, 2010.
- [249] Y. Wang, Z. Guo, L. V. Wang, *et al.*, "In vivo three-dimensional photoacoustic imaging based on a clinical matrix array ultrasound probe," *Journal of Biomedical Optics*, vol. 17, no. 6, p. 061 208, 2012.
- [250] M. Xu and L. V. Wang, "Universal back-projection algorithm for photoacoustic computed tomography," *Physical Review E*, vol. 71, no. 1, p. 016 706, 2005.
- [251] M. Xu and L. V. Wang, "Analytic explanation of spatial resolution related to bandwidth and detector aperture size in thermoacoustic or photoacoustic reconstruction," *Physical Review E*, vol. 67, no. 5, p. 056 605, 2003.
- [252] M. Pramanik, G. Ku, and L. V. Wang, "Tangential resolution improvement in thermoacoustic and photoacoustic tomography using a negative acoustic lens," *Journal of biomedical optics*, vol. 14, no. 2, p. 024 028, 2009.
- [253] M. Xu and L. V. Wang, "Pulsed-microwave-induced thermoacoustic tomography: Filtered backprojection in a circular measurement configuration," *Medical physics*, vol. 29, no. 8, pp. 1661–1669, 2002.
- [254] Y. Xu, D. Feng, and L. V. Wang, "Exact frequency-domain reconstruction for thermoacoustic tomography. i. planar geometry," *IEEE transactions on medical imaging*, vol. 21, no. 7, pp. 823–828, 2002.

- [255] S. K. Kalva and M. Pramanik, "Experimental validation of tangential resolution improvement in photoacoustic tomography using modified delay-and-sum reconstruction algorithm," *Journal of Biomedical Optics*, vol. 21, no. 8, p. 086 011, 2016.
- [256] M. Pramanik, "Improving tangential resolution with a modified delay-and-sum reconstruction algorithm in photoacoustic and thermoacoustic tomography," *JOSA A*, vol. 31, no. 3, pp. 621–627, 2014.
- [257] J. Xiao, X. Luo, K. Peng, and B. Wang, "Improved back-projection method for circular-scanning-based photoacoustic tomography with improved tangential resolution," *Applied Optics*, vol. 56, no. 32, pp. 8983–8990, 2017.
- [258] B. Wang, T. Ye, G. Wang, L. Guo, and J. Xiao, "Approximate back-projection method for improving lateral resolution in circular-scanning-based photoacoustic tomography," *Medical Physics*, vol. 48, no. 6, pp. 3011–3021, 2021.
- [259] L. Ding, X. L. Deán-Ben, and D. Razansky, "Real-time model-based inversion in cross-sectional optoacoustic tomography," *IEEE transactions on medical imaging*, vol. 35, no. 8, pp. 1883–1891, 2016.
- [260] M. A. A. Caballero, J. Gateau, X.-L. Déan-Ben, and V. Ntziachristos, "Model-based optoacoustic image reconstruction of large three-dimensional tomographic datasets acquired with an array of directional detectors," *IEEE transactions on medical imaging*, vol. 33, no. 2, pp. 433–443, 2013.
- [261] L. Ding, D. Razansky, and X. L. Deán-Ben, "Model-based reconstruction of large three-dimensional optoacoustic datasets," *IEEE Transactions on Medical Imaging*, vol. 39, no. 9, pp. 2931–2940, 2020.
- [262] L. Ding, X. L. Deán-Ben, and D. Razansky, "Efficient 3-d model-based reconstruction scheme for arbitrary optoacoustic acquisition geometries," *IEEE transactions on medical imaging*, vol. 36, no. 9, pp. 1858–1867, 2017.
- [263] J. Prakash, S. K. Kalva, M. Pramanik, and P. K. Yalavarthy, "Binary photoacoustic tomography for improved vasculature imaging," *Journal of Biomedical Optics*, vol. 26, no. 8, p. 086 004, 2021.
- [264] K. B. Chowdhury, J. Prakash, A. Karlas, D. Jüstel, and V. Ntziachristos, "A synthetic total impulse response characterization method for correction of hand-held optoacoustic images," *IEEE transactions on medical imaging*, vol. 39, no. 10, pp. 3218–3230, 2020.
- [265] D. Queirós, X. L. Déan-Ben, A. Buehler, D. Razansky, A. Rosenthal, and V. Ntziachristos, "Modeling the shape of cylindrically focused transducers in three-dimensional optoacoustic tomography," *Journal of biomedical optics*, vol. 18, no. 7, p. 076 014, 2013.
- [266] M. Schwarz, A. Buehler, and V. Ntziachristos, "Isotropic high resolution optoacoustic imaging with linear detector arrays in bi-directional scanning," *Journal of biophotonics*, vol. 8, no. 1-2, pp. 60–70, 2015.
- [267] S. Hakakzadeh and Z. Kavehvasht, "Blind angle and angular range detection in planar and limited-view geometries for photoacoustic tomography," in *2021 29th Iranian Conference on Electrical Engineering (ICEE)*, IEEE, 2021, pp. 922–926.

- [268] C. Li, G. Ku, and L. V. Wang, "Negative lens concept for photoacoustic tomography," *Physical Review E*, vol. 78, no. 2, p. 021 901, 2008.
- [269] L. Nie, Z. Guo, and L. V. Wang, "Photoacoustic tomography of monkey brain using virtual point ultrasonic transducers," *Journal of biomedical optics*, vol. 16, no. 7, p. 076 005, 2011.
- [270] M. Xu and L. V. Wang, "Analytic explanation of spatial resolution related to bandwidth and detector aperture size in thermoacoustic or photoacoustic reconstruction," *Physical Review E*, vol. 67, no. 5, p. 056 605, 2003.
- [271] H. Azhari, *Basics of biomedical ultrasound for engineers*. John Wiley & Sons, 2010.
- [272] M. Kazemi, Z. Kavehvash, and M. Shabany, "K-space aware multi-static millimeter-wave imaging," *IEEE Transactions on Image Processing*, vol. 28, no. 7, pp. 3613–3623, 2019.
- [273] B. E. Treeby and B. T. Cox, "K-wave: Matlab toolbox for the simulation and reconstruction of photoacoustic wave fields," *Journal of biomedical optics*, vol. 15, no. 2, p. 021 314, 2010.
- [274] H.-P. F. Brecht, R. Su, M. P. Fronheiser, S. A. Ermilov, A. Conjusteau, and A. A. Oraevsky, "Whole-body three-dimensional optoacoustic tomography system for small animals," *Journal of biomedical optics*, vol. 14, no. 6, p. 064 007, 2009.
- [275] R. S. Cobbold, *Foundations of biomedical ultrasound*. Oxford university press, 2006.
- [276] M. Mozaffarzadeh, M. Soozande, F. Fool, *et al.*, "Receive/transmit aperture selection for 3d ultrasound imaging with a 2d matrix transducer," *Applied Sciences*, vol. 10, no. 15, p. 5300, 2020.
- [277] D. M. van Willigen, E. Kang, J. Janjic, *et al.*, "A transceiver asic for a single-cable 64-element intra-vascular ultrasound probe," *IEEE Journal of Solid-State Circuits*, vol. 56, no. 10, pp. 3157–3166, 2021.
- [278] D. Van Willigen, M. Mozaffarzadeh, E. Noothout, *et al.*, "Fabrication and characterization of a prototype forward-looking single-cable 64-element intra-vascular ultrasound probe," in *2019 IEEE International Ultrasonics Symposium (IUS)*, IEEE, 2019, pp. 978–980.
- [279] C. Chen, Z. Chen, D. Bera, *et al.*, "A pitch-matched front-end asic with integrated subarray beamforming adc for miniature 3-d ultrasound probes," *IEEE Journal of Solid-State Circuits*, vol. 53, no. 11, pp. 3050–3064, 2018.
- [280] S. R. Miri Rostami, M. Mozaffarzadeh, M. Ghaffari-Miab, A. Hariri, and J. Jokerst, "Gpu-accelerated double-stage delay-multiply-and-sum algorithm for fast photoacoustic tomography using led excitation and linear arrays," *Ultrasonic imaging*, vol. 41, no. 5, pp. 301–316, 2019.
- [281] E. Schültke, "Theodor kocher's craniometer," *Neurosurgery*, vol. 64, no. 5, pp. 1001–1005, 2009.
- [282] N. K. Coulson, P. A. Chiarelli, D. K. Su, *et al.*, "Ultrasound stylet for non-image-guided ventricular catheterization," *Journal of Neurosurgery: Pediatrics*, vol. 16, no. 4, pp. 393–401, 2015.

- [283] D. Low, J. M. Drake, W. T. Seow, and W. H. Ng, "Management of ventriculo-peritoneal shunts in the paediatric population," *Asian Journal of Neurosurgery*, vol. 5, no. 1, p. 7, 2010.
- [284] J. A. Brown, C. E. Demore, and G. R. Lockwood, "Design and fabrication of annular arrays for high-frequency ultrasound," *IEEE transactions on ultrasonics, ferroelectrics, and frequency control*, vol. 51, no. 8, pp. 1010–1017, 2004.
- [285] F. L. Degertekin, R. O. Guldiken, and M. Karaman, "Annular-ring cmut arrays for forward-looking ivus: Transducer characterization and imaging," *IEEE transactions on ultrasonics, ferroelectrics, and frequency control*, vol. 53, no. 2, pp. 474–482, 2006.
- [286] D. N. Stephens, M. O'Donnell, K. Thomenius, *et al.*, "Experimental studies with a 9f forward-looking intracardiac imaging and ablation catheter," *Journal of Ultrasound in Medicine*, vol. 28, no. 2, pp. 207–215, 2009.
- [287] K Passler, R Nuster, S Gratt, P Burgholzer, and G Paltauf, "Piezoelectric annular array for large depth of field photoacoustic imaging," *Biomedical optics express*, vol. 2, no. 9, pp. 2655–2664, 2011.
- [288] P. Torke, R Nuster, and G Paltauf, "Combination of an annular array with a conical acoustic lens for large depth of field photoacoustic macroscopy," in *Photons Plus Ultrasound: Imaging and Sensing 2019*, SPIE, vol. 10878, 2019, pp. 398–404.
- [289] R. Bernardi, P. Peluso, R. O'Connell, S. Kellogg, and C. Shih, "A dynamically focused annular array," in *1976 Ultrasonics Symposium*, 1976, pp. 157–159. DOI: [10.1109/ULTSYM.1976.196654](https://doi.org/10.1109/ULTSYM.1976.196654).
- [290] H. Melton Jr and F. Thurstone, "Annular array design and logarithmic processing for ultrasonic imaging," *Ultrasound in medicine & biology*, vol. 4, no. 1, pp. 1–12, 1978.
- [291] D. Dietz, S. Parks, and M. Linzer, "Expanding-aperture annular array," *Ultrasonic Imaging*, vol. 1, no. 1, pp. 56–75, 1979.
- [292] S. P. Nasholm, T. F. Johansen, and B. A. Angelsen, "An annular array design proposal with multiple geometric pre-foci," *IEEE transactions on ultrasonics, ferroelectrics, and frequency control*, vol. 56, no. 1, pp. 146–155, 2009.
- [293] R. G. Kolkman, M. C. Pilatou, E. Hondebrink, and F. F. De Mul, "Photoacoustic a-scanning and monitoring of blood content in tissue," in *Biomedical Optoacoustics*, SPIE, vol. 3916, 2000, pp. 76–83.
- [294] R. G. Kolkman, E. Hondebrink, W. Steenbergen, and F. F. de Mul, "In vivo photoacoustic imaging of blood vessels using an extreme-narrow aperture sensor," *IEEE Journal of selected topics in quantum electronics*, vol. 9, no. 2, pp. 343–346, 2003.
- [295] R. G. Kolkman, J. H. Klaessens, E. Hondebrink, *et al.*, "Photoacoustic determination of blood vessel diameter," *Physics in Medicine & Biology*, vol. 49, no. 20, p. 4745, 2004.

- [296] S. Manohar, A. Kharine, J. G. van Hespen, W. Steenbergen, and T. G. van Leeuwen, "Photoacoustic imaging of blood vessels with a double-ring sensor featuring a narrow angular aperture," *Journal of biomedical optics*, vol. 9, no. 6, pp. 1327–1335, 2004.
- [297] R. G. Kolkman, W. Steenbergen, and T. G. van Leeuwen, "In vivo photoacoustic imaging of blood vessels with a pulsed laser diode," *Lasers in medical science*, vol. 21, no. 3, pp. 134–139, 2006.
- [298] X. Yang, M.-L. Li, and L. V. Wang, "Ring-based ultrasonic virtual point detector with applications to photoacoustic tomography," *Applied Physics Letters*, vol. 90, no. 25, p. 251 103, 2007.
- [299] J. Woo and Y. Roh, "Design and fabrication of an annular array high intensity focused ultrasound transducer with an optimal electrode pattern," *Sensors and Actuators A: Physical*, vol. 290, pp. 156–161, 2019.
- [300] P. van Neer, H. Vos, M. Danilouchkine, and N. de Jong, "Simple method for measuring phase transfer functions of transducers," in *2010 IEEE International Ultrasonics Symposium*, IEEE, 2010, pp. 1454–1457.
- [301] P. L. van Neer, G. Matte, J. Sijl, J. M. Borsboom, and N. de Jong, "Transfer functions of us transducers for harmonic imaging and bubble responses," *Ultrasonics*, vol. 46, no. 4, pp. 336–340, 2007.

ACKNOWLEDGEMENT

Life is short and people should enjoy it. I truly enjoyed my PhD studies and will keep enjoying by doing a PostDoctoral research :). I would like to say some words regarding people helped and supported me during my PhD studies

- Nico, thanks for your endless support and help. I learned many things from you, specially how to properly formulate nice and direct-to-the-point sentences in a scientific paper, and how to properly look at scientific problems.
- Martin, thanks for your support and the times you dedicated for me. You taught me how to critically look at papers in literature and be careful with projects I get involved, which made me more selective and increased my standards.
- Guillaume, thanks for your great support and supervision. We spent a lot of time discussing many topics and I learned a lot of things from you. You have been always there for me and made challenging situations easier.
- Nico, Martin and Guillaume, I know that I was very stubborn in the beginning of my PhD studies, but finally could thrive under your supervision and support. I'm still stubborn, but much less.
- Angela, thanks for many many things, your great help in solving all kinds of silly problems from beginning to end, to your hospitality and friendship. And, for speaking Nederlands with me.
- Henry, thanks for being always there and fixing all kinds of problems. I felt really good when I knew that there is always someone which would help me with my IT and computer-related problems.
- Ronald, thanks for your support for IT related problems and most importantly your infinite positive energy.
- My friends/colleagues Ulas, Fabian, Djalma, Boudewine, Jack, Agis, Martijn, Rick and Albe, thank you for the discussions about research and chatting about everything, specially during lunch time.
- My family, father, mother, sister, thank you for your love, endless support and encouragement. Thanks for everything. My hear beats and will beat for you.

Moein Mozaffarzadeh
Delft, the Netherlands
August, 2022

CURRICULUM VITÆ

Moein Mozaffarzadeh

26-Aug-1993 Born in Sary, Iran.

EDUCATION

2018–2022 PhD candidate in the Department of Applied Physics
Delft University of Technology, Delft, the Netherlands

2015–2017 MSc in Biomedical Engineering
Tarbiat Modares University, Tehran, Iran

2011–2015 BSc in Electrical Engineering
Babol University of Technology, Tehran, Iran

PUBLICATIONS

2017–present 24 journal papers, 24 conference proceedings
(please visit my [Google Scholar](#) page for more details)

PATENTS

2021 Methods and systems for transcranial ultrasound imaging

2019 Plane wave ultrasound imaging

WORK EXPERIENCE

2017–2018 Researcher at Tehran University of Medical Sciences, Tehran, Iran

2017–2018 Researcher at Tarbiat Modares University, Tehran, Iran

Reviewer of IEEE Transaction on Medical Imaging, IEEE Transactions on TUFFC, IEEE Transactions on Instrumentation and Measurement, Photoacoustics, Journal of BioPhotonics, Journal of Biomedical Optics, Optics Letters, Ultrasonics, Biomedical Optics Express, Computers in Biology and Medicine, Journal of Imaging.

SKILLS

Programming language	Matlab, C/C++, CUDA, Python
Softwares	Latex, MS Office, PZFlex, Visual Studio, Mendeley, Pycharm
Ultrasound-related Matlab toolbox	Field-II, k-Wave, SimSonic

LANGUAGES

English	Fluent, TOEFL iBT test score: 100
Dutch	A2 level
Farsi	Native

HOBBIES

Playing musical instrument (persian Santoor) at a semi-professional level, Financial market, Movie, Gym

LIST OF PUBLICATIONS

PATENTS

1. **M. Mozaffarzadeh**, G. Renaud, M. D. Verweij, N. De Jong, *METHOD AND SYSTEM FOR TRANSCRANIAL ULTRASOUND IMAGING* (2022).

JOURNAL PAPERS

1. **M. Mozaffarzadeh**, M. D. Verweij, N. De Jong and G. Renaud, *Comparison of Phase-Screen and Geometry-Based Phase Aberration Correction Techniques for Real-Time Transcranial Ultrasound Imaging*, [Applied Sciences](#) 12 (2020).
2. **M. Mozaffarzadeh**, E. Verschuur, M. D. Verweij, N. De Jong and G. Renaud, *Accelerated 2D Real-Time Refraction-Corrected Transcranial Ultrasound Imaging*, [IEEE Transactions on Ultrasonics, Ferroelectrics, and Frequency Control](#) 69 (2022).
3. S. Hakakzadeh, **M. Mozaffarzadeh**, S.M. Mostafavi, Z. Kavehvasht, P. Rajendran, M. D. Verweij, N. De Jong and M. Pramanik, *Multi-angle data acquisition to compensate transducer finite size in photoacoustic tomography*, [Photoacoustics](#) (2022).
4. **M. Mozaffarzadeh**, E. Verschuur, M. D. Verweij, V. Daeichin, N. De Jong and G. Renaud, *Refraction-Corrected Transcranial Ultrasound Imaging through the Human Temporal Window using a Single Probe*, [IEEE Transactions on Ultrasonics, Ferroelectrics, and Frequency Control](#) 69 (2022).
5. **M. Mozaffarzadeh**, C. Moore, E. Barzegar Golmoghani, Y. Mantri, A. Hariri, A. Jorns, L. Fu, M. D. Verweij, M. Orooji, N. de Jong, J. V. Jokerst, *Motion-compensated noninvasive periodontal health monitoring using handheld and motor-based photoacoustic-ultrasound imaging systems.*, [Biomedical Optics Express](#) 12 (2021).
6. **M. Mozaffarzadeh**, C. Minonzio, N. De Jong, M. D. Verweij, S. Hemm, G. Renaud and V. Daeichin, *Erratum: Lamb Waves and Adaptive Beamforming for Aberration Correction in Medical Ultrasound Imaging*, [IEEE Transactions on Ultrasonics, Ferroelectrics, and Frequency Control](#) 68 (2021).
7. **M. Mozaffarzadeh**, C. Minonzio, N. De Jong, M. D. Verweij, S. Hemm and V. Daeichin, *Lamb Waves and Adaptive Beamforming for Aberration Correction in Medical Ultrasound Imaging*, [IEEE Transactions on Ultrasonics, Ferroelectrics, and Frequency Control](#) 68 (2021).
8. **M. Mozaffarzadeh**, M. Soozande, F. Fool, M. A. P. Pertijs, H. J. Vos, M. D. Verweij, J. G. Bosch and N. de Jong, *Receive/Transmit Aperture Selection for 3D Ultrasound Imaging with a 2D Matrix Transducer*, [Applied Sciences](#) 10 (2020).
9. **M. Mozaffarzadeh**, M. Haji Heidari Varnosfaderani, A. Sharma, M. Pramanik, N. De Jong and M. D. Verweij, *Enhanced Contrast Acoustic-Resolution Photoacoustic Microscopy using Double-Stage Delay-Multiply-and-Sum Beamformer for Vasculature Imaging*, [Journal of Biophotonics](#) 12 (2019). e201900133.

CONFERENCE PAPERS

1. **M. Mozaffarzadeh**, M. D. Verweij, N. De Jong and G. Renaud, *A Comparison Study on Geometry-Based and Phase-Screen Aberration Correction Techniques for Transcranial Ultrasound Imaging*, in International Ultrasonics Symposium (IUS) (IEEE, 2022).
2. **M. Mozaffarzadeh**, M. D. Verweij, N. De Jong and G. Renaud, *Accelerated Real-Time Refraction-Corrected Transcranial Ultrasound Imaging with a Single Array Transducer*, in International Ultrasonics Symposium (IUS) (IEEE, 2022).
3. F. Hosseini, **M. Mozaffarzadeh**, A. Mahloojifar, M. D. Verweij, and N. De Jong, *Numerical Investigation of Multiple Scattering caused by Temporal Bone in Transcranial Photoacoustic Imaging*, in International Ultrasonics Symposium (IUS) (IEEE, 2022).
4. S. Hakakzadeh, **M. Mozaffarzadeh**, S. M. Mostafavi, M. Amjadian, Z. Kavehvasht, M. D. Verweij and N. de Jong, *Finite Transducer Size Compensation in Two-Dimensional Photoacoustic Computed Tomography*, in International Ultrasonics Symposium (IUS) (IEEE, 2021).
5. **M. Mozaffarzadeh**, E. Verschuur, M. D. Verweij, V. Daeichin, N. De Jong and G. Renaud, *Transcranial Ultrasound Imaging with Estimating the Geometry, Position and Wave-Speed of Temporal Bone*, in International Ultrasonics Symposium (IUS) (IEEE, 2021).
6. **M. Mozaffarzadeh**, C. Minonzio, M. D. Verweij, S. Hemm and V. Daeichin, *Phase Aberration Correction in Transcranial Ultrasound Imaging using Averaged Sound Velocity Map in Delay-and-Sum Beamformer*, in International Ultrasonics Symposium (IUS) (IEEE, 2019).
7. D. van Willigen, **M. Mozaffarzadeh**, E. Noothout, M. D. Verweij, N. de Jong, M. Pertijs, and V. Daeichin, *Fabrication and Characterization of a Prototype Forward-Looking Single-Cable 64-Element Intra-Vascular Ultrasound Probe*, in International Ultrasonics Symposium (IUS) (IEEE, 2019).
8. F. Fool, H.J. Vos, M. Shabanimotlagh, M. Soozande, **M. Mozaffarzadeh**, T. Kim, E. Kang, M. Pertijs, N. de Jong, M. D. Verweij, *3D high frame rate flow measurement using a prototype matrix transducer for carotid imaging*, in International Ultrasonics Symposium (IUS) (IEEE, 2019).